ATOMISTIC NORMAL MODE ANALYSIS OF LARGE BIOMOLECULAR SYSTEMS: THEORY AND APPLICATIONS

by

Eric Charles Dykeman

A Dissertation Presented in Partial Fulfillment
of the Requirements for the Degree
Doctor of Philosophy

ARIZONA STATE UNIVERSITY

May 2008

ATOMISTIC NORMAL MODE ANALYSIS OF LARGE BIOMOLECULAR SYSTEMS:

THEORY AND APPLICATIONS

by

Eric Charles Dykeman

has been approved

April 2008

Graduate Supervisory Committee:

Otto F. Sankey, Chair
John B. Page
Stuart M. Lindsay
John Shumway
Ralph V. Chamberlin

ACCEPTED BY THE GRADUATE COLLEGE

ABSTRACT

An Order (N) technique, the phonon functional method, for the study of the low frequency mechanical modes of large molecular systems is developed where the displacement patterns are modeled with atomic detail. The method is based on ideas from electronic structure theory and uses an energy functional to find the lowest frequency phonon states of a classical dynamical matrix below a pseudo-Fermi level. The resulting method is iterative and requires only the operation of the dynamical matrix on a set of vectors.

An analysis of the low frequency motions of three viral capsids, the satellite tobacco necrosis virus, the cowpea chlorotic mottle virus, and the M13 bacteriophage are calculated using the technique. The Raman spectra of the viral capsids are calculated using the atomistic displacement patterns and an empirical bond polarizability model. In addition, the mechanical modes and Raman spectra of the M13 bacteriophage are also found with continuum elastic theory and an amorphous isotropic bond polarizability model which are then compared with the atomistic calculations.

The mechanical modes of an adenosine triphosphate binding cassette are also calculated using the phonon functional method. The results indicate two clear modes that are responsible for the transport process. Based on the two normal modes a transport cycle is hypothesized.

The possibility of viron destruction through a resonant excitation of its capsids mechanical modes is examined next. A recent impulsive stimulated Raman scattering experiment of the M13 bacteriophage capsid is theoretically modeled using classical molecular dynamics. The results are analyzed with a simple driven harmonic oscillator approach and indicate the existence of an "amplitude threshold" which causes the virus capsid to break apart once reached.

Finally, the activation relaxation technique is extended to atomistic systems with explicit water. A test of the extension is performed on a small single amino acid protein. The results reveal difficulty extending the technique to systems with explicit water.

ACKNOWLEDGMENTS

There are many people that I would like to thank for their encouragement and support over the past few years. First I would like to thank my advisor Otto Sankey for providing unwavering encouragement, wisdom, and an infectious enthusiasm for science. All of the projects presented in this work have been done in collaboration with him and it has been a joy to work with him on all of them.

I would also like to thank all of my professors for providing a rigorous physics education and for always having the highest expectations of their students. They have all greatly guided me during my studies. I wish to give special thanks to professors John Page, Kevin Schmidt, William Kaufmann, and Otto Sankey.

Thanks to professor K.-T. Tsen and Dayrn Benson for many stimulating discussions about ISRS and virus vibrations.

Thanks to my friends as well as my fellow students for their friendship and guidance.

Finally, I would like to thank my family, especially my mom and sister, whose support has been so helpful during my studies.

TABLE OF CONTENTS

Page

Page

Page

LIST OF TABLES

LIST OF FIGURES

Figure Page

Figure Page

CHAPTER 1

INTRODUCTION

I. BACKGROUND AND MOTIVATION

The computational simulation of biological systems is a diverse and challenging field that involves modeling on nearly all length and time scales. On the nanoscale level, molecular dynamics has been a popular method for the computational simulation of biological processes. The molecular dynamics algorithm is quite simple, using Newtons equations to form a trajectory of the system over time. However, there are a variety of problems with molecular dynamics that have been difficult to overcome. For example, many biochemical processes in the cell, such as protein folding and enzymatic activities, can take place on the order of microseconds to milliseconds and often involve hundreds of thousands or even millions of atoms. Since a small time step of about 1 fs is required due to the fast hydrogen motions of the system, a molecular dynamics simulation will require 10^9 steps to reach the microsecond time range of many biochemical processes.

The proliferation of supercomputing centers has helped with the molecular dynamics time scale issue to some extent. For example, Freddolino *et al.* have recently performed a short 50 ns molecular dynamics simulation of an entire organism [1], the satellite tobacco mosaic virus. Yet, despite advances in computational power, molecular dynamics has yet to reach the time scale of milliseconds for large systems.

An alternative to molecular dynamics is normal mode analysis. Tama and Sanejouand [2] have noted that there is experimental evidence that the functional and enzymatic activity of most biological molecules can be explained by a few of the lowest frequency mechanical modes computed from a harmonic analysis. Sometimes a single low frequency normal mode is sufficient to describe nearly all of the functional motion. Normal mode analysis has had much success in recent years. For example, normal mode analysis has

successfully determined large scale motions of citrate synthase [3] that are involved in its enzymatic activity. A similar study of the mechanics of citrate synthase using molecular dynamics may require several microseconds of simulation time. This makes normal mode analysis a very attractive tool for the study of the mechanical motions of large biological molecules.

One of the key problems with using a normal mode analysis to study large molecules is that it requires the formation and diagonalization of an $3N \times 3N$ matrix (the dynamical matrix). The diagonalization typically scales as Order (N^3) while the computer memory required to store the dynamical matrix scales as Order (N^2). As a result, the number of atoms that can be treated with a direct formation and diagonalization of the dynamical matrix is on the order of a few thousand atoms at the present time.

In order to overcome the memory issue, most normal mode analysis employ coarse graining techniques [4, 5, 6]. In a coarse graining normal mode analysis, individual atomic motions are replaced by group motions such as the movement of a single protein in a large virus [7]. This reduces the dynamical matrix to a smaller size that is reasonable for storage in computer memory. The eigenvectors of the smaller dynamical matrix are then used to construct vibrational mode patterns using the smaller set of group motions. The result of the coarse graining procedure is that the fine detail of the vibrational mode patterns are muted and their corresponding frequencies approximate. Generally this approach works well for describing the low frequency modes of large molecules since these are likely to involve large groups of atoms moving in unison; and this is were the method is typically used. However, there are cases were atomic detail in the low frequency vibrational mode patterns of large molecules is useful, if not essential. For example, Babincova *et al.* [8] have suggested that the vibrational modes of viruses, such as HIV, can be resonantly excited through a hyper

sound or ultrasound excitation to produce damage. The theoretical study of such ideas requires an atomic level description of the vibrational modes in order to properly account for coupling to external probes.

The main work of this dissertation develops a low frequency normal mode analysis technique for large atomic systems ($> 10^4$ atoms) where the vibrational mode patters are modeled with atomic detail. The technique is based on Order (N) electronic structure methods and can be used to determine a subset of the lowest eigenvalues and eigenvectors of the full $3N \times 3N$ dynamical matrix. As discussed above, an atomistic normal mode analysis for large systems can be important for certain situations, but the work presented in this dissertation will show that their are numerous other applications were an atomistic normal mode analysis can be quite useful.

II. DISSERTATION OUTLINE

The presentation of material in this dissertation is broken into two parts; theoretical development and applications. The next four chapters (Chapters 2 - 5) present theoretical models and computational techniques that are used in specific applications that are discussed in Chapters 6 - 8. Readers comfortable with the theories presented in Chapters 2 through 5 may skip to Chapter 6 for an analysis of various applications.

In order to model biological systems using techniques other than molecular dynamics, the *Saguaro* biological simulation package was developed based on classical empirical potential energy models [9, 10, 11]. All of the calculations performed in this dissertation were done using the *Saguaro* package. Chapter 2 gives a general overview of the types of simulations that *Saguaro* is capable of as well as detailed descriptions of the molecular mechanical energy models used and the molecular dynamics integrator. Two methods used to

calculate electrostatic interactions, the particle mesh Ewald method [12] and the generalized Born model [13, 14], are discussed in detail.

Chapter 3 presents a necessary review of group theory which is needed for later chapters when symmetry operators for the icosahedral point group of viruses are used. In addition, a method for determining the group theory irreducible representation matrices *and* the character table from only the rotation matrices for the group is described. The advantage of this technique is that the irreducible representation matrices and basis vectors can be constructed using a simple computer algorithm.

In Chapter 4, a new method for the determination of *low* frequency vibrational modes called the phonon functional method is discussed. The method which is based on ideas from electronic structure theory [15, 16, 17, 18] is capable of finding the low frequency mode patterns of large molecules atomistically. This is in contrast to the usual methods of continuum theories or coarse graining were a reduced basis is used to construct approximate mode patterns for the molecule. The phonon functional method presented in Chapter 4 constructs vibrational displacement patterns from the full Cartesian basis of three degrees of freedom for each atom and will produce the correct displacement pattern. The method is discussed from both theoretical and computational standpoints.

Chapter 5 presents some additional theories that have been developed for specific applications. These include continuum elastic theory for vibrations of an isotropic material, formulas to predict Raman intensities, and an equation describing the coupling of light to the mechanical modes of a molecule for use in classical molecular dynamics simulations.

Chapter 6 begins the presentation and discussion of various applications. In Chapter 6, the mechanical modes of various viral capsids of two varieties, icosahedral and tubular, are calculated using the phonon functional method. The types of capsids studied include

the icosahedral satellite tobacco necrosis virus, the cowpea chlorotic mottle virus, and the tubular M13 bacteriophage. Comparisons of the phonon functional method with other models such as the elastic network model [4] are made whenever possible. Raman spectra predictions of all three viral capsids are made using an empirical bond polarizability model [19, 20, 21]. The Raman spectra predictions can be useful in determining which modes will couple to external probes the strongest and therefore may produce the most damage from a pulsed laser source.

Next in Chapter 7, the mechanical modes of large molecules and complex molecular assemblies are discussed. Though there are many large molecules that can be studied with a harmonic normal mode analysis only one family of large molecules, periplasmic binding proteins and adenosine triphosphate binding cassettes, will be examined. These molecules belong to a group of proteins that are responsible for the transport of nutrients (toxins) into (out) of the cell membrane. Understanding the conformational changes of these molecules can help to develop novel nano devices such as biosensors [22] that sense very small concentrations of chemicals, or the biochemical mechanisms involved in Human diseases such as cystic fibrosis [23, 24].

In Chapter 8, miscellaneous applications are presented. First, a molecular dynamics simulation of the M13 bacteriophage in the presence of a light source is discussed. The simulation is a classical theoretical investigation of impulsive stimulated Raman scattering experiments that have been performed on the phage [25, 26, 27]. Next, the activation relaxation technique (ART) [28, 29] is presented as a possible method of exploring the conformational states of peptides. Two ways of using ART are discussed. The first explores the ART method with a fully atomistic molecule and *implicit* water. The second examines

the ART method using *explicit* water. The conformational states of a small peptide, alanine dipeptide, are studied as an example.

In the last chapter, Chapter 9, the results and theories presented in this dissertation are concluded and summarized.

CHAPTER 2

SAGUARO SIMULATION PACKAGE

I. INTRODUCTION

The projects presented in this dissertation all require an atomistic classical energy model describing the various interactions between atoms. A typical classical empirical energy model that is used in molecular dynamics simulation packages such as AMBER [9] and CHARMM [10] is often the first choice when choosing an energy model (force field) that is atomistic in its description of forces. The difference between the AMBER and CHARMM force field is in the parametrization of the various terms in the energy equation (*e.g.* the point charges that are assigned to each atom of a molecule in order to describe its electrostatic potential).

While the AMBER and CHARMM packages are capable of calculating the energy and forces necessary for some of the projects presented in later chapters, the editing of the computer code that would be required to perform the specific calculations that are of interest would be difficult and time consuming. In addition, available molecular dynamics simulation packages are often limited to a single force field model. For these reasons, the *Saguaro* simulation package was developed for the specific applications described in this dissertation.

In this chapter, the *Saguaro* simulation package and its capabilities are discussed. First, the classical atomistic energy model used in *Saguaro* is discussed followed by a presentation of the particle mesh Ewald [12, 30] and generalized Born solvation model [13] used to calculate electrostatic interactions. Finally, each of the various simulations available in *Saguaro* are briefly described.

II. CLASSICAL FORCE FIELD MODEL

The general form used in nearly all classical atomistic molecular dynamics simulations is given by [9, 11]

$$\begin{aligned} V(\vec{r_1}, \vec{r_2}, \ldots) &= \sum_{bonds} k_b (r - r_{eq})^2 + \sum_{angles} k_a (\theta - \theta_{eq})^2 \\ &+ \sum_{dihedrals} \frac{v_n}{2} \left[1 + \cos\left(n\phi - \gamma\right)\right] + \frac{1}{2} \sum_{ij} \left(\frac{q_i q_j}{\epsilon r} + \frac{A}{r^{12}} - \frac{B}{r^6} \right). \end{aligned} \tag{2.1}$$

The parameters k_b, k_a, v_n along with the van der Walls coefficients A and B are determined empirically from experimental data from various molecules such as benzene. The q_i are the partial charges that are given to each atom in the molecule to reproduce its electrostatic potential. These are usually determined by fitting the electrostatic potential made by the system of point charges to the potential obtained from a quantum chemistry calculation [9].

The bonded interactions (bonds, angles and dihedrals) provide a classical description of the stretching of a bond, the bending between two bonds, or rotation about a single bond. The stretching, bending and rotating is illustrated in Figure 1. The stretching and bending is considered to be small and thus can be represented to a first approximation as a harmonic potential with spring constants k_b and k_a. The dihedral term describes a rotation about the bond and is given by a Fourier expansion. Typically, only one or two terms are needed to reproduce the potential energy. For example, the rotation about the C-C bond in C_2H_6 can be described by $1 + \cos(3\phi)$. A plot of the dihedral energy as a function of the dihedral angle ϕ for C_2H_6 is shown in Figure 2. The potential energy maxima correspond to the positions where the hydrogens (on opposite sides of the C-C bond) are aligned with each other. This occurs three times on the interval $[0, 2\pi]$. For C_2H_6, there are a total of nine unique paths (H-C-C-H) between a single hydrogen on one side to another hydrogen on

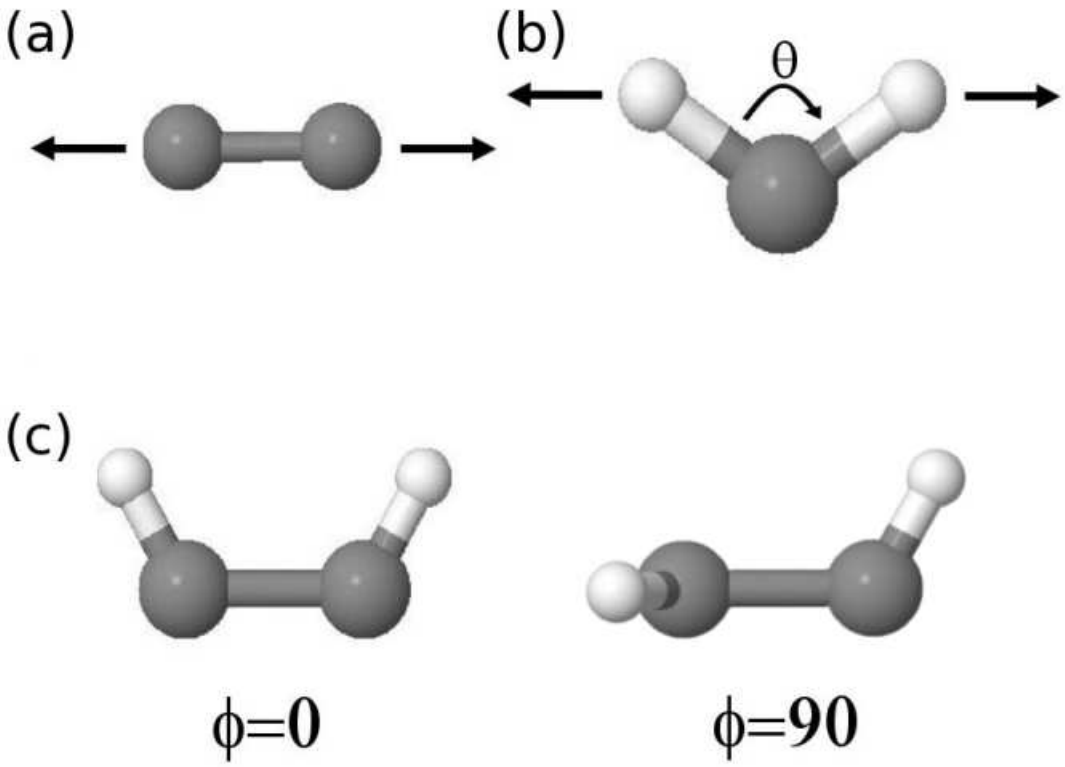

FIG. 1. Illustration of the three different types of bonded interactions used in a classical molecular mechanical force field. (a) Harmonic stretching of a bond. (b) Harmonic bending between two bonds. (c) A rotation about a single bond. Dihedral angles of $\phi = 0$ and $\phi = 90^\circ$ are shown.

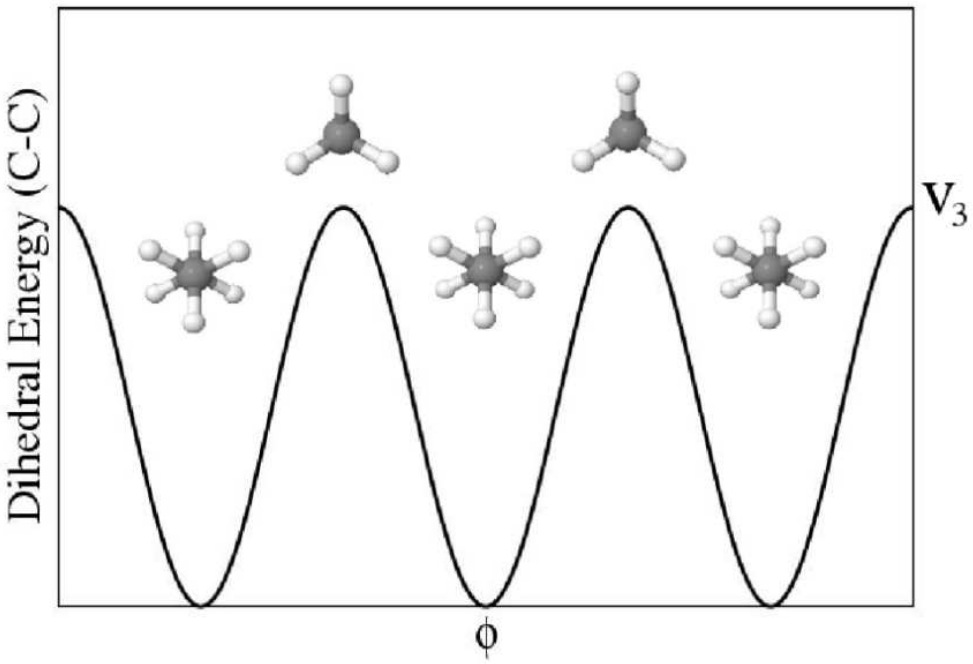

FIG. 2. A plot of the dihedral energy of ethane as a function of the dihedral angle ϕ. Here, the dihedral energy is given by the single Fourier term $E(\phi) = v_3 \left[1 + \cos\left(3\phi\right)\right]/2$. There are three energy maxima which correspond to the alignment of hydrogens on either side of the bond.

the other. To prevent over counting, the total dihedral energy of the bond (v_n) is equally divided among all bond paths.

The non-bonded interactions contain two terms that describe the electrostatics of the system, the Coulomb term and the van der Waals term. The non-bonded interactions extend over all atoms with two exceptions. The first corresponds to the situation when atoms in the same molecule are separated by, at most, two bonds. These interactions are completely excluded. The second exception is for two atoms separated by exactly three bonds. In this case, both the Coulomb and van der Waals interactions are then reduced by

a scaling factor, mimicking a weak dielectric. Typical scaling factors used for Coulomb and van der Waals interactions are 1/1.2 and 1/2.0 respectively.

The non-bonded terms have the most computational expense since they scale as Order (N^2), where N is the number of atoms in the system. A cutoff can be used for both the Coulomb and van der Waals terms reducing the computational expense to Order (N). Generally though, the Coulomb interactions are only truncated when using an implicit solvent model such as the generalized Born model [13] where there is a strong dielectric screening. For periodic systems however, the Coulomb sum is conditionally convergent and an Ewald sum [31] must be used. The calculation of a standard Ewald sum scales as N^2 but through the use of the particle mesh Ewald method [12, 30] the Coulomb part of the non-bonded interactions can be computed in Order ($N \log(N)$) operations.

III. PARTICLE MESH EWALD METHOD FOR COULOMB SUMS

For periodic boundary conditions, the Coulomb electrostatic energy of the unit cell is given by

$$E(\vec{r}_1, \vec{r}_2, \cdots, \vec{r}_N) = \frac{1}{2} \sum_{n}^{'} \sum_{i,j} \frac{q_i q_j}{\left| \vec{r}_i - \vec{r}_j + \vec{R}_n \right|}, \tag{2.2}$$

where $\vec{R}_n$ is a lattice vector of the crystal and the prime denotes that terms with $\vec{R}_0 = 0$ and $i = j$ are excluded. The lattice vectors can be written in terms of the primitive lattice vectors $\vec{a}_1$, $\vec{a}_2$, and $\vec{a}_3$ as, $\vec{R}_n = n_1\vec{a}_1 + n_2\vec{a}_2 + n_3\vec{a}_3$. The summation in Equation (2.2) can not be truncated due to its slow convergence.

In 1921, Ewald [31] published a paper which showed that slowly converging sums with $1/r$ dependence could be rewritten in terms of two rapidly converging sums. The first term is a sum of the "direct" lattice vectors ($\vec{R}_n$) and is thus called the direct sum. The second term is a sum over the reciprocal lattice vectors $\vec{G}_m = m_1\vec{b}_1 + m_2\vec{b}_2 + m_3\vec{b}_3$, where $\vec{b}_i$ are the primitive lattice vectors of the reciprocal unit cell. The direct sum, E_{dir}, takes

the form

$$E_{dir} = \frac{1}{2}\sum_{n}{}' \sum_{i,j=1}^{N} \frac{q_i q_j \mathrm{erfc}\left(\beta\left|\vec{r}_i - \vec{r}_j + \vec{R}_n\right|\right)}{\left|\vec{r}_i - \vec{r}_j + \vec{R}_n\right|}, \tag{2.3}$$

while the reciprocal sum, E_{rec}, is given by

$$E_{rec} = \frac{1}{2\pi V}\sum_{m\neq 0} \frac{\exp\left(-\pi^2|\vec{G}_m|^2/\beta^2\right)}{|\vec{G}_m|^2} S(\vec{G}_m)S(-\vec{G}_m). \tag{2.4}$$

The total Coulomb energy of the unit cell is then the sum of the direct term and the reciprocal term. Both Equation (2.3) and (2.4) can be truncated due to the fast convergence of the complementary error function and the Gaussian. The term $S(\vec{G}_m)$ in Equation (2.4) is the structure factor defined by

$$S(\vec{G}_m) = \sum_{j=1}^{N} q_j \exp\left(2\pi i \vec{G}_m \cdot \vec{r}_j\right). \tag{2.5}$$

The term β present in the direct and reciprocal sums can be chosen to be nearly any value. Larger values of β will force the reciprocal sum to extend over more reciprocal lattice vectors $\vec{G}_m$, while smaller values will cause an increase in the number of neighbor pairs to sum over in the direct energy term. The direct sum is easily calculated in Order (N) operations with an appropriate choice of β. The reciprocal sum however will then be of Order (N^2) since the structure factor must be calculated for each reciprocal lattice vector and the reciprocal sum will approximately extend over N vectors.

The goal of the particle mesh method [12, 30] is to calculate the reciprocal energy term in the Ewald summation in Order $(N\log(N))$ steps by interpolating the exponential in the structure factor at equally spaced points (mesh points) in the primitive (not reciprocal) cell using a Cardinal B-spline [32]. The structure factor can then be written in the form

$$\begin{aligned} S(\vec{G}_m) &= \sum_{k_1=0}^{K_1-1}\sum_{k_2=0}^{K_2-1}\sum_{k_3=0}^{K_3-1} Q(k_1,k_2,k_3)\exp\left[2\pi i\left(\frac{m_1k_1}{K_1}+\frac{m_2k_2}{K_2}+\frac{m_3k_3}{K_3}\right)\right] \\ &= F(Q)(k_1,k_2,k_3), \end{aligned} \tag{2.6}$$

where $F(Q)$ denotes the discrete three dimensional Fourier transform of the array Q. The numbers K_i correspond to the number of mesh points that the primitive cell is broken up into along each lattice vector. In general, the more mesh points used, the more accurate will be the interpolation and the final answer for E_{rec}. The $K_1 \times K_2 \times K_3$ array Q,

$$\begin{aligned} Q(k_1,k_2,k_3) &= \sum_{i=1}^{N} \sum_{n_1,n_2,n_3} q_i M_n(u_{1i} - k_1 - n_1 K_1) \\ &\times \quad M_n(u_{2i} - k_2 - n_2 K_2) M_n(u_{3i} - k_3 - n_3 K_3), \end{aligned} \tag{2.7}$$

is calculated in Order (N) steps by evaluating the Cardinal B-splines (M_n) at the scaled atomic positions $u_{1i} = \vec{a}_1 \cdot \vec{r}_i$, $u_{2i} = \vec{a}_2 \cdot \vec{r}_i$, *etc.* A simple formula describes the Cardinal B-spline functions and is given by

$$M_n(u) = \frac{1}{(n-1)!} \sum_{k=0}^{n} (-1)^k \frac{n!}{k!(n-k)!} (u-k)_+^{n-1}, \tag{2.8}$$

where n is an integer that denotes the order of the spline and the $+$ operator is defined as $u_+ = \max(u, 0)$. A spline order of $n = 4$ is typically used in most particle mesh applications. Since the Cardinal B-spline functions are non-zero in the range $0 < u < n$, only a finite number of lattice vector coefficients n_i in Equation (2.7) will contribute to Q.

The reciprocal energy term [Eq. (2.4)] takes the final form

$$E_{rec} = \frac{1}{2} \sum_{m_1=0}^{K_1-1} \sum_{m_2=0}^{K_2-1} \sum_{m_3=0}^{K_3-1} \theta \star Q(m_1,m_2,m_3) Q(m_1,m_2,m_3), \tag{2.9}$$

where $\theta \star Q$ denotes the convolution operation, $\theta = F(B \cdot C)$, and B and C are constant $K_1 \times K_2 \times K_3$ arrays given by

$$\begin{aligned} B(m_1,m_2,m_3) &= |b_1(m_1)|^2 \cdot |b_2(m_2)|^2, \cdot |b_3(m_3)|^2 \\ C(m_1,m_2,m_3) &= \frac{1}{\pi V} \frac{\exp\left(-\pi^2 |\vec{G}_m|^2 / \beta^2\right)}{|\vec{G}_m|^2}. \end{aligned} \tag{2.10}$$

The value of $C(0,0,0)$ is set to zero in order to properly exclude the $m \neq 0$ term in Equation (2.4). For the other m values, the reciprocal lattice vector is defined by $\vec{G}_m =$

$m_1'\vec{b}_1 + m_1'\vec{b}_1 + m_1'\vec{b}_1$ with $m_i' = m_i$ for $0 \leq m_i \leq K_i/2$ and $m_i' = m_i - K_i$ otherwise. The factors $b_1(m_1)$ are determined by

$$\begin{aligned} b_i(m_i) &= \exp\left(2\pi i(n-1)m_i/K_i\right) \\ &\times \left[\sum_{k=0}^{n-2} M_n(k+1)\exp\left(2\pi i m_i k/K_i\right)\right]^{-1}, \end{aligned} \tag{2.11}$$

where n is the order of the Cardinal B-spline.

The particle mesh procedure to evaluate the Coulomb energy of a periodic unit cell can now be described as follows. Using Equation (2.10) the constant array $B \cdot C$ is formed and permanently stored. Then for each energy evaluation, the array Q is calculated using Equation (2.7) and *inverse* fast Fourier transformed to obtain $F^{-1}(Q)$. Multiplying by the array $B \cdot C = F^{-1}(\theta)$ and fast Fourier transforming, the convolution $(\theta \star Q)$ is formed. Once the convolution $(\theta \star Q)$ is computed, the reciprocal energy term is calculated with Equation (2.9). This procedure takes $N \log(N)$ operations; N to form the Q array and perform the reciprocal sum, and $N \log(N)$ to form the convolution. The direct energy term is then easily calculated in Order (N) operations since the sum can be truncated.

IV. GENERALIZED BORN MODEL

Often in the simulation of large molecules (the solute), a disproportionate amount of time is spent on the calculation of solvent-solute and solvent-solvent interactions. This is due to the amount of solvent that is needed to place the solute in a periodic box of appropriate size so that electrostatic interactions of the solute with its periodic images are negligible.

A different route that is sometimes taken for very large molecules is to use an implicit solvation model for the solute-solvent interactions. This greatly reduces the size of the problem by removing the explicit solvent molecules from the simulation. There are many

methods for the treatment of solvation effects. The method that is used here is based on the Born model for solvation of ions [33], first published in 1920 and later developed into the generalized Born model by Bashford, Case, Still, and Tsui [13, 14, 34].

Born considered a charged ion with radius a (the intrinsic Born radius) and calculated the energy required to place the ion in a dielectric ϵ. The displacement field for the ion can be approximated as $\vec{D} \approx q\hat{r}/r^2$. This is sometimes referred to as the Coulomb field approximation [13]. For an ion, this approximation should be very good and the resulting energy of the ion in the dielectric is [35]

$$\begin{aligned} W &= \frac{1}{8\pi}\int \frac{\vec{D}}{\epsilon}\cdot\vec{D}dV \\ &= \frac{1}{8\pi}\int_{in}\frac{q^2}{r^4\epsilon_{in}}dV + \frac{1}{8\pi}\int_{ex}\frac{q^2}{r^4\epsilon_{ex}}dV. \end{aligned} \tag{2.12}$$

The integral has been split into two regions; the interior region of the charged ion ($r < a$) where the dielectric is ϵ_{in}, and the exterior region where the dielectric is ϵ_{ex}. The solvation energy is the amount of energy required to move the charged ion from vacuum where $\epsilon_{ex} = 1$ to the solvent where $\epsilon_{ex} = \epsilon_s$. Assuming that the interior dielectric remains constant as the ion is moved from vacuum to solvent, the solvation free energy due to the polarization of the solvent becomes

$$\begin{aligned} \Delta F_{pol} &= W_{solvent} - W_{vacuum} \\ &= -\frac{1}{8\pi}\left(1 - \frac{1}{\epsilon_s}\right)\int_{ex}\frac{q^2}{r^4}dV. \end{aligned} \tag{2.13}$$

For an ion with intrinsic Born radius a, the integral is calculated as

$$\begin{aligned} \int_{ex}\frac{1}{r^4}dV &= \int_a^\infty \frac{1}{r^4}dV \\ &= 4\pi a^{-1}, \end{aligned} \tag{2.14}$$

and the solvation free energy for a single ion becomes

$$\Delta F_{pol} = -\frac{1}{2}\left(1 - \frac{1}{\epsilon_s}\right)\frac{q^2}{a}. \tag{2.15}$$

Equation (2.15) gives the energy required to move a charged ion from vacuum to a solvent of dielectric ϵ_s. For a system of charged spheres (or point charges) separated by large distances, the total Coulomb energy in the dielectric is the sum of solvation energies for the ions [Eq. (2.15)] plus the Coulomb interaction energy in the dielectric medium,

$$E_{coul} = \frac{1}{2}\sum_{i,j}{}' \frac{q_i q_j}{\epsilon_s r_{ij}} - \frac{1}{2}\left(1 - \frac{1}{\epsilon_s}\right)\sum_i \frac{q_i^2}{a_i}, \tag{2.16}$$

where the prime denotes terms with $i = j$ are excluded from the sum. The intrinsic Born radius a is usually chosen such that the experimental free energy of solvation is the same as Equation (2.15).

For general cases where the system of charges are closely spaced and essentially form a cavity in the dielectric, Equation (2.16) is no longer valid and must be adjusted. Figure 3 (a) and (b) illustrates the formation of a cavity (with dielectric ϵ_{in}) in the dielectric medium. As a result, the displacement field is no longer radial and the Coulomb field approximation is no longer valid requiring an adjustment to the intrinsic Born radii. In addition, the cavity also introduces a distance dependent dielectric, so that the interaction energy between two charges in the molecule is no longer simply given by $q_i q_j/\epsilon_s r_{ij}$.

The generalized Born model [13, 34] attempts to fix these problems by introducing a function f_{GB} which replaces the distance between two atoms, *i.e.* $1/r_{ij} \to 1/f_{GB}$. The function is given by [34]

$$f_{GB} = \left(r_{ij}^2 + \alpha_i \alpha_j \exp\left(-r_{ij}^2/4\alpha_i\alpha_j\right)\right)^{\frac{1}{2}}, \tag{2.17}$$

where α_i are "effective" Born radii (described below). The generalized Born function attempts to "extrapolate" between two extremes; short distances where the dielectric is less

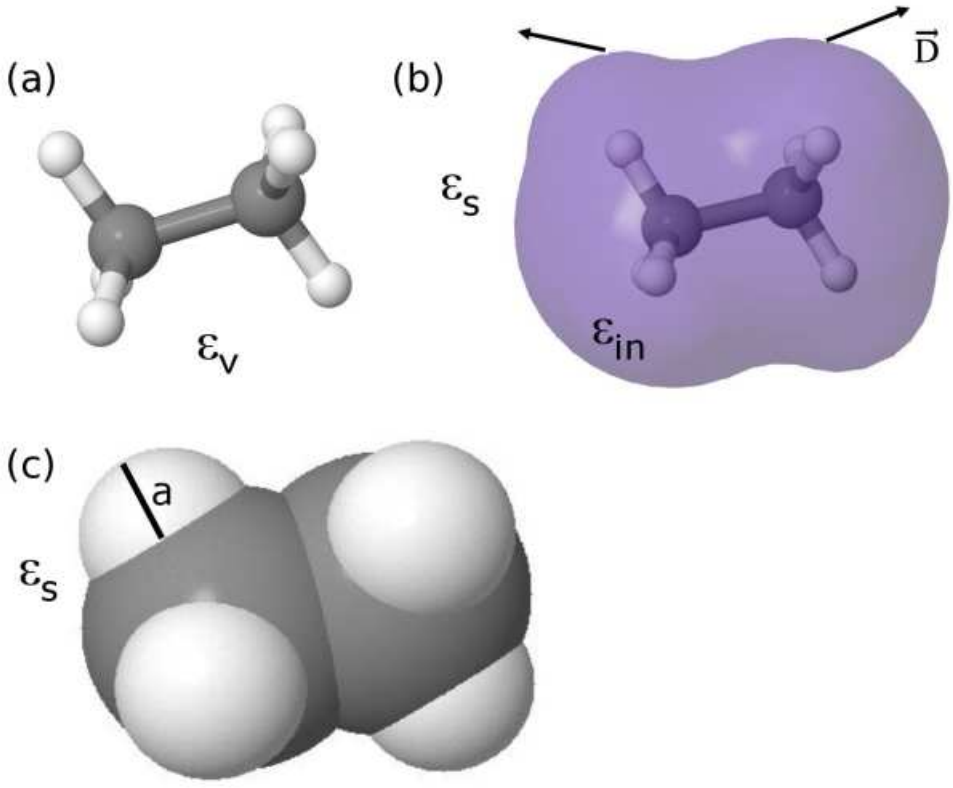

FIG. 3. Illustration of the effects of placing a single molecule of C_2H_6 into a dielectric medium of dielectric $\epsilon_s > 1$. (a) A single molecule of C_2H_6 in vacuum. (b) The placement of C_2H_6 into the dielectric forms a cavity of weaker dielectric ϵ_{in}. The displacement field is no longer radial. (c) Approximating the cavity using overlapping spheres with radii a_i, the intrinsic Born radii.

than that of the medium, and long distances where the interaction is essentially $q_i q_j/\epsilon_s r_{ij}$. The generalized Born function gives approximately the Onsager result for a dipole in a spherical cavity [34, 36] for the case when oppositely charged particles are separated by a short distance.

The effective Born radii (α_i) used in Equation (2.17) are approximated as

$$\alpha_i^{-1} = a_i^{-1} - \int_{in} \frac{1}{r^4} dV, \tag{2.18}$$

where again a_i are the intrinsic Born radii. The integral can be computed in many ways. One method developed by Hawkins *et al.* [37] involves using the intrinsic Born radii to approximate the cavity as a system of overlapping spheres. The integral in Equation (2.18) can then be calculated analytically in terms of nearest neighbor spheres that overlap. Figure 3 (c) shows the cavity approximated as overlapping spheres of radius a_i centered at the individual atomic positions.

The solvation energy of the molecule due to polarization effects is then given by

$$\Delta F_{pol} = -\frac{1}{2}\left(1 - \frac{1}{\epsilon_s}\right) \sum_{i,j} \frac{q_i q_j}{f_{GB}}. \tag{2.19}$$

Since ΔF_{pol} is the amount of energy that is required to move the molecule from vacuum to solvent, the total Coulomb energy in the dielectric is the sum of the vacuum Coulomb energy plus ΔF_{pol},

$$\begin{aligned} E_{coul} &= E_{vac} + \Delta F_{pol} \\ &= \frac{1}{2} {\sum_{i,j}}' \frac{q_i q_j}{r_{ij}} + \Delta F_{pol}. \end{aligned} \tag{2.20}$$

The summation in Equation (2.19) includes terms $i = j$ as these terms give the solvation energy of the ion itself but the vacuum summation does not (hence the prime). Both terms are calculated simultaneously during an energy evaluation.

In short, the generalized Born model provides a simple approximation for the solvation effects for a large solute molecule without having to calculate the numerous Coulomb interactions between the atoms in solute with those in the solvent.

V. MOLECULAR DYNAMICS SIMULATION

One of the simulations that the *Saguaro* simulation package is capable of is molecular dynamics using a classical force field, specifically the force field obtained using Equation (2.1). A classical molecular dynamics simulation of a system of N atoms begins by integrating the equations of motion,

$$\begin{aligned} F_{i\alpha} &= -\frac{\partial V}{\partial r_{i\alpha}} \\ &= m_i \ddot{r}_{i\alpha}, \end{aligned} \tag{2.21}$$

where $\alpha = x, y, z$ and i is the atom and the potential V is calculated using Equation (2.1). A simple velocity Verlet algorithm [38],

$$\begin{aligned} r_{i\alpha}(t_0 + \Delta t) &= r_{i\alpha}(t_0) + \dot{r}_{i\alpha}(t_0)\Delta t + \frac{\Delta t^2}{2m_i} F_{i\alpha}(t_0) \\ \dot{r}_{i\alpha}(t_0 + \Delta t) &= \dot{r}_{i\alpha}(t_0) + \frac{\Delta t}{2m_i} \left(F_{i\alpha}(t_0) + F_{i\alpha}(t_0 + \Delta t) \right), \end{aligned} \tag{2.22}$$

with appropriate time step ($\Delta t \approx 1$ fs) can be used to integrate Equation (2.21) providing a trajectory of the system of atoms as a function of time.

The corresponding trajectory samples the microcanonical ensemble of states where the number of atoms, volume, and energy are constant (NVE). In most molecular dynamics (MD) simulations one often desires the trajectory to sample other ensembles, such as the canonical ensemble, where the temperature is held constant (NVT).

There is a rich history of the development of methods to perform MD simulations in the various thermodynamic ensembles. Two examples are the extended systems method developed by Anderson, Nosé, Klein, Hoover, *et al.* [39, 40, 41, 42, 43] and the weak

coupling method developed by Bernsden *et al.* [44]. The weak coupling algorithm is a very popular choice since it is quite easy to implement in a MD algorithm when compared to the extended systems method which requires integration of complicated equations of motion. However unlike the extended systems method, the weak coupling method will sample the correct conformational space only for large number of atoms. For this reason the extended systems method is used in the *Saguaro* simulation package.

The Extended System Method for the isobaric-isoenthalpic ensemble (NPH) was originally derived by Anderson [39] to simulate a unit cell under the influence of a constant hydrostatic pressure. The resulting equations of motion allowed the unit cell to adjust isotropically, maintaining the cells shape. Parrinello and Rahman [45] extended this idea to the case where the unit cell is adjusted anisotropically. Further work done by Nosé and Klein, [43] extended the Parrinello and Rahman method to the isobaric-isothermal ensemble (NPT). By using the Nosé-Klein method, *Saguaro* allows for (NVE), (NVT), (NPH), and (NPT) simulations to be performed.

The Nosé-Klein method begins with the following Lagrangian for the system,

$$\begin{aligned} \mathcal{L} &= \sum_{i,\alpha\beta} \frac{1}{2} m_i s^2 \dot{u}_{i\alpha} G_{\alpha\beta} \dot{u}_{i\beta} - V \\ &+ \sum_{\alpha\beta} \frac{1}{2} W \dot{H}^2_{\alpha\beta} - P_{ex} Det(\overleftrightarrow{H}) + \frac{1}{2} Q \dot{s}^2 - N_f k_b T_{ex} Ln(s), \end{aligned} \tag{2.23}$$

where $u_{i\alpha}$ are the fractional coordinates of the atom in the unit cell ($\vec{r}_i = \overleftrightarrow{H}\ \vec{u}_i$) and s is the dynamical variable describing the heat coupling. Since the total energy of the Lagrangian is constant, s is essentially an "extended" variable that can absorb and release energy to the other degrees of freedom, thus mimicking an NVT simulation. The 3×3 matrix $\overleftrightarrow{G}$ is defined as $\overleftrightarrow{G} = \overleftrightarrow{H}^T \overleftrightarrow{H}$, where $\overleftrightarrow{H}$ is the 3×3 matrix of unit cell vectors placed in the columns. The determinant of the unit cell vector matrix, $Det(\overleftrightarrow{H})$, is then equivalent to the volume of

the unit cell V_c. The variables W and Q are effective masses that can be used to adjust the fluctuations of the pressure and temperature of the system respectively. The constants N_f and k_b are the number of spatial degrees of freedom and Boltzmann's' constant. Finally, P_{ex} and T_{ex} are the pressure and temperature of the external environment. The remaining discussion will now become quite technical as a set of equations that are capable of describing various thermodynamical ensembles is derived. A ten point summary of how the equations are used in the *Saguaro* molecular dynamics algorithm is given at the end of the section.

The Hamiltonian is obtained from Equation (2.23) [46] giving

$$\mathcal{H} = \sum_{i,\alpha\beta} \frac{\pi_{i\alpha} G^{-1}_{\alpha\beta} \pi_{i\beta}}{2 m_i s^2} + V + \sum_{\alpha\beta} \frac{\Pi^2_{\alpha\beta}}{2W} + P_{ex} Det(\overleftrightarrow{H}) + \frac{\pi_s^2}{2Q} + N_f k_b T_{ex} Ln(s), \tag{2.24}$$

where $\pi_{i\alpha}$,$\Pi_{\alpha\beta}$, and π_s are the canonical momentum. Einsteins' summation convention will now be used for the remainder of this section unless otherwise noted. Applying Hamilton's [46] equations of motion to Equation (2.24), the following equations of motion are obtained:

$$\begin{aligned} \dot{u}_{i\alpha} &= \frac{G^{-1}_{\alpha\beta}\pi_{i\beta}}{m_i s^2}, \\ \dot{\pi}_{i\alpha} &= -H_{\beta\alpha}\frac{\partial V}{\partial r_{i\beta}}, \end{aligned} \tag{2.25}$$

$$\begin{aligned} \dot{s} &= \frac{\pi_s}{Q}, \\ \dot{\pi}_s &= \frac{\pi_{i\alpha} G^{-1}_{\alpha\beta} \pi_{i\beta}}{m_i s^3} - \frac{N_f k_b T_{ex}}{s}, \end{aligned} \tag{2.26}$$

$$\begin{aligned} \dot{H}_{\alpha\beta} &= \frac{\Pi_{\alpha\beta}}{W}, \\ \dot{\Pi}_{\alpha\beta} &= \left(\Xi_{\alpha\gamma} - P_{ex}\delta_{\alpha\gamma}\right)\sigma_{\gamma\beta}. \end{aligned} \tag{2.27}$$

Here, $\delta_{\alpha\gamma}$ is the Kronecker delta and the tensors $\Xi_{\alpha\beta}$ and $\sigma_{\alpha\beta}$ are given by

$$\begin{aligned} \Xi_{\alpha\beta} &= \frac{1}{Det(\overleftrightarrow{H})}\left(\frac{1}{m_i s^2} H^{-1}_{\gamma\alpha}\pi_{i\gamma} H^{-1}_{\mu\beta}\pi_{i\mu} - \frac{\partial V}{\partial r_{i\alpha}}(\overleftrightarrow{H}\, u_i)_\beta\right), \\ \sigma_{\alpha\beta} &= Det(\overleftrightarrow{H}) H^{-1}_{\beta\alpha}. \end{aligned} \tag{2.28}$$

Nosé showed [41, 42] that with a scaling of the time such that, $sdt' = dt$, the coordinates and momentum in time t', given by

$$\begin{aligned} r_{i\alpha}(t') &= H_{\alpha\beta}u_{i\beta}, \\ p_{i\alpha}(t') &= \frac{H^{-1}_{\beta\alpha}\pi_{i\beta}}{s}, \end{aligned} \tag{2.29}$$

will sample the isothermal-isobaric ensemble with an average total kinetic energy of $N_f k_b T_{ex}/2$ and average pressure P_{ex}. Taking the derivative of $r_{i\alpha}(t')$ and $p_{i\alpha}(t')$ with respect to t' and using Equations (2.25)-(2.28) gives

$$\begin{aligned} \frac{dr_{i\alpha}}{dt'} &= \frac{dH_{\alpha\beta}}{dt'}u_{i\beta} + sH_{\alpha\beta}\frac{du_{i\beta}}{dt} \\ &= \frac{dH_{\alpha\gamma}}{dt'}H^{-1}_{\gamma\beta}r_{i\beta} + \frac{p_{i\alpha}}{m_i} \end{aligned} \tag{2.30}$$

and

$$\begin{aligned} \frac{dp_{i\alpha}}{dt'} &= \frac{dH^{-1}_{\beta\alpha}}{dt'}\frac{\pi_{i\beta}}{s} - H^{-1}_{\beta\alpha}\frac{\pi_{i\beta}}{s^2}\frac{ds}{dt'} + H^{-1}_{\beta\alpha}\frac{d\pi_{i\beta}}{dt} \\ &= -\frac{dH_{\beta\gamma}}{dt'}H^{-1}_{\gamma\alpha}p_{i\beta} - \frac{dLn(s)}{dt'}p_{i\alpha} - \frac{\partial V}{\partial r_{i\alpha}}. \end{aligned} \tag{2.31}$$

Equations (2.30) and (2.31) can now be put into a simpler form. With the definitions

$$\begin{aligned} \xi &= \frac{dLn(s)}{dt'}, \\ \eta_{\alpha\beta} &= \frac{1}{W}\left(\Xi_{\alpha\gamma} - P_{ex}\delta_{\alpha\gamma}\right)\sigma_{\gamma\beta}, \end{aligned} \tag{2.32}$$

and simplifications of Equation (2.28) to

$$\begin{aligned} \Xi_{\alpha\beta} &= \frac{1}{Det(\overleftrightarrow{H})}\left(\frac{p_{i\alpha}p_{i\beta}}{m_i} - \frac{\partial V}{\partial r_{i\alpha}}r_{i\beta}\right), \\ \sigma_{\alpha\beta} &= Det(\overleftrightarrow{H})H^{-1}_{\beta\alpha}, \end{aligned} \tag{2.33}$$

the equations of motion take the following form

$$\dot{r}_{i\alpha} = A_{\alpha\beta}r_{i\beta} + \frac{p_{i\alpha}}{m_i},$$

$$\begin{aligned}
\dot{p}_{i\alpha} &= -\frac{\partial V}{\partial r_{i\alpha}} - \left(A_{\beta\alpha} + \xi\delta_{\alpha\beta}\right) p_{i\beta}, \\
\dot{\xi} &= \frac{1}{Q}\left(\frac{p_{i\alpha}p_{i\alpha}}{m_i} - N_f k_b T_{ex}\right), \\
\ddot{H}_{\alpha\beta} &= \xi\dot{H}_{\alpha\beta} + s^2\eta_{\alpha\beta}. \qquad (2.34)
\end{aligned}$$

Here, the 3×3 matrix $\overleftrightarrow{A}$ has elements $A_{\alpha\beta} = \dot{H}_{\alpha\gamma}H^{-1}_{\gamma\beta}$. All of the dots in Equation (2.34) refer to the total derivative with respect to time t'. Since t' is essentially a dummy index at this point, the time will be simply referred to as t and not t' henceforth.

So far the equations of motion [Eqs. (2.32)-(2.34)] describe a system where the unit cell is allowed to change shape and volume. The equations of motion become modified for isotropic or anisotropic fixed angle scaling of the unit cell. The isotropic scaling allows only the lengths of the unit cell vectors to change at the same rate. The fixed angle scaling allows the lengths to change at different rates. The equations of motion for both types of scaling remain of the same form as Equations (2.32)-(2.34), but with $\eta_{\alpha\beta}$ modified. For isotropic scaling $\eta_{\alpha\beta}$ becomes

$$\eta_{\alpha\beta} = H_{\alpha\beta}\frac{Det(\overleftrightarrow{H})}{WL^2}Tr(\overleftrightarrow{\Xi} - P_{ex}\overleftrightarrow{I}), \qquad (2.35)$$

where Tr denotes the trace and L is from the relation $H_{\alpha\beta} = g_{\alpha\beta}L$ where $g_{\alpha\beta}$ is a constant tensor. The value L is somewhat of a free choice, since its purpose is to merely scale the unit cell vectors uniformly. A simple choice is $L = |\vec{a}|$ where $\vec{a}$ is any primitive unit cell vector. Similarly, for anisotropic fixed angle scaling, $\eta_{\alpha\beta}$ becomes

$$\eta_{\alpha\beta} = H_{\alpha\beta}\frac{Det(\overleftrightarrow{H})}{WL_\beta^2}\left(\overleftrightarrow{H}^T\ (\overleftrightarrow{\Xi} - P_{ex}\overleftrightarrow{I})\ \overleftrightarrow{H}^{-1T}\right)_{\beta\beta}, \qquad (2.36)$$

where L_β is from the relation $H_{\alpha\beta} = g_{\alpha\beta}L_\beta$ (no sum on β). Again a simple choice is for L is $L_\beta = |\vec{a}_\beta|$.

In a *Saguaro* molecular dynamics simulation, the Equations (2.32)-(2.34) are integrated using a velocity Verlet algorithm [38]. The resulting trajectory will then sample

both momentum and position space in the isobaric-isothermal (NPT) ensemble. These equations reduce to the equations of motion for the isobaric-isoenthalpic ensemble (NPH) when $\xi(t) = 0$ and $s(t) = 1$ for all time t. Likewise, by setting $\ddot{H}_{\alpha\beta} = 0$ and $\dot{H}_{\alpha\beta} = 0$ for all time t, the equations of motion reduce to the Nosé-Hoover equations and the trajectory will sample the isohoric-isothermal (NVT) ensemble of states [40, 41, 42]. In this fashion, *Saguaro* can perform an MD simulation in any of the ensembles (NVE) (NVT) (NPH) and (NPT) by an appropriate choice of the variables ξ, s, $\ddot{H}_{\alpha\beta}$, and $\dot{H}_{\alpha\beta}$.

The velocity Verlet integration scheme however can pose problems due to the extra integration of ξ and/or $H_{\alpha\beta}$ that is required. The *Saguaro* velocity Verlet integration scheme integrates ξ and $H_{\alpha\beta}$ to the same order in the time step as the velocities and coordinates, which yields an iterative procedure for their integration. With some work, Equations (2.32)-(2.34) can be formed into a velocity Verlet like form

$$\begin{aligned} r_{i\alpha}(t+\Delta t) &= \mu_{\alpha\beta}(t) r_{i\beta}(t) + p_{i\alpha}(t)\frac{\Delta t}{m_i} + (F^{tot}_{i\alpha}(t) + A_{\alpha\beta}p_{i\beta})\frac{(\Delta t)^2}{2m_i}, \\ p_{i\alpha}(t+\Delta t) &= p_{i\alpha}(t) + \frac{\Delta t}{2}(F^{tot}_{i\alpha}(t+\Delta t) + F^{tot}_{i\alpha}(t)), \end{aligned} \tag{2.37}$$

where μ is the scaling matrix with elements given by

$$\begin{aligned} \mu_{\alpha\beta}(t) &= \left(H_{\alpha\beta} + \dot{H}_{\alpha\beta}\Delta t + \ddot{H}_{\alpha\beta}\frac{(\Delta t)^2}{2} \right) H^{-1}_{\alpha\beta} \\ &\approx H_{\alpha\gamma}(t+\Delta t) H^{-1}_{\gamma\beta}(t), \end{aligned} \tag{2.38}$$

and $F^{tot}_{i\alpha}$ is the total force,

$$F^{tot}_{i\alpha} = -\frac{\partial V}{\partial r_{i\alpha}} - (A_{\beta\alpha} + \xi\delta_{\alpha\beta})p_{i\beta}, \tag{2.39}$$

that includes the forces of constraint from the external pressure and external temperature coupling.

The trajectories for $H_{\alpha\beta}$,$\dot{H}_{\alpha\beta}$, $Ln(s)$ and ξ can also be calculated using the velocity Verlet scheme as follows:

$$\begin{aligned} H_{\alpha\beta}(t+\Delta t) &= H_{\alpha\beta}(t) + \dot{H}_{\alpha\beta}(t)\Delta t + \ddot{H}_{\alpha\beta}(t)\frac{(\Delta t)^2}{2}, \\ \dot{H}_{\alpha\beta}(t+\Delta t) &= \dot{H}_{\alpha\beta}(t) + \frac{\Delta t}{2}(\ddot{H}_{\alpha\beta}(t+\Delta t) + \ddot{H}_{\alpha\beta}(t)), \end{aligned} \tag{2.40}$$

$$\begin{aligned} Ln[s](t+\Delta t) &= Ln[s](t) + \xi(t)\Delta t + \dot{\xi}(t)\frac{(\Delta t)^2}{2}, \\ \xi(t+\Delta t) &= \xi(t) + \frac{\Delta t}{2}(\dot{\xi}(t+\Delta t) + \dot{\xi}(t)). \end{aligned} \tag{2.41}$$

However, since F^{tot} depends on the momenta, integration of the velocity Verlet equations [Eqs. (2.37), (2.40), (2.41)] is no longer simple. The problem is that the new momenta at time $t+\Delta t$ in Equation (2.37) depend on ξ at time $t+\Delta t$ which in turn depends on the momenta at time $t+\Delta t$ [see Eq. (2.34)]. This can be fixed by using an iterative method for the integration of the momentum equations. The *Saguaro* integration algorithm begins by using the current momenta (computed using $F_{i\alpha} = -\frac{\partial V}{\partial r_{i\alpha}}$) to calculate ξ. New momenta are then formed by scaling with ξ ($p_{i\alpha} \rightarrow p_{i\alpha}/(1+\xi\Delta t/2)$). The procedure continues until ξ converges. Typically only two or three iterations need to be performed to achieve a good convergence for ξ. A similar problem also exists for the $H_{\alpha\beta}$ equations of motion [see Eq. (2.32)-(2.34) and Eq. (2.40)] and can be fixed using a iteration procedure similar to that of ξ.

To summarize, the following algorithm implemented in *Saguaro* follows the velocity Verlet technique and is capable of implementing either (NVE), (NVT), (NPH), or (NPT) simulations with an appropriate setting of a flag.

1. Calculate $H_{\alpha\beta}(t+\Delta t)$ and $S(t+\Delta t)$ using Equations (2.40) and (2.41).

2. Form $\overleftrightarrow{\mu}$ matrix and scale positions.

3. Calculate positions $r_{i\alpha}(t + \Delta t)$ using Equation (2.37)

4. Calculate new forces $F_{i\alpha}(t + \Delta t) = -\frac{\partial V}{\partial r_{i\alpha}}$

5. Obtain approximate momenta, kinetic energy and temperature using Equation (2.37) and the force $F_{i\alpha}$.

6. Calculate $\xi(t + \Delta t)$ and $\dot{H}_{\alpha\beta}$ using the iteration procedure.

7. Fix momenta, kinetic energy and temperature using converged values of $\xi(t+\Delta t)$ and $\dot{H}_{\alpha\beta}$.

8. Compute total force $F^{tot}_{i\alpha} = F_{i\alpha} - (A_{\beta\alpha} + \xi\delta_{\alpha\beta})p_{i\beta}$

9. Output any desired data

10. REPEAT

VI. ACTIVATION RELAXATION TECHNIQUE

The activation relaxation technique (ART) [28] is a method used in the *Saguaro* package to locate the many conformations of a molecule or a configuration of atoms by examining the energy landscape. The ART method was developed by Mousseau and colleagues and one of its first applications was to search for the various conformations that amorphous silicon can make using a Lennard Jones 6-12 potential [28, 29]. The ART algorithm was later applied to the study of aggregation formation in a four amino acid segment of Alzheimer's beta amyloid protein [47], and of the folding mechanisms of a few amino acids [48, 49].

The ART algorithm involves three basic steps: activation of the molecule along a random direction, location of a saddle point in the energy, and relaxation to a new local

minimum. Starting from a local minimum, the first step of ART, shown in Figure 4 (a), moves the molecule or configuration of atoms along a random direction (the activation direction), "activating" it by slowly moving away from the current local minimum in a series of small steps. During the activation procedure, the force is minimized perpendicular to the activation direction. Periodically the Hessian matrix $\Phi_{i\alpha j\beta}$ (with $i, j = [1, N]$ and $\alpha, \beta = x, y, z$) whose elements are given by

$$\Phi_{i\alpha j\beta} = \frac{\partial^2 V}{\partial r_{i\alpha} \partial r_{j\beta}}, \tag{2.42}$$

is calculated and diagonalized. If the diagonalization of the Hessian results in a negative eigenvalue, then the corresponding eigenvector gives the direction to a local saddle point, shown in Figure 4 (b). At this point, step two of the ART procedure begins by following the eigenvector corresponding to the largest negative eigenvalue. During step two, the force perpendicular to the eigenvector is minimized as in step one. Eventually, the total force is zero and the molecule has converged to a local saddle point. The third and final ART step moves the molecule over the saddle point, shown in Figure 4 (c), and the molecule is minimized to a new local minimum.

If desired, the Metropolis criterion can then be used to accept or reject the new structure based on the energy difference between the old local minimum and the new local minimum. Decreases in energy are always excepted while increases in energy are accepted randomly with probability $e^{-\beta \Delta E}$. The addition of the Metropolis step has the effect of forcing the molecule into a set of native states that will tend to be accessible at a given temperature.

The ART procedure is very adaptable since nearly any conformational space can be used to generate activation directions and search for new local minimums. The *Saguaro* simulation package implements the ART procedure using two different sampling techniques.

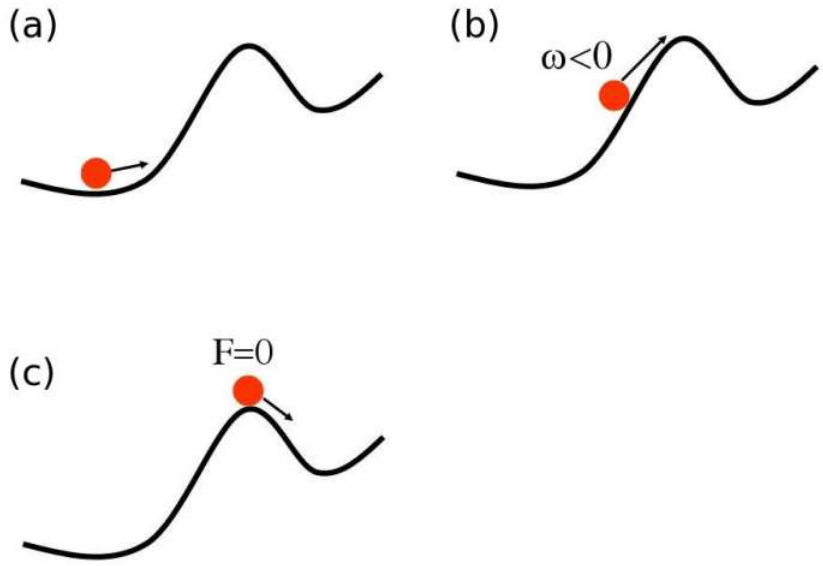

FIG. 4. The three steps of the activation relaxation technique. (a) Step one. The molecule is moved along a random direction, the activation direction, in small steps. After each step, the force is minimized perpendicular to the activation direction. Periodically, the Hessian matrix is calculated and diagonalized. (b) Step two. A negative eigenvalue of the Hessian is found and the activation direction is reset to follow the corresponding eigenvector which is a direction of negative curvature in the energy landscape. The forces perpendicular to the activation direction are still minimized after each activation step. (c) Step three. A saddle point is located when the total force vanishes. The molecule is perturbed away from the saddle point and a full relaxation is performed. The final result is that the molecule resides in a new local minimum of the energy landscape.

The first technique samples the conformational space of a molecule by moving individual atoms. The second sampling technique is used to locate conformations of peptide chains by searching the Ramachandran space of the peptide. The ART method and two applications involving a simple peptide are discussed in detail in Chapter 8.

VII. FREE ENERGY PERTURBATION

The goal of a free energy perturbation calculation is to find the free energy difference between two conformations of a molecule. Here, the word conformation is used very broadly since the variety of free energy calculations that can be performed is quite large. For example, the simplest of free energy perturbation calculations is the free energy of solvation which seeks to find the change in free energy of a molecule when the molecule is moved from vacuum to an aqueous solution (usually water). An example of a more complicated free energy perturbation calculation is the problem of finding the binding free energy of a molecule where a small molecule docks into a specific region of a much larger molecule resulting in a change in free energy due to the docking.

The free energy perturbation method used in *Saguaro* calculates the free energy difference between conforms by using a thermodynamic integration technique [50, 51]. From a classical perspective, the free energy difference between two states of a molecule (state 0 and state 1) is given by

$$e^{-\beta(F_1-F_0)} = \frac{\int e^{-\beta H_1} d\Gamma}{\int e^{-\beta H_0} d\Gamma}, \tag{2.43}$$

where H_0 is the Hamiltonian of the molecule in state 0 and H_1 is the Hamiltonian in state 1. Equation (2.43) results directly from the free energy relation $F = -k_b T \ln(Z)$. The phase space of the molecule (both position and momentum) is denoted by Γ. Equation (2.43) can be rewritten in the form

$$e^{-\beta(F_1-F_0)} = \frac{\int e^{-\beta V} e^{-\beta H_0} d\Gamma}{\int e^{-\beta H_0} d\Gamma}, \tag{2.44}$$

where V is the difference between the two Hamiltonians, $V = H_1 - H_0$. Typically the number of degrees of freedom in each state are the same so that Equation (2.44) can be written in terms of an ensemble average

$$e^{-\beta(F_1 - F_0)} = \langle e^{-\beta V} \rangle_0. \tag{2.45}$$

The notation $\langle x \rangle_0$ denotes the ensemble average of the quantity x in state 0. If the difference V is small, then *both* exponentials can be expanded to first order so that

$$(F_1 - F_0) \approx \langle V \rangle_0. \tag{2.46}$$

In general the free energy difference is not small enough to be approximated by Equation (2.46). The thermodynamic integration procedure calculates the free energy difference, $F_1 - F_0$, by creating intermediate states λ, where $0 \leq \lambda \leq 1$. These intermediate states can be described by a Hamiltonian H_λ. The intermediate states make the difference between successive Hamiltonians, $V_\lambda = H_{\lambda + d\lambda} - H_\lambda$, small allowing Equation (2.46) to be used to calculate the free energy differences between intermediate states $\Delta F_\lambda = F_{\lambda + d\lambda} - F_\lambda$. The total free energy difference is then just the sum of the smaller free energy differences between intermediate states ΔF_λ. As the number of intermediate states goes to infinity, the sum over ΔF_λ takes the form of an integral,

$$F_1 - F_0 = \int_0^1 \langle V_\lambda \rangle_\lambda d\lambda, \tag{2.47}$$

where $V_\lambda = \partial H_\lambda / \partial \lambda$ and the free energy difference is now exact.

The intermediate states can be made to follow any path between states 0 and 1 since the free energy is a function of state. A very simple path is $H_\lambda = H_0 + \lambda V$, with $V = H_1 - H_0$. This path takes state 0 to state 1 linearly. This is the current implementation in *Saguaro*. The number and location of points that the integrand can be evaluated at is

chosen by the user. The integral can then be done by any integration scheme. However, Hummer and Szabo [50] show that the calculation of the free energy difference can be improved upon by choosing specific locations to evaluate the integrand.

VIII. FULLY ATOMISTIC VIBRATIONAL ANALYSIS

The last type of calculation that *Saguaro* is capable of is a fully atomistic vibrational analysis of a large molecule, where each degree of freedom (x, y, z for each atom) is used to construct the vibrational patterns. The "standard" procedure for a vibrational or normal mode analysis (NMA) of a molecule of N atoms requires the formation and diagonalization of a $3N \times 3N$ matrix equation. Unlike molecular dynamics simulations where computational cost scales roughly linearly with the number of atoms simulated, a NMA will scale cubically with the number of atoms since the cost of diagonalizing a square matrix goes as the cube of the dimension of the matrix. But more importantly, the computer memory required to store the matrix increases quadratically with the number of atoms. As a result, even a few thousand atoms will require hundreds of Gigabytes (10^9) of computer memory far exceeding the few Gigabytes of memory available on most machines. Thus, as parallelization and supercomputer centers have allowed molecular dynamics time scales to proceed into the microsecond realm, similar progress for NMA has been limited.

In the majority of large molecule NMA, it is the low frequency vibrational modes that are of the most interest since these will most likely exhibit the large global motion of the molecule that give rise to large conformational changes of the molecule. The *Saguaro* package exploits this by implementing an iterative procedure where only the few lowest frequency mode patterns need to be stored in computer memory [52]. A detailed discussion on the vibrational analysis method is given in Chapter 4 and applications to specific systems such as viral capsids and large protein complexes can be found in later chapters.

CHAPTER 3

GROUP THEORY

I. INTRODUCTION AND MOTIVATION

Molecules and macromolecular complexes often exhibit symmetry amongst their constituent atoms. For example, viral capsids are large molecules that are built from a set of proteins by assembling them in a symmetrical fashion to construct a tube (helical symmetry) or spherical shell (icosahedral symmetry). Viral capsids are enormous in terms of the number of atoms that they contain ($N > 10^5$) which have made studies of their vibrational frequencies and mode patterns extremely difficult using standard techniques. Utilization of symmetry properties from group theory can allow for significant reductions in the size of the dynamical matrix by breaking the problem up into separate (but equivalent) problems based on the irreducible representations of the symmetry group of the molecule.

Group theory has been used by van Vlijmen and Karplus in the study of viral capsids [53, 54]. The reduction in the size of the dynamical matrix however is still insufficient without the use of a reduced basis set [53] so that the total number of degrees of freedom is significantly less than the full Cartesian set of $3N$ variables. The basis set chosen by van Vlijmen and Karplus in their studies of Polio virus [54] consisted of only dihedral rotations which reduced the number of basis vectors from 24,252 (full Cartesian basis) to 3,438 (dihedral motions only).

For the study of low frequency modes of viral capsids or other molecules having symmetry, the phonon functional method, which is discussed in detail in Chapter 4, should be capable of solving for the few lowest frequency modes using a full Cartesian basis. However, the use of group theory can dramatically speed up the calculation of the low frequency mode patterns by decreasing the size of the dynamical matrix while providing useful insights into symmetry related motions. But as the resulting smaller dynamical

matrix is still too large to store in computer memory, the operation of the matrix on a vector must be computed in a way that does not require its explicit storage.

The main purposes of this chapter is to provide the reader with a basic review of group theory and to prepare the necessary theoretical framework that will be needed for the calculation of the group theory dynamical matrix (group dynamical matrix) operating on a vector. The notation that will be used is similar to notation used in *Group Theory in Physics* [55]. After a brief review of some basic principals in group theory, a computational method to construct group theory basis vectors from only the rotation matrices is described. For the reader that is familiar enough with group theory, this chapter may be skipped. Those needing a detailed review of group theory should consult a group theory textbook.

II. REVIEW OF BASIC GROUP THEORY

Consider a molecule with N atoms which are located at equilibrium positions $\vec{R}_i$. The complete vector for the equilibrium positions, of length $3N$, will be denoted by $|R\rangle$. Suppose that this molecule has symmetry properties of a finite group $\mathcal{G}$ with elements $T\epsilon\mathcal{G}$ and that the total number of elements in the group is n_g. Each of the elements describe a basic operation such as a rotation about an axis or reflection through a plane that, when applied to the molecule, leave it identical to its original structure.

A two-dimensional example of a simple finite group, c_{3v}, is shown in Figure 5. In the figure, the group of three identical atoms form an equilateral triangle with sides of length a. When the system of atoms are operated on by one of the $n_g = 6$ elements of the group (E, A, B, C, C_{3z}, C_{3z}^{-1}), the new system that results is indistinguishable from the first. The element E is the identity, A, B, and C are the reflection operators and C_{3z}, C_{3z}^{-1} are the rotation operators.

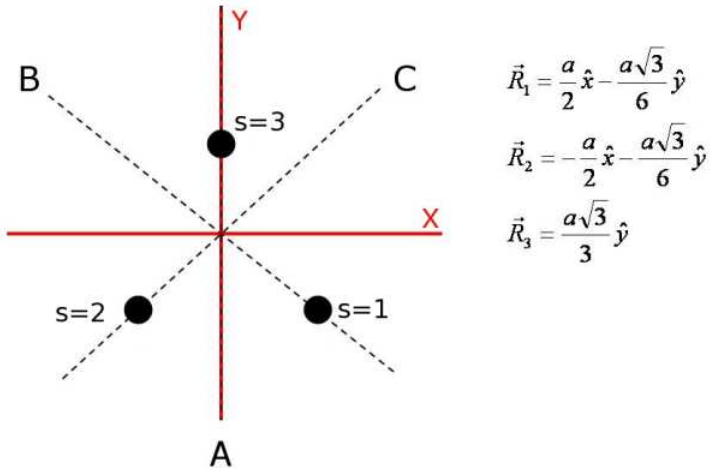

FIG. 5. The three identical atoms shown represent the finite group c_{3v}. There are a total of six group elements T that describe the group. Each atom is a distance of a from the other two atoms. The reflection planes are shown as dashed lines and each atom site is numbered $s = [1, 3]$. The coordinates listed are the equilibrium positions of each atom.

The system of three atoms in Figure 5 can be constructed by applying three of the six group operators to just one atom. For some molecules, it is possible to construct the full molecule from a basis of N_b atoms by applying the group operators $\hat{\Phi}(T)$ to the equilibrium positions of the N_b basis atoms. Thus, the full molecule of N atoms can be thought of as N_b atoms copied N_s times ($N = N_b N_s$), where N_s is the number of unique atom sites. For example, C_{60} has symmetry of the group I_h which has a total of $n_g = 120$ group elements. Only 60 of the group elements are needed to construct the full C_{60} molecule with 60 atoms. Thus, C_{60} has one basis atom and 60 unique sites ($N_b = 1$,$N_s = 60$). This type of interpretation is needed for spherical viruses (icosahedral symmetry group, I) since they are constructed from 60 copies of one or more proteins that contain many atoms. Figure 6 shows an illustration of two basis atoms ($N_b = 2$) placed at the sites of the original triangle

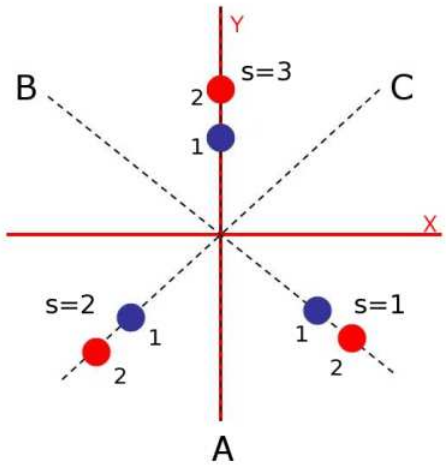

FIG. 6. Diagram showing two basis atoms (one red, one blue) placed at the sites (vertexes) of the equilateral triangle. The resulting set of six atoms has symmetry of the group c_{3v} which can be easily verified. The two atoms are numbered as 1 and 2 and the three sites are labeled $s = [1, 3]$. The reflection planes are drawn with dashed lines.

structure (shown in Figure 5). The two basis atoms need not be identical to have the symmetry of c_{3v}. The description of a symmetrical molecule being composed of N_b atoms repeated N_s times will be used henceforth.

Each of the n_g elements T can be denoted by the operators $\hat{\Phi}(T)$ which perform a rotation and permutation of the set of atoms in the molecule. A mathematical formulation of the invariance of the molecule to one of the group elements is written as

$$\hat{\Phi}(T)|R\rangle = |R\rangle. \tag{3.1}$$

Again, $|R\rangle$ is the vector of length $3N$ (3 dimensions times N atoms) that gives the equilibrium coordinates of the atoms. Equation (3.1) is satisfied for every element T of the group. The $\hat{\Phi}(T)$ operators can instead be represented as $3N \times 3N$ matrices $\overleftrightarrow{\Gamma}^{D}(T)$ which are the

direct product of a 3×3 rotation matrix $\overleftrightarrow{R}(T)$ and a $N \times N$ permutation matrix $\overleftrightarrow{P}(T)$,

$$\overleftrightarrow{\Gamma}^{D}(T) = \overleftrightarrow{R}(T) \otimes \overleftrightarrow{P}(T). \tag{3.2}$$

As an example, the reflection operation about the plane A for the three identical atoms in Figure 5 can be represented in two dimensions by a 2×2 rotation matrix and a 3×3 permutation matrix given by

$$\overleftrightarrow{R}(A) = \begin{bmatrix} -1 & 0 \\ 0 & 1 \end{bmatrix}, \quad \overleftrightarrow{P}(A) = \begin{bmatrix} 0 & 1 & 0 \\ 1 & 0 & 0 \\ 0 & 0 & 1 \end{bmatrix}. \tag{3.3}$$

Using Equation (3.2), these two matrices can be combined into the 6×6 matrix

$$\overleftrightarrow{\Gamma}^{D}(A) = \begin{bmatrix} 0 & 0 & -1 & 0 & 0 & 0 \\ 0 & 0 & 0 & 1 & 0 & 0 \\ -1 & 0 & 0 & 0 & 0 & 0 \\ 0 & 1 & 0 & 0 & 0 & 0 \\ 0 & 0 & 0 & 0 & -1 & 0 \\ 0 & 0 & 0 & 0 & 0 & 1 \end{bmatrix}. \tag{3.4}$$

One can easily verify that the vector $|R\rangle$ of equilibrium coordinates,

$$|R\rangle = \frac{1}{6} \begin{bmatrix} 3a \\ -a\sqrt{3} \\ -3a \\ -a\sqrt{3} \\ 0 \\ 2a\sqrt{3} \end{bmatrix}, \tag{3.5}$$

operated on by the matrix $\overleftrightarrow{\Gamma}^{D}(A)$ satisfies Equation (3.1).

For a general molecule with symmetry of the group $\mathcal{G}$ and N_b basis atoms at N_s sites, the n_g $3N \times 3N$ matrices $\overleftrightarrow{\Gamma}^{D}(T)$ form a representation of the group $\mathcal{G}$ for the molecule which Cornwell [55] calls the "displacement representation." This representation of $\mathcal{G}$ has the important property,

$$\overleftrightarrow{\Gamma}^{D\dagger}\overleftrightarrow{D}\overleftrightarrow{\Gamma}^{D}(T) = \overleftrightarrow{D}, \tag{3.6}$$

for all $T \epsilon \mathcal{G}$ where $\overleftrightarrow{D}$ is the $3N \times 3N$ dynamical matrix. Thus, the dynamical matrix is invariant under a unitary transformation with any group operator.

There are many ways to form a matrix representation $\overleftrightarrow{\Gamma}(T)$ of the group. Two representations, $\overleftrightarrow{\Gamma}(T)$ and $\overleftrightarrow{\Gamma}'(T)$, are said to be *equivalent* if there exists a unitary transformation $\overleftrightarrow{U}$ such that,

$$\overleftrightarrow{\Gamma}'(T) = \overleftrightarrow{U}^{\dagger}\overleftrightarrow{\Gamma}(T)\overleftrightarrow{U}, \tag{3.7}$$

for every element T. However, if there exists a unitary transformation $\overleftrightarrow{U}$, such that $\overleftrightarrow{U}^{\dagger}\overleftrightarrow{\Gamma}(T)\overleftrightarrow{U}$ is block diagonal for *every* element T, with each $\overleftrightarrow{\Gamma}$ having the same block structure, then the representation is said to be completely reducible. For every group there are a set of *irreducible* representations of dimension d_p denoted by $\overleftrightarrow{\Gamma}^{p}(T)$, where p is the pth irreducible representation of $\mathcal{G}$. These irreducible representations satisfy the powerful orthogonality relation ("the grand orthogonality theorem")

$$\frac{d_p}{n_g}\sum_{T\epsilon\mathcal{G}}\Gamma^{p*}_{jk}(T)\Gamma^{q}_{st}(T) = \delta_{pq}\delta_{js}\delta_{kt}, \tag{3.8}$$

where the asterisk denotes the complex conjugate, j, k, s, t label the d_p^2 elements of the irreducible representation, and δ_{pq} *etc.* are Kronecker deltas.

The number of irreducible representations of a group is equal to the number of unique classes, which are distinguished by their character $\chi(T)$. For a general matrix representation

TABLE I. Character table for the group c_{3v}. The three irreducible representations are labeled A_1, A_2, and E. The numbers next to each of the three classes correspond to the number of group elements that belong to the class.

	E	$2C_3$	$3\sigma_v$
A_1	1	1	1
A_2	1	1	-1
E	2	-1	0

of the group, $\overleftrightarrow{\Gamma}(T)$, the characters are defined as

$$\chi(T) = Tr\left(\overleftrightarrow{\Gamma}(T)\right), \tag{3.9}$$

where Tr denotes the trace operation. Every element in the group belongs to one and only one of the unique classes and every element in the class has the same character. Since the number of irreducible representations is equal to the number of classes, a square table relating the classes and irreducible representations can be formed called the character table. The entries of the character table are simply the characters $\chi^p(T)$ for a class of elements in the p^{th} irreducible representation.

Table I shows the character table for the group c_{3v}. There is a total of three unique classes of elements. The first is the identity class which contains only the identity element E. The next class is the class of threefold rotations, C_3, which contains the elements C_{3z} and C_{3z}^{-1}. Finally the last class, σ_v, is the class of reflections which contains the elements A, B, and C.

The representation $\overleftrightarrow{\Gamma}^D$ is a reducible representation of the group that can be made block diagonal *for all* elements T of $\mathcal{G}$ by applying a unitary transformation $(\overleftrightarrow{V})$ to all n_g

matrices $\overleftrightarrow{\Gamma}^{D}(T)$. Applying the unitary transformation to $\overleftrightarrow{\Gamma}^{D}$ gives

$$\overleftrightarrow{V}^{\dagger}\overleftrightarrow{\Gamma}^{D}(T)\overleftrightarrow{V}=\begin{pmatrix} \overleftrightarrow{\Gamma}^{1}(T) & & & & \\ & \overleftrightarrow{\Gamma}^{1}(T) & & & \\ & & \overleftrightarrow{\Gamma}^{2}(T) & & \\ & & & \ddots & \end{pmatrix}. \tag{3.10}$$

The smaller matrices $\overleftrightarrow{\Gamma}^{p}$ are the irreducible representations of $\mathcal{G}$. Each of the irreducible representations may occur more than once along the diagonal [as can be seen in Eq. (3.10)]. The number of times, n_p, that the pth irreducible representation occurs in a reducible representation is given by

$$n_p = \frac{1}{n_g}\sum_{T\epsilon\mathcal{G}}\chi^{p*}(T)\chi(T), \tag{3.11}$$

where $\chi(T)$ corresponds to the character of element T in the reducible representation and can be calculated using Equation (3.9). The characters for the irreducible representation, $\chi^p(T)$, can either be obtained from $\chi^p(T) = Tr(\overleftrightarrow{\Gamma}^{p}(T))$ or the character table.

The matrix $\overleftrightarrow{V}$ is a $3N \times 3N$ orthogonal matrix formed from group theory basis vectors $|v_m^p\rangle$ of the irreducible representations which have the property

$$\hat{\Phi}(T)|v_n^p\rangle = \sum_{m=1}^{d_p}\Gamma_{mn}^{p}(T)|v_m^p\rangle. \tag{3.12}$$

It is usually said that $|v_m^p\rangle$ transforms as the m^{th} row if the irreducible representation p. Equation (3.10) can be easily verified through the use of Equation (3.12) and the orthogonality of the columns of $\overleftrightarrow{V}$.

In total, $n_p d_p$ basis vectors can be constructed for the irreducible representation p; d_p vectors due to the dimension of $\overleftrightarrow{\Gamma}^{p}$ times n_p for each time the irreducible representation p appears in $\overleftrightarrow{\Gamma}^{D}$. Since the irreducible representation p will usually occur more than once, the

group theory basis vectors will be denoted by the notation, $|v^p_{m\alpha}\rangle$, where m corresponds to the row number ($m = 1, 2, \cdots, d_p$) that the basis vector transforms as, and $\alpha = 1, 2, \cdots, n_p$.

The $3N \times 3N$ dynamical matrix $\overleftrightarrow{D}$ can also be made block diagonal by performing a similarity transform with the $\overleftrightarrow{V}$ matrix of group theory basis vectors

$$\overleftrightarrow{V}^{\dagger}\overleftrightarrow{D}\overleftrightarrow{V} = \begin{pmatrix} \overleftrightarrow{D}^1 & & & & \\ & \overleftrightarrow{D}^2 & & & \\ & & \overleftrightarrow{D}^2 & & \\ & & & \ddots & \end{pmatrix}. \tag{3.13}$$

The $\overleftrightarrow{D}^p$ are smaller dynamical matrices (group dynamical matrices) of dimension $n_p \times n_p$ for irreducible representation p and are repeated d_p times. Thus, the eigenvalue equation for the full dynamical matrix,

$$\overleftrightarrow{D}\,|e(\lambda)\rangle = \lambda|e(\lambda)\rangle, \tag{3.14}$$

can be broken up into smaller eigenvalue problems of size $n_p \times n_p$ each satisfying the equation

$$\overleftrightarrow{D}^p\,|e^p(\lambda)\rangle = \lambda|e^p(\lambda)\rangle. \tag{3.15}$$

Equation (3.15) shows the power of group theory and why it is so important. From just the symmetry properties of a molecule, group theory can be used to greatly reduce the size of the eigenvector problem.

The eigenvectors of $\overleftrightarrow{D}$ are constructed from the group theory basis vectors and the vectors $|e^p(\lambda)\rangle$ via

$$|e(\lambda)\rangle = \sum_{\alpha=1}^{n_p} |v^p_{m\alpha}\rangle e^p_\alpha(\lambda), \tag{3.16}$$

where α labels the n_p components of $|e^p(\lambda)\rangle$. Since $\overleftrightarrow{D}^p$ is repeated d_p times, the eigenvalues λ corresponding to the matrix $\overleftrightarrow{D}^p$ are d_p fold degenerate. The degenerate eigenvectors can be constructed using basis vectors that transform as a different row m in Equation (3.16).

Hence, it is only necessary to use group theory basis vectors that transform as a single row for the construction of $\overleftrightarrow{D}^{p}$ with Equation (3.13). However, in order to calculate the *operation* of the group dynamical matrix on a general vector, all of the basis vectors for the irreducible representation will be needed. A method to construct these basis vectors is discussed in the next section.

III. CONSTRUCTION OF BASIS VECTORS

Group theory basis vectors have special properties with respect to the rotation operators $\hat{\Phi}(T)$ [see Eq. (3.12)] that allow for the block diagonalization of the displacement representation $\overleftrightarrow{\Gamma}^{D}(T)$. As such, they are required for the calculation of the group dynamical matrix operating on a general vector. The basis vectors that will be required for the group dynamical matrix operating on a vector are basis vectors for the point group where $N_b = 1$. This section provides a computational method to construct them, which can then be used in an automated fashion on any biomolecule with symmetry. Since the symmetry properties of a biomolecule are typically listed in the protein data bank file (PDB), this procedure will be of great use. An explicit derivation of the group dynamical matrix operating on a vector will be left until Chapter 4 Section VII.

The construction of basis vectors for the case $N_b = 1$ can be done quite simply by operating the projection operator

$$\hat{\mathcal{P}}^{p}_{mn} = \frac{d_p}{n_g} \sum_{T \epsilon \mathcal{G}} \Gamma^{p*}_{mn}(T) \hat{\Phi}(T), \tag{3.17}$$

on a random vector $|r\rangle$ which has a length of $3N_s$ when $N_b = 1$. The rotation operator $\hat{\Phi}(T)$ can be written as a $3N_s \times 3N_s$ matrix [see Eq. 3.2]. Typically only the rotation operators and number of group elements are known and one must find the irreducible representation matrices in a table [56]. The projector uses a linear combination of rotations

of the random vector to construct a basis vector of the irreducible representation p. The projection operator $\hat{\mathcal{P}}^p_{mm}$ projects the random vector onto the m^{th} row of the irreducible representation p whereas $\hat{\mathcal{P}}^p_{mn}$ takes a basis vector transforming as row n and generates its orthogonal partner, a basis vector transforming as row m.

Using Equation (3.17), one can easily construct the n_p basis vectors transforming as row 1 in two steps. First, apply the projector $\hat{\mathcal{P}}^p_{11}$ to a set of n_p random vectors. Second, use a orthogonalization procedure such as Gram Schmidt to obtain an orthogonal set of basis vectors that span the space of vectors transforming as row 1. The orthogonal partners of the row 1 basis vectors can then be easily obtained by applying the projector $\hat{\mathcal{P}}^p_{m1}$ to each of the row 1 basis vectors.

The use of Equation (3.17) however requires that all n_g matrices for the irreducible representation p are known. Typically, one can find a detailed table of the n_g matrices for all irreducible representations of a particular group in a reference book or other source [56, 57]. The tables for the irreducible representations can be cumbersome to work with from a computational standpoint since the matrices must be imported into the computer in some fashion. For somewhat large groups such as I or I_h, this can be time consuming. Instead, it would be very useful to be able to construct the matrices $\Gamma^p_{mn}(T)$ from a computer algorithm where only a small amount of information is needed. Blokker and Dixon [58, 59] both describe computational methods to construct the characters and irreducible representation matrices. Here, a much simpler method is employed that only requires the rotation operators of the group. As these are easy to construct, the character table and irreducible representation matrices can be computed for nearly any point group allowing the basis vectors to be constructed using Equation (3.17).

A naive method to construct the irreducible representation matrices would be to first project a random vector onto a single irreducible representation using the character projector

$$\hat{\mathcal{P}}^p = \frac{d_p}{n_g} \sum_{T \epsilon \mathcal{G}} \chi^{p*}(T) \hat{\Phi}(T). \tag{3.18}$$

The group characters are easy to work with (as they are single numbers) which makes this an attractive idea. This method assumes that the projected vector can be chosen to transform as a single row of the irreducible representation, thereby allowing the matrix elements Γ^{p*}_{mn} to be computed by applying the rotation operators $\hat{\Phi}(T)$ and using Equation (3.12). The problem with this method is that the number of basis vectors transforming as row 1 is usually greater than one ($n_p > 1$). Thus, the rotation operators often generate *more* than d_p orthogonal vectors since $n_g > d_p$. Another method to construct a vector transforming as row 1 must be developed as this clearly violates Equation (3.12).

In general, a random vector of length $3N_s$ can be expanded in terms of the complete set of group theory basis vectors $|v^p_{m\alpha}\rangle$ as

$$|r\rangle = \sum_p \sum_{\alpha=1}^{n_p} \sum_{m=1}^{d_p} C^p_{m\alpha} |v^p_{m\alpha}\rangle. \tag{3.19}$$

Of course the set of vectors $|v^p_{m\alpha}\rangle$ is not by any means unique. In particular, there is a set of basis vectors for which the coefficients $C^p_{m\alpha}$ have the following "orthogonality" property for all irreducible representations p,

$$\sum_{\alpha=1}^{n_p} C^{p*}_{m\alpha} C^p_{n\alpha} = C^p_m \delta_{mn}, \tag{3.20}$$

where C^p_m is a constant given by $\sum_\alpha |C^p_{m\alpha}|^2$. The reason for using this set of basis vectors will be apparent shortly. However, it is not obvious that a set of basis vectors with this property exists.

To show that a set of basis vectors with this property indeed exists, consider the example system of three atoms in two-dimensions shown in Figure 5 which have symmetry of the group c_{3v}. The number of times that the irreducible representation E (see Table I) occurs in the displacement representation can be calculated using Equation (3.11) and is $n_E = 2$. The E representation has dimension 2 and since this representation appears twice, there are a total of 4 orthogonal basis vectors of length 6 that can be made. These basis vectors can be denoted by the set $|v^E_{m\alpha}\rangle$, where m is the row number that the basis vector transforms as and $\alpha = 1, 2$ labels the basis vector number. This simply corresponds to the number of times the E representation appears in $\overleftrightarrow{\Gamma}^D$.

This set of 4 orthogonal vectors spans the space of all basis vectors for the irreducible representation E that exist in the displacement representation. In addition, any unitary transform of the vectors *i.e*,

$$\begin{bmatrix} u_{11} & u_{12} & u_{13} & u_{14} \\ u_{21} & u_{22} & u_{23} & u_{24} \\ u_{31} & u_{32} & u_{33} & u_{34} \\ u_{41} & u_{42} & u_{43} & u_{44} \end{bmatrix} \begin{bmatrix} |v^E_{11}\rangle \\ |v^E_{12}\rangle \\ |v^E_{21}\rangle \\ |v^E_{22}\rangle \end{bmatrix} = \begin{bmatrix} |w^E_{11}\rangle \\ |w^E_{12}\rangle \\ |w^E_{21}\rangle \\ |w^E_{22}\rangle \end{bmatrix}, \tag{3.21}$$

will form a set of basis vectors $|w^E_{m\alpha}\rangle$ that span the same space. Clearly the coefficients $C^E_{m\alpha}$ must also satisfy a similar equation of the form

$$\begin{bmatrix} u_{11} & u_{12} & u_{13} & u_{14} \\ u_{21} & u_{22} & u_{23} & u_{24} \\ u_{31} & u_{32} & u_{33} & u_{34} \\ u_{41} & u_{42} & u_{43} & u_{44} \end{bmatrix} \begin{bmatrix} C^E_{11} \\ C^E_{12} \\ C^E_{21} \\ C^E_{22} \end{bmatrix} = \begin{bmatrix} D^E_{11} \\ D^E_{12} \\ D^E_{21} \\ D^E_{22} \end{bmatrix}, \tag{3.22}$$

where $D^E_{m\alpha} = \langle w^E_{m\alpha}|r\rangle$. It is now apparent that there must exist a set of basis vectors for the irreducible representation such that Equation (3.20) is satisfied.

So far it has been shown that a random vector can be expanded in terms of a set of basis vectors such that Equation (3.20) is satisfied. The reason for choosing this set of basis vectors can be seen by examining the operation of the projector [Eq. (3.17)] on a random vector expanded in the basis,

$$\begin{aligned}\hat{\mathcal{P}}^p_{mn}|r\rangle &= \sum_q \sum_{\alpha=1}^{n_q} \sum_{s=1}^{d_q} C^q_{s\alpha} \hat{\mathcal{P}}^p_{mn}|v^q_{s\alpha}\rangle \\ &= \sum_{\alpha=1}^{n_p} C^p_{n\alpha}|v^p_{m\alpha}\rangle. \end{aligned} \tag{3.23}$$

The property (see Cornwell [55] page 94)

$$\hat{\mathcal{P}}^p_{mn}|v^q_{s\alpha}\rangle = \delta_{pq}\delta_{ns}|v^p_{m\alpha}\rangle, \tag{3.24}$$

has been used to simplify Equation (3.23). Taking the inner product of two projected vectors, $|\hat{\mathcal{P}}^p_{mn}r\rangle$, one obtains

$$\begin{aligned}\langle\hat{\mathcal{P}}^q_{st}r|\hat{\mathcal{P}}^p_{mn}r\rangle &= \sum_{\alpha\beta} C^{q*}_{t\beta} C^p_{n\alpha} \langle v^q_{s\beta}|v^p_{m\alpha}\rangle \\ &= \delta_{pq}\delta_{sm} \sum_{\alpha} C^{p*}_{t\alpha} C^p_{n\alpha}. \end{aligned} \tag{3.25}$$

Exploiting Equation (3.20) and rewriting the left hand side using Equation (3.17), Equation (3.25) becomes

$$\sum_{ij} \Gamma^q_{st}(T_i)\langle\hat{\Phi}(T_i)r|\hat{\Phi}(T_j)r\rangle\Gamma^{p*}_{mn}(T_j) = \delta_{pq}\delta_{sm}\delta_{tn}\left(\frac{n_g}{d_p}\right)^2 C^p_t. \tag{3.26}$$

One can see that using basis vectors which satisfy Equation (3.20) forces all of the vectors $\hat{\mathcal{P}}^p_{mn}|r\rangle$ to be orthogonal.

Equation (3.26) shows that the $n_g \times n_g$ matrix $\langle\hat{\Phi}(T_i)r|\hat{\Phi}(T_j)r\rangle$ is diagonalized by the orthogonal elements of the irreducible representation matrices. Since there are a total of n_g unique projectors, (d_p^2 per representation) the eigenvectors are simply given by

$$\left(\frac{d_p}{n_g}\right)^{\frac{1}{2}} \begin{bmatrix} \Gamma^{p*}_{mn}(T_1) \\ \Gamma^{p*}_{mn}(T_2) \\ \vdots \\ \Gamma^{p*}_{mn}(T_{n_g}) \end{bmatrix}. \tag{3.27}$$

The factor of $\sqrt{d_p/n_g}$ ensures that the vector is normalized and can be verified with the grand orthogonality theorem. The eigenvalues of the eigenvector in Equation (3.27) are $C^p_n n_g/d_p$. There are d_p eigenvectors that will have this eigenvalue corresponding to the d_p different m values that can be used. Thus, there will be a total of d_p eigenvectors that are d_p fold degenerate for each irreducible representation p.

A procedure for generating a set of group theory basis vectors from only the rotation matrices can now be described. First, the overlap matrix, $\langle\hat{\Phi}(T_i)r|\hat{\Phi}(T_j)r\rangle$, is formed using a random vector $|r\rangle$ and the n_g rotation operators. Next, the overlap matrix is diagonalized. Any eigenvector of the overlap matrix with non-zero eigenvalue can be used to generate a vector transforming as row 1 of an irreducible representation by taking a linear combination of rotated vectors $\hat{\Phi}(T)|r\rangle$ and normalizing. The irreducible representation matrices can then be calculated by rotating the new vector and using Equation (3.12). Once the irreducible representation matrices are formed, Equation (3.17) can be used to generate basis vectors for the representation and the characters can be calculated. The procedure is repeated (after first orthogonalizing the random vector to any basis vectors generated) until a complete set of basis vectors for all irreducible representations is formed. In practice, the procedure takes less than a second on a single desktop processor and the computer code required is approximately 500 lines of fortran code. The only input required for the procedure is the set of rotation operators which are easily found (often as BIOMT operators in a protein data bank file).

CHAPTER 4

VIBRATIONAL ANALYSIS OF LARGE MOLECULES

I. INTRODUCTION

One of the standard routes for the study of vibrational mode patterns of a molecule and their corresponding frequencies ω is through the use of the harmonic approximation. The harmonic approximation describes the potential energy of the molecule as completely harmonic in nature, allowing the motions of the atoms to be described as a superposition of harmonic oscillators that vibrate *independently* of each other at various frequencies.

There are well known problems with this approximation, mainly relating to the lack of higher order energy terms that describe the anharmonicity which can couple the harmonic oscillators to each other. But one of the major problems with the harmonic approximation is that the calculation of the vibrational modes and frequencies scales as Order (N^3) (where N is the number of atoms) since a diagonalization of a $3N \times 3N$ matrix (the dynamical matrix) is required. In addition, the dynamical matrix can become quite difficult to store in computer memory since its storage typically scales as N^2. Even if the storage requirement for the dynamical matrix could be reduced by only including interactions within a finite range, the diagonalization procedure requires an N^2 workspace to store the resulting eigenvectors. Because of these issues, calculation of the vibrational modes and frequencies of molecules using the harmonic approximation has not extended beyond a few thousand atoms despite the development of faster computers. For large molecules or macromolecular complexes such as viruses which can have $N > 10^5$, calculating the vibrational modes and corresponding frequencies by forming a $3N \times 3N$ matrix and diagonalizing it is clearly unfeasible at the present time.

The goal of many vibrational problems is to study large scale motions of the molecule in its native state. These large scale motions allow one to obtain insights into the mechanical

motion involved in enzymatic activity of a protein, the binding of substrates, or the coupling of light scattering to large scale vibrational modes. As such, only information about the *low* frequency motion is wanted since these motions give the large globular movements that are sought.

Methods such as the rotation translation block (RTB) method [6], which is based upon on the elastic network model (ENM) [4], have been developed to predict these low frequency motions of large molecules by coarse graining. Often this coarse graining can be quite extensive. For example, the coarse graining procedure in the RTB method considers groups of atoms to form a ridged block with only six degrees of freedom. For large macromolecular complexes such as virus capsids, the ridged block is formed from a single protein unit [7] which often consists of several thousand atoms. This scheme was used by Tama *et al.* to study the vibrational modes of a plant virus [60] where each protein consisted of roughly 2500 atoms. In addition, the energy model used in the ENM is purely phenomenological. The model attaches springs of identical spring constants between any two atoms that are separated by a distance less than a specified cutoff, usually 8-10 Å. While some advances [5, 7] have been made in the study of low frequency vibrations of very large molecules, there is much opportunity for improvement.

In this chapter, a theory for determining the *lowest* frequency vibrational modes of a large molecule is developed called the phonon functional method. As will be seen, the theory extends well known ideas in electronic structure theory to the study of phonons. Instead of an explicit calculation of the complete dynamical matrix followed by its diagonalization, the method only requires the repeated *operation* of the dynamical matrix on a set of vectors. Sections VI and VII show how the operation can be done in Order (N) steps. In addition, since only the low frequency states are calculated, the storage of the full displacement

patterns in computer memory for each mode becomes feasible. The method developed in this chapter improves upon the ENM and RTB methods in two ways. First, it provides a description of the vibrational pattern that is entirely atomistic. Second, it uses an energy model typically used in molecular dynamics simulations for the calculation of the dynamical matrix elements. Thus, the theory is capable of providing a greatly improved assessment of vibrational mode patterns and their corresponding frequencies.

II. HARMONIC APPROXIMATION

In the harmonic approximation, the dynamics of a molecule is represented by a set of harmonic oscillators which perform small oscillations about a stable minimum (equilibrium position). Each of the harmonic oscillators move the atoms in the molecule along specific directions called the normal modes. The small oscillation approximation allows the potential energy of a molecule V (which is a function of only atomic positions) to be written as a Taylor series expanded to second order about the equilibrium position of each atom,

$$\begin{aligned} V(\vec{r_1}, \vec{r_2}, \ldots) &= V_0 + \sum_{i\alpha} \left.\frac{\partial V}{\partial r_{i\alpha}}\right|_{r=R} (r_{i\alpha} - R_{i\alpha}) \\ &+ \frac{1}{2} \sum_{i\alpha, j\beta} \left.\frac{\partial^2 V}{\partial r_{i\alpha} \partial r_{j\beta}}\right|_{r=R} (r_{i\alpha} - R_{i\alpha})(r_{j\beta} - R_{j\beta}). \end{aligned} \tag{4.1}$$

The indices i and j label the atom number ($i, j = 1, 2, \cdots, N$) while $\alpha, \beta = x, y, z$. The term V_0 is the energy of the molecule at equilibrium and can be neglected. Since the second term in the expansion vanishes for each atom at the minimum, Equation (4.1) takes the form

$$V(\vec{r_1}, \vec{r_2}, \cdots) = \frac{1}{2} \sum_{i\alpha, j\beta} \left.\frac{\partial^2 V}{\partial r_{i\alpha} \partial r_{j\beta}}\right|_{r=R} q_{i\alpha} q_{j\beta}, \tag{4.2}$$

where $q_{i\alpha}$ is the displacement of the atom from its equilibrium position ($q_{i\alpha} = r_{i\alpha} - R_{i\alpha}$).

The kinetic energy of the molecule,

$$T = \frac{1}{2} \sum_{i\alpha} m_i \dot{q}_{i\alpha}^2, \tag{4.3}$$

along with Equation (4.2) for the potential energy can be used to form the Lagrangian,

$$\begin{aligned}\mathcal{L} &= T - V \\ &= \sum_{i\alpha} \frac{1}{2} m_i \dot{q}_{i\alpha}^2 - \frac{1}{2} \sum_{i\alpha, j\beta} \left. \frac{\partial^2 V}{\partial r_{i\alpha} \partial r_{j\beta}} \right|_{r=R} q_{i\alpha} q_{j\beta}. \end{aligned} \tag{4.4}$$

The Lagrangian along with Euler's equations [46] yield the following set of $3N$ coupled equations of motion,

$$-m_i \ddot{q}_{i\alpha} = \sum_{j\beta} \left. \frac{\partial^2 V}{\partial r_{i\alpha} \partial r_{j\beta}} \right|_{r=R} q_{j\beta}. \tag{4.5}$$

The solution to Equation (4.5) is given by

$$q_{i\alpha} = A \eta_{i\alpha} e^{-i\omega t}, \tag{4.6}$$

where A is an amplitude constant. Substitution of Equation (4.6) into Equation (4.5) gives

$$m_i \omega^2 \eta_{i\alpha} = \sum_{j\beta} \left. \frac{\partial^2 V}{\partial r_{i\alpha} \partial r_{j\beta}} \right|_{r=R} \eta_{j\beta}. \tag{4.7}$$

If the following definitions are made:

$$\begin{aligned} e_{i\alpha} &= \sqrt{m_i} \eta_{i\alpha}, \\ D_{i\alpha j\beta} &= \frac{1}{\sqrt{m_i m_j}} \left. \frac{\partial^2 V}{\partial r_{i\alpha} \partial r_{j\beta}} \right|_{r=R}, \\ \lambda &= \omega^2, \end{aligned} \tag{4.8}$$

then Equation (4.7) takes the familiar form of an eigenvector equation,

$$\overleftrightarrow{D} \, |e(\lambda)\rangle = \lambda |e(\lambda)\rangle. \tag{4.9}$$

There are $3N$ distinct solutions (denoted by λ) of Equation (4.9), each one providing a unique mass weighted displacement pattern $|e(\lambda)\rangle$ for each frequency ω. The matrix $\overleftrightarrow{D}$ is the real, symmetric, dynamical matrix formed from the second derivatives of the potential energy function for the molecule. The $3N$ solutions of $\overleftrightarrow{D}$ form a complete orthonormal set

that span the space of all possible displacements of the molecule. While Equation (4.9) is easy to solve for small molecules, it becomes a challenge for large molecular complexes such as viral capsids. In order to study the vibrational patterns of large molecules atomistically, new techniques must be developed to solve Equation (4.9).

III. BAND-STRUCTURE ENERGY FOR ELECTRONS

A typical problem encountered in electronic structure theory (ES) pertains to the calculation of the band-structure energy. In general, the band-structure energy G is given by (neglecting spin)

$$G = \sum_i \epsilon_i, \tag{4.10}$$

where the sum is over occupied energy states ψ_i satisfying $\hat{H}\psi_i = \epsilon_i\psi_i$ and $\hat{H}$ is the Hamiltonian operator. Instead of summing over only the occupied states, the sum can instead be changed to included all states by writing Equation (4.10) as a trace over *any* complete orthonormal basis,

$$G = Tr(Hf), \tag{4.11}$$

where $\beta = 1/k_bT$ and $f(\hat{H}, \mu)$ is the Fermi function defined by

$$f(\hat{H}, \mu) = \frac{1}{e^{\beta(\hat{H}-\mu)} + 1}. \tag{4.12}$$

Equation (4.11) is cumbersome to work with computationally due to the difficulty in applying the Fermi function on a general state ψ. In addition, Equation (4.11) requires a complete basis set of states which can be quite large.

However, at room temperature the Fermi energy (E_f) of most materials is much larger than k_bT and the electrons essentially only occupy the the lowest lying energy levels. The Fermi function then becomes a step function with values of $f(\epsilon, \mu) = 1$ when $\epsilon < \mu$ (occupied) and $f(\epsilon, \mu) = 0$, when $\epsilon > \mu$ (unoccupied). This allows for a functional

minimization to be introduced in place of Equation (4.11) of the form

$$G = Min\{\, Tr_M(H)\}. \tag{4.13}$$

The minimization is preformed over the M occupied basis states of the Hamiltonian. This choice for G is not without some problems. These are easily seen by examining the energy functional in Equation (4.13) for a one level Hamiltonian,

$$\begin{aligned} G &= \langle\psi|\hat{H}|\psi\rangle \\ &= -\epsilon_0\langle\psi|\psi\rangle. \end{aligned} \tag{4.14}$$

Figure 7 shows a plot of Equation (4.14) as the norm of ψ changes. Clearly Equation (4.14) has no minimum and any attempt to minimize it will force the norm to infinity, $\langle\psi|\psi\rangle \rightarrow \infty$. Equation (4.13) is essentially ignorant of the Pauli exclusion principal and basis states must be kept orthonormal by other means during the minimization process (*e.g.* Gram Schmidt orthogonalization).

A much simpler solution presented by Ordejon, Drabold, Martin, and Grumbach (ODMG) [17], is to instead add a harmonic potential centered around the value $\langle\psi|\psi\rangle = 1$. The ODMG functional given by

$$G = Min\{\, Tr_M(H + H(1 - S))\}, \tag{4.15}$$

creates an "energy penalty" for states ψ that are not normalized and orthogonal to all others. This type of method is often referred to as orderN electronic structure methods as the operation of the Hamiltonian on a state can be computed in Order (N) steps. The ODMG energy functional is just one example of many [15, 16, 18] that enforce the orthonormality requirements.

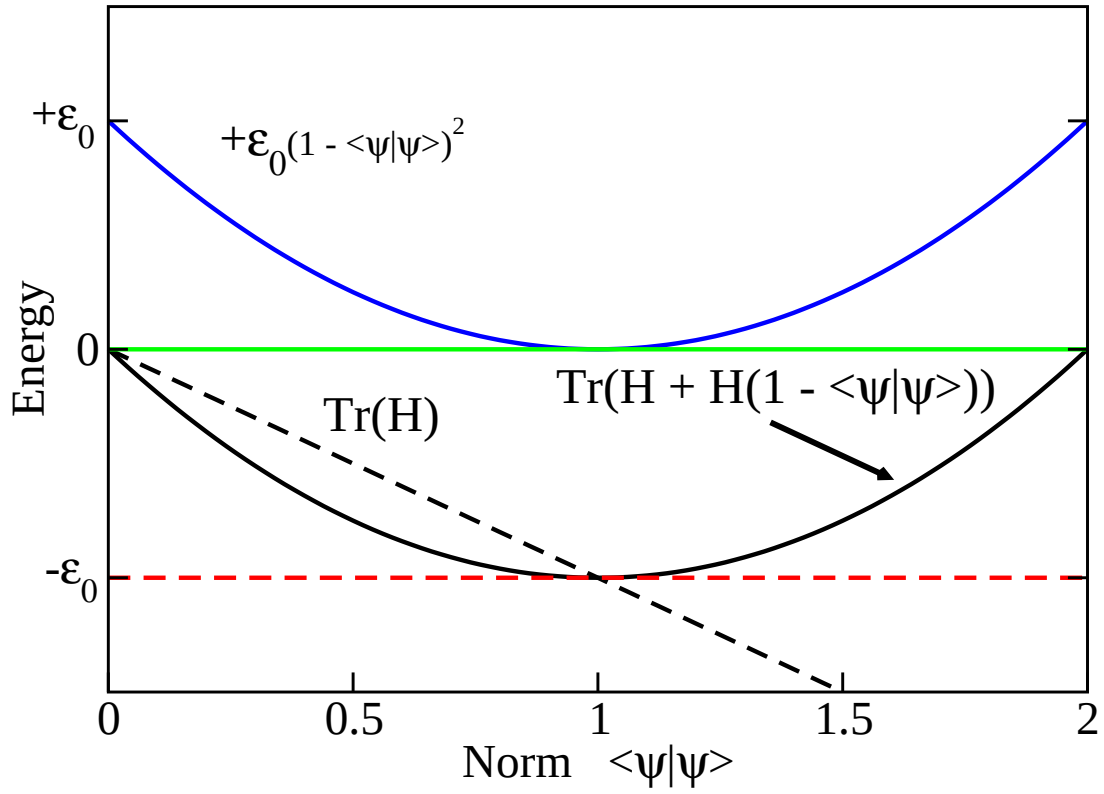

FIG. 7. Plots of the energy functional $G = Tr(H) = -\epsilon_0\langle\psi|\psi\rangle$ and the ODMG energy functional $G = -\epsilon_0 + \epsilon_0(1 - \langle\psi|\psi\rangle)^2$ for a single state Hamiltonian. No minimum occurs in the energy functional $Tr(\hat{H})$ since the condition $\langle\psi|\psi\rangle = 1$ is not enforced. The ODMG functional enforces $\langle\psi|\psi\rangle = 1$ by placing a harmonic potential about $\langle\psi|\psi\rangle = 1$ creating a stable minimum.

For the case of the one level Hamiltonian, Equation (4.15) can be written as

$$G = -\epsilon_0 + \epsilon_0(1 - \langle\psi|\psi\rangle)^2. \tag{4.16}$$

A plot of Equation (4.16) is shown in Figure 7. The effect of Equation (4.16) is to place the harmonic potential $+\epsilon_0(1 - \langle\psi|\psi\rangle)^2$ at the proper norm of $\langle\psi|\psi\rangle = 1$ then shift it so that the correct value of $Tr(H)$ is given at the minimum.

It should be noted that the curvature of the harmonic potential ($+\epsilon_0$) is affected by the sign of the eigenvalues of $\hat{H}$. As such, only eigenvalues of $\hat{H}$ that are strictly negative will produce a minimum. Positive eigenvalues will invert the curvature causing a maximum to occur at the proper norm. This is easily fixed by introducing the "shifted Hamiltonian", $\hat{H}_s = \hat{H} - \epsilon_L\hat{I}$, where ϵ_L is the largest positive eigenvalue of $\hat{H}$. This forces the entire spectrum of $\hat{H}$ to be negative. The states ψ will be unaffected by the shift in the Hamiltonian.

A final examination of the properties of the ODMG energy functional is made using a two level Hamiltonian. The Hamiltonian matrix,

$$H = \begin{bmatrix} 1 & -1 \\ -1 & 1 \end{bmatrix}, \tag{4.17}$$

has eigenvalues of $\epsilon = 0, 2$ with eigenvectors,

$$|\psi_\pm\rangle = \frac{1}{\sqrt{2}} \begin{bmatrix} 1 \\ \pm 1 \end{bmatrix}. \tag{4.18}$$

The energy landscape of Equation (4.15) for this Hamiltonian can now be examined for one occupied state ($M = 1$) given by

$$|\phi\rangle = \begin{bmatrix} C_1 \\ C_2 \end{bmatrix}. \tag{4.19}$$

The state vector $|\phi\rangle$ can be varied by the two coefficients C_1 and C_2 allowing a plot of the energy landscape to be formed.

Equation (4.15) for this Hamiltonian can be written as $G = \langle\phi|\hat{H}|\phi\rangle(2 - \langle\phi|\phi\rangle)$. A three-dimensional plot of G is shown in Figure 8 (a). Since both eigenvalues are greater than or equal to zero, maxima occur at $(C_1, C_2) = (1/\sqrt{2}, -1/\sqrt{2})$ and $(C_1, C_2) = (-1/\sqrt{2}, 1/\sqrt{2})$. Both of these maxima correspond to the largest eigenvalue of $\epsilon = 2$. It is clear from Figure 8 (a) that a Hamiltonian with a positive spectrum cannot be used. Instead, the Hamiltonian matrix is shifted by $\epsilon_L = 2$, giving new elements: $H_{11} = -1$, $H_{12} = H_{21} = -1$, and $H_{22} = -1$. The three-dimensional plot for the shifted Hamiltonian is shown in Figure 8 (b). Two minima occur at $(C_1, C_2) = (1/\sqrt{2}, 1/\sqrt{2})$ and $(C_1, C_2) = (-1/\sqrt{2}, -1/\sqrt{2})$ which both correspond to the lowest eigenvalue of $\epsilon = 0$. For this example one can see that using a shifted Hamiltonian creates a global minimum in the ODMG functional at the lowest energy state.

IV. EFFECTIVE BAND-STRUCTURE ENERGY FOR PHONONS

Typically in the course of a vibrational analysis of a molecule, the low frequency phonon states are usually of great interest. This is especially true for large molecules or macromolecular complexes such as viruses, as these low frequency phonon states give a detailed description of the large global motions of the molecule or complex.

The standard method of studying the phonon states of a molecule using a full basis set (where the individual displacements of each atom are accounted for) was outlined in Chapter 4 Section II. This procedure required the formation and diagonalization of the dynamical matrix [Eq. (4.9)]. As such, the *full* phonon spectrum was calculated and stored in memory. This can be seen as quite wasteful on both computer memory and time as

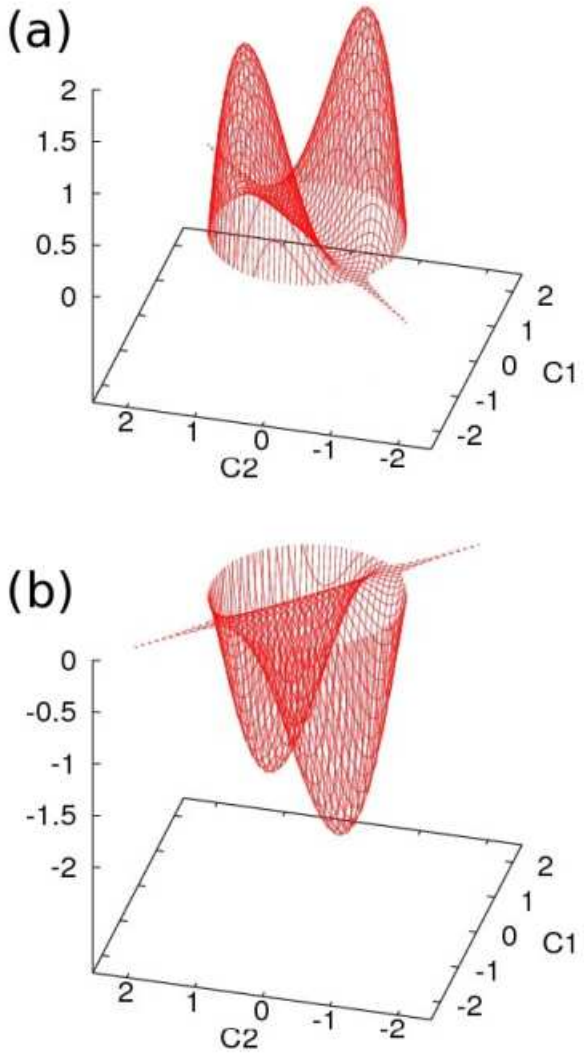

FIG. 8. Plots of the ODMG energy functional for a two level Hamiltonian with one occupied state. (a) A three-dimensional plot of the ODMG functional using the unshifted Hamiltonian $\hat{H}$. Two maxima are created both corresponding to the eigenfunction of the largest eigenvalue of $\hat{H}$. (b) Same as (a) except the shifted Hamiltonian $\hat{H}_s = \hat{H} - \epsilon_L \hat{I}$ is used where ϵ_L is the largest eigenvalue of $\hat{H}$. Two minima are produced both corresponding to the eigenfunction of the smallest eigenvalue of $\hat{H}$.

the high frequency phonon states, which are usually due to localized bond stretching or bending, must be calculated in addition to the low frequency ones.

Most linear algebra packages such as LAPACK [61] have routines that can solve for eigenvalues and eigenvectors below a certain cutoff reducing computational time. However, the memory requirement for these routines increases quadratically with the number of atoms because the matrix elements of the dynamical matrix must be stored. For a large molecule that has, as an example, ten thousand atoms; storage of the matrix elements (or all eigenvectors) can require several gigabytes of computer memory. This is clearly unfeasible at the present time for widespread use. Thus, a method that does not require explicit storage of the dynamical matrix is necessary.

One alternative technique that does not require the explicit storage of the dynamical matrix, only the *operation* of the matrix on a vector, is the Lanczos iteration method (see the p-q algorithm in *Applied Analysis* [62]). The Lanczos scheme uses the iterative operation of a matrix on a random vector to quickly amplify the extreme eigenvalues. However, the method does have some problems and should be used with caution. In the Lanczos procedure, a random vector must be repeatedly multiplied by the matrix. This has the tendency to produce "clones" where a previously found eigenvector is found again despite an initial orthogonalization at the beginning of the Lanczos procedure [63]. A large biomolecule may also have frequencies that range from as low as 0.4 cm^{-1} to as high as 4000 cm^{-1}, which means the ratio of the smallest eigenvalue to the largest is on the order of 10^8. This produces an ill conditioned dynamical matrix that is particularly sensitive to numerical round off. This makes the small eigenvectors and eigenvalues particularly difficult to find with the Lanczos method even with matrix shifting schemes.

Instead a different route is taken here based on the electronic band-structure problem. If low (high) frequency states are thought of as an "occupied" ("unoccupied") set of phonon states below (above) a pseudo-Fermi level, an *effective* band-structure energy functional for phonons can be introduced. By treating phonons as Fermions (from a purely mathematical perspective), a subspace of states spanning the lowest states of the dynamical matrix can be found. Figure 9 illustrates the "occupied" and "unoccupied" phonon states for a general molecule. Unlike the electron problem, the number of occupied states M can be chosen to be any number. Since the density of states is small at low frequencies, M will be quite small compared with the dimension of the dynamical matrix making the storage of the M state vectors in memory feasible. Minimization of this functional can also be designed to be iterative since only the *operation* of the dynamical matrix on the set of M "occupied" basis states are needed in order to compute the local gradient of the energy functional (see Chapter 4 Section V).

The effective band-structure energy function for phonons, G_p, can be formed from Equation (4.15) by defining $M \times M$ "Hamiltonian" and overlap matrices in terms of basis vectors $|u_i\rangle$ as

$$\begin{aligned} H_{ij} &= \langle u_i|\hat{D}_s|u_j\rangle, \\ S_{ij} &= \langle u_i|u_j\rangle. \end{aligned} \tag{4.20}$$

The phonon energy functional then takes the form

$$\begin{aligned} G_p &= Min\{\, Tr_M(H + H(1 - S))\} \\ &= 2\sum_i \langle u_i|\hat{D}_s|u_i\rangle - \sum_{ij}\langle u_i|u_j\rangle\langle u_j|\hat{D}_s|u_i\rangle. \end{aligned} \tag{4.21}$$

The operator $\hat{D}_s = \hat{D} - \lambda_L\hat{I}$ is the shifted dynamical matrix operator which must be used in order to insure G_p has a minimum. The largest eigenvalue of $\hat{D}$, λ_L, is calculated quite

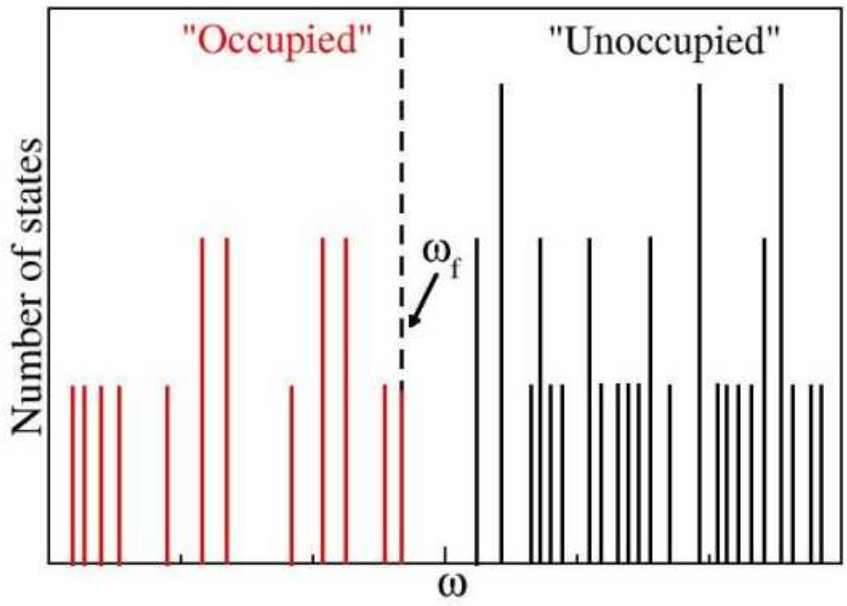

FIG. 9. An illustration of the phonon states of a general molecule. The value ω_f is the pseudo-Fermi level for the phonon states. Phonon states at or below ω_f are a set of wanted ("occupied") states of the dynamical matrix. Those states above the pseudo-Fermi level are unwanted ("unoccupied").

easily with an iterative scheme such as the Lanczos p-q algorithm [62] where the calculation of the large eigenvalues of an ill conditioned matrix pose no problems.

The M basis vectors $|u_i\rangle$ have length equal to the dimension of the dynamical matrix. This set of basis vectors can be chosen initially at random and do not need to be orthogonal or normalized as the energy functional will enforce orthonormality at the minimum. Once the phonon energy functional is minimized, the final basis vectors $|u_i\rangle$ form an orthonormal set of vectors that span the space of the lowest M eigenvectors of the dynamical matrix. At this point the basis vectors $|u_i\rangle$ are not necessarily the true eigenvectors of the dynamical matrix. The true eigenvectors of the dynamical matrix, $|e(\lambda)\rangle$, are obtained by taking a linear combination of the minimized basis vectors $|u_i\rangle$,

$$|e(\lambda)\rangle = \sum_j C_j(\lambda)|u_j\rangle. \tag{4.22}$$

Operating on Equation (4.22) with the shifted dynamical matrix operator gives

$$\hat{D}_s|e(\lambda)\rangle = \sum_j C_j(\lambda)\hat{D}_s|u_j\rangle. \tag{4.23}$$

Using the relation $\hat{D}_s|e(\lambda)\rangle = (\lambda - \lambda_L)|e(\lambda)\rangle = \lambda'|e(\lambda)\rangle$ along with Equation (4.22) for $|e(\lambda)\rangle$, Equation (4.23) can be written as

$$\begin{aligned} \sum_j C_j(\lambda)\hat{D}_s|u_j\rangle &= \lambda'|e(\lambda)\rangle \\ &= \lambda' \sum_j C_j(\lambda)|u_j\rangle. \end{aligned} \tag{4.24}$$

Multiplying by $\langle u_k|$ and making use of Equations (4.20), the small $M \times M$ matrix equation relating the basis vectors $|u_i\rangle$ to the eigenvectors $|e(\lambda)\rangle$ is obtained,

$$HC(\lambda) = \lambda' SC(\lambda). \tag{4.25}$$

Equation (4.25) must be diagonalized in order to determine the true eigenvectors, however,

the matrix to be diagonalized is quite small (*e.g.* 200×200). Since the eigenvectors are unaffected by the shift in the dynamical matrix, the resulting eigenvalue of $|e(\lambda)\rangle$ will be λ.

By minimizing the phonon energy functional [Eq. (4.21)] for a set of M basis vectors $|u_i\rangle$, one can [using Eq. (4.22) and Eq. (4.25)] form the lowest M phonon states of the dynamical matrix $\overleftrightarrow{D}$. Since the operation of the dynamical matrix on a vector can be computed in Order (N) steps (for finite ranged interactions), the calculation of a small set of low frequency states of a large biomolecule is approximately an Order (N) procedure. The method will be referred to as the phonon functional method henceforth.

V. MINIMIZATION OF THE PHONON ENERGY FUNCTIONAL

In general, the phonon energy functional [Eq. (4.21)] can be optimized by any minimization procedure. A very common minimization scheme that is used for the minimization of multi-dimensional functions is the method of conjugate gradients (CG) [64]. There are many flavors of CG, including the "traditional" Flecher-Revees method and the method of Polak and Ribiere to name two. Though the Flecher-Revees procedure is more efficient on memory requirements, the Polak and Ribiere method often provides a much faster rate of convergence (as is the case with phonon energy functional).

The Polak-Ribiere CG minimization of Equation (4.21) begins with a set of M vectors $|u_k^0\rangle$ with $k = 1, 2 \ldots M$. At each minimization step n, the vectors $|u_k^n\rangle$ are used to construct the gradient of Equation (4.21) for each vector $|u_k^n\rangle$ which is given by

$$|g_k^n\rangle = 4\hat{D}_s|u_k^n\rangle - 2\sum_i \hat{D}_s|u_i^n\rangle\langle u_i^n|u_k^n\rangle - 2\sum_i |u_i^n\rangle\langle u_i^n|\hat{D}_s|u_k^n\rangle. \tag{4.26}$$

The gradient is then used to construct search directions $|p_k^n\rangle$ for each of the M vectors,

$$|p_k^n\rangle = -|g_k^n\rangle + \beta^n|p_k^{n-1}\rangle, \tag{4.27}$$

where β_k^n is the Polak-Ribiere CG coefficient [64] given by

$$\beta^n = \frac{\sum_k \left[\langle g_k^n | g_k^n \rangle - \langle g_k^n | g_k^{n-1} \rangle\right]}{\sum_k \langle g_k^{n-1} | g_k^{n-1} \rangle}. \tag{4.28}$$

The updated vectors $|u_k^{n+1}\rangle$ are then found by line minimization of the phonon energy functional along the search directions $|p_k^n\rangle$,

$$|u_k^{n+1}\rangle = |u_k^n\rangle + \delta^n |p_k^n\rangle, \tag{4.29}$$

where δ^n is step size determined from the line minimization. Since each vector takes the same step size (due to the CG algorithm) the line minimization can be done *analytically*.

Substituting Equation (4.29) into the phonon energy functional [Eq. (4.21)], G_p at step $n+1$ can be written in terms of δ^n as

$$G_p^{n+1} = G_p^n - \frac{A}{4}(\delta^n)^4 - \frac{B}{3}(\delta^n)^3 - \frac{C}{2}(\delta^n)^2 - D(\delta^n), \tag{4.30}$$

where the coefficients A, B, C, and D are given by (using Einstein summation):

$$\begin{aligned}
A &= 4\langle p_i^n | p_j^n \rangle \langle p_j^n | \hat{D}_s | p_i^n \rangle \\
B &= 3\langle p_i^n | \hat{D}_s | p_j^n \rangle \left[\langle p_j^n | u_i^n \rangle + \langle u_j^n | p_i^n \rangle\right] + 3\langle p_i^n | p_j^n \rangle \left[\langle p_j^n | \hat{D}_s | u_i^n \rangle + \langle u_j^n | \hat{D}_s | p_i^n \rangle\right] \\
C &= -4\langle p_i^n | \hat{D}_s | p_i^n \rangle + 2\left[\langle p_i^n | \hat{D}_s | u_j^n \rangle + \langle u_i^n | \hat{D}_s | p_j^n \rangle\right]\left[\langle p_j^n | u_i^n \rangle + \langle u_j^n | p_i^n \rangle\right] \\
&+ 2\langle p_i^n | \hat{D}_s | p_j^n \rangle \langle u_j^n | u_i^n \rangle + 2\langle u_i^n | \hat{D}_s | u_j^n \rangle \langle p_j^n | p_i^n \rangle \\
D &= -4\langle p_i^n | \hat{D}_s | u_i^n \rangle + \langle u_i^n | \hat{D}_s | u_j^n \rangle \left[\langle p_j^n | u_i^n \rangle + \langle u_j^n | p_i^n \rangle\right] \\
&+ \langle u_i^n | u_j^n \rangle \left[\langle p_j^n | \hat{D}_s | u_i^n \rangle + \langle u_j^n | \hat{D}_s | p_i^n \rangle\right].
\end{aligned} \tag{4.31}$$

Taking the derivative of Equation (4.30) and setting the result equal to zero yields a cubic equation in terms of δ^n. The cubic equation has either one real solution and two imaginary solutions or three real solutions. In the case where there are three real solutions to the cubic equation, the δ^n which decreases G_p by the largest amount is used.

Thus, the Polak-Ribiere CG procedure requires the following sets of M vectors be stored in memory (for a total of $5M$ vectors): $|u_i^n\rangle$, $|g_i^{n-1}\rangle$, $|g_i^n\rangle$, $\hat{D}_s|u_i^n\rangle$, and $\hat{D}_s|p_i^n\rangle$. If the basis vectors $|u_i^n\rangle$ and the vectors $\hat{D}_s|u_i^n\rangle$ are updated via

$$\begin{aligned} |u_i^{n+1}\rangle &= |u_i^n\rangle + \delta^n |p_i^n\rangle, \\ \hat{D}_s|u_i^{n+1}\rangle &= \hat{D}_s|u_i^n\rangle + \delta^n \hat{D}_s|p_i^n\rangle, \end{aligned} \tag{4.32}$$

then only M dynamical matrix operations on the vectors $|p_i^n\rangle$ are required for each CG step.

VI. CALCULATION OF THE DYNAMICAL MATRIX OPERATING ON A VECTOR

As shown in the previous section, the key calculation required for the minimization of Equation (4.21) is the operation of the dynamical matrix on a vector. Since the dynamical matrix can not be explicitly stored in memory when studying large molecules, the dynamical matrix operating on a vector must be calculated in a way that does not require storage of the matrix.

Generally classical potential energy models used to study molecules can be written as a sum of individual energy terms that depend on the distances between two or more atoms. This is true of the classical potential energy models used in molecular dynamics calculations (see Chapter 2 Section II), where the potential energy is given by

$$\begin{aligned} V(\vec{r_1}, \vec{r_2}, \ldots) &= \sum_{bonds} k_b (r - r_{eq})^2 + \sum_{angles} k_a (\theta - \theta_{eq})^2 \\ &+ \sum_{dihedrals} \frac{v_n}{2} \left[1 + \cos\left(n\phi - \gamma\right)\right] + \frac{1}{2} \sum_{ij} \left(\frac{q_i q_j}{\epsilon r} + \frac{A}{r^{12}} - \frac{B}{r^6} \right). \end{aligned} \tag{4.33}$$

The Coulomb, van der Waals, and bond terms are "two center" energy terms that depend only on the distance between two atoms. The angle and dihedral terms are "three center"

and "four center" energy terms respectively, since they depend on the distances between either three or four atoms.

Since the potential energy is a sum of individual energy terms, the contribution to the vector $\hat{D}|u\rangle = |\hat{D}u\rangle$ can be computed term by term in the same fashion that the total force on each atom is calculated during a molecular dynamics simulation. In the force calculation, the first derivatives of the energy are calculated one energy term at a time and are added into the total force vector. The calculation of the dynamical matrix operating on a vector is done analytically and can also proceed one energy term at a time. For each energy term, the second derivatives, which contribute to a specific set of dynamical matrix elements, are calculated. These derivatives are then multiplied by the appropriate components of the vector $|u\rangle$ and the result is added in to the appropriate components of the vector $|\hat{D}u\rangle$.

As an example of how the accumulation of the vector $|\hat{D}u\rangle$ proceeds, consider just one of the energy terms in the potential energy of a molecule; a Coulomb energy term between atoms i and j. The second derivative of the Coulomb terms, as well as the other energy terms in Equation (4.33), are calculated analytically. The second derivative of the Coulomb term is

$$\frac{\partial^2}{\partial r_{m\alpha}\partial r_{n\beta}}\left(\frac{q_i q_j}{\epsilon r}\right) = \frac{3q_i q_j}{\epsilon r^3}\frac{\partial r}{\partial r_{m\alpha}}\frac{\partial r}{\partial r_{n\beta}} - \frac{q_i q_j}{\epsilon r^3}\delta_{\alpha\beta}(\delta_{mi}-\delta_{mj})(\delta_{ni}-\delta_{nj}), \tag{4.34}$$

where $\delta_{\alpha\beta}$ *etc.* are Kronecker deltas. The derivative of $r = |\vec{r}_i - \vec{r}_j|$ is given by

$$\frac{\partial r}{\partial r_{m\alpha}} = \frac{(\vec{r}_i - \vec{r}_j)_\alpha}{r}(\delta_{mi}-\delta_{mj}). \tag{4.35}$$

Since the Coulomb term is a "two center" energy term, it will contribute to 36 dynamical matrix elements of $\overleftrightarrow{D}$, more specifically the terms $D_{m\alpha,n\beta}$ with $\alpha,\beta = x,y,z$ and $m = i,j$ and $n = i,j$. The contribution of this one Coulomb term to the dynamical matrix

is written in matrix form as

$$\begin{pmatrix} & \vdots & & \vdots & \\ \cdots & \overleftrightarrow{D}_{ii} & \cdots & \overleftrightarrow{D}_{ij} & \cdots \\ & \vdots & & \vdots & \\ \cdots & \overleftrightarrow{D}_{ji} & \cdots & \overleftrightarrow{D}_{jj} & \cdots \\ & \vdots & & \vdots & \end{pmatrix}, \tag{4.36}$$

where the $\overleftrightarrow{D}_{mn}$ are 3×3 matrices with elements $D_{m\alpha,n\beta}$. All other elements in Equation (4.36) are zero. The contribution of this one Coulomb term to the elements $Du_{m\alpha}$ of the vector $|\hat{D}u\rangle$ is simply,

$$Du_{m\alpha} = \sum_{n\beta} D_{m\alpha,n\beta} u_{n\beta}. \tag{4.37}$$

The total number of bond, angle, and dihedral terms in Equation (4.33) all scale roughly linearly with the number of atoms in the molecule. Though the Coulomb and van der Waals terms scale as the number of atoms squared, a cutoff can be used for both (especially in the presence of a dielectric) reducing the scaling to Order (N). For the test case of the ubiquitin protein, the introduction of a cutoff for the electrostatic terms resulted in negligible errors to the calculated frequencies and vibrational displacement patterns (see Section VIII). Thus, the total calculation of the dynamical matrix operating on a vector scales linearly with the number of atoms in the molecule. Since the vector $|\hat{D}u\rangle$ is accumulated term by term in the same fashion as the total force vector in a molecular dynamics simulation, each dynamical matrix operation on a vector is approximately equivalent to a single molecular dynamics step. This description helps in making estimates of running time since it allows vibrational calculations to be thought of in terms of a molecular dynamics run of a certain time.

VII. GROUP DYNAMICAL MATRIX OPERATING ON A VECTOR

In this section, a method to calculate the operation of the group dynamical matrix on a vector is developed. The group dynamical matrix is the matrix that results after group theory and symmetry properties of the molecule have been used to reduce the size of the full dynamical matrix. For molecules with no symmetry, which includes single proteins, this step is not necessary. The remaining portion of the section assumes that the reader has a basic understanding of group theory. Chapter 3 or a group theory textbook should be referred to if a review of group theory is needed.

The operation of the group dynamical matrix, $\overleftrightarrow{D}^p$, on a vector $|u^p\rangle$ of length n_p can be calculated in a similar fashion to that of the regular dynamical matrix operating on a vector. The dimension of the group dynamical matrix, n_p, is the number of times that irreducible representation p occurs in the displacement representation. The dynamical matrix in group theory for the irreducible representation p (see Chapter 3 Section II) is given by

$$\overleftrightarrow{D}^p = \overleftrightarrow{V}^{p\dagger} \overleftrightarrow{D} \overleftrightarrow{V}^p, \tag{4.38}$$

where $\overleftrightarrow{V}^p$ is the $3N \times n_p$ matrix formed from the n_p group theory basis vectors for irreducible representation p placed in the columns. Only a set of basis vectors transforming as a single row of the irreducible representation are needed for the construction of $\overleftrightarrow{V}^p$. Thus, vectors transforming as the first row will be used.

In Chapter 3 Section II, the full molecule was described as N_b atoms copied to N_s unique sites for a total of $N = N_b N_s$ atoms (see Figure 6). This allows the n_p orthogonal basis vectors to be constructed from $n'_p = n_p/N_b$ basis vectors for the case when only one atom is at each unique site, *i.e.* $N_b = 1$. A method for constructing these vectors using the rotation operators was presented in Chapter 3 Section III. The basis vectors for the case of

one atom at each site ($N_b = 1$) will have a total length of $3N_s$. They can be written in terms of N_s vectors of length 3 (one at each site s) as $\vec{v}^{p}_{s,m\alpha}$. Here, $s = 1 \cdots N_s$ labels the site number, $m = 1 \cdots d_p$ labels the row that the basis vector transforms as, and $\alpha = 1 \cdots n'_p$ is the basis vector number.

To construct $\overleftrightarrow{V}^{p}$, the basis vectors $\vec{v}^{p}_{s,m\alpha}$ are applied to each atom individually for each $\alpha = 1 \cdots n'_p$. This will form an orthogonal set of $n_p = n'_p N_b$ basis vectors that transform according to Equation (3.12). A vector for the full molecule will have $3N$ components. The first $3N_b$ components correspond to atoms at site 1. The next $3N_b$ components correspond to atoms at site 2 and so forth. Using this notation, the matrix of basis vectors for the full molecule, $\overleftrightarrow{V}^{p}$, takes the form

$$\overleftrightarrow{V}^{p} = \begin{bmatrix} \vec{v}^{p}_{1,11} & \vec{v}^{p}_{1,12} & \cdots & \vec{v}^{p}_{1,1n'_p} & 0 & \\ 0 & 0 & & 0 & \vec{v}^{p}_{1,11} & \cdots \\ 0 & 0 & & 0 & 0 & \\ \vdots & \vdots & & \vdots & \vdots & \\ \vec{v}^{p}_{2,11} & \vec{v}^{p}_{2,12} & \cdots & \vec{v}^{p}_{2,1n'_p} & 0 & \\ 0 & 0 & & 0 & \vec{v}^{p}_{2,11} & \cdots \\ 0 & 0 & & 0 & 0 & \\ \vdots & \vdots & & \vdots & \vdots & \end{bmatrix}. \tag{4.39}$$

The first n'_p columns of $\overleftrightarrow{V}^{p}$ have the vectors $\vec{v}^{p}_{s,m\alpha}$ applied to only atom 1 at each site. The next n'_p columns have the vectors $\vec{v}^{p}_{s,m\alpha}$ applied to only atom 2 at each site and so forth.

The components of the vector $|u^p\rangle$, which is of length n_p, can be labeled as

$$|u^p\rangle = \begin{bmatrix} u^p_{11} \\ \vdots \\ u^p_{n'_p 1} \\ u^p_{12} \\ \vdots \\ u^p_{n'_p 2} \\ \vdots \end{bmatrix}. \tag{4.40}$$

The first set of n'_p elements correspond to atom 1 and the second set to atom 2 and so forth. For a general element $u^p_{\alpha i}$, α labels the basis vector number and i labels the atom number. When $|u^p\rangle$ is operated on by $\overleftrightarrow{V}^p$, the result is a vector of length $3N$ which can be written in terms of N_s vectors $|z_{s,1}\rangle$ of length $3N_b$ as

$$\overleftrightarrow{V}^p |u^p\rangle = \begin{bmatrix} |z_{1,1}\rangle \\ \vdots \\ |z_{s,1}\rangle \\ \vdots \\ |z_{N_s,1}\rangle \end{bmatrix}. \tag{4.41}$$

The individual components of $|z_{s,1}\rangle$ for atom i (a vector of length 3) are

$$\vec{z}_{s,1i} = \sum_{\alpha=1}^{n'_p} \vec{v}^p_{s,1\alpha} u^p_{\alpha i}, \tag{4.42}$$

where the 1 denotes that the vector $|z_{s,1}\rangle$ is formed from row 1 basis vectors $\vec{v}^p_{s,1\alpha}$.

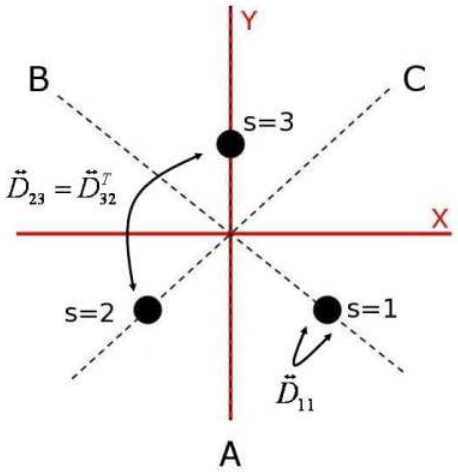

FIG. 10. A diagram illustrating the interaction between the various sites of a symmetric molecule with symmetry of the group c_{3v}. The interactions between sites i and j contribute to the dynamical matrix $\overleftrightarrow{D}_{ij}$. The dynamical matrices $\overleftrightarrow{D}_{ii}$ describe interactions of atoms at site i with other atoms at site i.

The full dynamical matrix of the entire molecule can be thought of in the following form

$$\overleftrightarrow{D} = \begin{bmatrix} \overleftrightarrow{D}_{11} & \overleftrightarrow{D}_{12} & \cdots & \overleftrightarrow{D}_{1N_s} \\ \overleftrightarrow{D}_{21} & \overleftrightarrow{D}_{22} & & \\ \vdots & & \ddots & \\ \overleftrightarrow{D}_{N_s1} & & & \overleftrightarrow{D}_{N_sN_s} \end{bmatrix}, \tag{4.43}$$

where the matrix $\overleftrightarrow{D}_{ij}$ is $3N_b \times 3N_b$ and describes the interaction of the basis atoms at site i with the basis atoms at site j. In general, only the coordinates of the basis atoms at a single site (arbitrarily assigned as site 1) are given and this information is sufficient to calculate the *operation* of the matrices $\overleftrightarrow{D}_{1i} = \overleftrightarrow{D}_{i1}^{\dagger}$ on a vector in *exactly* the same method as described in Chapter 4 Section VI. Figure 10 shows a schematic diagram of the interaction of site 1 with sites i for the group c_{3v}.

However, the vector $\overleftrightarrow{V}^{p}\,|u^{p}\rangle$ has components that will operate on matrices other than $\overleftrightarrow{D}_{1i}$ which can be seen in Equation (4.41). To alleviate this problem, the vector $\overleftrightarrow{V}^{p}\,|u^{p}\rangle$ is broken up in the following fashion,

$$\overleftrightarrow{V}^{p}\,|u^{p}\rangle = \begin{bmatrix} |z_{1,1}\rangle \\ 0 \\ 0 \\ \vdots \\ 0 \end{bmatrix} + \begin{bmatrix} 0 \\ |z_{2,1}\rangle \\ 0 \\ \vdots \\ 0 \end{bmatrix} + \cdots + \begin{bmatrix} 0 \\ \vdots \\ |z_{s,1}\rangle \\ \vdots \\ 0 \end{bmatrix} + \cdots . \tag{4.44}$$

According to Equation (4.42), $|z_{s,1}\rangle$ is formed from a linear combination of basis vectors that transform as row 1. This implies that

$$\hat{\Phi}(T_{s\rightarrow 1}) \begin{bmatrix} 0 \\ \vdots \\ |z_{s,1}\rangle \\ \vdots \\ 0 \end{bmatrix} = \sum_{m=1}^{d_p} \Gamma^{p}_{m1}(T_{s\rightarrow 1}) \begin{bmatrix} |z_{1,m}\rangle \\ 0 \\ 0 \\ \vdots \\ 0 \end{bmatrix}, \tag{4.45}$$

where the operator $\hat{\Phi}(T_{s\rightarrow 1})$ rotates site s to site 1. The components of $|z_{1,m}\rangle$ can be calculated using basis vectors that transform as row m in Equation (4.42). The vector in Equation (4.45) will now only be affected by the matrices $\overleftrightarrow{D}_{i1}$. Exploiting the invariance of the dynamical matrix to rotation operators [see Eq. (3.6)] *i.e.*,

$$\overleftrightarrow{D} = \hat{\Phi}^{\dagger}(T_{s\rightarrow 1})\; \overleftrightarrow{D}\; \hat{\Phi}(T_{s\rightarrow 1}), \tag{4.46}$$

the vector $\overleftrightarrow{D}\overleftrightarrow{V}^{p}\,|u^{p}\rangle$ can be written as

$$\overleftrightarrow{D}\overleftrightarrow{V}^{p}\ |u^{p}\rangle = \sum_{s=1}^{N_s}\sum_{m=1}^{d_p}\Gamma^{p}_{m1}(T_{s\to 1})\hat{\Phi}^{\dagger}(T_{s\to 1})\ \overleftrightarrow{D}\begin{bmatrix} |z_{1,m}\rangle \\ 0 \\ 0 \\ \vdots \\ 0 \end{bmatrix}. \tag{4.47}$$

In general, there may be more than one element T that rotates atoms at site s to the first site. Since an element that takes site s to the first site occurs the same number of times for each site, n_g/N_s times, Equation (4.47) can be written as a sum over all group elements as

$$\overleftrightarrow{D}\overleftrightarrow{V}^{p}\ |u^{p}\rangle = \frac{N_s}{n_g}\sum_{T\epsilon\mathcal{G}}\sum_{m=1}^{d_p}\Gamma^{p}_{m1}\hat{\Phi}^{\dagger}(T)\begin{bmatrix} \overleftrightarrow{D}_{11}\ |z_{1,m}\rangle \\ \overleftrightarrow{D}_{21}\ |z_{1,m}\rangle \\ \vdots \\ \overleftrightarrow{D}_{N_s1}\ |z_{1,m}\rangle \end{bmatrix}. \tag{4.48}$$

The d_p vectors $|z_{1,m}\rangle$ are of length $3N_b$ and have components defined by Equation (4.42).

Multiplying Equation (4.48) by $\overleftrightarrow{V}^{p\dagger}$, Equation (4.48) becomes the group dynamical matrix operating on vector $|u^{p}\rangle$,

$$\hat{D}^{p}|u^{p}\rangle = \frac{N_s}{n_g}\sum_{T\epsilon\mathcal{G}}\sum_{m=1}^{d_p}\Gamma^{p}_{m1}\left[\hat{\Phi}(T)\ \overleftrightarrow{V}^{p}\right]^{\dagger}\begin{bmatrix} \hat{D}_{11}|z_{1,m}\rangle \\ \hat{D}_{21}|z_{1,m}\rangle \\ \vdots \\ \hat{D}_{N_s1}|z_{1,m}\rangle \end{bmatrix}. \tag{4.49}$$

After a bit of algebra and applying the grand orthogonality theorem discussed in Chapter 3 Section II [Eq. (3.8)], the n_p components of $\overleftrightarrow{D}^{p}\ |u^{p}\rangle$ are obtained,

$$Du^{p}_{\beta i} = \frac{N_s}{d_p}\sum_{m=1}^{d_p}\sum_{s=1}^{N_s}\vec{v}^{\,p}_{s,m\beta}\cdot\vec{w}^{\,p}_{s,mi}. \tag{4.50}$$

The vector of length 3, $\vec{w}^{p}_{s,mi}$, are the components for atom i of the vector of length $3N_b$,

$$|w_{s,m}\rangle = \hat{D}_{s1}|z_{1,m}\rangle. \tag{4.51}$$

Though the mathematics to get to this point were involved and quite complicated, the procedure to calculate $\hat{D}^p|u^p\rangle$ can now be described in a simple three step process. First, the d_p vectors of length $3N_b$, $|z_{1,m}\rangle$, are computed using Equation (4.42). For example, the icosahedral group would have one vector for irreducible representation A, three for T2 *etc.* Second, the *operation* of the dynamical matrices $\overleftrightarrow{D}_{s1}$ on the vectors $|z_{1,m}\rangle$ are computed term by term in the same fashion for the regular dynamical matrix and the vectors of length $3N_b$, $|w_{s,m}\rangle$ are determined. Each energy term in Equation (4.33) will contribute to only one of the various matrices $\overleftrightarrow{D}_{s1}$ and is easily kept track of through a neighbor map. In the third and final step, the dot product with the basis vectors $\vec{v}^{p}_{s,m\beta}$ is taken and the components of $\hat{D}^p|u^p\rangle$ are determined using Equation (4.50).

The overall operation of $\hat{D}^p$ on a vector approximately scales as Order $(d_p N_b)$ operations, much smaller than the Order $(N_s N_b)$ operations that would be required for the calculation of the full dynamical matrix on a vector. Some computational tricks can be applied so that only $2d_p$ vectors of length $3N_b$ need to be stored during the calculation.

VIII. LOW FREQUENCY ANALYSIS OF UBIQUITIN

Computation of the low frequency mode patterns and frequencies using the phonon functional method developed in Section IV is essentially exact from a mathematics standpoint. However, when the procedure is implemented on a computer, finite precision mathematics can introduce round off errors compromising the final answer. This is especially true for iterative procedures.

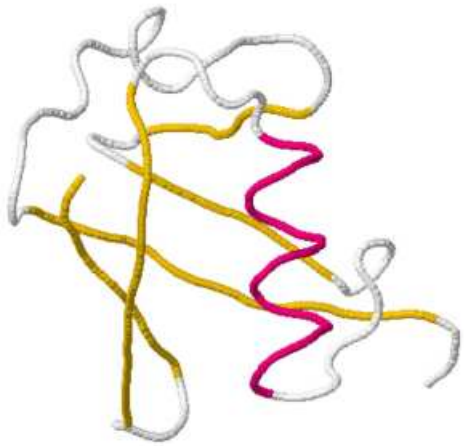

FIG. 11. The ubiquitin protein drawn as a trace of the protein backbone. Alpha helices are colored red, beta sheets yellow, and random coils white.

There are two possible sources for errors that can arise when determining the low frequency vibrational modes using the phonon functional method that should be examined. The first corresponds to the electrostatic cutoff approximation used to calculate the dynamical matrix operating on a vector in Order (N) steps. The second corresponds to errors that can be introduced from only a partial minimization of Equation (4.21).

To test the phonon functional method for calculating low frequency vibrational modes, the full dynamical matrix for the small protein ubiquitin, which consists of 1231 atoms, is calculated and diagonalized using standard techniques. A picture of the ubiquitin protein, drawn by tracing the backbone, is shown in Figure 11. The coordinates for the protein were obtained from the protein data bank (PDB code UBQ).

The parameters required in Equation (4.33) for the potential energy were obtained from the AMBER 94 force field model [9]. Interactions of the protein with water were modeled using the Generalized Born model for implicit solvation [13, 14, 37]. The protein was minimized to a RMS force of 0.001 eV/Å using a 10 Å cutoff for the electrostatic

TABLE II. Comparison of approximate Frequencies $\bar{\omega}$ and overlaps $\langle\bar{e}|e\rangle$ of ubiquitin calculated with varying electrostatic cutoff distance. The values ω and $|e\rangle$ correspond to the frequencies and eigenvectors for a cutoff of 60 Å where all possible electrostatic interactions are accounted for. Data for the lowest 10 frequencies are shown. All frequencies and eigenvectors were calculated by a standard diagonalization using LAPACK routines. Frequencies are listed in cm^{-1}.

	$\bar{\omega}$ ($\langle\bar{e}\|e\rangle$)			
ω	10 Å	15 Å	20 Å	25 Å
2.61695	1.77359	2.36610	2.54437	2.60925
	(0.99465)	(0.99875)	(0.99978)	(0.99999)
3.89102	3.66105	3.82239	3.84144	3.88511
	(0.99821)	(0.99969)	(0.99993)	(0.99999)
5.61328	5.44633	5.55615	5.59091	5.61335
	(0.99761)	(0.99977)	(0.99996)	(0.99999)
6.48471	6.26527	6.40495	6.46261	6.48497
	(0.99700)	(0.99971)	(0.99995)	(0.99999)
7.38389	6.99979	7.25301	7.35471	7.37703
	(0.99446)	(0.99887)	(0.99995)	(0.99999)
8.42460	7.96745	8.18604	8.23867	8.25354
	(0.85766)	(0.95572)	(0.99700)	(0.99993)
8.25679	8.15373	8.29575	8.37212	8.40900
	(0.85778)	(0.95624)	(0.99685)	(0.99991)
8.84597	8.63655	8.77978	8.82538	8.84432
	(0.98905)	(0.99959)	(0.99987)	(0.99999)
9.70602	9.58659	9.66414	9.69292	9.70453
	(0.99892)	(0.99992)	(0.99996)	(0.99999)
10.30379	9.95376	10.21614	10.27663	10.30137
	(0.99563)	(0.99961)	(0.99990)	(0.99999)

TABLE III. Convergence of the frequencies $\bar{\omega}$, overlaps $\langle\bar{e}|e\rangle$, and residual magnitudes $|r| = |\overleftrightarrow{D}\,|\bar{e}\rangle - \bar{\omega}^2|\bar{e}\rangle|$ for the 10 lowest frequencies of the ubiquitin protein using a 10 Å cutoff. The approximate frequencies and eigenvectors (denoted with a bar) were calculated by minimizing the phonon energy functional [Eq. (4.21)] until a final gradient of magnitude $|g| = \sum_k \langle g_k|g_k\rangle = 0.1$ or 0.01 was reached. The exact frequencies ω and eigenvectors $|e\rangle$ were calculated by diagonalizing the dynamical matrix with LAPACK routines at a 10 Å cutoff. Frequencies are listed in cm^{-1}.

	$\|g\| = 0.1$			$\|g\| = 0.01$		
ω	$\bar{\omega}$	$\langle\bar{e}\|e\rangle$	$\|r\|$	$\bar{\omega}$	$\langle\bar{e}\|e\rangle$	$\|r\|$
1.77359	3.31796	0.83751	0.00140	1.78593	0.99998	0.00061
3.66105	4.37188	0.97038	0.00142	3.66637	0.99999	0.00056
5.44633	5.82843	0.99621	0.00136	5.44932	0.99999	0.00048
6.26527	6.74868	0.99003	0.00139	6.26835	0.99999	0.00037
6.99979	7.37614	0.99392	0.00135	7.00227	0.99999	0.00049
7.96745	8.23958	0.95989	0.00135	7.96957	0.99999	0.00036
8.15373	8.56683	0.94914	0.00142	8.15625	0.99999	0.00036
8.63655	8.93564	0.98849	0.00142	8.63841	0.99999	0.00041
9.58659	9.85912	0.99626	0.00140	9.58853	0.99999	0.00050
9.95376	10.1502	0.99871	0.00136	9.95545	0.99999	0.00047

interactions. Since the protein was not exactly minimized to an RMS force of zero, negative eigenvalues may appear in the frequency spectrum. The purpose of this study however is to compare the quality of the low frequency modes predicted by minimizing the phonon energy functional to those predicted from a standard diagonalization of $\overleftrightarrow{D}$. Hence any low frequency spectrum of the molecule should be sufficient for this purpose.

To determine how the electrostatic cutoff will effect the frequencies and vibrational patterns, the dynamical matrix can be calculated and diagonalized for various cutoffs using a fixed structure for the protein. Since the ubiquitin molecule has a diameter of 55 Å, an electrostatic cutoff of 60 Å was used to calculate the frequencies ω and eigenvectors $|e\rangle$ where all interactions are accounted for. These frequencies and eigenvectors were then compared with calculations which used cutoffs that ranged from 10 Å to 25 Å. The data

in Table II shows good agreement between the frequencies and eigenvectors calculated with the much smaller cutoffs of 10 - 25 Å compared with those calculated with a 60 Å cutoff that includes all electrostatic interactions. Somewhat surprisingly, the smallest cutoff of 10 Å reproduces the eigenvectors and eigenvalues rather well.

The convergence properties of the phonon energy functional can be tested by stopping the minimization procedure once a specified non-zero tolerance for the magnitude of the gradient [Eq. (4.26)] is reached. Overlaps between the computationally exact eigenvectors ($|e\rangle$) computed with a diagonalization of the dynamical matrix and the approximate eigenvectors ($|\bar{e}\rangle$) formed using Equation (4.25) can be used to determine the quality of the approximate eigenvector. Another quantity, the residual vector $|r\rangle = \overleftrightarrow{D}\,|\bar{e}\rangle - \bar{\omega}^2|\bar{e}\rangle$, can also be used to access the quality of the approximate eigenvector $|\bar{e}\rangle$ with approximate eigenvalue $\bar{\omega}^2$. An analysis of Table III shows excellent agreement between the eigenvectors and frequencies calculated by minimizing the phonon energy functional [Eq. (4.21)] and those computed with a standard diagonalization routine typically found in LAPACK [61].

CHAPTER 5

MISCELLANEOUS MODELS

I. INTRODUCTION

In this chapter, various additional theoretical models are presented. These models are used to calculate mechanical vibrations of an elastic isotropic material, predict the relative Raman intensity of vibrational modes, and determine the force exerted from a pulse light source on a molecule.

The first model that will be discussed is used to predict mechanical vibrations of a continuous isotropic elastic material. Using elastic wave theory, analytic equations governing the displacement of the material are derived for the specific case of a cylindrical shell. This model will be used to predict mechanical modes of the M13 bacteriophage (see Chapter 6 Section II). Next, the bond polarizability model [19, 20] of Cardona, Snoke and Go is presented. The bond polarizability model is used to derive the change in susceptibility of a molecule due to a phonon excitation. In the following section, the bond polarizability model is extended to the case of a continuum amorphous isotropic material (amorphous isotropic bond polarizability model). The amorphous isotropic bond polarizability model allows for the prediction of relative Raman intensities (by calculating the change in susceptibility of the material) when little or no information about the location and orientation of the bonds in a molecule is known.

A general model for the calculation of the *average* relative Raman spectra of many molecules in solution is presented next. The model was derived for the case of molecules in solution due to a specific application to viral particles where its structure must be stabilized in a solution. With the change in susceptibility calculated with one of the two bond polarizability models, a Raman spectra for the molecule emerges.

Finally in the last section, a theoretical model is developed based on the bond polarizability model to predict the force on the individual atoms in a molecule from a pulsed laser source. The theory can then be used in a molecular dynamics simulation where a molecule is probed by an external *pulsed* laser source. A brief discussion on predictions for the total energy that can be delivered from the laser source to the molecule concludes the chapter.

II. CONTINUUM ELASTIC THEORY OF VIBRATIONS

Continuum elastic theory is a simple way to model the vibrational mode patterns of isotropic elastic materials. When applied to such "materials" as a virus capsid, the resulting mode patterns can give a simple description of the types of vibrations that are possible, along with an estimate of their corresponding frequencies.

The continuum theory for vibrations, or elastic wave theory (EWT), allows for a general analytic solution to the mode patters and frequencies for certain symmetric geometries (*e.g* a cylindrical shell). Some of the first derivations of the analytic solutions of elastic waves in materials of various geometries was done by Graff [65]. Following Graff's work, Balandin and Fonoberov [66] applied the EWT to two cylindrical viral capsids, the M13 bacteriophage and the tobacco mosaic virus. In this section, the analytic formulas for wave motion in an elastic cylindrical shell in the absence of external forces are reproduced for use with cylindrical shell viral capsids. In Chapter 6, the EWT will be applied to the M13 bacteriophage, a virus with a cylindrical shell shaped capsid and compared with predictions from other models.

In EWT, one considers a general displacement per unit length $\vec{u}$ of an elastic material at particular location $\vec{r}$ within the material. With this information at each location within the material, any deformation of the elastic material can be described completely. These

deformations of the material obey Hook's Law and according to elastic theory [67], the equations of motion can be obtained from the equation

$$(\lambda + \mu)\vec{\nabla}(\vec{\nabla} \cdot \vec{u}) + \mu\nabla^2\vec{u} = \rho\ddot{\vec{u}}, \tag{5.1}$$

where λ and μ are the Lamé coefficients and ρ is the density of the material. Taking the divergence of Equation (5.1) gives

$$\nabla^2\triangle = \frac{1}{c_l^2}\frac{\partial^2\triangle}{\partial t^2}, \tag{5.2}$$

where c_l is the longitudinal speed of sound in the material and is related to the Lamé coefficients via

$$c_l^2 = \frac{\lambda + 2\mu}{\rho}. \tag{5.3}$$

The symbol $\triangle$ denotes the divergence of the displacement $\vec{u}$, $\triangle = \vec{\nabla} \cdot \vec{u}$. Similarly, taking the curl of Equation (5.1) results in

$$\nabla^2\vec{\omega} = \frac{1}{c_t^2}\frac{\partial^2\vec{\omega}}{\partial t^2}, \tag{5.4}$$

where c_t is the transverse speed of sound in the material given in terms of the Lamé coefficients as

$$c_t^2 = \frac{\mu}{\rho}. \tag{5.5}$$

The vector $\vec{\omega}$ in Equation (5.4) is defined in terms of the curl of the displacement $\vec{u}$, $\vec{\omega} = \vec{\nabla} \times \vec{u}$.

Since transverse and longitudinal displacements obey the following relations:

$$\begin{aligned} \vec{\nabla} \cdot \vec{u}_t &= 0, \\ \vec{\nabla} \times \vec{u}_l &= 0, \end{aligned} \tag{5.6}$$

Equations (5.2) and (5.4) describe the wave motions for longitudinal and transverse waves respectively and their speed of propagation in the elastic medium is given by c_l and c_t. In general, the equations of motion can be simplified by introducing gauge invariant scalar and vector potentials Φ and $\vec{H}$. This allows the displacement $\vec{u}$ to be written in the form

$$\vec{u} = \vec{\nabla}\Phi + \vec{\nabla} \times \vec{H}. \tag{5.7}$$

Using the gauge such that $\vec{\nabla} \cdot \vec{H} = 0$ and substituting Equation (5.7) into Equation (5.1) gives the result

$$\vec{\nabla}\left[(\lambda + 2\mu)\nabla^2\Phi - \rho\ddot{\Phi}\right] + \vec{\nabla} \times \left[\mu\nabla^2\vec{H} - \rho\vec{H}\right] = 0. \tag{5.8}$$

This equation will only be satisfied if each bracketed term vanishes separately. Thus, the following scalar and vector wave equations for an elastic medium are obtained from Equation (5.8):

$$\begin{aligned} \nabla^2\Phi &= \frac{1}{c_l^2}\frac{\partial^2\Phi}{\partial t^2}, \\ \nabla^2\vec{H} &= \frac{1}{c_t^2}\frac{\partial^2\vec{H}}{\partial t^2}. \end{aligned} \tag{5.9}$$

At this point, the scalar and vector wave equations are completely general and can be used for any elastic material with any geometry by applying appropriate boundary conditions. Equations (5.9) can also be solved numerically for non symmetrical geometries. For an elastic cylindrical shell of inner radius a and outer radius b (see Figure 12), which is the specific case of interest here, the wave equations can be solved analytically to obtain the displacement patterns $\vec{u}$ as a function of position and time.

Working in cylindrical coordinates, the scalar wave equation becomes

$$\frac{1}{c_l^2}\frac{\partial^2\Phi}{\partial t^2} = \frac{\partial^2\Phi}{\partial r^2} + \frac{1}{r}\frac{\partial\Phi}{\partial r} + \frac{1}{r^2}\frac{\partial^2\Phi}{\partial\theta^2} + \frac{\partial^2\Phi}{\partial z^2}. \tag{5.10}$$

Using the following relations for derivatives of the unit direction vectors:

$$\begin{aligned} \frac{\partial \hat{e}_r}{\partial \theta} &= \hat{e}_\theta, \\ \frac{\partial \hat{e}_\theta}{\partial \theta} &= -\hat{e}_r, \end{aligned} \tag{5.11}$$

and combining like terms, the vector wave equation takes the form

$$\begin{aligned} \frac{1}{c_t^2}\frac{\partial^2 \vec{H}}{\partial t^2} &= \left[\nabla^2 H_r - \frac{H_r}{r^2} - \frac{2}{r^2}\frac{\partial H_\theta}{\partial \theta}\right]\hat{e}_r \\ &+ \left[\nabla^2 H_\theta - \frac{H_\theta}{r^2} + \frac{2}{r^2}\frac{\partial H_r}{\partial \theta}\right]\hat{e}_\theta + \nabla^2 H_z \hat{e}_z. \end{aligned} \tag{5.12}$$

The scalar and vector wave equations can be written as the product of purely radial, angular and axial functions, *i.e.* solutions of the form

$$\begin{aligned} \Phi &= f(r)\Theta_\phi(\theta)\exp(ikz - iwt), \\ H_r &= h_r(r)\Theta_r(\theta)\exp(ikz - iwt), \\ H_\theta &= h_\theta(r)\Theta_\theta(\theta)\exp(ikz - iwt), \\ H_z &= h_z(r)\Theta_z(\theta)\exp(ikz - iwt). \end{aligned} \tag{5.13}$$

Plugging the Φ solution into the scalar wave equation yields

$$\left[\frac{\partial^2 f}{\partial r^2} + \frac{1}{r}\frac{\partial f}{\partial r}\right]\Theta_\phi \exp(ikz - iwt) + \frac{1}{r^2}\frac{\partial^2 \Theta_\phi}{\partial \theta^2} f \exp(ikz - iwt) - k^2\Phi = -\frac{w^2}{c_l^2}\Phi. \tag{5.14}$$

Multiplying by r^2/Φ and rearranging results in the separable equation,

$$\left[r^2\frac{\partial^2 f}{\partial r^2} + r\frac{\partial f}{\partial r}\right]\frac{1}{f} + \alpha^2 r^2 = -\frac{\partial^2 \Theta_\phi}{\partial \theta^2}\frac{1}{\Theta_\phi}, \tag{5.15}$$

where $\alpha^2 = w^2/c_l^2 - k^2$. Setting each side of Equation (5.15) equal to a constant, the following ordinary differential equations are obtained:

$$\begin{aligned} -\frac{\partial^2 \Theta_\phi}{\partial \theta^2}\frac{1}{\Theta_\phi} &= n^2, \\ \frac{\partial^2 f}{\partial r^2} + \frac{1}{r}\frac{\partial f}{\partial r} + \left(\alpha^2 - \frac{n^2}{r^2}\right) f &= 0. \end{aligned} \tag{5.16}$$

The Θ_ϕ equation is the trigonometric differential equation with solution,

$$\Theta_\phi(\theta) = A\cos(n\theta) + B\sin(n\theta). \tag{5.17}$$

Applying the boundary condition $\Theta(0) = \Theta(2\pi)$ requires that n be an integer. Furthermore, later requirements that the boundary conditions be satisfied for all θ will require that either $A = 0$ or $B = 0$. Here, the solutions for the displacement will be derived for the case $B = 0$. The additional solutions for the case $A = 0$ can be obtained by replacing $\cos(n\theta)$ for $\sin(n\theta)$ and $\sin(n\theta)$ for $-\cos(n\theta)$ in the final displacement formulas [see Eq. (5.28)]. The additional solutions are a direct result of the symmetry of the cylindrical shell. For $n > 0$, a rotation of a displacement pattern by $\pi/4$ about the shell axis results in another displacement pattern that is orthogonal to the first.

Since n is required to be an integer, the differential equation for $f(r)$ in Equation (5.16) is the cylindrical Bessel equation with solution,

$$f(r) = A_\phi J_n(\alpha r) + B_\phi Y_n(\alpha r), \tag{5.18}$$

where J_n and Y_n are the cylindrical Bessel functions of first and second kind respectively. At this point it is important to point out that for certain k vectors it is possible for α to be imaginary. In this situation, the solution for $f(r)$ becomes

$$f(r) = A_\phi I_n(|\alpha| r) + B_\phi K_n(|\alpha| r), \tag{5.19}$$

where I_n and K_n are modified cylindrical Bessel equations of the first and second kind respectively. To account for both possibilities, the function $f(r)$ is written in the form

$$f(r) = A_\phi Z_n(\alpha_1 r) + B_\phi W_n(\alpha_1 r). \tag{5.20}$$

The functions Z_n and W_n represent the regular cylindrical Bessel functions when $\alpha^2 > 0$

and the modified cylindrical Bessel functions $\alpha^2 < 0$. In either case α is required to be real, thus $\alpha_1 = |\alpha|$ is used to enforce this requirement.

Examining the vector wave equation, Equation (5.12), the z component of the vector field satisfies a wave equation similar to the scalar field, but with c_l replaced with c_t. Thus, the solution for H_z is the same as Φ but with α^2 replaced by $\beta^2 = w^2/c_t^2 - k^2$. However, the requirement that later boundary conditions be satisfied at all θ requires the Θ_z solution to take the form

$$\Theta_z(\theta) = B\sin(n\theta). \tag{5.21}$$

The solutions for H_r and H_θ are slightly more complicated due to the coupling of the radial differential equations for $h_r(r)$ and $h_\theta(r)$. Once again, boundary conditions on θ will require that the Θ_r and Θ_θ functions be written as

$$\begin{aligned} \Theta_r(\theta) &= B\sin(n\theta), \\ \Theta_\theta(\theta) &= A\cos(n\theta). \end{aligned} \tag{5.22}$$

Writing the two coupled radial differential equations h_r and h_θ as

$$\begin{aligned} \frac{\partial^2 h_r}{\partial r^2} + \frac{1}{r}\frac{\partial h_r}{\partial r} + \left(\beta^2 - \frac{n^2+1}{r^2}\right) h_r + \frac{2n}{r^2} h_\theta &= 0, \\ \frac{\partial^2 h_\theta}{\partial r^2} + \frac{1}{r}\frac{\partial h_\theta}{\partial r} + \left(\beta^2 - \frac{n^2+1}{r^2}\right) h_\theta + \frac{2n}{r^2} h_\theta &= 0, \end{aligned} \tag{5.23}$$

then adding and subtracting them yields the following two equations:

$$\begin{aligned} \left[\frac{\partial^2}{\partial r^2} + \frac{1}{r}\frac{\partial}{\partial r} + \beta^2 - \frac{(n-1)^2}{r^2}\right](h_r + h_\theta) &= 0, \\ \left[\frac{\partial^2}{\partial r^2} + \frac{1}{r}\frac{\partial}{\partial r} + \beta^2 - \frac{(n+1)^2}{r^2}\right](h_r - h_\theta) &= 0. \end{aligned} \tag{5.24}$$

Since the scalar and vector fields are gauge invariant, one can choose the gauge such that $h_r = -h_\theta$ while still satisfying $\vec{\nabla}\cdot\vec{H} = 0$. The solution for $h_r(r)$ in this gauge will be

$$h_r(r) = A_r Z_{n+1}(\beta_1 r) + B_r W_{n+1}(\beta_1 r), \tag{5.25}$$

with $\beta_1 = |\beta|$ and Z_{n+1}, W_{n+1} denote either regular or modified cylindrical Bessel functions depending on the sign of β^2.

The solution to the scalar and vector field equations for a cylindrical shell now take the final form

$$\begin{aligned} \Phi &= f(r)\cos(\theta)\exp(ikz - iwt), \\ H_r &= h(r)\sin(\theta)\exp(ikz - iwt), \\ H_\theta &= -h(r)\cos(\theta)\exp(ikz - iwt), \\ H_z &= h_z(r)\sin(\theta)\exp(ikz - iwt), \end{aligned} \tag{5.26}$$

where the radial functions $f(r)$,$h_r(r)$, and $h_z(r)$ are given by

$$\begin{aligned} f(r) &= A_\phi Z_n(\alpha_1 r) + B_\phi W_n(\alpha_1 r), \\ h_r(r) &= A_r Z_{n+1}(\beta_1 r) + B_r W_{n+1}(\beta_1 r), \\ h_z(r) &= A_z Z_n(\beta_1 r) + B_z W_n(\beta_1 r). \end{aligned} \tag{5.27}$$

Using Equation (5.7), the components of the displacement are formed and simplified through the use of Equations (5.26) and (5.27) to give

$$\begin{aligned} u_r(r,\theta,z,t) &= \left[f' + \frac{n}{r}h_z + ikh_r\right]\cos(n\theta)\exp(ikz - iwt), \\ u_\theta(r,\theta,z,t) &= \left[-\frac{n}{r}f + ikh_r - h_z'\right]\sin(n\theta)\exp(ikz - iwt), \\ u_z(r,\theta,z,t) &= \left[ikf - \frac{n+1}{r}h_r - h_r'\right]\cos(n\theta)\exp(ikz - iwt). \end{aligned} \tag{5.28}$$

The prime notations (f',h_r', *etc.*) denote the derivative of the function with respect to the radial component.

Boundary conditions can now be applied for the case of a cylindrical shell of inner radius a and outer radius b. A diagram is shown in Figure 12 to illustrate the geometry.

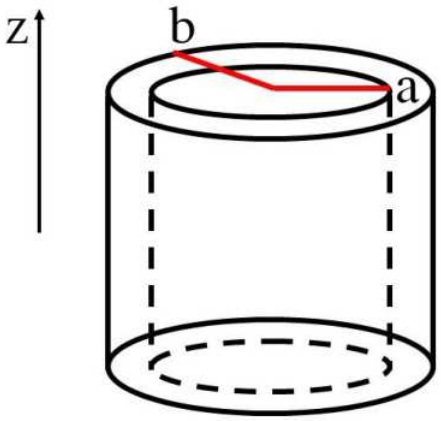

FIG. 12. A simple diagram of an elastic cylindrical shell with inner and outer radii a and b. The axis of the shell is located along the $\hat{z}$ axis. Analytic solutions for the propagating waves in the elastic shell can be determined from elastic wave theory.

Enforcement of the boundary conditions on the shell will determine the frequencies ω and the six coefficients A_ϕ, B_ϕ, A_r, B_r, A_z, and B_z that can be used in Equations (5.27) and (5.28) to predict the displacement patterns. For the case where no external forces are applied to the shell, the boundary conditions require that the radial components of the net force on the inner and outer surfaces of the shell must vanish in order to satisfy Newton's second law. This requires that $\sigma_{rr} = \sigma_{r\theta} = \sigma_{rz} = 0$, where σ_{ij} is the ij component of the stress tensor matrix. The stress tensor can be derived from the free energy per unit volume of an elastic medium [67],

$$\sigma_{ij} = \frac{\partial f}{\partial u_{ij}}, \tag{5.29}$$

where the free energy per unit volume, f, and the strain tensor u_{ij} are defined as

$$\begin{aligned} f &= \frac{\lambda}{2}\left(\sum_i u_{ii}\right)^2 + \mu \sum_{ij} u_{ij}^2, \\ u_{ij} &= \frac{1}{2}\left(\frac{\partial u_i}{\partial x_j} + \frac{\partial u_j}{\partial x_i}\right). \end{aligned} \tag{5.30}$$

Here, $i, j = r, \theta, z$ while x_j denotes a specific variable (r, θ, z). Likewise, u_i is the displacement along the direction i (r, θ, z).

The required radial stress elements can be written in cylindrical coordinates as

$$\begin{aligned} \sigma_{rr} &= \lambda \vec{\nabla} \cdot \vec{u} + 2\mu u_{rr}, \\ \sigma_{r\theta} &= 2\mu u_{r\theta}, \\ \sigma_{rz} &= 2\mu u_{rz}, \end{aligned} \tag{5.31}$$

where λ and μ are the lamé constants. Similarly, the strain tensor elements u_{ij} in cylindrical coordinates are

$$\begin{aligned} u_{rr} = \tfrac{\partial u_r}{\partial r}, \quad u_{\theta\theta} = \tfrac{1}{r}\tfrac{\partial u_\theta}{\partial \theta} + \tfrac{u_r}{r}, \\ u_{zz} = \tfrac{\partial u_z}{\partial z}, \quad 2u_{r\theta} = \tfrac{1}{r}\tfrac{\partial u_r}{\partial \theta} + \tfrac{\partial u_\theta}{\partial r} - \tfrac{u_\theta}{r}, \\ 2u_{rz} = \tfrac{\partial u_z}{\partial r} + \tfrac{\partial u_r}{\partial z}, \quad 2u_{\theta z} = \tfrac{1}{r}\tfrac{\partial u_z}{\partial \theta} + \tfrac{\partial u_\theta}{\partial z}. \end{aligned} \tag{5.32}$$

Requiring the three stress elements [Eq. (5.31)] to vanish at the inner and outer radii a and b yields the following six boundary conditions (three each for both the inner and outer radii):

$$\left[-\lambda(\alpha^2 + k^2) f + 2\mu \left\{ f'' + \frac{n}{r}\left(h_z' - \frac{h_z}{r}\right) + ikh_r' \right\}\right]_{r=a,b} = 0, \tag{5.33}$$

$$\left[-\frac{2n}{r}\left(f' - \frac{f}{r}\right) - (2h_z'' + \beta^2 h_z) - ik\left(\frac{n+1}{r}h_r - h_r'\right)\right]_{r=a,b} = 0, \tag{5.34}$$

$$\left[2ikf' - \frac{n}{r}\left(\frac{n+1}{r}h_r + h_r'\right) + (\beta^2 - k^2)h_r + ik\frac{n}{r}h_z\right]_{r=a,b} = 0. \tag{5.35}$$

These six equations can be written in matrix form, $\overleftrightarrow{C}\ \vec{A} = 0$, where $\vec{A}$ is the column vector of radial function coefficients, $\vec{A} = (A_\phi, A_r, A_z, B_\phi, B_r, B_z)$. The following recurrence relations for the regular and modified cylindrical Bessel functions [68],

$$\begin{aligned} \mathcal{C}_{n+1}(z) &= \frac{2n}{z}\mathcal{C}_n(z) - \mathcal{C}_{n-1}, \\ \mathcal{C}_n'(z) &= \mathcal{C}_{n-1}(z) - \frac{n}{z}\mathcal{C}_n, \end{aligned}$$

$$\begin{aligned}
\mathcal{L}_{n+1}(z) &= -\frac{2n}{z}\mathcal{L}_n(z) + \mathcal{L}_{n-1}, \\
\mathcal{L}'_n(z) &= \mathcal{L}_{n-1}(z) - \frac{n}{z}\mathcal{L}_n,
\end{aligned} \tag{5.36}$$

where $\mathcal{C}_n$ denotes either J_n or Y_n and $\mathcal{L}_n$ denotes either I_n or $e^{in\pi}K_n$. The prime denotes the derivative of the function with respect to argument z. These can be used to simplify the final matrix equation. The matrix elements C_{ij} [Eq. (5.37)] are explicitly written for the first three rows. The last three rows are easily obtained from the first three by simply replacing a with b.

$$\begin{aligned}
C_{11} &= \left\{2n(n-1) - (\beta^2 - k^2)a^2\right\} Z_n(\alpha_1 a) + 2\lambda_\alpha \alpha_1 a Z_{n+1}(\alpha_1 a) \\
C_{12} &= 2ik\beta_1 a^2 Z_n(\beta_1 a) - 2ika(n+1)Z_{n+1}(\beta_1 a) \\
C_{13} &= 2n(n-1)Z_n(\beta_1 a) - 2\lambda_\beta n\beta_1 a Z_{n+1}(\beta_1 a) \\
C_{14} &= \left\{2n(n-1) - (\beta^2 - k^2)a^2\right\} W_n(\alpha_1 a) + 2\alpha_1 a W_{n+1}(\alpha_1 a) \\
C_{15} &= 2\lambda_\beta ik\beta_1 a^2 W_n(\beta_1 a) - 2ika(n+1)W_{n+1}(\beta_1 a) \\
C_{16} &= 2n(n-1)W_n(\beta_1 a) - 2n\beta_1 a W_{n+1}(\beta_1 a) \\
C_{21} &= -2n(n-1)Z_n(\alpha_1 a) + 2\lambda_\alpha n\alpha_1 a Z_{n+1}(\alpha_1 a) \\
C_{22} &= ik\beta_1 a^2 Z_n(\beta_1 a) - 2ika(n+1)Z_{n+1}(\beta_1 a) \\
C_{23} &= -\left\{2n(n-1) - \beta^2 a^2\right\} Z_n(\beta_1 a) - 2\lambda_\beta n\beta_1 a Z_{n+1}(\beta_1 a) \\
C_{24} &= -2n(n-1)W_n(\alpha_1 a) + 2n\alpha_1 a W_{n+1}(\alpha_1 a) \\
C_{25} &= \lambda_\beta ik\beta_1 a^2 W_n(\beta_1 a) - 2ika(n+1)W_{n+1}(\beta_1 a) \\
C_{26} &= -\left\{2n(n-1) - \beta^2 a^2\right\} W_n(\beta_1 a) - 2n\beta_1 a W_{n+1}(\beta_1 a) \\
C_{31} &= -2nkaZ_n(\alpha_1 a) + 2\lambda_\alpha k\alpha_1 a^2 Z_{n+1}(\alpha_1 a) \\
C_{32} &= -in\beta_1 a Z_n(\beta_1 a) + (\beta^2 - k^2)ia^2 Z_{n+1}(\beta_1 a) \\
C_{33} &= -knaZ_n(\beta_1 a)
\end{aligned}$$

$$
\begin{aligned}
C_{34} &= -2nkaW_n(\alpha_1 a) + 2k\alpha_1 a^2 W_{n+1}(\alpha_1 a) \\
C_{35} &= -\lambda_\beta in\beta_1 aW_n(\beta_1 a) + (\beta^2 - k^2)ia^2 W_{n+1}(\beta_1 a) \\
C_{36} &= -knaW_n(\beta_1 a)
\end{aligned} \tag{5.37}
$$

Again, $\alpha_1 = |\alpha|$ and the coefficient λ_α is defined as

$$
\lambda_\alpha = \begin{cases} 1 & \alpha^2 \geq 0 \\ -1 & \alpha^2 \leq 0 \end{cases}, \tag{5.38}
$$

with a similar definitions for β_1 and λ_β.

The frequencies are determined from the matrix equation $\overleftrightarrow{C}\ \vec{A} = 0$. Since a non trivial solution is required, *i.e.* $\vec{A} \neq 0$, the determinant of the matrix $\overleftrightarrow{C}$ must vanish for a given frequency ω. This frequency and the corresponding non zero eigenvector correspond to a natural vibrational mode for the cylindrical shell. The displacement pattern can be obtained by substitution of the eigenvector coefficients into Equation (5.27) to produce the radial functions $f(r)$, $h_r(r)$, and $h_z(r)$ needed in the displacement formulas [Eq. (5.28)].

III. BOND POLARIZABILITY MODEL

The main purpose of the bond polarizability model is to calculate the *change* in susceptibility of the medium due to distortions. Once this is calculated, it can be used to predict the inelastic (Raman) scattered light intensity, or as will be seen in Section VI, the force on the individual atoms in a molecule from a light source. The bond polarizability model can be thought of in simple terms as representing the polarizability of a single bond to first order in an expansion about the bonds equilibrium position. The bond polarizability model was first described by Cardona, Go and Blitz [19, 20] for the purpose of reproducing the experimental Raman spectra of C_{60}. Later, the work was extended by Guha, Menendez, Page, and Adams [21].

In general, the polarizability of each bond is dependent on the charge density distribution surrounding it, hence a bonds polarizability will be dependent on the relative position of each atom in the crystal or molecule. As such, the ability of the bond polarizability model to reproduce *exact* Raman spectra for molecules other than C_{60} may be poor. However, the bond polarizability model can be used as a first approximation to obtain a fairly good picture of the vibrational modes of the molecule that are either strongly or weakly Raman active, or Raman silent due to near or exact symmetries.

Assuming that the polarizability of each bond behaves roughly linearly with respect to the bond distance, the polarizability for a given bond can be written to first order in the bond distance l as

$$\overleftrightarrow{\alpha}\,(l+dl) = \begin{pmatrix} \alpha_\perp + \alpha'_\perp dl & 0 & 0 \\ 0 & \alpha_\perp + \alpha'_\perp dl & 0 \\ 0 & 0 & \alpha_\parallel + \alpha'_\parallel dl \end{pmatrix}, \tag{5.39}$$

where the bond has been assumed to be orientated along the z axis. The model parametrizes two main coefficients. The first, (denoted $\alpha'_\parallel$), describes an induced polarization due to a stretching of the bond along the axis while the second, (denoted $\alpha'_\perp$), describes an induced polarization due to a shearing of the bond. The polarizability of the bond is often referred to as the bond polarizability ellipse. A schematic picture illustrating the polarization ellipse of a single bond is shown in Figure 13.

The coefficients $\alpha'_\perp$ and $\alpha'_\parallel$ represent the directional derivatives of the polarizability tensor, $\overleftrightarrow{\alpha}$, perpendicular and parallel to the bond axis for a given bond length l. Thus, the *induced* polarizability (or change in polarization) due to a small displacement of the atoms

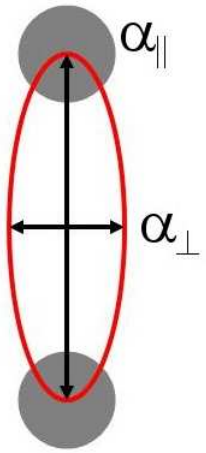

FIG. 13. Schematic picture of the polarization ellipse. The parameter $\alpha'_{\perp}$ is the induced polarization of the bond perpendicular to the bond axis resulting from a stretching of the bond. Likewise, $\alpha'_{\parallel}$ is the induced polarization of the bond along the axis of the bond.

along the bond direction is given by

$$\Delta \overleftrightarrow{\alpha} = \begin{pmatrix} \alpha'_{\perp}\Delta l & 0 & 0 \\ 0 & \alpha'_{\perp}\Delta l & 0 \\ 0 & 0 & \alpha'_{\parallel}\Delta l \end{pmatrix}. \tag{5.40}$$

The total induced susceptibility $\Delta \overleftrightarrow{\chi}$ for the molecule is found by summing over all bonds in the molecule, taking into account the orientation of each bond.

In reality, each bond should have its own unique $\alpha'_{\parallel}$ and $\alpha'_{\perp}$ associated with it in order to achieve the best results. However, for the purposes of simplifying the model, the set of α' is reduced to one or two unique types. This is the approach taken here. It should be noted that the main goal of any bond polarizability calculation in this dissertation is to reproduce *approximate* Raman spectra that predict strong, weak, and silent Raman modes, not to reproduce accurate experimental measurements (*i.e.* intensity measurements). Only a "rough" prediction of the Raman profile is desired. For these reasons, the bond polarizability

parameters are chosen to be identical for all bonds. The parameters chosen are intended to reflect an "average" or "reasonable" bond in biological molecules, carbon.

Cardona and Snoke [20] calculate bond polarizability parameters for single and double bonds in C_{60}. The parameters used for calculations in the continuum model are as follows: $(\alpha'_{\parallel} - \alpha'_{\perp})/d^2 = 1.2$, $(2\alpha'_{\parallel} + \alpha'_{\perp})/d^2 = 1.7$, and $(\alpha_{\parallel} - \alpha_{\perp})/d^3 = 0.5$. The units of $\alpha_{\parallel}$ and $\alpha_{\perp}$ are in Å^3, and the derivatives $\alpha'_{\parallel}$ and $\alpha'_{\perp}$ have units of Å^2. Later, specifically in atomistic approaches, the parameters of Guha *et al.* [21] given by $(\alpha'_{\parallel} - \alpha'_{\perp}) = 2.3$ Å^2, $(2\alpha'_{\parallel} + \alpha'_{\perp}) = 2.3$ Å^2, and $(\alpha_{\parallel} - \alpha_{\perp}) = 1.28$ Å^3 have also been used.

IV. AMORPHOUS ISOTROPIC BOND POLARIZABILITY MODEL

The bond polarizability model (BP) discussed in Section III is microscopic, taking into account each bond and its orientation with respect to every other bond in the molecule. When one uses the bond polarizability model, the position of each atom in the molecule is required.

The amorphous isotropic bond polarizability model (AIBP) is an extension of the traditional BP model to situations where the atomic detail of a medium is either unknown or much too large to be taken fully into account. A macroscopic treatment of the BP model results in an induced polarizability per unit volume of the material, which when integrated over the entire volume, gives the total induced susceptibility. The AIBP model further assumes that the material is a network of randomly orientated bonds (an amorphous material) which is then applicable to proteins and protein structures such as viral capsids where the individual bonds tend to be more randomly orientated. Here, a specific equation for the polarizability per unit volume is derived in terms of the strain tensor u_{ij} which can then be used directly with elastic wave theory.

The AIBP model begins by consider a macroscopic volume which is sufficiently large such that all bond orientations are equally likely. The quantity sought is then the *average* induced polarization per unit volume due to a small elastic deformation of the material. This can be calculated by averaging the orientations of a single bond. The polarizability $\overleftrightarrow{\alpha}$ of a single bond can be written in terms of the 3×3 projection operator matrix,

$$\hat{P} = |\hat{d}\rangle\langle\hat{d}|, \tag{5.41}$$

where $\hat{d}$ is the unit direction vector of the bond. This projection operator will then give the component of any vector along the bond axis. In terms of the projection operator, the polarizability tensor for a bond can be written as

$$\overleftrightarrow{\alpha} = \alpha_{\parallel}\hat{P} + \alpha_{\perp}(\hat{I} - \hat{P}), \tag{5.42}$$

where the parallel and perpendicular polarizabilities, $\alpha_{\parallel}$ and $\alpha_{\perp}$, depend on the length of the bond distance d. A small change in polarization can occur in two ways; by stretching or squishing the bond, or by changing the bond direction. Taking into account both possibilities, the induced polarizability of the bond takes the form

$$\Delta\overleftrightarrow{\alpha} = \Delta\alpha_{\parallel}\hat{P} + \Delta\alpha_{\perp}(\hat{I} - \hat{P}) + (\alpha_{\parallel} - \alpha_{\perp})\Delta\hat{P}. \tag{5.43}$$

The terms $\Delta\alpha_{\parallel}$ and $\Delta\alpha_{\perp}$ describe changes in the parallel and perpendicular polarizabilities respectively due to a change in bond length. The term $\Delta\hat{P}$ describes the change in the projection operator that occurs due to a change in direction of the bond. Averaging Equation (5.43) over all bond orientations then dividing by the average volume of a bond will yield the induced polarizability per unit volume in the AIBP model. Since the final goal is a formula which can be used with elastic theory, the terms $\Delta\alpha_{\parallel}$, $\Delta\alpha_{\perp}$ and $\Delta\hat{P}$ must be represented in terms of the elastic strain tensor u_{ij}.

The quantities $\Delta\alpha_{\parallel}$ and $\Delta\alpha_{\perp}$ can be written to linear order in Δd as

$$\begin{aligned} \Delta\alpha_{\parallel} &= \alpha'_{\parallel}\Delta d, \\ \Delta\alpha_{\perp} &= \alpha'_{\perp}\Delta d, \end{aligned} \tag{5.44}$$

where $\alpha'_{\parallel}$ and $\alpha'_{\perp}$ are constants. In terms of the strain, a small change in the bond distance can be represented as [see Eq. (5.30)]

$$(d+\Delta d)^2 \approx d^2 \sum_{ij}(\delta_{ij}+2u_{ij})\hat{d}_i\hat{d}_j, \tag{5.45}$$

where the second order term $(\Delta d)^2$ has been neglected. The notation $\hat{d}_i$ represents the ith component of the unit direction vector for the bond. Solving for Δd in Equation (5.45) and only keeping terms to linear order in the strain gives

$$\begin{aligned} \Delta d &= d\left(1+2\sum_{ij}u_{ij}\hat{d}_i\hat{d}_j\right)^{\frac{1}{2}} - d \\ &\approx d\sum_{ij}u_{ij}\hat{d}_i\hat{d}_j. \end{aligned} \tag{5.46}$$

Combining Equation (5.46) with Equation (5.44) gives the change in polarizabilities ($\Delta\alpha_{\parallel}$ and $\Delta\alpha_{\perp}$) in terms of the strain tensor.

The change in the projection operator $\Delta\hat{P}$ also needs to be written in terms of the strain tensor. Using $\hat{d}'$ to describe the orientation of a bond after a deformation, $\Delta\hat{P}$ becomes

$$\Delta\hat{P} = |\hat{d}'\rangle\langle\hat{d}'| - |\hat{d}\rangle\langle\hat{d}|. \tag{5.47}$$

Writing $\hat{d}'$ in terms of the strain tensor operator $\hat{U}$,

$$|\hat{d}'\rangle = \frac{(\hat{I}+\hat{U})|\hat{d}\rangle}{\sqrt{\langle\hat{d}|(\hat{I}+\hat{U})(\overleftrightarrow{I}+\hat{U})|\hat{d}\rangle}}, \tag{5.48}$$

and keeping terms to linear order in strain tensor yields a simplified formula for $|\hat{d}'\rangle$,

$$|\hat{d}'\rangle = \left[1-\langle\hat{d}|\hat{U}|\hat{d}\rangle\hat{I}\right]|\hat{d}\rangle + \hat{U}|\hat{d}\rangle. \tag{5.49}$$

Substitution of Equation (5.49) into Equation (5.47) and again keeping terms to linear order in the strain tensor gives the following result for $\Delta\hat{P}$,

$$\Delta\hat{P} = |\hat{d}\rangle\langle\hat{d}|\hat{U} + \hat{U}|\hat{d}\rangle\langle\hat{d}| - 2\langle\hat{d}|\hat{U}|\hat{d}\rangle|\hat{d}\rangle\langle\hat{d}|. \tag{5.50}$$

The fact that the strain tensor is symmetric and real has been used for simplification of the formula.

Now with a form for the induced polarization of a single bond in terms of the local deformation of the material *i.e.* the strain, the macroscopic induced polarization per unit volume can now be found by averaging Equation (5.43) over the solid angle Ω,

$$\langle\Delta\alpha\rangle_\Omega = (\alpha'_\parallel - \alpha'_\perp)\langle\hat{P}\Delta d\rangle_\Omega + \alpha'_\perp\langle\Delta d\rangle_\Omega + (\alpha_\parallel - \alpha_\perp)\langle\Delta\hat{P}\rangle_\Omega. \tag{5.51}$$

A specific component of Equation (5.51) is given by

$$\begin{aligned}
\langle\Delta\alpha_{ij}\rangle_\Omega &= d(\alpha'_\parallel - \alpha'_\perp)\sum_{mn} u_{mn}\langle\hat{d}_i\hat{d}_j\hat{d}_m\hat{d}_n\rangle_\Omega + \delta_{ij}d\alpha'_\perp\sum_{mn} u_{mn}\langle\hat{d}_m\hat{d}_n\rangle_\Omega \\
&+ (\alpha_\parallel - \alpha_\perp)\sum_m \left(u_{jm}\langle\hat{d}_i\hat{d}_m\rangle_\Omega + u_{im}\langle\hat{d}_j\hat{d}_m\rangle_\Omega\right) \\
&- 2(\alpha_\parallel - \alpha_\perp)\sum_{mn} u_{mn}\langle\hat{d}_i\hat{d}_j\hat{d}_m\hat{d}_n\rangle_\Omega.
\end{aligned} \tag{5.52}$$

Equation (5.52) is now dependent on only the average of bond orientations. Using polar coordinates for the bond directions, one can easily show that the only surviving averages are

$$\begin{aligned}
\langle\hat{d}_i\hat{d}_j\rangle_\Omega &= \delta_{ij}\frac{1}{3}, \\
\langle\hat{d}_i^2\hat{d}_j^2\rangle_\Omega &= \delta_{ij}\frac{1}{5} + (1-\delta_{ij})\frac{1}{15}.
\end{aligned} \tag{5.53}$$

As a result, Equation (5.52) simplifies to

$$\begin{aligned}
\langle\Delta\alpha_{ij}\rangle_\Omega &= \frac{2}{15}d(\alpha'_\parallel - \alpha'_\perp)\left(u_{ij} + \frac{1}{2}Tr(\hat{U})\delta_{ij}\right) + \frac{1}{3}d\alpha'_\perp Tr(\hat{U})\delta_{ij} \\
&+ \frac{2}{5}(\alpha_\parallel - \alpha_\perp)\left(u_{ij} - \frac{1}{3}Tr(\hat{U})\delta_{ij}\right).
\end{aligned} \tag{5.54}$$

Defining the shear (α_s) and compressional (α_c) polarizability constants as

$$\begin{aligned} \alpha_s &= \frac{2}{5}\left(\frac{d(\alpha'_{\parallel}-\alpha'_{\perp})}{3}+(\alpha_{\parallel}-\alpha_{\perp})\right), \\ \alpha_c &= \frac{d}{9}(\alpha'_{\parallel}+2\alpha'_{\perp}), \end{aligned} \tag{5.55}$$

and using the shear stress tensor,

$$\hat{U}_s = \hat{U} - \frac{1}{3}Tr(\hat{U})\hat{I}, \tag{5.56}$$

the final result for the average induced polarizability of a single bond is

$$\Delta \overleftrightarrow{\alpha} = \alpha_s \hat{U}_s + \alpha_c Tr(\hat{U})\hat{I}. \tag{5.57}$$

Assuming that each bond occupies an average volume of V_b, the formula for the induced polarizability per unit volume is then

$$\Delta \overleftrightarrow{\alpha} = \frac{\alpha_s}{V_b}\hat{U}_s + \frac{\alpha_c}{V_b}Tr(\hat{U})\hat{I}. \tag{5.58}$$

Equation (5.58) can now be used with elastic wave theory (see Section II) to calculate the total induced susceptibility of a elastic isotropic material treated as a network of randomly orientated bonds. Combined with the Raman intensity formula which will be derived in Section V, Equation (5.58) provides a simple means to approximate the Raman spectra of a material, such as a viral capsid, without knowing explicit atomic positions.

V. RAMAN INTENSITY FOR PARTICLES IN SOLUTION

Interaction of a polarizable medium with an oscillating electric field (light for example) produces radiation. The polarization field produced by the electric field is given in terms of the susceptibility tensor $\overleftrightarrow{\chi}$ as

$$\vec{P} = \overleftrightarrow{\chi}\ \vec{E}. \tag{5.59}$$

If the susceptibility of the medium remains unchanged in the presence of the electric field then the radiation produced by the resulting oscillating dipole also has frequency ω_L. This is elastic scattering of light or Raleigh scattering. If however the susceptibility of the medium changes due to a rearrangement of the atoms as the result of a vibration of the medium at frequency ω, then the resulting radiation produced will oscillate at frequencies $\omega_L - \omega$ (Stokes shift) and $\omega_L + \omega$ (anti-Stokes shift). This type of scattering is inelastic light scattering or Raman scattering as the light adds (or subtracts for anti-Stokes) energy to the medium via a phonon. A basic illustration of Raleigh and Raman scattering of light by a medium is shown in Figure 14.

A general Raman experimental setup is shown in Figure 15. The angle shown (Θ) is the polar angle with respect to the $\hat{z}$ axis. Not shown in the figure is the azimuthal angle Φ which is the standard angle in the x-y plane. The light is emitted (assumed unpolarized) with respect to the laboratory frame of reference along the $\hat{z}$ axis. The light then interacts with the sample and is scattered in all directions. The detector located at angles Φ and Θ then receives a portion of the scattered light. A general formula for the relative Raman intensity as a function of detector location (*i.e.* cross section) is sought.

The first step in calculating the relative Raman intensity is to consider the polarization field as a function of time. Using Equation (5.59) and considering an electric field that oscillates with frequency ω_L, one finds that the polarization field is given by

$$\vec{P} = \overleftrightarrow{\chi}\ \vec{E}_0 \cos(\omega_L t). \tag{5.60}$$

If the medium vibrates, then the susceptibility of the medium will oscillate at the natural frequency of the vibration ω, producing an induced polarization field,

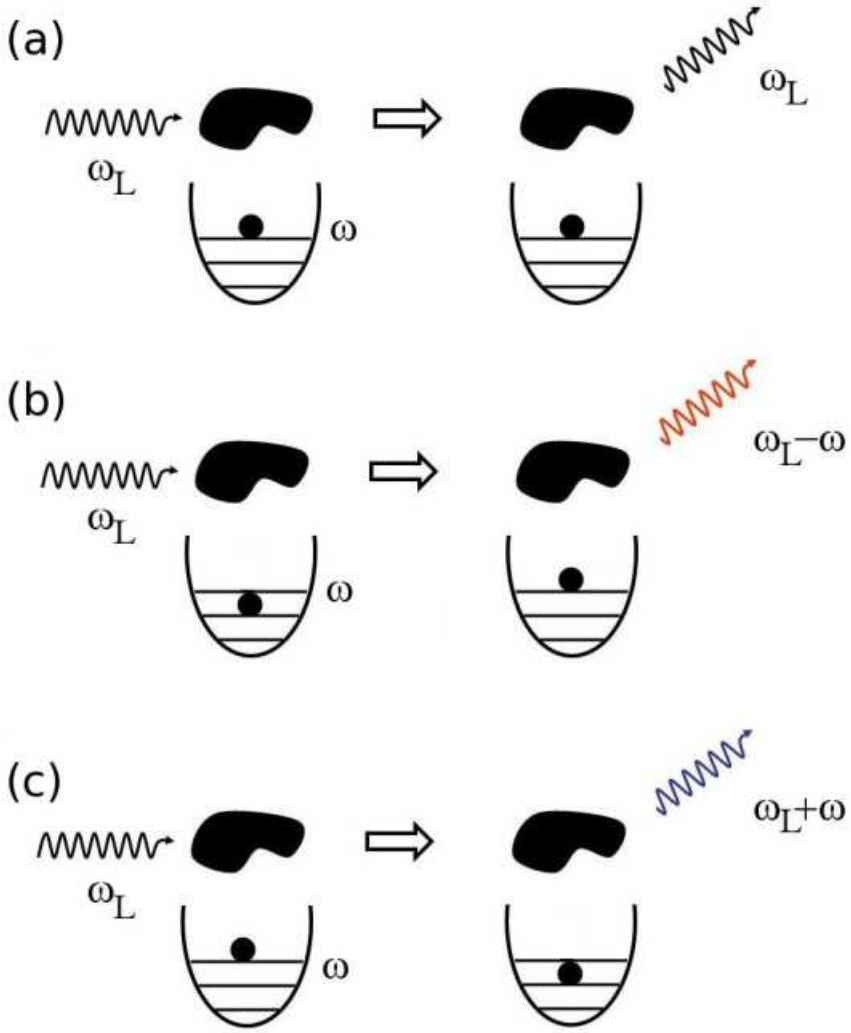

FIG. 14. Diagram illustrating elastic Raleigh scattering and inelastic Raman scattering. (a) Raleigh scattering of a sample. The incident light is elastically scattered by the medium. As a result, the frequency of the incident and scattered light is the same. (b) Raman scattering of a sample that results in the creation of a phonon of frequency ω. The frequency of the scattered light is shifted (Stokes shift) to $\omega_L - \omega$ as a result. (c) Raman scattering of a sample that results in the annihilation of a phonon of frequency ω. The frequency of the scattered light is shifted (anti-Stokes shift) to $\omega_L + \omega$ as a result.

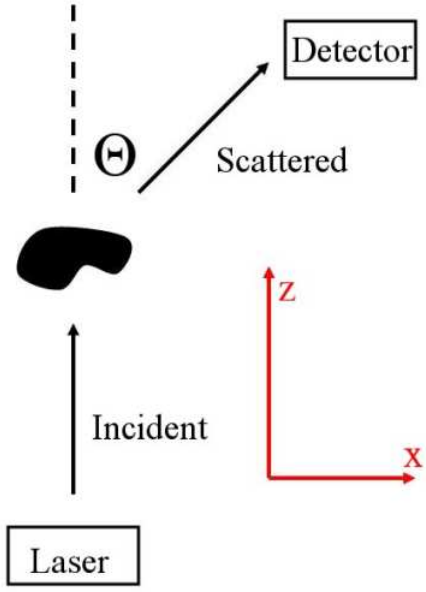

FIG. 15. The setup of a general Raman experiment. The incident light is emitted along the laboratory $\hat{z}$ axis then scattered by the sample. The detector, placed at arbitrary polar angles of Θ and Φ, receives a portion of the scattered light.

$$\begin{aligned} \Delta\vec{P} &= \Delta \overleftrightarrow{\chi}\, \vec{E}_0 \cos(\omega_L t)\cos(\omega t) \\ &= \frac{1}{2}\Delta \overleftrightarrow{\chi}\, \vec{E}_0 \left[\cos((\omega_L+\omega)t) + \cos((\omega_L-\omega)t)\right]. \end{aligned} \tag{5.61}$$

The induced polarization field will radiate electromagnetic radiation with an intensity I. The intensity can be written as [20]

$$I \propto \frac{1}{\omega}\left|\hat{d}_s \cdot \Delta\vec{P}\right|^2, \tag{5.62}$$

where $\hat{d}_s$ is the direction of the electric field for the scattered light. For the Raman intensity being calculated here, the sample consists of many particles in a solution that are randomly orientated with respect to each other. As such, the final Raman intensity formula must be averaged over all possible orientations of the particles in the sample.

Two frames of reference must be considered for the derivation, the laboratory frame of reference (unprimed frame) where light is emitted and received, and the frame of reference

for individual particles in the sample (primed frame). These two frames are connected via a simple rotation matrix ($\hat{x}' = \overleftrightarrow{R}\,\hat{x}$) which can be written as the function of three angles θ, ϕ, and ψ. For simplicity θ, ϕ, and ψ can be chosen to be the Euler angles [46]. This rotation matrix is then capable of describing any orientation of a particle in the sample with respect to the Lab frame.

Substitution of Equation (5.61) into Equation (5.62) and time averaging over one period of ω_L results in

$$I \propto \frac{1}{\omega} \left| \hat{d}'_s \Delta \overleftrightarrow{\chi}\, \hat{d}'_i \right|^2, \tag{5.63}$$

where $\hat{d}'_s$ and $\hat{d}'_i$ are the electric field directions of the scattered and incident light in the particle frame of reference. It is important to note that the directions vectors must be written in terms of the particle's frame of reference since the induced susceptibility $\overleftrightarrow{\chi}$ is calculated with respect to the particle. In addition, there are two possible polarizations for the scattered light corresponding to the two mutually orthogonal directions ($\hat{d}_{s1}$ and $\hat{d}_{s2}$) in the plane perpendicular to the direction of propagation. Taking this into account, the total scattered intensity is

$$I \propto \frac{1}{\omega} \left| \hat{d}'_{s1} \Delta \overleftrightarrow{\chi}\, \hat{d}'_i \right|^2 + \frac{1}{\omega} \left| \hat{d}'_{s2} \Delta \overleftrightarrow{\chi}\, \hat{d}'_i \right|^2. \tag{5.64}$$

The induced susceptibility tensor $\Delta \overleftrightarrow{\chi}$ describes the *maximum* change in the susceptibility of the particle due to a vibrational mode. There are many ways to calculate the tensor. Regardless, the relative Raman intensity can be worked out for general $\Delta \overleftrightarrow{\chi}$.

The electric field direction vector for the incident light is considered to be unpolarized, thus the general direction of the electric field can be written in terms of x and y unit directions in the Laboratory frame as

$$\hat{d}_i = \cos\theta_i \hat{x} + \sin\theta_i \hat{y}. \tag{5.65}$$

The scattered light propagates along a direction in the laboratory frame given by the spherical polar angles Φ and Θ. Two mutually orthogonal directions perpendicular to the propagation direction can be written in the Laboratory frame as

$$\begin{aligned} \hat{d}_{s1} &= \cos\Phi\cos\Theta\hat{x} + \sin\Phi\cos\Theta\hat{y} - \sin\Theta\hat{z}, \\ \hat{d}_{s2} &= -\sin\Phi\hat{x} + \cos\Phi\hat{y}. \end{aligned} \tag{5.66}$$

The coordinate axis of the Laboratory frame ($\hat{x}$, $\hat{y}$, $\hat{z}$) can be written in terms of the Fiber frame axis ($\hat{x}'$, $\hat{y}'$,$\hat{z}'$) by applying the Euler rotation matrix. The result is

$$\begin{aligned} \hat{x} &= (\cos\phi\cos\psi - \cos\theta\sin\phi\sin\psi)\hat{x}' \\ &+ (\sin\phi\cos\psi + \cos\theta\cos\phi\sin\psi)\hat{y}' \\ &+ (\sin\theta\sin\psi)\hat{z}', \end{aligned} \tag{5.67}$$

$$\begin{aligned} \hat{y} &= (-\cos\phi\sin\psi - \cos\theta\sin\phi\cos\psi)\hat{x}' \\ &+ (-\sin\phi\sin\psi + \cos\theta\cos\phi\cos\psi)\hat{y}' \\ &+ (\sin\theta\cos\psi)\hat{z}', \end{aligned} \tag{5.68}$$

$$\hat{z} = \sin\theta\sin\phi\hat{x}' - \sin\theta\cos\phi\hat{y}' + \cos\theta\hat{z}'. \tag{5.69}$$

For simplicity, these will be written in the following short hand notation:

$$\begin{aligned} \hat{x} &= x_1\hat{x}' + x_2\hat{y}' + x_3\hat{z}', \\ \hat{y} &= y_1\hat{x}' + y_2\hat{y}' + y_3\hat{z}', \\ \hat{z} &= z_1\hat{x}' + z_2\hat{y}' + z_3\hat{z}'. \end{aligned} \tag{5.70}$$

All that remains is to calculate the average intensity,

$$I_{avg} = \langle I \rangle = \int P(\phi,\theta,\psi,\theta_i) I d\Omega, \tag{5.71}$$

where ϕ, θ, and ψ are the Euler angles that give the orientation of a particle in the sample with respect to the Laboratory frame and θ_i is the angle that describes the polarization of the incident light [see Eq. (5.65)]. Since all angles are equally likely, the probability must be given by a constant, $P(\phi, \theta, \psi, \theta_i) = 1/16\pi^3$, with the integration angle given by $d\Omega = \sin\theta d\theta d\phi d\psi d\theta_i$.

Combining Equations (5.64) through (5.66) and using the short hand notation for the Euler coefficients [Eq. (5.70)] the average intensity formula yields terms of the following forms

$$\begin{aligned} &\langle \cos^2\theta_i a_i b_m x_j x_n\rangle, \Delta\chi_{ij}\Delta\chi_{mn}, \\ &\langle \cos\theta_i \sin\theta_i a_i b_m x_j y_n\rangle \Delta\chi_{ij}\Delta\chi_{mn}, \\ &\langle \sin^2\theta_i a_i b_m y_j y_n\rangle \Delta\chi_{ij}\Delta\chi_{mn}. \end{aligned} \tag{5.72}$$

The variables a_i and b_i denote any of the Euler coefficients x_i, y_i, or z_i. The second of the three terms vanishes when integrated over θ_i. In addition, one can show that the only surviving averages $\langle a_i b_m x_j x_n\rangle$ are

$$\begin{aligned} \langle a_i a_i a_i a_i\rangle &= \frac{1}{5}, \\ \langle a_i a_i a_j a_j\rangle &= \frac{1}{15}, \\ \langle a_i a_i b_i b_i\rangle &= \frac{1}{15}, \\ \langle a_i a_i b_j b_j\rangle &= \frac{2}{15}, \\ \langle a_i a_j b_i b_j\rangle &= \frac{-1}{30}. \end{aligned} \tag{5.73}$$

After a bit of algebra, one can obtain the average intensity,

$$\begin{aligned}
\omega I_{avg} &\propto \left(\cos^2\Theta\cos^2\Phi+\sin^2\Phi\right)\sum_{ijmn}\Delta\chi_{ij}\Delta\chi_{mn}\left[\langle x_i x_m x_j x_n\rangle+\langle x_i x_m y_j y_n\rangle\right] \\
&+ \left(\cos^2\Theta\sin^2\Phi+\cos^2\Phi\right)\sum_{ijmn}\Delta\chi_{ij}\Delta\chi_{mn}\left[\langle y_i y_m x_j x_n\rangle+\langle y_i y_m y_j y_n\rangle\right] \\
&+ \left(\cos^2\Theta\sin^2\Phi+\sin^2\Phi\right)\sum_{ijmn}\Delta\chi_{ij}\Delta\chi_{mn}\left[\langle z_i z_m x_j x_n\rangle+\langle z_i z_m y_j y_n\rangle\right]. \quad (5.74)
\end{aligned}$$

Utilizing the averages in Equation (5.73) and assuming that the susceptibility tensor is symmetric, Equation (5.74) simplifies to

$$\begin{aligned}
\omega I_{avg} &\propto \left[16-4\sin^2\Theta\right]\left(|\Delta\chi_{xx}|^2+|\Delta\chi_{yy}|^2+|\Delta\chi_{zz}|^2\right) \\
&+ \left[4-6\sin^2\Theta\right]\left(\Delta\chi_{xx}\Delta\chi_{yy}+\Delta\chi_{xx}\Delta\chi_{zz}+\Delta\chi_{yy}\Delta\chi_{zz}\right) \\
&+ \left[14-\sin^2\Theta\right]\left(|\Delta\chi_{xy}|^2+|\Delta\chi_{xz}|^2+|\Delta\chi_{yz}|^2\right). \quad (5.75)
\end{aligned}$$

Finally, this equation can be simplified into a form similar to the elastic free energy of a material with Lamé constants λ_R and μ_R,

$$I_{avg} \propto \frac{1}{2}\frac{\lambda_R}{\omega}\left[Tr(\Delta\overleftrightarrow{\chi})\right]^2+\frac{\mu_R}{\omega}Tr\left(\left[\Delta\overleftrightarrow{\chi}\right]^2\right). \quad (5.76)$$

The Raman Lamé coefficients λ_R and μ_R are dependent only on the azimuthal angle Θ and are given by

$$\begin{aligned}
\lambda_R &\equiv \left[14-\sin^2\Theta\right], \\
\mu_R &\equiv \left[4-6\sin^2\Theta\right]. \quad (5.77)
\end{aligned}$$

VI. IMPULSIVE STIMULATED RAMAN SCATTERING

When *pulsed* laser light is used to excite phonon vibrations in a medium though stimulated scattering, the electric field of the laser applies a force on the medium which drives the vibration. When the duration of the pulse is short, the driving force is impulsive (like the force from a hammer driving a nail into a wall). The use of short pulses from a laser source to excite vibrational modes in a molecule or medium is called impulsive stimulated

Raman scattering (ISRS). Yan, Gamble and Nelson [69] present a theoretical discussion of the ISRS method and the types of spectroscopy that can be performed.

Yan, Gamble, and Nelson's work argues that properly time delayed pulses can be used to amplify certain vibrational modes of a molecule. The ISRS method is then of great interest as a possible method to resonantly pump the low frequency mechanical modes of viruses to produce damage [25]. From a theoretical standpoint, a detailed molecular mechanical simulation of a virus being probed by ISRS can provide key insights into its vulnerabilities. This section develops a model to calculate the coupling of light to a viral particle (or any general molecule) necessary for a theoretical ISRS simulation.

The bond polarizability model [19, 20] can be used to predict the atomistic coupling of light to molecular vibrations, since the model predicts the susceptibility of the molecule from individual atomic positions. This allows individual impulsive forces for each atom and overall amplitudes of vibrational modes to be calculated. Both will be discussed in this section. In addition, an estimate of the total energy delivered to all vibrational modes in a molecule resulting from ISRS is also presented.

In the bond polarizability model (see Section III and Section IV) the susceptibility of the medium is calculated from a sum over the polarizabilities of individual atomic bonds,

$$\overleftrightarrow{\chi} = \sum_{bonds} \overleftrightarrow{\alpha}, \tag{5.78}$$

where the bond polarizability for a single bond $\overleftrightarrow{\alpha}$ is given by Equations (5.41) and (5.42). Treating the molecule as a network of polarizable bonds, the potential energy of the bond network in the presence of an electric field (from the generalization of $-\vec{p}\cdot\vec{E}$ for a non-induced dipole) is given by

$$V(t) = -\frac{1}{2}\sum \vec{E}(t)\cdot \overleftrightarrow{\alpha} \cdot \vec{E}(t). \tag{5.79}$$

In ISRS, the electric field comes from a light source in which its duration is short (*i.e.* short pulse). The electric field from such a light source, propagating along the $\hat{z}$ axis, can be represented in the form of a Gaussian wave packet,

$$\begin{aligned} \vec{E}(t) &= \vec{E}_0 e^{-(t-zn/c)^2/2\tau_L^2} \cos\left[\omega_L(t-zn/c)\right] \\ &\approx \vec{E}_0 e^{-t^2/2\tau_L^2} \cos\left[\omega_L t\right], \end{aligned} \tag{5.80}$$

where the electric field amplitude is given by $\vec{E}_0$ and the dimensions of the molecule have been assumed to be small so that retardation effects can be dropped. Taking the derivative with respect to atomic position of Equation (5.79) gives the force on an individual atom due to the electric field of the light,

$$F_{i\alpha}^L(t) = \frac{1}{2} \sum \vec{E}(t) \cdot \frac{\partial \overleftrightarrow{\alpha}}{\partial r_{i\alpha}} \cdot \vec{E}(t). \tag{5.81}$$

Here, i represents the atom number and α one of the directions x,y, or z.

The derivative of the polarizability tensor for a single bond $\overleftrightarrow{\alpha}$ is non-zero only if the bond contains atom i. If this is the case, the resulting derivative is

$$\frac{\partial \overleftrightarrow{\alpha}}{\partial r_{i\alpha}} = \frac{\partial d}{\partial r_{i\alpha}} \left[\alpha'_{\parallel} \hat{P} + \alpha'_{\perp}(\hat{I} - \hat{P})\right] + (\alpha_{\parallel} + \alpha_{\perp}) \frac{\partial \hat{P}}{\partial r_{i\alpha}}. \tag{5.82}$$

Small bond oscillations have been assumed so that the polarizability constants are evaluated at the equilibrium length of the bond d. The components of the projection operator $\hat{P}$ are $\hat{P}_{\beta\gamma} = \hat{d}_\beta \hat{d}_\gamma$, where $\hat{d}_\beta$ is the β component of the unit direction vector for the bond. Using the relation

$$\frac{\partial \hat{d}_\beta}{\partial r_{i\alpha}} = -\frac{1}{d} \frac{\partial d}{\partial r_{i\alpha}} \hat{d}_\beta + \frac{\delta_{\alpha\beta}}{d}, \tag{5.83}$$

followed by some algebra, one obtains (using Einstein summation)

$$\frac{\partial \overleftrightarrow{\alpha}}{\partial r_{i\alpha}} = \left[\alpha'_{\parallel} \hat{P} + \alpha'_{\perp}(\hat{I} - \hat{P}) - \frac{2}{d}(\alpha_{\parallel} - \alpha_{\perp})\hat{P}\right] \hat{d}_\alpha + (\alpha_{\parallel} - \alpha_{\perp}) \left[\frac{\delta_{\alpha\gamma}}{d} \hat{d}_\beta + \frac{\delta_{\alpha\beta}}{d} \hat{d}_\gamma\right]. \tag{5.84}$$

Taking the dot product with the electric field, the final result for the force of the light on atom i resulting from a single bond is

$$F^L_{i\alpha}(t) = \left[f_d \hat{d}_\alpha + f_E \hat{E}_\alpha\right] |E_0|^2 e^{-t^2/\tau_L^2} \cos^2(\omega_L t), \tag{5.85}$$

where the variables f_d and f_E are defined as

$$\begin{aligned} f_d &= \frac{(\hat{E}_0 \cdot \hat{d})^2}{2}\left[\alpha'_\parallel - \alpha'_\perp - \frac{2(\alpha_\parallel - \alpha_\perp)}{d}\right] + \frac{\alpha'_\perp}{2}, \\ f_E &= (\alpha_\parallel - \alpha_\perp)\frac{(\hat{E}_0 \cdot \hat{d})}{d}. \end{aligned} \tag{5.86}$$

Using Equation (5.85), the force on each atom can be calculated for a given electric field strength and direction. The resulting force can be used in an atomistic molecular dynamics simulation (along with the the standard molecular forces) to provide a real time simulation of the interaction of the molecule with light.

The pulse width of the light τ_L will determine the frequency of the vibrational modes that are stimulated by the impulsive force. Short pulse widths will deliver the most energy to high frequency phonons while longer pulses will give more energy to the low frequency phonons. To understand why this is, consider the driven harmonic oscillator with normal coordinate Q,

$$\ddot{Q}_i + \omega^2 Q_i = F_{Q_i}(t). \tag{5.87}$$

The force $F_{Q_i}(t)$ describes the force on vibrational mode i due to the light source and is the component of the total force due to the light along the vibrational displacement. Using the notation $I_0 = |E_0|^2$ where I_0 is proportional to the peak laser intensity I (Watts/cm^2), the force on mode i becomes

$$F_{Q_i}(t) = \langle \eta_i | F_L \rangle I_0 e^{-t^2/\tau_L^2} \cos^2(\omega_L t), \tag{5.88}$$

where $|\eta_i\rangle = \overleftrightarrow{M}^{-\frac{1}{2}} |e_i\rangle$ and $|F_L\rangle$ is a column vector with components for each atom determined by the terms in the square bracket in Equation (5.85). Thus the force on mode i depends on the displacement pattern of the mode determined from the dynamical matrix.

The solution to Equation (5.87) can be found by using the Greens' function method,

$$Q_i(t) = \int_{-\infty}^{t} G_i(t,t') F_{Q_i}(t) dt', \tag{5.89}$$

where the Greens' function for the harmonic oscillator is

$$G_i(t,t') = \begin{cases} 0 & t < t' \\ \frac{1}{\omega}\sin(\omega\,[t-t']) & t > t'. \end{cases} \tag{5.90}$$

Looking at long times after the initial pulse has passed (*i.e.* $t \to \infty$) and assuming that $\omega << \omega_L$, the normal coordinate of mode i is given by

$$Q_i(t) = \langle \eta_i | F_L \rangle I_0 \frac{\sqrt{\pi}\tau_L}{2\omega} e^{-\omega^2 \tau_L^2/4} \sin(\omega t). \tag{5.91}$$

The resulting amplitude of vibration for mode i is given by

$$A_i = \langle \eta_i | F_L \rangle I_0 \frac{\sqrt{\pi}\tau_L}{2\omega} e^{-\omega^2 \tau_L^2/4}. \tag{5.92}$$

The pulse width dependence on the vibrational amplitudes can now be seen. If $\langle \eta_i | F_L \rangle$ is assumed roughly constant for all modes (at least over some frequency range), then the maximum amplitude occurs when $\tau_L = \sqrt{2}T/2\pi \approx T/4$, where T is the period of the molecular vibration.

The energy delivered to the molecule can be estimated using the above driven harmonic oscillator approach. Again $\langle \eta_i | F_L \rangle$ will be assumed roughly constant over all modes. When the molecule is stimulated with a short laser pulse, the electric field will excite many vibrational modes of the molecule, each with an amplitude determined from Equation (5.92).

The energy of mode i is then

$$\begin{aligned} E_i &= \frac{\omega^2}{2} A_i^2 \\ &= (\langle \eta_i | F_L \rangle)^2 I_0^2 \frac{\pi \tau_L^2}{4} e^{-\omega^2 \tau_L^2/2}. \end{aligned} \tag{5.93}$$

Approximating the density of states for the molecule as $D(\omega) \propto \omega^2$, the total energy delivered to the molecule (TED) can be estimated as

$$\begin{aligned} TED &\propto \int \omega^2 E(\omega) d\omega \\ &\propto (\langle \eta_i | F_L \rangle)^2 \frac{I_0^2}{\tau_L}. \end{aligned} \tag{5.94}$$

Equation (5.94) gives a qualitative understanding of how the TED scales with the intensity and pulse width of the laser light. A simple interpretation shows that the delivered energy increases approximately as the intensity of light squared and decreases as the pulse width increases. The term $\langle \eta_i | F_L \rangle$ contains information of the polarizability of the system [see Eq. (5.85)] and its coupling to individual modes. This term will effect the TED to some unknown extent. In Chapter 8 Section II, the effects of the $\langle \eta_i | F_L \rangle$ term on the TED will be examined in more detail by examining data from a molecular dynamics simulation of impulsive stimulated Raman scattering on an M13 bacteriophage capsid.

A plot of $\omega^2 E(\omega)$ for various pulse widths is shown in Figure 16. Though the density of states for a molecule is not exactly proportional to ω^2 and there will be some dependence on the term $\langle \eta_i | F_L \rangle$, the TED calculation provides a basic interpretation of the energy delivered to a molecule by excitation of its vibrational modes using the ISRS scheme.

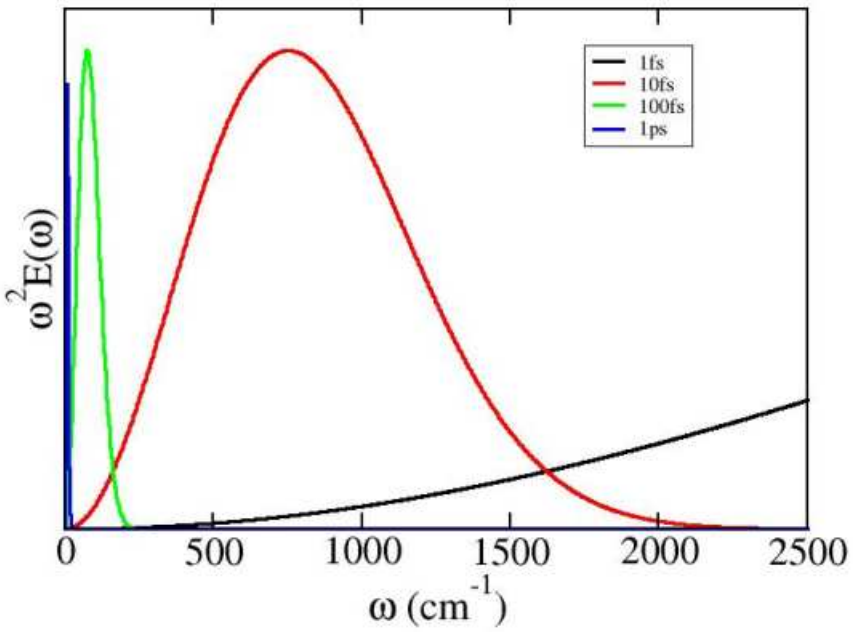

FIG. 16. Energy density $\omega^2 E(\omega)$ for vibrational modes probed with light of various pulse widths τ_L. The energy density for four different pulse widths of $\tau_L = 1, 10, 100$, and $1000 fs$ are shown.

CHAPTER 6

MECHANICAL MODES OF VIRAL CAPSIDS

I. INTRODUCTION

Viruses, having dimensions on the order of a few tens or hundreds of nanometers, are one of the smallest living creatures. They are incredibly simple, consisting of a protein coat (capsid) which takes a specific structure and genetic material. They infect bacteria, animal, and plant cells, commandeering the host cells metabolism in order to replicate. Although the structure of viral capsids is diverse, a majority can be categorized into four main types. In each of the four structural types, a set of one or more protein building blocks are assembled into the viral capsid. The purpose of the capsid is to encapsulate and protect the genetic material which can be either single or double stranded DNA or RNA.

The first structural type is constructed from one or more protein building blocks which assemble into a long hollow cylindrical tube. The inside of the tube houses the viruses genome and protects it. A well known example of a tubular virus is the tobacco mosaic virus which infects tobacco plants causing a yellow mosaic on the leaves of the plant. Another type of tubular virus, which will be studied in Section IV, is the M13 bacteriophage which infects the *E. coli* bacterium. Figure 17 (a) shows a general diagram of a tubular virus capsid.

The second type of a viral capsid structure is the spherical icosahedral capsid. This type of virus capsid is assembled from 60 copies of one or more protein building blocks. The structure of the icosahedral virus capsid is analogous to the C_{60} molecule. The set of proteins building blocks form a basis of atoms that, when placed on the icosahedral surface, form the full icosahedral capsid. The number of protein building blocks that are used to construct the basis of atoms is called the T number. The T number varies widely from 1,3,4,7$\cdots$13 or even hundreds. Examples of icosahedral viruses include the satellite tobacco

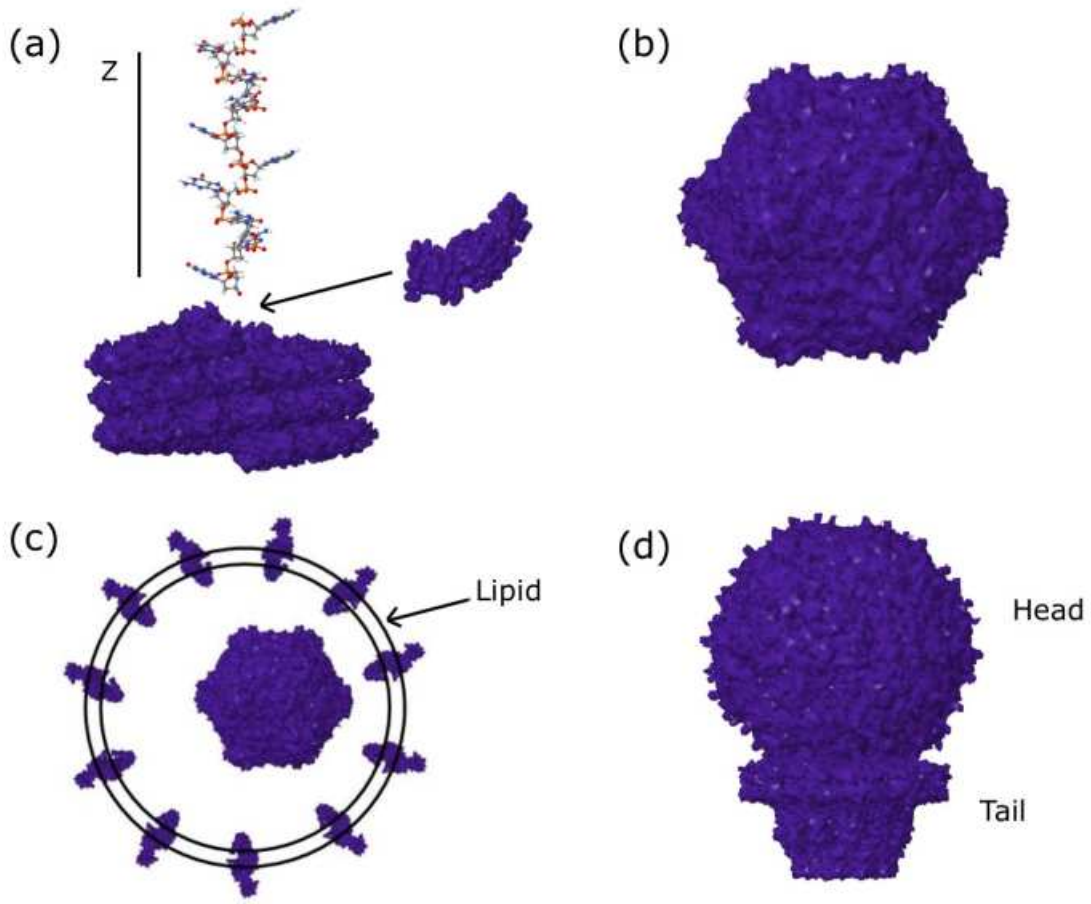

FIG. 17. Diagram of four types of viral structures and their capsids. (a) The structure of a tubular virus. Protein building blocks assemble in a helical fashion around the viruses genome. (b) The structure of an icosahedral virus. A T=1 capsid constructed from 60 copies of one protein building block is shown. (c) The structure of an enveloped virus with icosahedral capsid. Both icosahedral and tubular capsids can be enveloped. (d) Schematic of the tailed phage ϕ 29 consisting of an icosahedral head bound to a tail.

necrosis virus, hepatitis B, polio, and the cowpea chlorotic mottle virus. An illustration of the naked capsid icosahedral virus is shown in Figure 17 (b). Two icosahedral viruses, the satellite tobacco necrosis virus and cowpea chlorotic mottle virus, are studied in detail in Sections II and III.

The last two types of viral capsids, which will not be studied here, are enveloped and complex viruses (tailed phages). The enveloped virus is usually formed from either an icosahedral or tubular capsid, which surrounds the genetic material, and an additional lipid bilayer which surrounds the capsid itself. The lipid bilayer serves as additional protection for the genetic material and is acquired as the virus exits the host cell. Examples of enveloped viruses include influenza and HIV (icosahedral capsids), and the deadly Ebola virus (tubular capsid). A diagram of an enveloped virus can be seen in Figure 17 (c).

The structure of a tailed phage on the other hand consists of an icosahedral protein capsid (head) which is connected to a filamentous tube. In some instances, such as the T4 phage, the end of the tube has fibrous like legs attached to it. Tailed phages typically infect bacteria and their diversity has led to ingenious ways in which they infect their hosts. The most well known tailed phages are the T4, λ, and $\phi 29$ phages. A diagram of one type of tailed phage (the $\phi 29$ phage) is shown in Figure 17 (d).

A normal mode analysis (NMA) of viral capsids can offer important insights into the types of conformational changes that the protein coat is capable of, thus providing a possible description of how viruses infect the host cell. For example, it has been suggested [70] that the Rhino virus infects a host cell by injecting its genetic material with a "puckering" of its icosahedral capsid. It has also been suggested that the polio virus uses a similar method to enter the host cell [71]. In Section III, an analysis of the normal modes of the cowpea chlorotic mottle virus will reveal possible motions that lead to a reversible swelling of the

capsid that is induced by a either a loss of calcium ions or an increase in pH. It has been hypothesized that the virus uses the swelling processes to remove its genome from the capsid during infection [60].

The mechanical modes of viral capsids are of particular interest here since it may be possible to excite them using a laser or other type of probe. Theoretically this would result in mechanical resonances that may damage the capsid shell rendering it inactive or even destroyed. This is an interesting idea since each viral capsid will have a set of unique frequencies and mode patterns due to the shape and composition of its capsid. The hypothesis is that this can allow viruses to be selectively destroyed while leaving the host cell (with different resonant frequencies) undamaged. Such an idea has been explored recently in the ASU laboratory of Prof. K.-T. Tsen [25, 26, 27] using impulsive stimulated Raman scattering (ISRS) [69] on M13 bacteriophages and other pathogens. In one experiment, M13 phages were subjected to *short* pulses of visible (or infrared) light which resulted in there inactivation. So far the experimental evidence suggests that the M13 phages were inactivated through resonant excitation of their capsids mechanical modes. In order to fully explore this idea, a theoretical understanding of the mechanical modes and their coupling to light at the atomic level is necessary.

In the past, mechanical modes of viral capsids have been studied using coarse graining procedures since the full dynamical matrix (of size $3N \times 3N$ where N is the number of atoms) is too large to be directly diagonalized. Each of the various coarse graining procedures varies in the level of atomic description ranging from none at all (continuum elastic theory [66, 72]) to a reduced description (elastic network model [4] and rotation translation block method [6]). For example, the rotation translation block procedure (RTB) usually treats an entire protein building block (1 of 60 for a $T = 1$ icosahedral virus) as a rigid block

that is capable of only rotational and translational motions [6, 7]. This reduces the number of degrees of freedom from 10^5 or more to a mere 360 for a $T = 1$ virus (3 translations plus 3 rotations, times 60). Another coarse graining procedure reduces the number of degrees of freedom by considering only dihedral motions [54] (for a diagram of a dihedral motion see Figure 1 c). This will reduce the number of degrees of freedom by a factor of roughly 30. For any of the coarse graining procedures, the reduction in the number of degrees of freedom may cause some of the low frequency modes to be missed resulting in an incomplete picture of the mode patterns and frequencies.

In this chapter, a detailed analysis of the mechanical modes of three viral capsids, the satellite tobacco necrosis virus, cowpea chlorotic mottle virus, and M13 bacteriophage, are examined using the fully atomistic phonon functional method (see Chapter 4 Section IV for a detailed description of the method) with an empirical energy model. Since the phonon functional method takes into account all $3N$ degrees of freedom, a complete picture the low frequency normal modes of the viral capsid will emerge. In addition, the Raman spectra of all three viruses (in solution) are predicted using an empirical bond polarizability model [19, 20, 21] (see Chapter 5 Section III for details of the model). The Raman spectra predictions can be used to estimate which modes will couple the strongest to light.

II. SATELLITE TOBACCO NECROSIS VIRUS

In this section, the mechanical modes and frequencies of the icosahedral $T = 1$ satellite tobacco necrosis virus are examined with atomistic detail using the phonon functional method. With a detailed atomistic description of the displacement patterns of the viral capsid, an estimate of the low frequency Raman spectra of virus particle in solution is made using the bond polarizability model and Raman intensity formula derived in Chapter 5.

The satellite tobacco necrosis virus (STNV) is a particularly small virus having a diameter of roughly 16 nm. It is called a "satellite" virus because it requires another virus (a helper virus) to initiate the entrance into the host cell and replicate its genome. Satellite viruses tend to exacerbate the symptoms exhibited by the host that result from infection with the helper virus. The STNV is a satellite of the tobacco necrosis virus (TNV) which infects the tobacco plant. The STNV genome consists of single stranded RNA with a length of 1239 base pairs [73]. The ss-RNA has an encoding region of roughly 600 base pairs that codes for a single protein, the capsid coat. The STNV genome is particularly simple since all of the enzymes needed for replication are contained in the genome of the TNV which STNV uses.

Since STNV is a $T = 1$ icosahedral virus, the capsid is constructed from a single protein building block copied 60 times to form a spherical shell. Inside the capsid shell lies the ss-RNA genome of the virus. The structure of the STNV capsid was determined by X-ray crystallography [74]. In addition to the 60 proteins, the X-ray experiment also found calcium ions and water molecules present in the crystallized capsid. The full capsid structure contains a total of 198824 atoms (including hydrogen). Out of the 198824 atoms, a total of 170820 atoms are from the 60 proteins, 27912 atoms are from water molecules, and 92 atoms are from calcium ions. Out of the 92 calcium ions, 12 were located directly on the C5 symmetry axes, 20 directly on the C3 symmetry axes, and 60 slightly away from the C3 axis. Some of the water molecules were found to accompany each calcium ion to form an octahedral like structure on the C3 axis with each positively charged calcium ion surrounded by water oxygens which have a slight negative charge. The C5 axis on the other hand has a single calcium ion surrounded by two water oxygens. Due to the placement of calcium ions with water directly on the C3 and C5 symmetry axises, the virus capsid will

not have icosahedral symmetry. This is because of the water molecule which lacks both five-fold and three-fold symmetry.

An illustration of the calcium ion and two water molecules on the C5 axis is shown in Figure 18 (a) from two viewpoints. It is quite clear that this arrangement will lack icosahedral symmetry. For the NMA, a capsid with icosahedral symmetry is desirable as this greatly reduces the size of the problem. One way to force the capsid into icosahedral symmetry is to create extra calcium ions and water molecules at the C3 and C5 axes and energy minimize the structure; taking into account interactions from neighboring icosahedral sites using the group rotation operators. The final minimized capsid structure will then have the appropriate symmetry. It is expected that this procedure will effect the frequencies only slightly. An alternative is to simply remove the water molecules since the generalized Born method will be used to model solvent interactions with the virus. However, this procedure results in a capsid structure that cannot be described as N_b basis atoms copied $N_s = 60$ times. This is due to the calcium ions on the C5 axis which only generate 12 atoms with the group rotation operators instead of 60. In order to handle such situations, substantial changes to the group theory dynamical matrix operator algorithm would be necessary. Thus, removal of the water was avoided. In the future, a more robust group dynamical matrix operator algorithm will be developed that can handle such situations. A diagram of the C5 symmetry axis after the energy minimization is shown in Figure 18 (b) from the same two viewpoints as in (a). A similar situation exists for the C3 symmetry axes and is fixed in the same manner as the C5 axes.

A single protein building block of STNV is shown in Figure 19 (a). The locations of the three calcium ions are indicated by green dots. The locations of water molecules are not shown in the figure although they are apart of the building block. The lines with

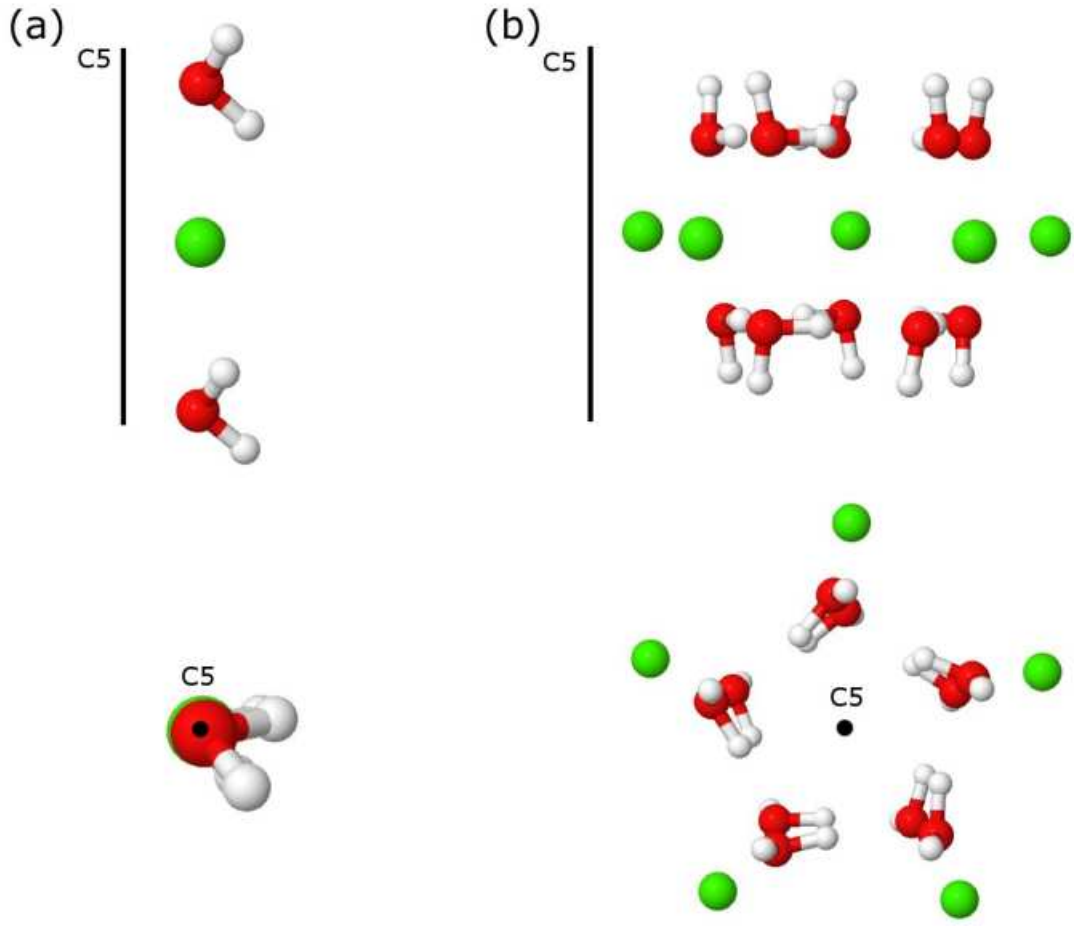

FIG. 18. Illustration showing the structure of calcium ions located at the C5 symmetry axes before and after energetic minimization. (a) The structure before minimization. The water molecules above and below the calcium ions breaks the icosahedral symmetry of the virus. (b) The structure after minimization. Additional calcium ions and water molecules are placed on the C5 symmetry axes to force the virus capsid into icosahedral symmetry. Energetic minimization of the structure adjusts the relative positions to a favorable conformation.

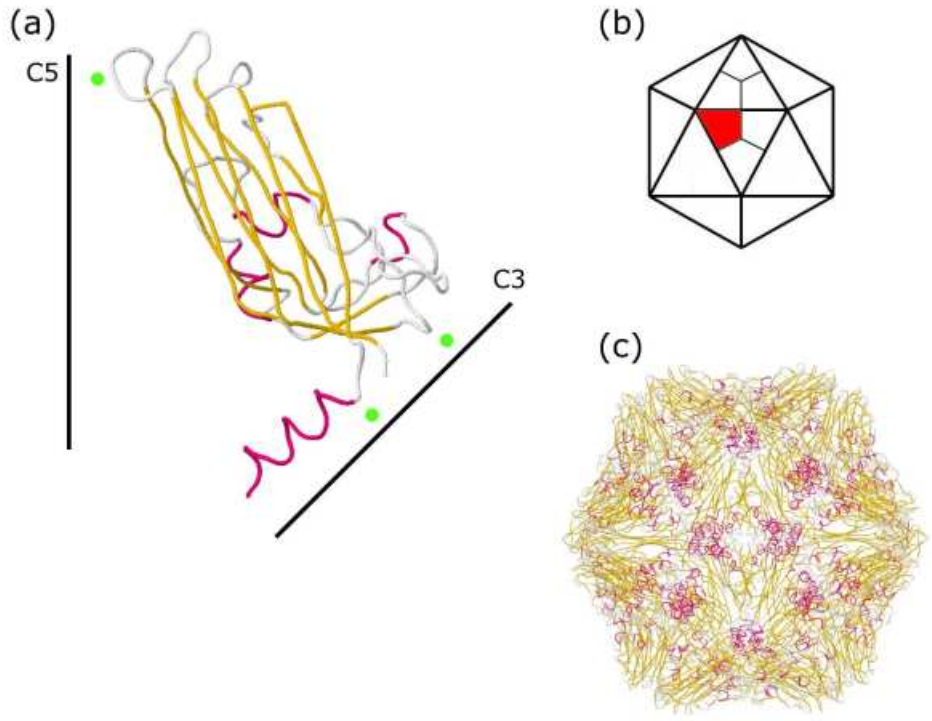

FIG. 19. The structure of the satellite tobacco necrosis virus. (a) The structure of a single icosahedral site of the virus (1 of 60). The protein is drawn as a backbone trace. The green dots indicate the positions of Ca^{2+} ions. The lines show the approximate directions of the C3 and C5 symmetry axes with respect to the protein. Water molecules that are present in the structure are not shown. (b) The icosahedral surface for a $T = 1$ virus. The protein building block in (a) consisting of protein, calcium ions, and water are copied to each cell (in red) for a total of 60 copies. (c) The full virus structure.

labels C3 and C5 indicate the approximate direction of the symmetry axes with respect to the protein. Coordinates for STNV atoms were obtained from the protein data bank (PDB code 2BUK). The coordinate file 2BUK contained 3324 atoms (including hydrogen). The full virus structure is obtained by copying all 3324 atoms in the PDB file 2BUK 60 times using the rotation operators of the regular icosahedral group (group I). A diagram showing the icosahedral surface for a $T = 1$ virus which illustrates the placement of individual protein units is shown in Figure 19 (b). The full virus structure is shown in Figure 19 (c).

In Chapter 3, a symmetric molecule was described as a set of N_b basis atoms copied N_s times. The satellite tobacco necrosis virus can be described in the same manner *i.e.* as $N_b = 3324$ basis atoms copied $N_s = 60$ times. The coordinates for the 3324 basis atoms at a single icosahedral site were energetically minimized by allowing atoms to move energetically downhill due to forces (power quench method). The forces were calculated using the AMBER 94 force field [9] taking into account interactions from neighboring icosahedral sites using the group rotation operators. The interactions of the viral capsid with water were modeled using the Generalized Born [13, 14, 37] implicit solvent model. Generalized Born and van der Waals parameters for the calcium ions were obtained from Babu *et al.* [75]. A cutoff of 10 Å was used for the Coulomb and van der Waals interactions. The minimization was performed until a root mean square (RMS) force of 0.001 eV/Å was achieved. This minimization procedure is consistent with other work [76] where the goal is to keep RMS deviations of the final optimized structure within 1 Å of the X-ray structure. The resulting RMS deviation from the original X-ray structure was 0.7 Å. Since the RMS force was not exactly zero to machine precision, negative eigenvalues ($\omega^2 < 0$) of the dynamical matrix can occur. However, analysis of any resulting negative eigenvalues showed that they were small in magnitude and the corresponding displacement pattern was highly localized on a few atoms, usually a single water molecule or the atoms of a single amino acid side chain. As such, they were physically irrelevant to the *low* frequency modes and can be ignored.

Once a single icosahedral site of STNV was energetically minimized, the optimized structure was used to predict the lowest 100 frequency modes of each irreducible representation of the regular icosahedral group using the phonon functional method (see Chapter 4 Sections IV-VII for details on the procedure). Including all representaions, this resulted in a total of 1600 low frequency modes of STNV being found. Table IV lists the irre-

TABLE IV. Character table for the group I. The five irreducible representations are labeled A, T1, T2, G, and H. The numbers next to each of the five classes (E, C_5 *etc.*) correspond to the number of group elements that belong to the class. The number τ is the golden mean defined as $\tau = (1 + \sqrt{5})/2$.

	E	$12C_5$	$12C_5^2$	$20C_3$	$15C_2$
A	1	1	1	1	1
T1	3	τ	$1-\tau$	0	-1
T2	3	$1-\tau$	τ	0	-1
G	4	-1	-1	1	0
H	5	0	0	-1	1

ducible representations of the regular icosahedral group along with the group characters. For STNV, the sizes of the reduced dynamical matrices (group dynamical matrices) for the irreducible representations A, T1, T2, G, and H were 9972, 29916, 29916, 39888, and 49860 respectively. For each irreducible representation, approximately 3000 conjugate gradient steps were performed on the phonon energy functional [Eq. (4.21)].

After minimization of the phonon energy functional, Equation (4.25) was used to construct the final eigenvectors of the group dynamical matrices. The eigenvectors of the full dynamical matrix can then be found by taking a linear combination of group theory basis vectors using Equation (3.16). Since minimization on a computer is never exact, the eigenvectors and eigenvalues calculated with the phonon energy functional are approximate. One way that the quality of the eigenvectors and eigenvalues can be assessed is by calculating the magnitude of the residual vector, $|r^p\rangle = \hat{D}^p|\bar{e}^p\rangle - \bar{\omega}^2|\bar{e}^p\rangle$ where $\bar{\omega}^2$ and $|\bar{e}^p\rangle$ are the approximate eigenvalues and eigenvectors found with Equation (4.25). The index p is the usual notation that denotes one of the irreducible representations. The magnitude of the residual vectors where found to be approximately 10^{-4}. In the test case of ubiquitin (Chapter 4 Section VIII), it was found that the errors in the eigenvalues were around 0.01

cm^{-1} for residual magnitudes on the order of 5×10^{-4}. Thus it is expected that the error in the eigenvalues should be similar here as well.

The lowest five frequency modes corresponding to each of the irreducible representations A, T1, T2, G, and H are listed in Table V. The value W_λ for each mode λ corresponds to the participation number for the mode. A small value for W_λ indicates that very few atoms participate in the displacement and that the mode is localized. A large value on the other hand indicates that the mode involves the displacement of many atoms and is a global mode. The formula for W_λ is given by

$$\begin{aligned} W_\lambda &= e^{S_\lambda} \\ S_\lambda &= -\sum_i P_i(\lambda) \ln [P_i(\lambda)], \end{aligned} \tag{6.1}$$

where S_λ is the informational entropy of the mode and $P_i(\lambda)$ is the probability for atom i in mode λ defined by

$$P_i(\lambda) = \vec{\eta}_i(\lambda) \cdot \vec{\eta}_i(\lambda). \tag{6.2}$$

The displacement pattern $\vec{\eta}_i$ for atom i is calculated from the eigenvector of the dynamical matrix via $|\eta(\lambda)\rangle = \overleftrightarrow{M}^{\frac{1}{2}} |e(\lambda)\rangle$. Here the displacement vector $|\eta(\lambda)\rangle$ is normalized instead of the eigenvector $|e(\lambda)\rangle$ in order to have a properly normalized probability. If the displacement is uniformly distributed over each atom, as in a translation, then the participation is equal to the number of atoms. For STNV, W_λ computed in Equation (6.1) is divided by 60 so that the participation number is per site. Full participation for STNV in this case is 3324.

Examination of Table V shows that some of the low frequency modes are localized on a few atoms. For instance, the second lowest frequency mode of the irreducible representation A located at 4.73 cm^{-1} has only 142 atoms participating. The mode is located on the floppy alpha helix "tail" of the protein that points inward along the C3 axis (see

TABLE V. The five lowest frequency modes and their corresponding participation number W per site of the satellite tobacco necrosis virus by irreducible representation. The frequencies are given in cm^{-1}.

	ω_1 (W_1)	ω_2 (W_2)	ω_3 (W_3)	ω_4 (W_4)	ω_5 (W_5)
A	2.41	4.73	5.29	6.08	7.10
	(2610)	(142)	(1607)	(1752)	(104)
T1	2.89	3.57	3.60	4.70	4.89
	(2689)	(457)	(603)	(834)	(562)
T2	2.02	3.42	3.43	3.84	4.30
	(2741)	(1714)	(2460)	(497)	(616)
G	2.38	2.60	3.55	3.95	4.14
	(2605)	(2523)	(2802)	(848)	(412)
H	1.95	2.39	2.86	3.57	3.82
	(2857)	(2951)	(2065)	(1210)	(543)

Figure 19 a). Since the phonon energy functional uses the full Cartesian basis to construct the normal modes, low frequency localized states can be found. Such modes are difficult to predict with coarse graining procedures such as the rotation translation block method [6] since the modes are constructed from small basis sets such as the set of uniform rotations and translations of the protein building blocks.

The first of the low frequency A modes at 2.41 cm^{-1} corresponds to the breathing mode of the virus. This mode can be described as an expansion/contraction of the viral capsid along the radial direction. Unlike the RTB method which treats the entire protein as rigid, the fully atomistic phonon functional method predicts rigid and floppy sections of the protein. This results in sections of the protein that have very small displacements and other regions that exhibit most of the motion that results in the breathing of the capsid. Figure 20 (a) shows the individual displacements of each backbone atom (N, C_α, C) of a single protein for the breathing mode. A short arrow indicates a small relative displacement of the atom about its equilibrium site whereas a long arrow indicates a large displacement.

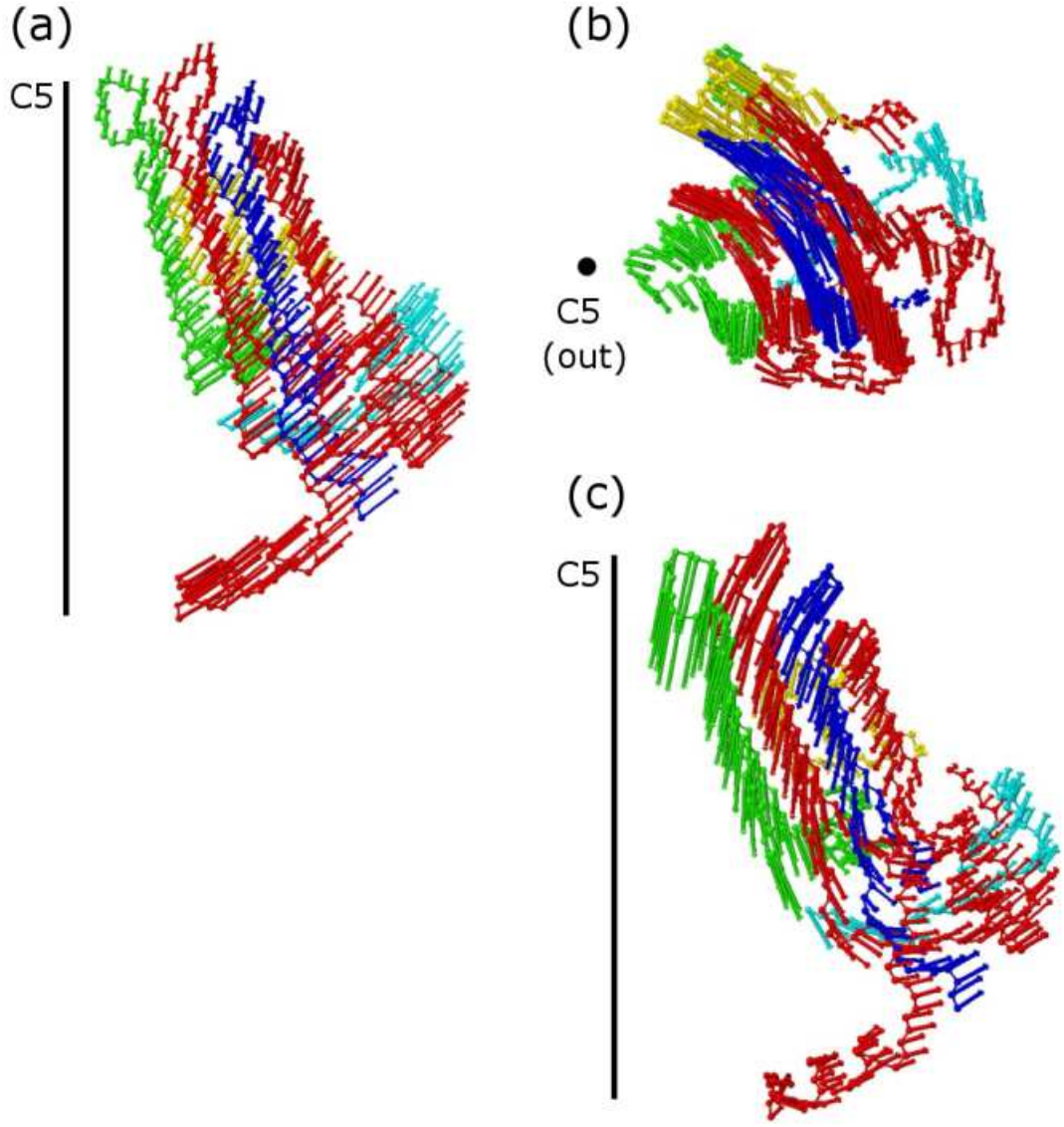

FIG. 20. Three low frequency modes of the satellite tobacco necrosis virus that have symmetry of the A irreducible representation. Displacements of the backbone atoms (N, C_α, C) of one protein of the capsid are shown. Each of the four β sheets in the protein are colored differently (green-red-blue-red) for clarity. The yellow and teal areas correspond to alpha helical regions of the protein. Short (long) arrows indicate a small (large) relative displacement of the atom from its equilibrium position. (a) The breathing mode at 2.41 cm^{-1}. (b) The rotational mode at 5.29 cm^{-1}. (c) The puckering mode at 6.08 cm^{-1}.

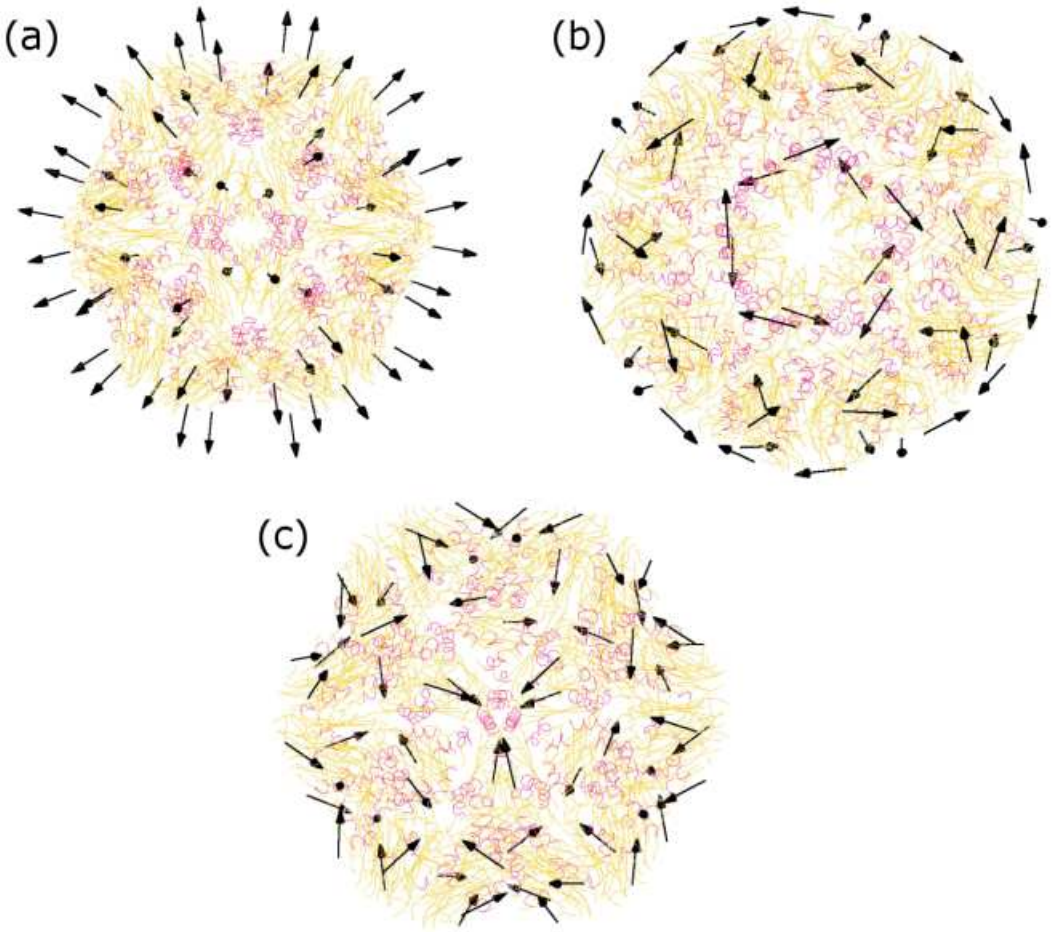

FIG. 21. Three low frequency modes of the satellite tobacco necrosis virus that have symmetry of the A irreducible representation. The full virus capsid composed of all 60 protein building blocks is shown. The arrows represent the direction of the center of mass motion for each protein building block and are not relative. (a) The breathing mode at 2.41 cm^{-1}. (b) The rotational mode at 5.29 cm^{-1}. (c) The puckering mode at 6.08 cm^{-1}.

The figure shows that atoms near the C5 axis have very small displacements and form a rigid region. Figure 21 (a) illustrates the breathing mode for the entire capsid with each protein building block drawn as a trace of the backbone. The arrows indicate the center of mass motion of each protein building block.

Two more important A modes are shown in Figures 20 (b) and (c) and 21 (b) and (c). The low frequency mode at 5.29 cm^{-1} corresponds to a rotation of the protein building blocks about each of the C5 symmetry axes. The motion can be described as the "gliding" of the four beta sheet structures past each other. This is illustrated in Figure 20 (b). The displacements of all 60 protein building blocks for the rotational mode are shown in Figure 21 (b). Finally the low frequency mode at 6.08 cm^{-1} corresponds to a "puckering" of the proteins around the C5 symmetry axes. Figure 20 (c) shows the displacements for the individual backbone atoms of a single protein while Figure 21 (c) gives the displacements for all proteins.

The lowest modes from the remaining irreducible representations T1, T2, G, and H are depicted in Figures 22 and 23. Figure 22 shows the lowest modes of the T1, T2, and G representations while Figure 23 depicts the three lowest H modes. All of the modes are represented by a full virus capsid and the direction of the center of mass motion for each protein of the capsid is shown using arrows. The individual backbone displacements are not illustrated since they are different for each protein as a result of the symmetry of the irreducible representation. However, an examination of any one of the protein building blocks for the T1, T2, G, and H low frequency modes reveals similar floppy and rigid sections of the protein similar to the A modes.

Finally, the relative Raman spectra for satellite tobacco necrosis virus capsids in solution is calculated using the bond polarizability model [19, 20, 21] to predict the total

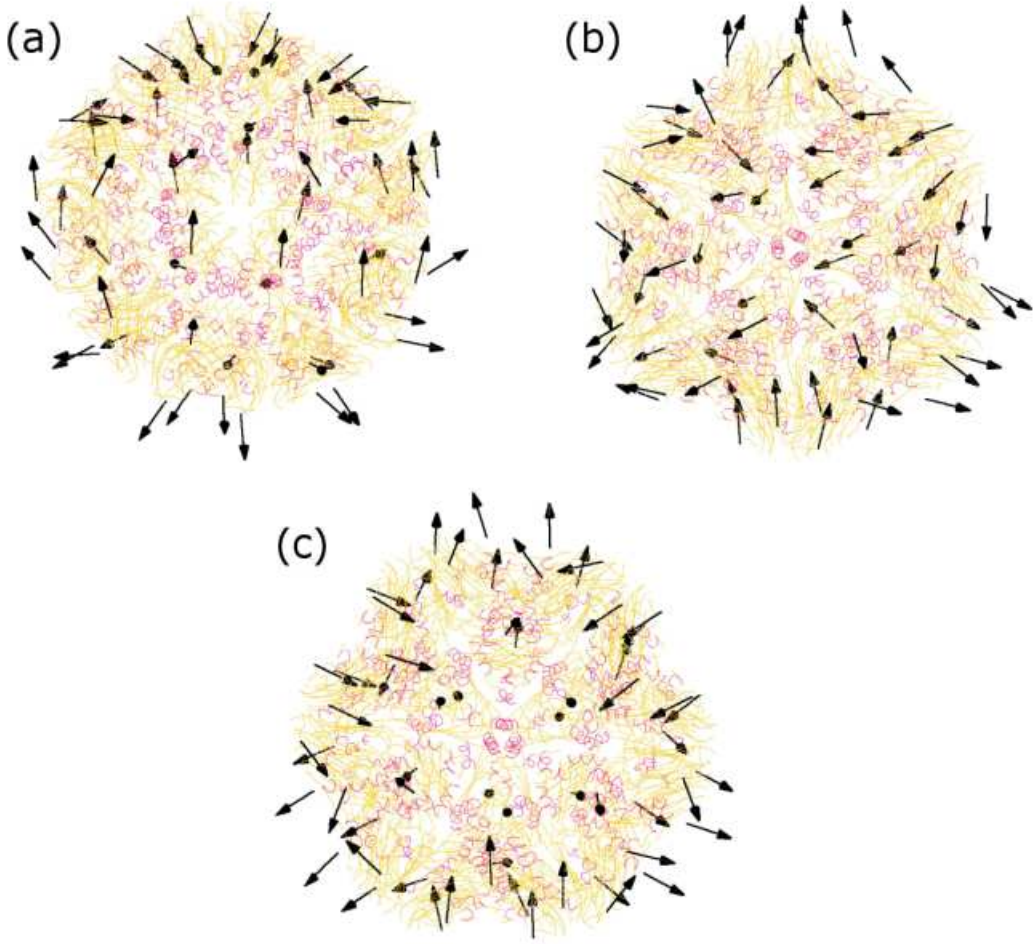

FIG. 22. The lowest frequency modes of the satellite tobacco necrosis virus that have symmetry of the irreducible representations T1, T2, and G. The full virus capsid composed of all 60 protein building blocks is shown. The arrows represent the direction of the center of mass motion for each protein building block and are not relative. (a) The lowest T1 mode at 2.89 cm^{-1}. (b) The lowest T2 mode at 2.02 cm^{-1}. (c) The lowest G mode at 2.38 cm^{-1}.

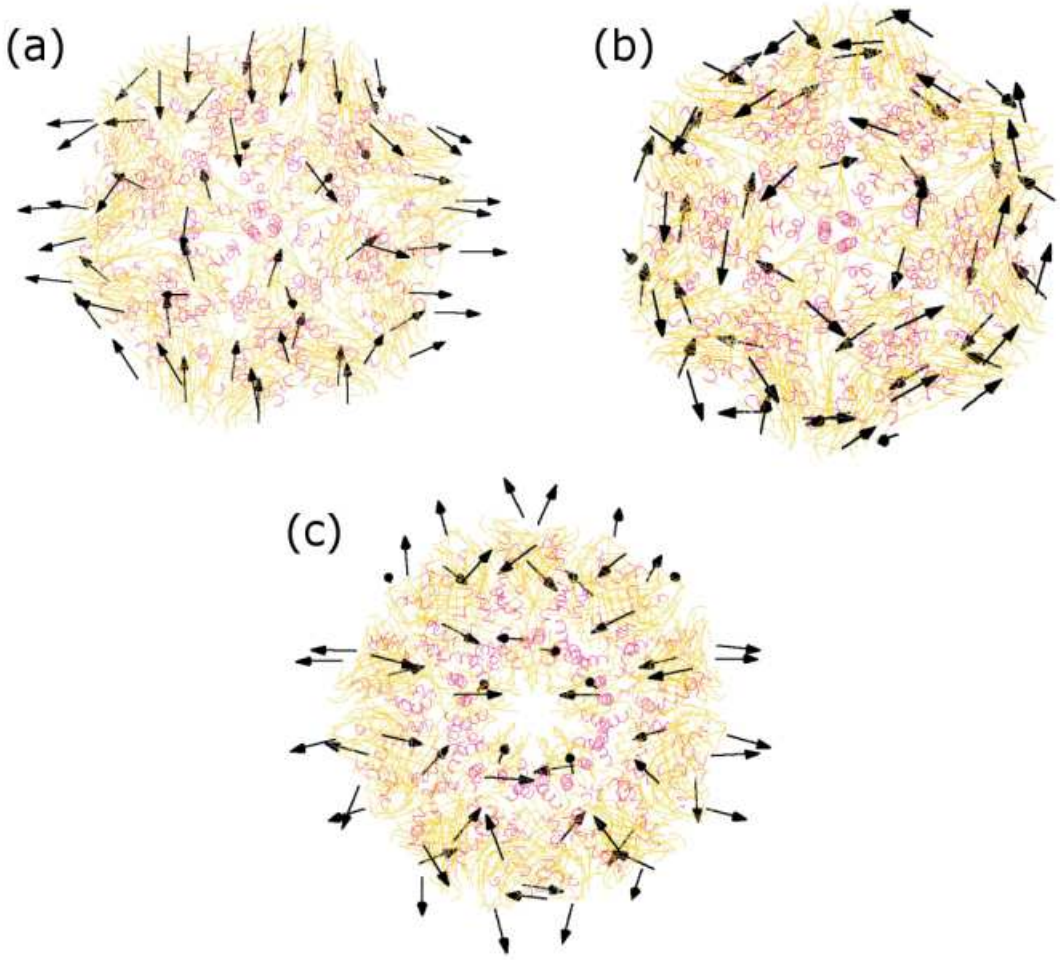

FIG. 23. The three lowest frequency modes of the satellite tobacco necrosis virus that have symmetry of the irreducible representation H. The full virus capsid composed of all 60 protein building blocks is shown. The arrows represent the direction of the center of mass motion for each protein building block and are not relative. (a) The lowest H mode at 1.95 cm^{-1}. (b) The second lowest H mode at 2.39 cm^{-1}. (c) The third lowest H mode at 2.86 cm^{-1}.

susceptibility of the virus capsid. The susceptibility tensor can then be used in Equation (5.76) to give the relative Raman intensity of the viral capsids in solution. The bond polarizability model requires polarizability parameters $\alpha'_{\parallel}$, $\alpha'_{\perp}$, $\alpha_{\parallel}$, and $\alpha_{\perp}$ in order to predict relative Raman intensities. Although each bond will in general have a unique set of polarizability parameters, the main goal here is to reproduce relative Raman intensities that will enable a qualitative understanding of which modes will be most stimulated by Raman scattering. As such, it should be sufficient to use the same polarizability parameters for each bond in the capsid. Future work will utilize a more diverse set of polarizability parameters. The polarizability parameters for carbon, a common element in polypeptides, will be used to estimate the Raman intensity of the capsid. The specific parameters used come from Snoke and Cardona [20] for single carbon-carbon bonds (see page 91).

The only Raman active modes are those from the irreducible representations A and H. The modes from the other irreducible representations have zero Raman intensity due to their symmetry. The relative Raman spectra of STNV in solution is given in Figure 24 for a detector angle of $\Theta = 90^{\circ}$ (see Figure 15). The Raman spectra for the A modes are drawn with a solid line and the H modes with a dashed line. Since the H modes are five fold degenerate, the intensity of a single mode can be expected to be roughly five times greater than that of an A mode. A large difference in Raman intensity for the A and H modes is clearly seen in the figure. Thus it is expected that the H modes will likely be excited the strongest from inelastic Raman scattering experiments such as ISRS.

Since no other methods are known to have been used to predict the low frequency modes of the satellite tobacco necrosis virus, a direct comparison to the phonon functional method cannot be made. However, the phonon functional method has revealed a fairly complicated picture of the low frequency motions of STNV.

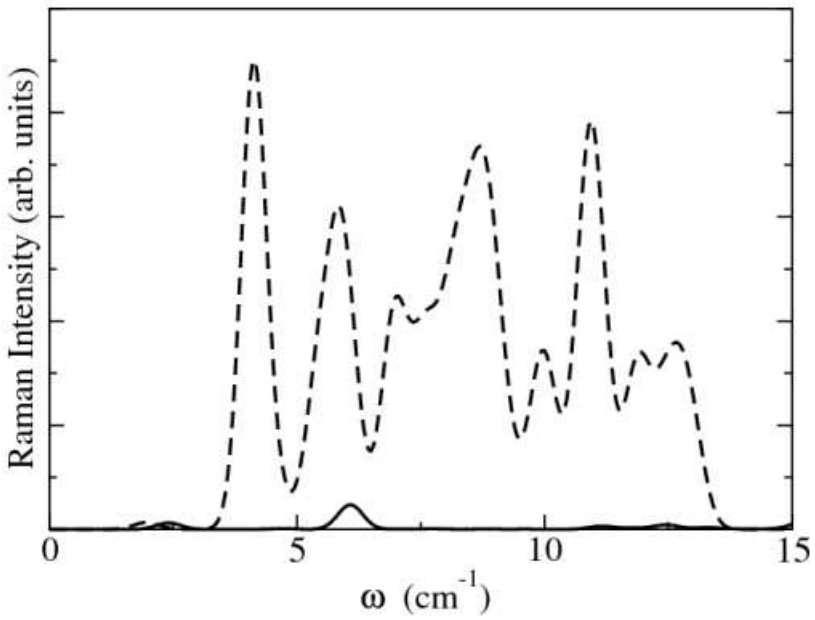

FIG. 24. Relative Raman spectra prediction for the satellite tobacco necrosis virus capsid in solution with a detector angle of $\Theta = 90°$. A broadening of 0.75 cm^{-1} was applied to the intensity predictions. The Raman active modes have symmetry of the irreducible representations A and H. All others are Raman silent. The solid line indicates the relative Raman intensity of the modes having symmetry of the irreducible representation A. The dashed line indicates the relative Raman intensity for the H modes. The five fold degeneracy of the H modes has been included in the spectra predictions.

III. COWPEA CHLOROTIC MOTTLE VIRUS

The study of icosahedral viruses is continued in this section with the examination of the low frequency modes and relative Raman spectra of the cowpea chlorotic mottle virus (CCMV) using the phonon functional method. The cowpea chlorotic mottle virus is a small to medium sized plant virus with a capsid diameter of approximately 26 nm. It is a $T = 3$ icosahedral virus constructed from 180 copies of a single protein.

The CCMV capsid is of particular interest in theoretical and experimental studies because of its ability to swell when calcium ions are removed from the capsid at neutral pH [77]. For CCMV, the swelling occurs due to the repulsion of acidic residues in the vicinity of the calcium binding sites that commences once the stabilizing calcium ions are removed [78]. The swelling process results in the formation of 60 pores in the capsid structure. Experimentally, the swelling is usually accomplished by adjusting the pH instead of the calcium concentration. Since the calcium deficient CCMV capsid is stable in the unswollen form at low pH (around 5), a simple adjustment of the pH results in a *reversible* unswollen to swollen transition.

The ability to open pores in the CCMV capsid by a simple change in pH has presented the possibility of using CCMV as vector for the delivery of chemical agents. So far, nanoparticles and organic compounds have been successfully loaded into empty CCMV capsids using the swelling procedure [77]. Such experiments pave the way for drug or gene therapies that are delivered by viral capsids that have been engineered to swell to allow for the efficient "loading" of the capsid cargo.

Although the mechanism that causes swelling of the CCMV capsid is somewhat understood, a detailed swelling pathway has yet to be formed. Recently some work on the subject has been done by Tama and Brooks [60]. Using NMA with the elastic network

and RTB models, Tama and Brooks constructed a series of capsid structures representing a proposed swelling pathway. Starting with the unswollen CCMV capsid, the eigenvectors from the NMA were used to predict intermediary structures. These intermediary structures were obtained by moving the capsid structure along the eigenvector that had the greatest overlap with a single vector constructed by taking the difference in the C_α positions between the intermediary and final swollen CCMV capsid structures. One of the main problems with calculating a proposed swelling pathway in this manner is that the elastic network model uses a phenomenological treatment of the potential, *i.e.* identical springs connecting atoms, which cannot properly account for calcium ion interactions in a NMA. The phonon functional method on the other hand is capable of using an empirical energy model and a full basis set to construct the eigenvectors. This may provide better detail in the types of atomic reconstructions that initiate the swelling process and will be explored later.

The CCMV has a range of plants that it infects which includes beets and soybeans. Infection of a plant with CCMV requires a vector which is able to pass the virus directly into a host cell. An example of a vector would be an insect, such as an aphid, which carries the virus and infects the plant as it feeds. Once a plant is infected, the virus is systemic, moving throughout the tissues of the plant. The most noticeable indication that a plant is infected with CCMV is the appearance of necrotic lesions and streaks on the leaves of the plant.

The genome of CCMV consists of ss-RNA with an approximate length of 8.444 kilo bases [79]. The genome is split into three distinct segments which are labeled RNA1, RNA2, and RNA3. The three segments contain a total of four genes. Each RNA segment codes for one enzyme labeled 1a, 2a, and 3a according to the respective RNA segment that contains

the encoding region for the enzyme. In addition to coding for the 3a enzyme, the RNA3 segment also codes for the single protein that makes the capsid.

The structure of the CCMV capsid protein is shown in Figure 25 (a). This single protein forms a trimer of units A, B, and C shown in Figure 25 (b). The trimer is then placed on the icosahedral surface using the rotation operators for the regular icosahedral group. Since the CCMV capsid is constructed from a trimer of proteins using the 60 icosahedral rotation operators, the capsid is referred to as a $T = 3$ capsid. A diagram of the $T = 3$ icosahedral surface for the CCMV capsid is illustrated in Figure 25 (c). Red cells correspond to the A proteins, blue cells to the B proteins, and green cells to the C proteins of the trimer depicted in (b). The full capsid structure is shown in Figure 25 (d).

The structure of the CCMV capsid was determined from X-ray crystallography [80]. In addition to the 180 proteins, the X-ray experiment also found calcium ions and small segments of ss-RNA bound to capsid proteins. The RNA-capsid interactions are believed to help stabilize the capsid shell in addition to the calcium. The full capsid structure contained a total of 451200 atoms (including hydrogen). Out of the 451200 atoms, 432120 atoms are from the 180 proteins, 18900 atoms are from the ss-RNA, and 180 atoms are calcium ions. Using the nomenclature developed in Chapter 3, the CCMV capsid consists of $N_b = 7520$ basis atoms copied $N_s = 60$ times. The basis atoms include the trimer of coat proteins (units A, B and C) as well as three short ss-RNA chains and three calcium ions. The three calcium ion binding sites are illustrated by green dots in Figure 25 (b). The calcium ions are not located around the exact C3 axis but a local pseudo C3 axis. The binding site coordinates for the calcium ions were obtained from the X-ray structure [80].

A single icosahedral site of the CCMV capsid consisting of $N_b = 7520$ basis atoms (protein, ss-RNA, and calcium ions) was energetically minimized using the AMBER 94 force

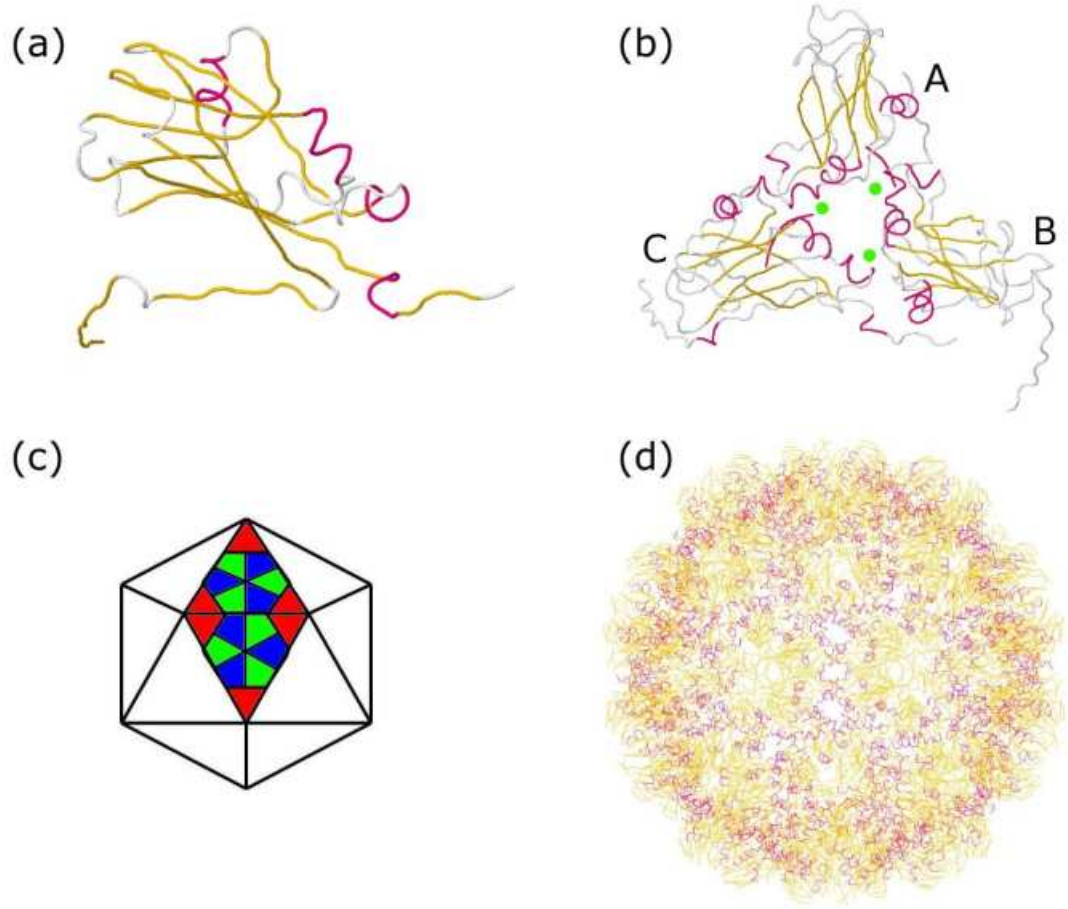

FIG. 25. Structure of the cowpea chlorotic mottle virus. (a) The structure of a single protein that makes up the capsid. The protein is drawn as a backbone trace. (b) A trimer of proteins that make up one icosahedral site (1 of 60) of the virus. The three Ca^{2+} ions that stabilize the trimer are drawn as green dots. The proteins are labeled A, B, and C. The RNA segments that bind to the capsid are not shown (c) The icosahedral surface for a $T = 3$ virus. The full virus is obtained by placing the A, B, and C proteins along with one calcium ion in the appropriate cells (see text for a description of the placement). (d) The structure of the full virus.

field [9], taking into account neighboring atoms using the icosahedral rotation operators. Interactions of the capsid with water were modeled with the generalized Born implicit solvent model [13, 14, 37]. The generalized Born and van der Waals parameters for the calcium ions were obtained from Babu *et al.* [75]. After energy minimization was performed, the final RMS force was 6.6×10^{-5} eV/Å and the RMS deviation from the original X-ray structure was approximately 3.7 Å. At this RMS force value, only two negative eigenvalues in the T1 T2 G, and H representations were found. All were highly localized on the same atoms (approximately 80) in a few side chains in the B subunit, away from the calcium binding sites. As such, they are physically irrelevant to the low frequency normal modes and can be ignored.

Using group theory for the regular icosahedron, the full dynamical matrix is reduced to the five smaller dynamical matrices corresponding to the irreducible representations A, T1, T2, G, and H. The group dynamical matrices for each of these representations have sizes of 22560 for A, 67680 for T1 and T2, 90240 for G, and 112800 for H. Using the optimized structure for a single icosahedral site, the lowest 100 eigenvectors and eigenvalues for each irreducible representation were found by applying 6000 conjugate gradient steps to the phonon energy functional [Eq. (4.21)]. This resulted in a total of 1600 low frequency modes of CCMV being found.

Using Equation (4.25) the final eigenvectors of the group dynamical matrices were constructed for each irreducible representation. The eigenvectors of the full dynamical matrix can then be found by taking a linear combination of group theory basis vectors using Equation (3.16). Since the eigenvectors and eigenvalues calculated using Equation (4.25) are approximate, a calculation of the residual vector $|r^p\rangle = \hat{D}^p|\bar{e}^p\rangle - \bar{\omega}^2|\bar{e}^p\rangle$, was used to estimate the quality of the eigenvectors and eigenvalues. The magnitude of the

TABLE VI. The five lowest frequency modes and their corresponding participation number W per site for the cowpea chlorotic mottle virus by irreducible representation. The frequencies are given in cm^{-1}.

	ω_1 (W_1)	ω_2 (W_2)	ω_3 (W_3)	ω_4 (W_4)	ω_5 (W_5)
A	1.18	2.14	2.58	3.17	3.26
	(7168)	(5585)	(5152)	(816)	(903)
T1	1.35	1.56	1.77	2.29	2.40
	(7169)	(6628)	(6350)	(6356)	(6775)
T2	0.89	1.46	1.66	2.23	2.43
	(6950)	(6187)	(6955)	(5654)	(5014)
G	0.91	1.16	1.54	1.94	1.99
	(6706)	(6792)	(6591)	(5059)	(6137)
H	0.71	1.04	1.24	1.45	1.74
	(7381)	(7364)	(7183)	(6672)	(6825)

residual vectors were found to be approximately 10^{-4}. Thus, the errors in the eigenvalues are expected to be consistent with ubiquitin at around 0.01 cm^{-1} (see Table III).

Table VI lists the five lowest frequencies and their participation numbers W_λ for each mode λ which were calculated using Equation (6.1). For CCMV, a mode that has full participation, such as a translation, would have a participation value of 7520 (per site). The lowest frequency mode listed in Table VI is at 0.71 cm^{-1} and is of the H irreducible representation. Nearly all of the modes are global, having at least 5000 atoms participating. However, the A irreducible representation modes at 3.17 cm^{-1} and 3.26 cm^{-1} have less than a thousand atoms participating in the mode. These are modes that are localized on just one of the A, B, C units of the trimer.

The lowest frequency mode of the A irreducible representation, located at 1.18 cm^{-1}, is the breathing mode of the virus capsid. The next lowest frequency A mode at 2.14 cm^{-1} corresponds to the "puckering" mode of the virus. Unlike the puckering mode for the STNV were each protein on the C5 axis expands out, the CCMV puckering mode has sections that

expand outward while other sections expand inward towards the center of the capsid. The sections that expand outward are the A units of the protein trimer on the C5 axis while the sections expanding inwards are the B and C units on the C3 axis. The third lowest frequency A mode at 2.58 cm^{-1} is the rotational mode. For the CCMV rotational mode, the A units of the trimer on the C5 axis rotate in one direction while the B and C units on the C3 axis rotate in the opposite direction. Essentially the CCMV rotation mode has the pentagons and hexagons of the capsid rotating in opposite directions. The breathing, puckering, and rotation modes are illustrated in Figure 26 (a), (b), and (c) respectively. Each arrow in Figure 26 represents the center of mass motion of one of the 180 proteins.

The lowest frequency modes of the T1, T2, and G irreducible representations are shown in Figure 27. Again, the center of mass motions of each protein are represented as an arrow. The lowest frequency T1 mode can be characterized as a dipole like motion and is illustrated in Figure 27 (a). The lowest frequency T2, and G modes are illustrated in Figures 27 (b) and (c) respectively. Finally Figure 28 illustrates the three lowest H modes. One mode in particular, the second lowest frequency H mode at 1.04 cm^{-1}, can be described as the upper and lower hemispheres of the virus rotating in opposite directions.

The CCMV normal modes have also been analyzed in other studies with the RTB method [7] and with a method which used the reduced basis set of dihedral angles [54]. The phonon functional predictions for the CCMV frequencies compare quite well with those calculated with the dihedral angle basis set. In that study, the lowest frequency mode was also an H mode with frequency 0.80 cm^{-1}. The RTB method however tends to yield frequencies that are several times higher [54]. In general it seems that reduced basis sets result in higher frequency predictions.

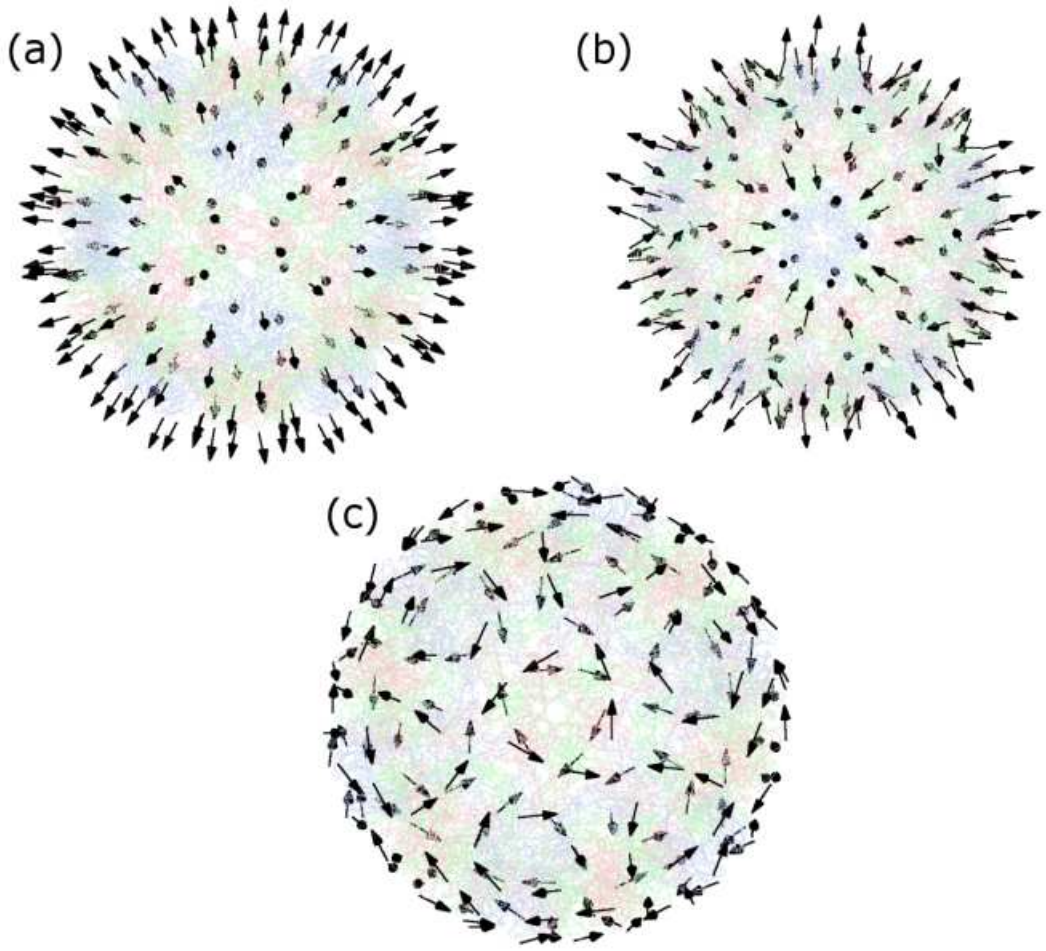

FIG. 26. Three low frequency modes of the cowpea chlorotic mottle virus that have symmetry of the A irreducible representation. The full virus capsid composed of all 180 protein building blocks is shown. The arrows represent the direction of the center of mass motion for each protein building block and are not relative. (a) The breathing mode at 1.18 cm^{-1}. (b) The puckering mode at 2.14 cm^{-1}. (c) The rotational mode at 2.58 cm^{-1}.

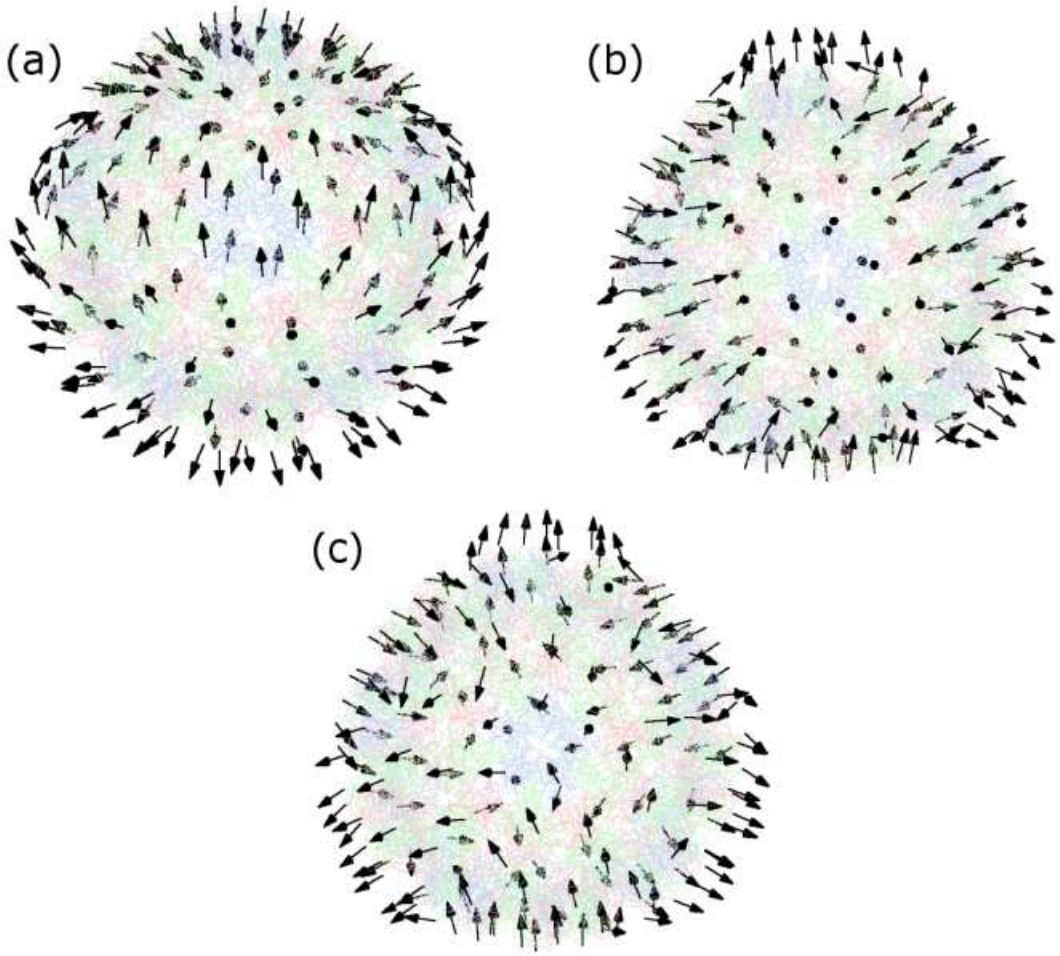

FIG. 27. The lowest frequency modes of the cowpea chlorotic mottle virus that have symmetry of the irreducible representations T1, T2, and G. The full virus capsid composed of all 180 protein building blocks is shown. The arrows represent the direction of the center of mass motion for each protein building block and are not relative. (a) The lowest T1 mode at 1.35 cm^{-1}. (b) The lowest T2 mode at 0.89 cm^{-1}. (c) The lowest G mode at 0.91 cm^{-1}.

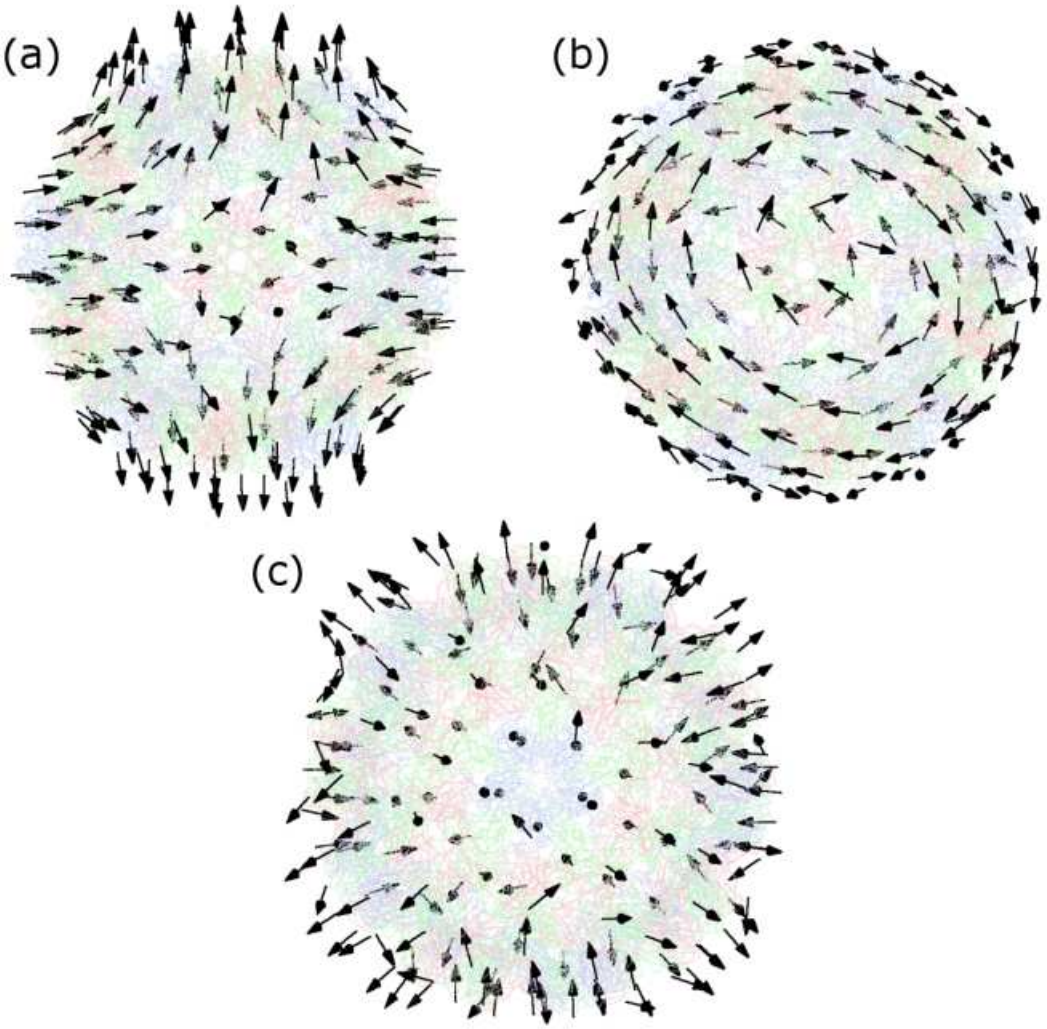

FIG. 28. The three lowest frequency modes of the cowpea chlorotic mottle virus that have symmetry of the irreducible representation H. The full virus capsid composed of all 180 protein building blocks is shown. The arrows represent the direction of the center of mass motion for each protein building block and are not relative. (a) The lowest H mode at 0.71 cm^{-1}. (b) The second lowest H mode at 1.04 cm^{-1}. (c) The third lowest H mode at 1.24 cm^{-1}.

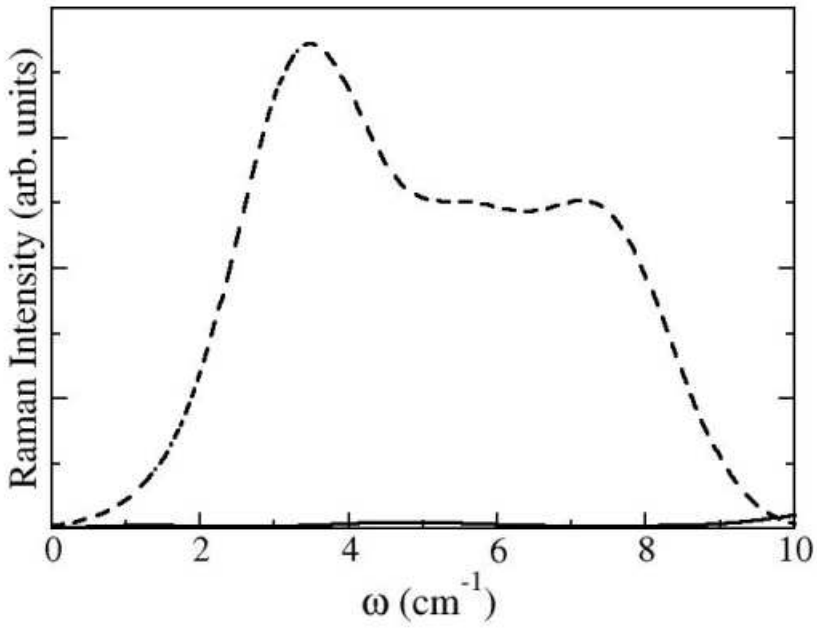

FIG. 29. Relative Raman spectra prediction for the cowpea chlorotic mottle virus capsid in solution with a detector angle of $\Theta = 90°$. A broadening of 0.75 cm^{-1} was applied to the intensity predictions. The Raman active modes have symmetry of the irreducible representations A and H. All others are Raman silent. The solid line indicates the relative Raman intensity of the modes having symmetry of the irreducible representation A. The dashed line indicates the relative Raman intensity for the H modes. The five fold degeneracy of the H modes has been included in the spectra predictions.

The relative Raman intensity of the CCMV capsid in solution was calculated using the bond polarizability model discussed in Chapter 5 Section III and Equation (5.76). Polarizability parameters for single carbon-carbon bonds (see page 91) were used to predict the induced susceptibility due to a vibrational mode. The final result is shown in Figure 29. The Raman active A modes are indicated by the solid line and the Raman active H modes by a dashed line. The H modes contribute to most of the intensity creating a broad plateau with a peak at 3.5 cm^{-1}.

Finally, the swelling process of CCMV is examined by calculating the normal modes of the optimized structure while *ignoring* interactions with the calcium ions. The optimized structure was obtained by minimizing *with* calcium interactions accounted for (see above). Since the swelling process is initiated by the removal of the stabilizing calcium ions, the NMA should reveal unstable modes, *i.e.* modes that have negative eigenvalues. This procedure is well suited for the phonon functional method because these negative modes will automatically become the lowest in the CCMV spectrum.

The 50 lowest modes were calculated for each irreducible representation using the optimized structure and no calcium interactions by minimizing the phonon energy functional as described above. Interestingly, unstable modes appear in each of the irreducible representations A, T1, T2, G, and H and have frequencies that range from -0.35 cm^{-1} to -92.66 cm^{-1}. While most of the modes are very localized in the calcium binding regions (see Figure 25 b) there are roughly four or five modes that have several thousand atoms participating in the motion. Two of these modes, an A mode at -2.12 cm^{-1} with 1717 atoms participating and a T2 mode at -0.72 cm^{-1} with 1978 atoms participating are shown in Figure 30. Both modes are particularly interesting because they describes a restructuring of the trimer of proteins that is preferential to the AC interface. Overall, the results provide fresh evidence that the swelling process is much more complex than a simple expansion and may involve multiple stages.

IV. M13 BACTERIOPHAGE

The last virus examined in this chapter is the tubular M13 bacteriophage virus. The M13 bacteriophage is a filamentous virus were the capsid takes the shape of a long, cylindrical tube. It has a particularly simple structure which makes theoretical studies of the mechanical modes of its capsid easy using continuum models [66, 72]. Here, the

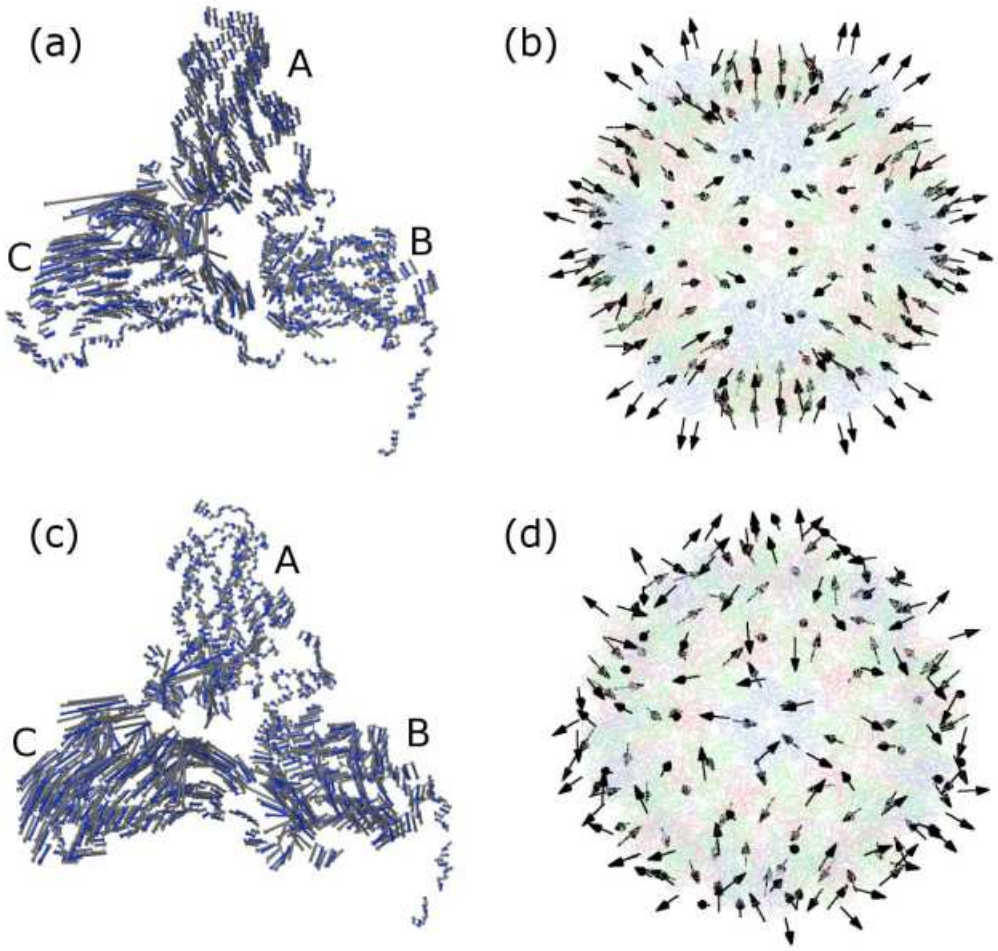

FIG. 30. Two unstable modes of the calcium ion free cowpea chlorotic mottle virus. Displacements of the protein backbone atoms at a single icosahedral site are shown along with the center of mass motion of each protein in the full virus. (a) The relative displacements of the protein backbone atoms (N, C_α, C) for the unstable A mode at -2.12 cm^{-1}. Short (long) arrows represent small (large) relative displacements of the atom. (b) The displacements for the full virus structure for the unstable A mode at -2.12 cm^{-1}. The arrows represent the direction of the center of mass motion for each protein building block and are not relative. (c) Same as (a) except for the unstable T2 mode at -0.72 cm^{-1}. (d) Same as (b) except for the unstable T2 mode at -0.72 cm^{-1}.

mechanical modes and relative Raman spectra of the bacteriophage are studied from both the continuum and fully atomistic perspectives and a comparison between the two is made.

The genome of M13 consists of single stranded circular DNA with an approximate length of 6000 base pairs. The M13 genome encodes for a total of 11 proteins [81], of which five; P3, P6, P7, P9, and P8, are used to create the M13 capsid. The major coat protein, P8, is 50 amino acids in length and forms an alpha helix structure that makes up the tubular body of the M13 phage. The remaining four proteins make small "caps" that cover the ends of the helical tube. The proteins P3 and P6 cover one end of the tube while P7 and P9 cover the other end. The P3 protein is required for entrance into the host cell, in this case the *E. coli* bacterium. Once infected, the host cell will replicate M13 clones indefinitely. This is due to new M13 capsids being constructed at the outer membrane surface of the host cell which allows it to remain intact without rupturing [81].

The structure of the major coat protein, shown in Figure 31 (a), was determined by X-ray diffraction [82]. The small alpha helix proteins assemble into a tubular capsid of roughly 850 nm in length. The final resulting capsid will have helical symmetry and a diameter of approximately 6 nm. The M13 capsid also has translational symmetry along the tube axis. A periodic segment of the capsid can be constructed by assembling 50 of the protein building blocks. The periodic unit, shown in Figure 31 (b), has a unit cell length along the tube axis of 161.5 Å.

In Chapter 5 Section II, elastic wave theory was used to develop a set of equations that described the mechanical modes of an isotropic elastic cylindrical shell. These equations can be used to predict the mechanical mode patterns and corresponding frequencies of the M13 capsid. The model requires only four parameters, the inner and outer radius of the M13 capsid, and the transverse and longitudinal speeds of sound. The inner and outer radius

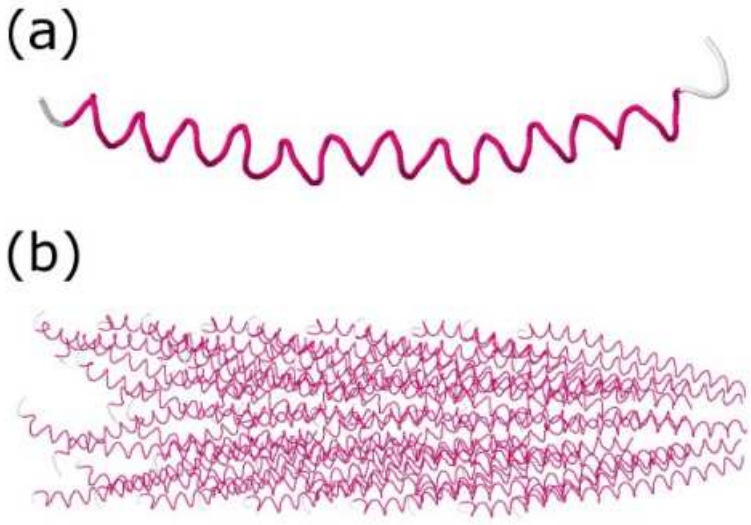

FIG. 31. The structure of the M13 bacteriophage capsid. (a) Structure of the major coat protein P8. The protein is drawn as a backbone trace. (b) One periodic segment of the M13 capsid constructed from 50 alpha helix building blocks shown in figure (a). The resulting segment has translational symmetry along the tube axis. The length of the periodic segment is 161.5 Å.

can be approximated from the molecular structure predicted from X-ray crystallography. Orientating the capsid structure along the $\hat{z}$ axis and averaging over the distances between atoms in the x-y plane yields an inner radius of 1.9 and 3.4 nm respectively. The transverse and longitudinal speeds of sound can be approximated from experimental speeds of sound in proteins. The lysozyme protein has an experimentally measured transverse and longitudinal speed of sound of 915 and 1817 m/s respectively [83].

Equations (5.27) and (5.28) determine the mode patterns of the capsid shell in continuum theory. The coefficients A_ϕ, B_ϕ *etc.* required in Equation (5.27) are determined by solving the 6×6 eigenvalue equation,

$$\overleftrightarrow{C}\,\vec{A} = 0. \tag{6.3}$$

The coefficients of the matrix $\overleftrightarrow{C}$, determined from Equation (5.37), are dependent on the

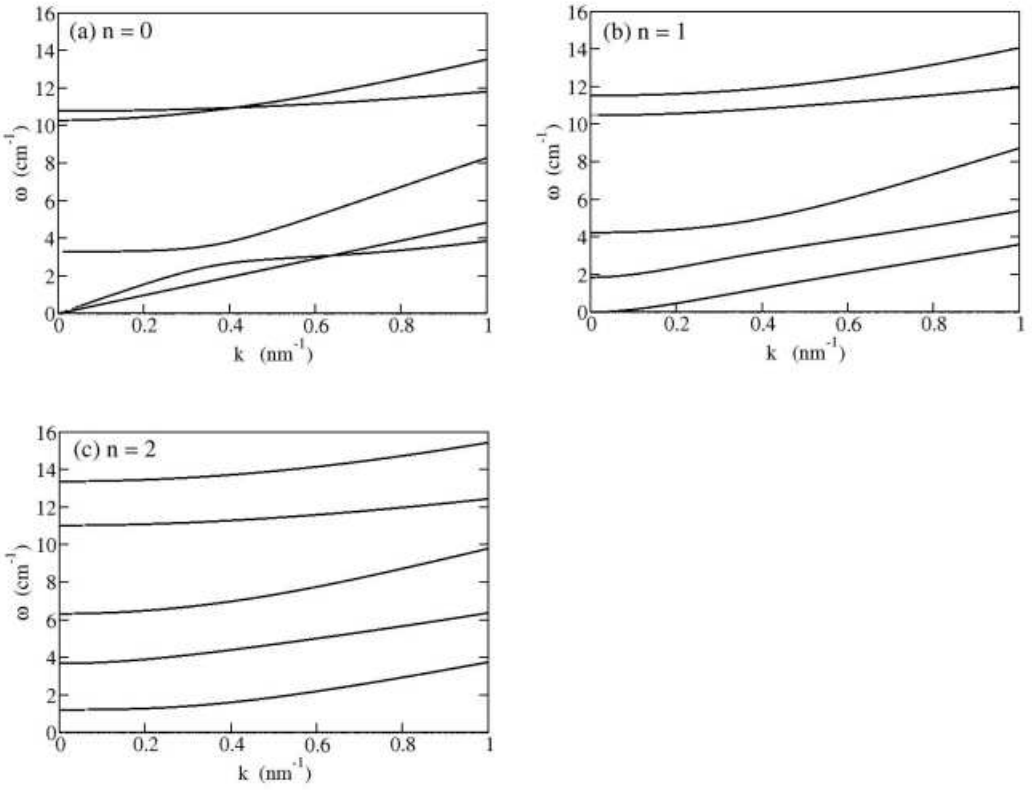

FIG. 32. Frequency dispersion curves for the M13 bacteriophage capsid predicted with continuum elastic theory. Dispersion curves for $n = 0, 1, 2$ with n denoting the cosine/sine dependence ($\cos(n\theta)$) are shown. (a) Dispersion curve for $n = 0$. (b) Dispersion curve for $n = 1$. (c) Dispersion curve for $n = 2$.

frequency ω and will only satisfy Equation (6.3) for certain values of ω. A solution to Equation (6.3) is found by varying ω in steps, producing a unique matrix $\overleftrightarrow{C}$ at each step. At each step, the eigenvalues and eigenvectors of $\overleftrightarrow{C}$ are calculated. Once a zero eigenvalue of $\overleftrightarrow{C}$ is found, the value of ω used to construct $\overleftrightarrow{C}$ corresponds to a natural frequency of the capsid shell. The eigenvector associated with the zero eigenvalue gives the coefficients $\vec{A} = (A_\phi, A_r, A_z, B_\phi, B_r, B_z)$ required in Equation (5.27) to predict the mode patterns.

Frequency dispersion relations, $\omega(k)$, are shown in Figure 32 for the M13 capsid shell. The n values of $n = 0, 1, 2$ correspond to the n value of the cosine/sine term in Equation

TABLE VII. The low frequency modes of the M13 bacteriophage predicted using continuum elastic theory. Frequencies of the capsid shell were determined for $k = 0$, with parameters $a = 1.9$ nm, $b = 3.4$ nm, $c_t = 915$ m/s, and $c_l = 1817$ m/s. The first five lowest frequency modes for $n = 0, 1, 2$ are shown along with the mode type of either axial (A), radial (R), or radial-torsional (RT). The frequencies are given in cm^{-1}.

	ω_1 (Type)	ω_2 (Type)	ω_3 (Type)	ω_4 (Type)	ω_5 (Type)
$n = 0$	3.29	10.29	10.78	20.40	20.47
	(R)	(A)	(A)	(A)	(R)
$n = 1$	1.85	4.23	10.48	11.54	19.47
	(A)	(RT)	(A)	(RT)	(RT)
$n = 2$	1.22	3.68	6.33	11.03	13.38
	(RT)	(A)	(RT)	(A)	(RT)

(5.28). As discussed in Chapter 5, solutions with $n > 0$ will be two fold degenerate due to the additional solutions that can be obtained by swapping $\cos(n\theta)$ for $\sin(n\theta)$. The Raman active vibrational modes of the M13 capsid shell will have $k \approx 0$ due to the relatively long wavelength of light (≈ 500 nm) that is used in Raman experiments [84, 85]. At $k = 0$, the matrix $\overleftrightarrow{C}$ can be factored into 2×2 and 4×4 matrices. The 2×2 matrix determines the axial modes of the capsid. These modes have $u_r = u_\theta = 0$ and $u_z \neq 0$. The 4×4 matrix determines the radial and radial-torsional modes. These modes have $u_\theta = u_z = 0$ and $u_r \neq 0$ or $u_z = 0$ with $u_r \neq 0$ and $u_\theta \neq 0$.

Table VII shows the frequencies and mode types for the first few lowest frequency modes. The three lowest modes at 1.22, 1.85, and 3.29 cm^{-1} are illustrated in Figure 33. The continuum model predicts the capsid breathing mode at 3.29 cm^{-1}, an axial shearing mode at 1.85 cm^{-1}, and a compressional mode at 1.22 cm^{-1}.

Using the amorphous isotropic bond polarizability model (AIBP) derived in Chapter 5 Section IV specifically for continuum elastic theory, the relative Raman intensity of the modes can be predicted. The susceptibility for a single M13 bacteriophage capsid can be

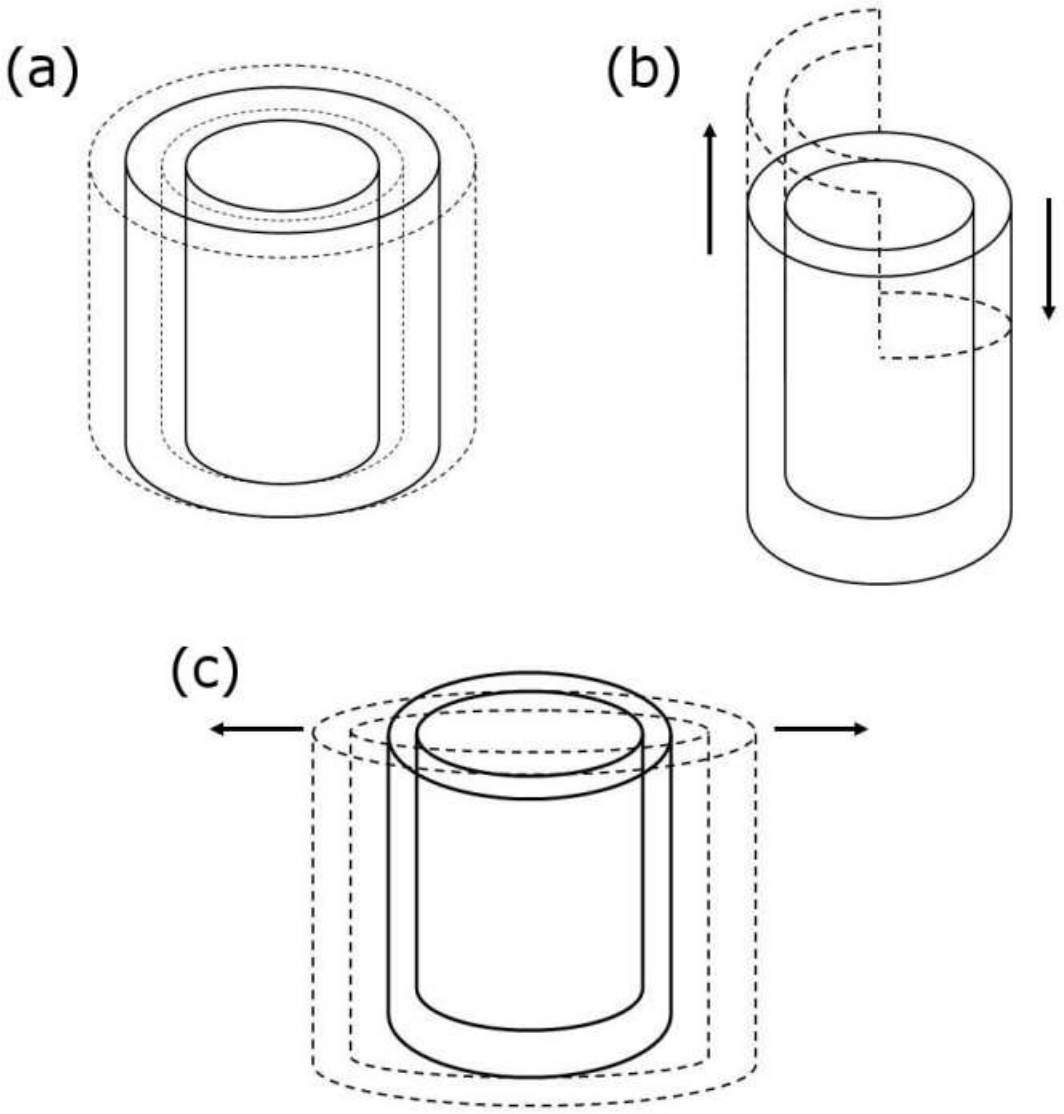

FIG. 33. Three low frequency displacement patterns of the M13 capsid predicted with continuum elastic theory. (a) A radial $n = 0$ breathing mode at 3.29 cm^{-1}. (b) An $n = 1$ axial shearing mode at 1.85 cm^{-1}. (c) An $n = 2$ radial-torsional mode at 1.22 cm^{-1}.

calculated via

$$\Delta \overleftrightarrow{\chi} = \int \Delta \overleftrightarrow{\alpha}\, dV, \tag{6.4}$$

where the integral is computed over the entire capsid volume and the induced polarization per unit volume, $\Delta \overleftrightarrow{\alpha}$, is calculated using Equation (5.58). The strain tensor elements required for the AIBP model can be obtained from Equation (5.32). Integrating Equation (6.4) over the cylindrical shell and taking into account the degeneracy factor for modes with $n > 0$ produces the following non-zero susceptibility elements (in Cartesian coordinates) for $n = 0, 1, 2$:

$$\begin{aligned}
\Delta\chi_{xx} = \Delta\chi_{yy} &= -\pi\frac{\alpha_s}{V_b}\left(\frac{1}{3} + 2\frac{\alpha_c}{\alpha_s}\right)\Gamma_0 \quad \text{for} \quad n = 0, \\
\Delta\chi_{xz} = \Delta\chi_{zx} &= -\pi\frac{\alpha_s}{V_b}\Gamma_1 \quad \text{for} \quad n = 1, \\
\Delta\chi_{xx} = \Delta\chi_{yy} &= -\frac{\pi}{2}\frac{\alpha_s}{V_b}\Gamma_2 \quad \text{for} \quad n = 2.
\end{aligned} \tag{6.5}$$

The constants α_c and α_s are the compressional, and shear polarizabilities defined in Equation (5.55) and the constant V_b is the average volume of a single bond. The quantities Γ_n are integrals of cylindrical Bessel functions given by

$$\begin{aligned}
\Gamma_0 &\equiv \textstyle\int_a^b \alpha^2 r f\, dr, \\
\Gamma_1 &\equiv \textstyle\int_a^b r\left[\left(\frac{2}{r^2} - \frac{\beta^2}{2}\right)h_r + \frac{h_r'}{r}\right] dr, \\
\Gamma_2 &\equiv \textstyle\int_a^b r\left[\frac{3}{r}(f' + h_z') + \frac{4}{r^2}(f + h_z) - \alpha^2 f - \beta^2 h_z\right] dr.
\end{aligned} \tag{6.6}$$

The radial functions f, h_r, and h_z are defined in Equation (5.27). Using Equation (5.76), a closed form solution for the relative Raman intensity for each n value is obtained:

$$\begin{aligned}
I &\propto \tfrac{(2\lambda_R+\mu_R)}{\omega}\left[\tfrac{1}{3} + 2\tfrac{\alpha_c}{\alpha_s}\right]^2\Gamma_0^2 \quad \text{for} \quad n = 0, \\
I &\propto 2\tfrac{\mu_R}{\omega}\Gamma_1^2 \quad \text{for} \quad n = 1, \\
I &\propto \tfrac{(2\lambda_R+\mu_R)}{\omega}\tfrac{\Gamma_2^2}{2} \quad \text{for} \quad n = 2.
\end{aligned} \tag{6.7}$$

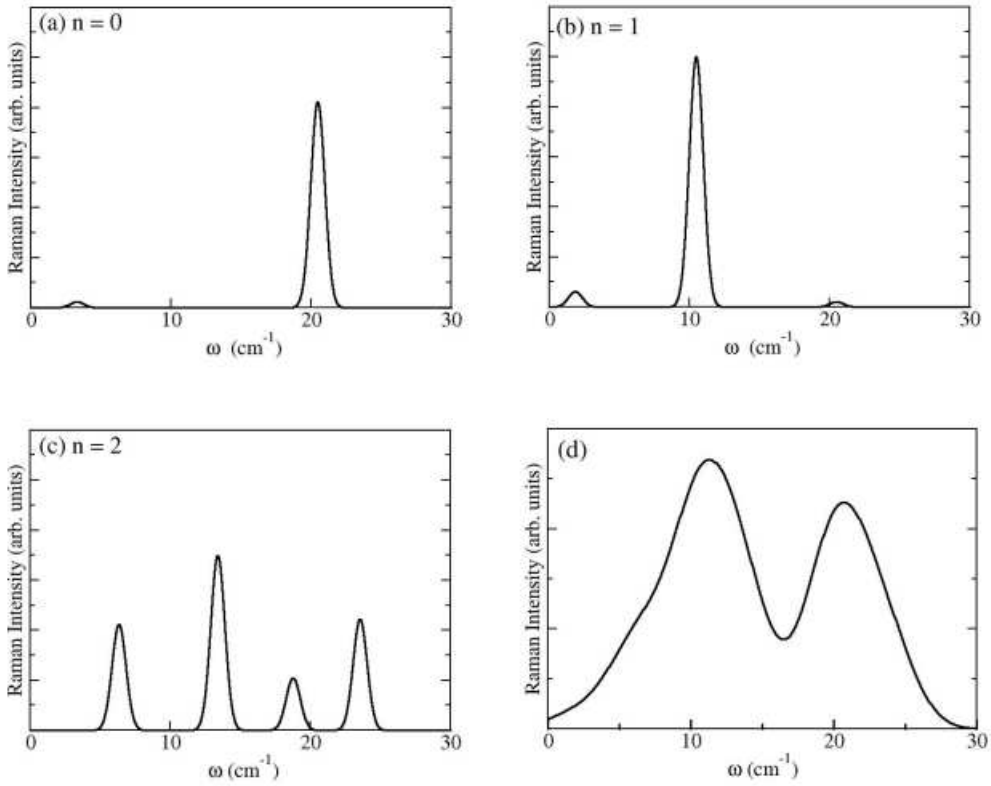

FIG. 34. Relative Raman spectra predictions for the M13 bacteriophage capsid in solution using the AIBP model with a detector angle of $\Theta = 90°$. (a) Relative Raman spectra for active $n = 0$ radial modes. (b) Relative Raman spectra for active $n = 1$ axial modes. (c) Relative Raman spectra for active $n = 2$ radial-torsional modes. (d) Total combined relative Raman spectra for $n = 0, 1, 2$. A broadening of 5.0 cm^{-1} is used to account for experimentally observed broadening.

Since at $k = 0$ the axial and radial-torsional solutions separate, continuum elastic theory predicts that only $n = 1$ axial modes and $n = 0, 2$ radial modes will be Raman active.

To predict the relative Raman intensity of the M13 bacteriophage in solution, Equation (6.7) requires the polarizability constants α_c and α_s. A reasonable expectation is that the majority of the bonds in the M13 capsid are carbon like since the majority of bonds in peptides contain carbon. Using Equation (5.55) and polarizability parameters from Snoke and Cardona for carbon (see page 91) gives a ratio of $\alpha_c/\alpha_s = 0.52$. The resulting relative

Raman intensity predicted by the continuum elastic model is shown in Figure 34. Figures (a) - (c) show the Raman intensity for $n = 0, 1, 2$. The total combined Raman intensity for all three n values is shown in (d). A broadening of 5.0 cm^{-1} was used for the total Raman intensity prediction to account for the experimentally observed broadening [84, 85] (a broadening of 0.75 cm^{-1} was used in all other Raman intensity examples presented in this dissertation).

Comparison of the theoretical Raman intensity with experiment [84, 85] shows an anomalous peak at 20.4 cm^{-1} due to a single radial mode. It is important to note that no damping of the M13 phage from the surrounding water has been considered. A reasonable expectation is that radial modes will be heavily damped when compared to axial modes. This is due to the increased surface area that can interact with the water when the capsid expands radially outward. If this hypothesis is valid, then the intensity for the 20.4 cm^{-1} mode should be significantly reduced resulting in a single peak at 10.4 cm^{-1}. Thus, it is expected that the mode at 10.4 cm^{-1} will produce the most damage to the capsid from ISRS stimulation.

Although continuum elastic theory can be used to predict the mechanical mode patterns, frequencies, and relative Raman intensities of the M13 capsid, the phonon functional method will provide a more detailed picture of the mechanical modes. To study the mechanical modes of the M13 bacteriophage capsid using the phonon functional method, 50 protein building blocks (Figure 31 a) were assembled to create a periodic tubular structure aligned along the $\hat{z}$ axis (shown in Figure 31 b) with a unit cell length of 161.5 Å. The resulting tubular structure contained a total of 37050 atoms.

Although the M13 capsid is finite in length, periodic boundary conditions can be used to treat the tubular segment as a infinite cylindrical tube. Unit cell vectors of $\vec{a_1} = 100\hat{x}$,

$\vec{a_2} = 100\hat{y}$, and $\vec{a_3} = 161.5\hat{z}$ were chosen. The x-y lattice constants were chosen to eliminate interactions of one infinite tube with its nearest neighbors. Using periodic boundary conditions, the unit cell was energetically minimized using the AMBER 94 force field [9]. Interactions with water were modeled using the generalized Born implicit solvent model [13, 14, 37] using a cutoff of 10 Å for the electrostatic interactions. Since the generalized Born method introduces a dielectric screening, no Ewald summation was needed for the Coulomb interactions although periodicity exists. Thus, only a direct sum was used in the computation of electrostatic interactions which extended only slightly into neighboring cells. The final optimized structure had a final RMS force of 0.001 eV/Å and an RMS deviation from the original X-ray structure of 1.61 Å.

Using the optimized structure, the lowest 200 eigenvalues and eigenvectors of the dynamical matrix were found by minimizing the phonon energy functional [Eq. (4.21)] with 4000 conjugate gradient steps. Only modes with a k state vector of $\vec{k} = 0$ are solved for. Here $\vec{k} = 0$ means that each cell performs the same motion. However, since the cell is 161.5 Å in length, internal waves with that wavelength or integer divisions of that wavelength can appear. Once the phonon functional was minimized, the final eigenvectors and eigenvalues were obtained from Equation (4.25). Residual vectors were calculated using the final eigenvectors and their magnitude was on the order of 10^{-4}. It is expected that the errors in the frequencies should be on the order of 0.01 cm^{-1} consistent with ubiquitin (see Chapter 4 Section VIII).

Table VIII lists the 25 lowest frequencies in cm^{-1}, the participation number for each mode, and the percentage of the mode that is axial, radial, or torsional. To calculate the percentage of the mode that is axial, radial, or torsional, the components of the *normalized* displacement pattern for each mode λ and atom i were projected along the cylindrical unit

TABLE VIII. The 25 lowest frequency modes of the M13 bacteriophage capsid calculated with the phonon functional method. The participation number W and percentage radial, torsional, and axial are also shown. The frequencies are given in cm^{-1}.

ω	W	% R	% T	% A
1.45	10616	42.5	39.7	17.8
1.62	30496	39.3	47.6	13.1
1.74	34123	46.9	43.9	9.2
1.89	26039	45.6	42.9	11.5
2.20	6690	47.8	33.8	18.4
2.49	4224	39.6	39.7	20.7
2.67	24955	7.8	88.3	3.9
2.72	21293	18.3	73.1	8.6
3.15	18103	58.1	20.5	21.4
3.25	22763	68.8	20.8	10.4
3.28	20219	63.0	22.9	14.1
3.31	21853	58.0	22.9	19.1
3.36	23557	61.7	25.2	13.1
3.40	23112	58.8	25.4	15.8
3.54	24201	57.2	25.1	17.7
3.57	23408	54.3	25.6	20.1
3.60	17527	50.4	23.8	25.8
3.65	22527	55.6	24.4	20.0
3.72	19154	50.1	24.3	25.6
3.80	25295	40.4	23.4	36.2
3.82	23583	48.9	27.9	23.2
3.88	22497	43.9	31.3	24.8
3.97	23500	24.2	18.4	57.4
3.98	24860	28.7	21.4	49.9
4.02	22820	35.3	27.3	37.4

directions $\hat{e}_r$, $\hat{e}_\theta$, and $\hat{e}_z$. For example, the percentage of the displacement that is radially directed is simply given by the sum,

$$\% \text{ R} = \sum_i \left[\vec{\eta}_i(\lambda) \cdot \hat{e}_r\right]^2, \tag{6.8}$$

with similar definitions for the torsional and axial percentages.

The modes predicted using the atomistic phonon functional method show a much richer spectrum of frequencies when compared with the continuum model. Also, the mode patterns tend not to be orientated along a specific axial or radial direction. This is due to the increased complexity of the capsid structure (when viewed atomistically) that tends not to permit purely radial, torsional, or axial displacements except for the zero frequency modes. However, a few of the lowest frequency modes compared quite well with continuum elastic theory. It should be noted that some $\vec{k} = 0$ modes in the atomistic model correspond to $k = 2\pi/16.15$ nm $= 0.38$ nm^{-1} modes in the continuum model. This is due to the finite cell length of 16.15 nm used in the atomistic model.

The four lowest frequency modes predicted by the phonon functional method are located at 1.45, 1.62, 1.74, and 1.89 cm^{-1}. These modes correspond to string modes of the capsid. Figure 35 (a) and (b) shows two different ways that the string modes can form on the M13 capsid. The arrows show the center of mass displacement of each of the 50 alpha helix building blocks in the unit cell. The two modes have have either $\cos(kz)$ or $\sin(kz)$ dependence with their displacements along the $\hat{x}$ axis the capsid. The two remaining string modes have perpendicular displacement patterns along the $\hat{y}$ axis. If the capsid was isotropic (as it is treated in the continuum elastic theory) then these four frequencies would be degenerate. Continuum elastic theory predicts that these string modes will have a frequency of roughly 1.87 cm^{-1}, very close to the highest frequency predicted in the atomistic model. It is interesting to note that a quick estimate of the transverse speed

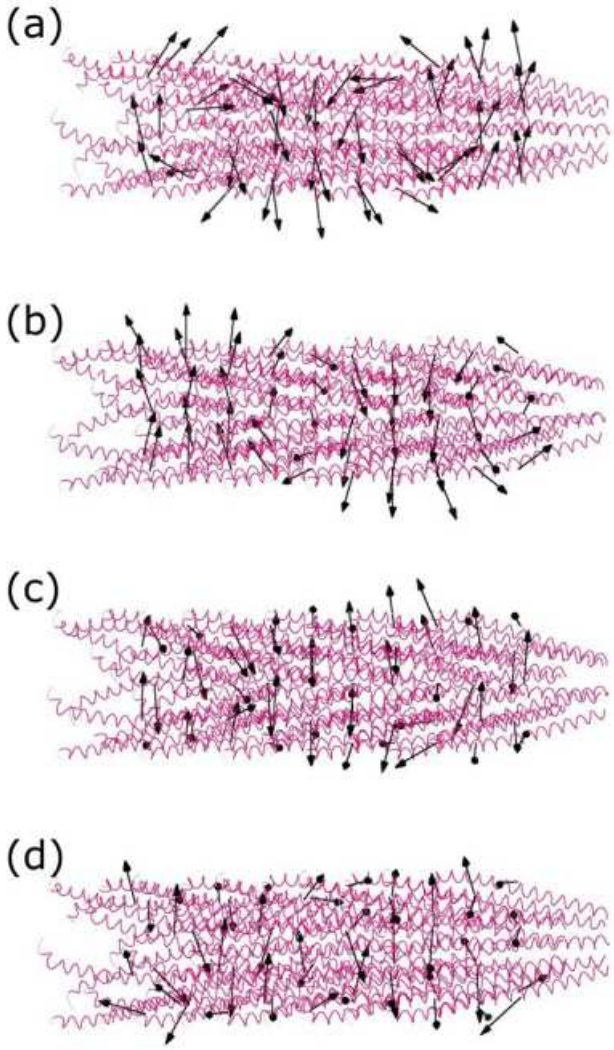

FIG. 35. Displacement patterns for the string and torsional modes of the M13 bacteriophage capsid predicted with the phonon functional method. These modes have approximate $\cos(kz)$ or $\sin(kz)$ dependence and can be compared with continuum model predictions at $k = 0.38\text{nm}^{-1}$. The arrows represent the center of mass motion of a single alpha helix building unit and are not relative. (a) String mode at 1.45 cm^{-1} with $\cos(k_c z)$ dependence. (b) String mode at 1.74 cm^{-1} with $\sin(k_c z)$ dependence. (c) Torsional mode at 2.67 cm^{-1} with $\cos(k_c z)$ dependence. (d) Torsional mode at 2.72 cm^{-1} with $\sin(k_c z)$ dependence.

of sound using $\omega = ck$ results in speeds of sound for the atomistic calculation that vary from 702.5 to 915.7 m/s. The value of 915.7 m/s is very close to the speed of sound that used in the continuum model based on lysozyme experiments (915 m/s). However, it is clear that possible problems may arise if a single value for the speeds of sound are used to model the mechanical modes of virus capsids using continuum elastic theory.

The next set of modes that can be compared with continuum elastic theory are located at 2.67 cm^{-1} and 2.72 cm^{-1}. These modes are torsional modes that can be pictured as a twisting of the ends of the capsid tube in opposite directions. The two modes are shown in Figure 35 (c) and (d) and have either $\cos(kz)$ or $\sin(kz)$ dependence. Once again there is a small splitting in the frequencies that is due to the non-uniform structure of the capsid. In continuum theory, the predicted frequency for these modes is approximately 2.60 cm^{-1}, very close to the atomistic model prediction.

So far only modes in continuum theory with $k \neq 0$ have been compared with the phonon functional method. The three lowest modes predicted by continuum elastic theory for $k = 0$ (shown in Figure 33) can also be directly compared with the phonon functional predictions. Figure 36 (a) shows the displacement pattern for the M13 breathing mode calculated with the phonon functional method. The mode has a frequency of 5.22 cm^{-1}, slightly different from the continuum elastic theory frequency of 3.29 cm^{-1}. Figure 36 (b) illustrates the compression mode of the M13 capsid calculated with the phonon functional method. A second mode can also be obtained by rotating the displacement pattern about the $\hat{z}$ axis by 45 degrees. The frequency of the two modes are 3.25 cm^{-1} and 3.28 cm^{-1}. Continuum elastic theory predicts a frequency of 1.22 cm^{-1} for both. Finally, Figure 36 (c) shows an axial mode. A second axial mode can be obtained by rotating the displacement pattern about the $\hat{z}$ axis by 90 degrees. The predicted frequencies for these modes are 3.97

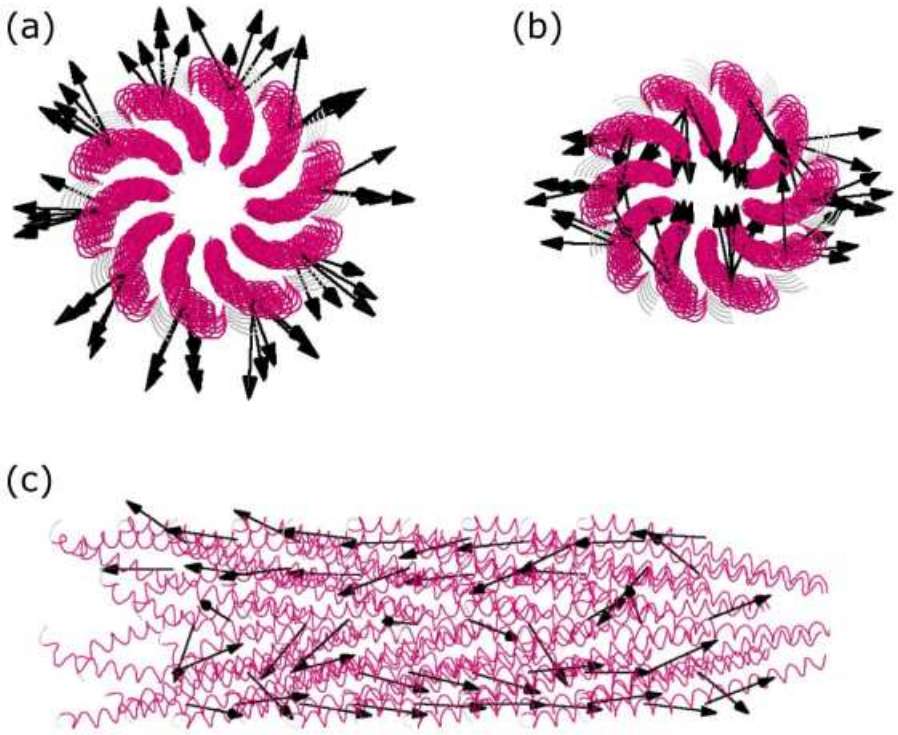

FIG. 36. Displacement patterns for radial and axial modes of the M13 bacteriophage capsid predicted with the phonon functional method. These modes have no $\cos(kz)$ or $\sin(kz)$ dependence and can be compared with continuum model predictions at $k = 0$. The arrows represent the center of mass motion of a single alpha helix building unit and are not relative. (a) Breathing mode at 5.22 cm^{-1}. (b) A compressional mode at 3.25 cm^{-1}. (c) An axial mode at 3.97 cm^{-1}.

cm^{-1} and 3.98 cm^{-1}, compared with the continuum models 1.85 cm^{-1} for both.

Finally, the relative Raman spectra of the M13 capsid in solution is calculated using the *atomistic* bond polarizability model (Chapter 5 Section III). A detector angle of $\Theta = 90°$ was used in the Raman intensity formula. A broadening of 0.75 cm^{-1} was applied to the final intensity predictions. The relative Raman intensity predicted from the atomistic calculation is shown in Figure 37 and was calculated using bond polarizability parameters from Snoke and Cardona as well as parameters from Guha *et al.* (see page 91 for parameters). The atomistic calculation finds a single peak near 5.5 cm^{-1} which is very similar to experimental

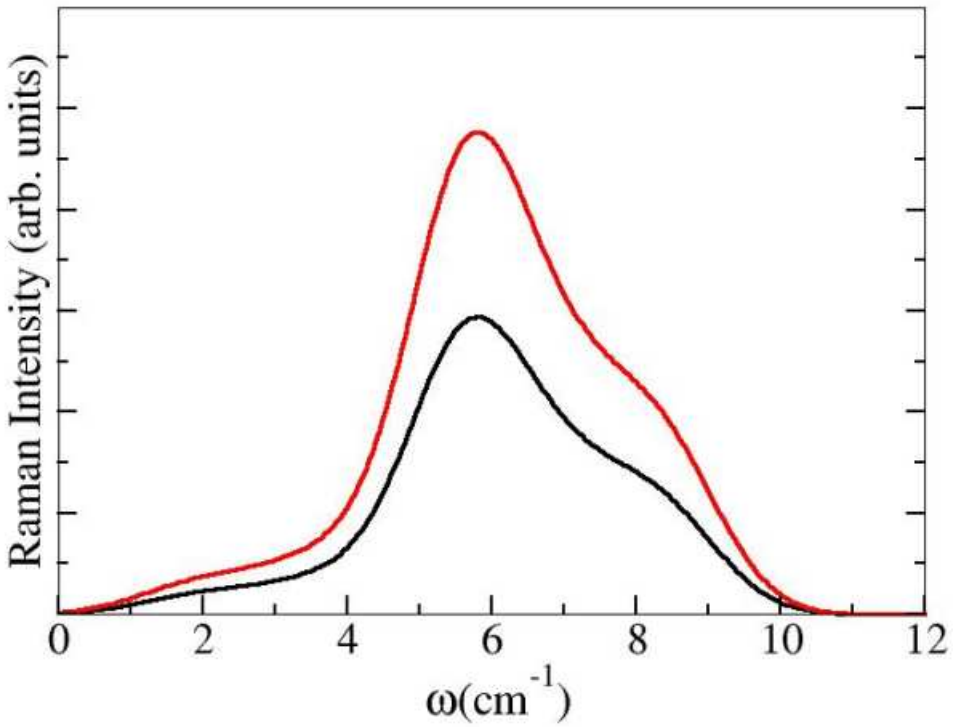

FIG. 37. Relative Raman spectra predictions for the M13 bacteriophage capsid in solution using an atomistic model. The black line corresponds to the Raman spectra for M13 calculated using bond polarizability parameters from Snoke and Cardona [20] while the red line was calculated using parameters from Guha *et al.* [21]. A broadening of 0.75 cm^{-1} was applied to the intensity predictions. A detector angle of $\Theta = 90°$ was used in the Raman intensity formula.

measurements [84, 85]. In addition, the Raman profile calculated using parameters from Snoke and Cardona is very similar to the profile calculated with parameters from Guha *et al.* In the atomistic calculation, the modes that contribute the strongest Raman intensity have radial-torsional dependence. This is in contrast to the arguments made above that suggest that Raman intensities from radial modes are diminished due to dampening by water. Reducing radial mode intensities to zero in the continuum calculation of the Raman intensity may not be justified.

Overall, the first few *lowest* mode patterns and frequencies predicted for the M13 phage by the continuum model compare rather well to those of the fully atomistic phonon functional method. The Raman spectra predictions however highlight important differences between the two methods.

CHAPTER 7

MECHANICAL MODES OF LARGE MOLECULES

I. INTRODUCTION

Many proteins in biological systems exhibit functional motion where the flexible regions of the protein perform certain enzymatic or binding activity. Essentially these flexible areas of the protein can give rise to large scale conformational changes that allow for its function. Understanding the conformational changes involved can provide important insights into how enzymes work from a mechanical perspective. There is evidence that most of the conformational change can be described by a few of the molecules low frequency vibrational modes [2]. Thus, from a theoretical standpoint, a normal mode analysis (NMA) can provide important clues about the functional motions involved in the enzymatic or binding processes of proteins.

There are numerous examples of problems in biology that have been addressed using NMA. Valadie *et al.* have used NMA to explore the large conformational changes involved in the opening of the transmembrane pore MscL in *E. coli* [86]. This protein pore opens and closes in response to changes in tension of the cell membrane (turgor pressure). It has been suggested that this mechanism provides the cell an "emergency valve" that prevents the cell wall from rupturing as the result of high osmotic pressure [87]. Another example pertains to the study of conformational changes in citrate synthase, an enzyme necessary for the citric acid cycle and the production of adenosine triphosphate. Marques and Sanejouand [3] used NMA to determine a first approximation of the conformational changes between the open and closed structures of citrate synthase.

In both of these examples, the NMA was performed using a phenomenological energy model, the Tirion potential [4]. In addition, a coarse graining procedure was also used to decrease the size of the dynamical matrix. The coarse graining procedure amounts to using a

subset of the full $3N$ Cartesian degrees of freedom (*i.e.* a reduced basis set) to construct the displacement patterns. Often the coarse graining can be significant. For example, a common coarse graining procedure for large proteins considers only the motions of C_α carbons [5]. While these studies have provided constructive information about the functional motions of these large systems, a fully atomistic NMA will likely provide a more complete picture of the functional motions of proteins.

In this chapter, the phonon functional method is used to perform a low frequency NMA on a class of molecules and molecular complexes that are used in the transport of substrates across cellular membranes. This class of molecules are called adenosine triphosphate binding cassette (ABC) transporters. At the present time, little is known about the functional motions that are involved in the transport of diverse substrates across the cellular membrane by these complex biological machines. In fact, only very recently have the atomic structures of a few complete ABC transporters been found with X-ray crystallography [88, 89, 90, 91]. With the atomic structures of several ABC transporters now determined, a NMA may provide helpful clues as to how the transport process occurs.

The next section begins with a NMA of four periplasmic binding proteins. These proteins bind to substrates in the periplasm of gram-negative bacteria and deliver them to the ABC transporter for importation into the cytoplasm of the cell. A NMA of these proteins will show similar functional motions that are believed to be responsible for substrate binding. The following section examines a NMA of a *complete* ABC transporter, the molybdate ABC transporter of the thermophilic bacteria *A. fulgidus*. It is hoped that a NMA will provide the first theoretical insights into how a translocation pathway opens in the ABC structure to allow for the transport of nutrients into a cell.

II. PERIPLASMIC BINDING PROTEINS

Periplasmic binding proteins (PBP) are a class of proteins that are located between the inner and outer membranes of gram-negative bacteria. They sense nutrients vital to the cell and bind to them. Once the nutrient (substrate) is bound, the PBP delivers the substrate to an ABC transporter located in the inner membrane. Although the different substrates that PBP can bind to is diverse, their structure is remarkably similar. They consist of two lobes and a handle which forms a connection between the two lobes. The dynamic motions of the two lobes that allow for the substrate to bind are often referred to as the "Venus flytrap" mechanism [92, 93].

The ability of PBP to sense molecules and bind to them has led some to propose using them for biosensing applications [22]. Since PBP undergo large conformational changes when they are bound to their substrate, strategically placed fluorescent compounds on the PBP can allow for the detection of chemical compounds by observing changes in the fluorescence spectroscopy. Theoretically, this would allow for chemical compounds to be detected at extraordinarily small concentration levels. Techniques such as Raman spectroscopy may also be a viable candidate for the detection process. As the substrate binds, the low frequency modes of the PBP will shift to some degree, possibly allowing Raman scattering experiments to distinguish between bound and unbound PBP. Thus, a detailed understanding of the conformational and frequency changes that PBP undergo when bound to their substrate is an important first step in developing novel biosensing tools.

Before a complete ABC transporter is considered, the phonon functional method will first be used to find the low frequency mechanical modes of four periplasmic binding proteins without their corresponding substrate. The four PBP that will be examined are the *E. coli* vitamin B12 binding protein BtuF, the *T. pallidum* Zn^{2+} binding protein TroA, the

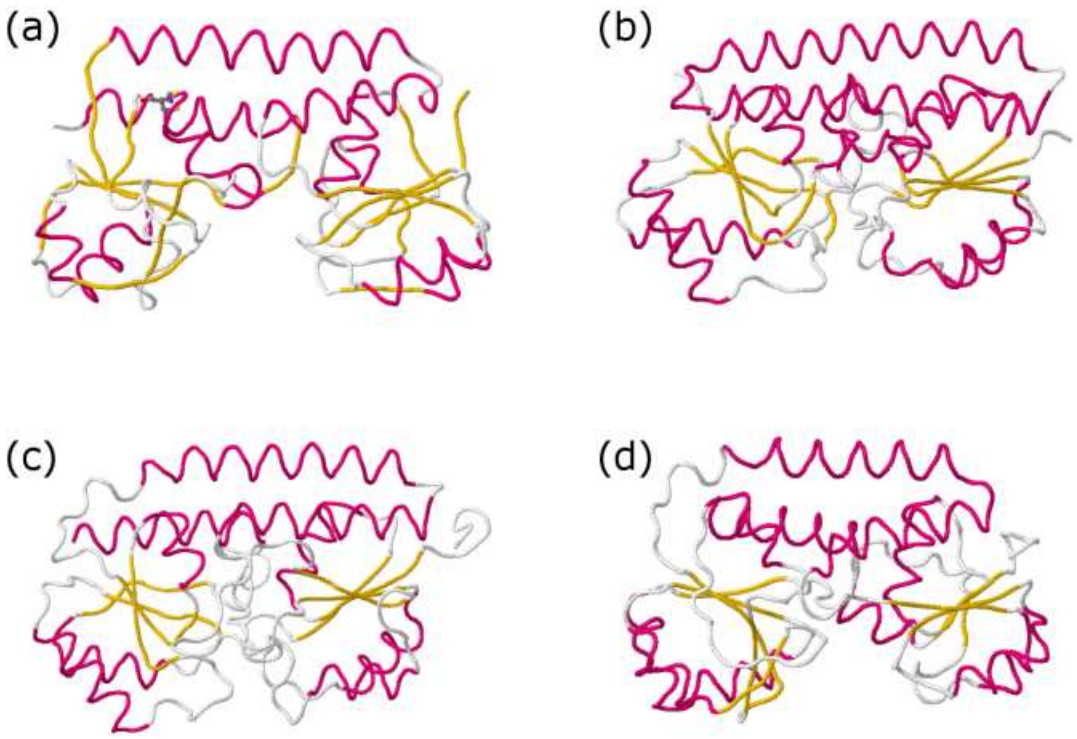

FIG. 38. The structures of the four periplasmic binding proteins BtuF, TroA, PsaA, and FhuD. Each protein is drawn as a backbone trace with yellow representing beta sheet structures, red representing alpha helix structures, and white random coil. (a) Structure of the periplasmic vitamin B12 binding protein BtuF. (b) Structure of the periplasmic Zn^{2+} binding protein TroA. (c) Structure of the periplasmic Mn^{2+} binding protein PsaA. (d) Structure of the periplasmic ferrichrome binding protein FhuD.

S. pneumoniae Mn^{2+} binding protein PsaA, and the *E. coli* ferrichrome binding protein FhuD. Figure 38 (a) - (d) depict all four PBP as a backbone trace and the similarity of their structures can be readily seen. In past work, only the dynamics of the Venus flytrap mechanism of these proteins were studied with molecular dynamics and/or the elastic network model (ENM) [92]. Here, the frequencies will also be estimated as well.

Coordinates for the BtuF vitamin B12 binding protein were obtained from the protein data bank from the larger ABC transporter structure (PDB code 2QI9). The coordinates for the remaining three PBP TroA, PsaA, and FhuD, were also obtained from the

protein data bank (PDB codes 1K0F, 1PSZ, and 1EFD respectively). All structures were determined from X-ray crystallography experiments [88, 94, 95, 96].

All four PBP were energetically minimized without their substrates using the AMBER 94 [9] force field. The interactions with solvent were modeled with the generalized Born implicit solvent model [13, 14, 37]. A 10 Å cutoff was used for all electrostatic interactions. Minimization was stopped when the root mean square (RMS) force was less than 10^{-4} eV/Å. At this RMS force value, only one negative eigenvalue ($\omega^2 < 0$) was found on each of the PsaA and FhuD proteins. An examination of these negative eigenvalues showed that they were highly localized on structures that were physically irrelevant to the Venus flytrap mechanism. For example, the negative eigenvalue on the PsaA protein was located on the floppy random coil loop that extends in front of the protein (see Figure 38 c). No negative eigenvalues were found on the BtuF and TroA periplasmic binding proteins. The final RMS deviation of the optimized coordinates from the original X-ray structure were 1.78, 1.23, 0.98, and 1.53 Å for BtuF, TroA, PsaA, and FhuD respectively.

Using the optimized coordinates, the phonon energy functional [Eq. (4.21)] was minimized for 100 vectors using the conjugate gradient scheme described in Chapter 4 Section V for each PBP. Approximately 4000 conjugate gradient steps were applied to the phonon energy functional in each case. The five lowest frequencies for each PBP are listed in Table IX. The participation numbers W_λ, correspond to the average number of atoms that participate in the mode λ. A global mode will have most atoms in the molecule participating. A mode where all atoms participate in the motion (such as a translation) will have the maximum possible participation number which is equal to the total number of atoms in the molecule. For a detailed discussion of how W_λ is calculated, see Equations (6.1) and (6.2) on page 120.

TABLE IX. The five lowest frequency modes and their corresponding participation number W for the four periplasmic binding proteins BtuF, TroA, PsaA, and FhuD. The number N corresponds to the total number of atoms in each protein, *i.e.* the maximum participation number. The frequencies are given in cm^{-1}.

PBP (N)	ω_1 (W_1)	ω_2 (W_2)	ω_3 (W_3)	ω_4 (W_4)	ω_5 (W_5)
BtuF	2.71	2.99	3.74	5.33	6.06
(3835)	(2748)	(2384)	(2381)	(1205)	(218)
TroA	3.43	3.79	4.26	5.28	5.61
(4274)	(2279)	(2437)	(2561)	(322)	(1815)
PsaA	3.27	4.35	4.97	5.13	6.05
(4541)	(2745)	(2545)	(297)	(2777)	(1823)
FhuD	3.58	3.98	4.80	5.65	5.76
(4004)	(2516)	(2218)	(2189)	(1682)	(1466)

Kandt *et al.* have provided both molecular dynamics simulations and normal mode analysis (NMA) using the ENM for the BtuF periplasmic binding protein [92]. Their NMA results find that the dynamics of the two lobes can be described by the two low frequency modes. Interestingly, the ENM predicted the same two low frequency modes in the other three PBP with nearly identical displacement patterns. One mode consisted of a shearing of the lobes while the other consisted of the Venus flytrap mechanism. The reader should refer to Ref. [92] for diagrams of the two modes.

In order to make a direct comparison of the ENM predictions with those of the phonon functional method, the two mode types predicted by the ENM are identified (as best as possible) in the phonon functional results. Figure 39 (a) - (d) shows the two identified modes for BtuF. Figures 39 (a) and (b) show the lowest frequency mode of BtuF located at 2.71 cm^{-1}. Figure 39 (a) shows the displacements of the backbone atoms of the protein. Long arrows represent large relative displacements of the atom from its equilibrium position while small arrows represent small relative displacements. Figure 39 (b) gives a general idea

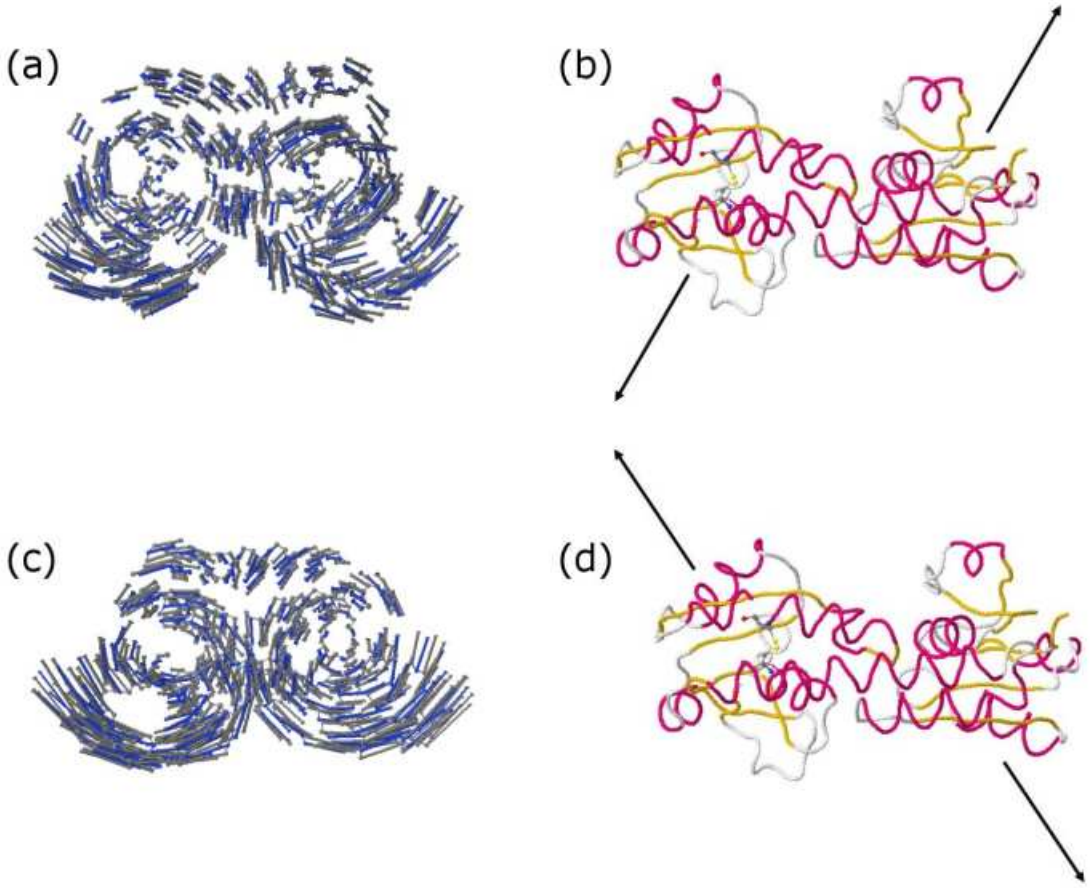

FIG. 39. Two low frequency "cross-shearing" modes of the periplasmic binding protein BtuF found with the phonon functional method as viewed from the front of the protein. (a) Backbone displacements of the low frequency mode at 2.71 cm^{-1}. Large (small) arrows represent a large (small) relative displacement of the backbone atom. (b) Illustration of the lobe displacements for the 2.71 cm^{-1} mode as viewed from the top of the protein. The arrows only indicate the direction that each lobe moves and are not relative. (c) Similar to (a) but for the mode at 2.99 cm^{-1}. (d) Similar to (b) but for the mode at 2.99 cm^{-1}.

of the movement of the two lobes (represented by arrows). Figures 39 (c) and (d) are similar to (a) and (b), but for the second lowest frequency mode at 2.99 cm^{-1}.

The phonon functional results for the periplasmic binding proteins TroA, PsaA, and FhuD are given in Figures 40, 41, and 42 respectively. The TroA PBP has the distinctive shearing [Fig. 40 (a) and (b)] and Venus flytrap mode [Fig. 40 (c) and (d)] that were found with the ENM. Likewise, the PsaA PBP also exhibits these same two mode patterns. It is very interesting to note that the BtuF and FhuD PBP have "cross-shearing modes" which are different from the shearing-flytrap modes of the TroA and PsaA PBP. This could simply be an artifact of the harmonic approximation or the generalized Born model used for the potential energy. However another possible explanation may have to do with the size of the substrate that the PBP must bind. Both the BtuF and FhuD proteins with cross-shearing modes bind rather large molecules (vitamin B12 for BtuF and ferrichrome for FhuD) while both TroA and PsaA with shearing-flytrap modes bind small metal ions. The difference in BtuF and FhuD modes may reflect a need for the binding pocket to open up wide enough to allow these larger molecules to bind. A concerted motion of the two cross-shearing modes may open the binding pocket wider. The molecular dynamics results [92] offered little insight into this question but seemed to show an opening and closing of the lobes that more closely resembled the Venus flytrap mode. The phonon functional results suggest that this is the result of two modes simultaneously opening.

Overall, the low frequency modes predicted by the fully atomistic phonon functional method compare quite well with those from the phenomenological ENM. However, the NMA with the phonon functional method shows some discrepancies with the ENM calculations regarding the exact opening and closing motions of the two lobes. These discrepancies illuminate the importance of reliable predictions for the opening and closing motions since

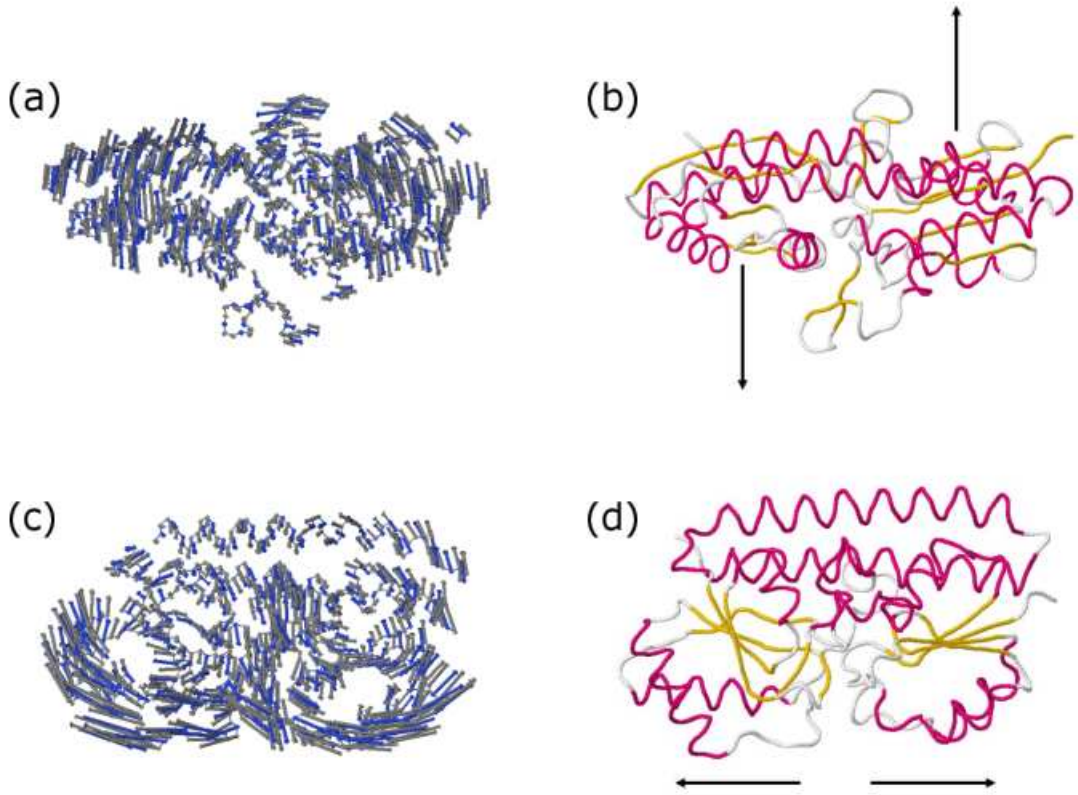

FIG. 40. Two low frequency modes of the periplasmic binding protein TroA found with the phonon functional method. All views are from the top of the protein. (a) Backbone displacements of the low frequency shearing mode at 3.43 cm^{-1}. Large (small) arrows represent a large (small) relative displacement of the backbone atom. (b) Illustration of the lobe displacements for the 3.43 cm^{-1} shearing mode. The arrows only indicate the direction that each lobe moves and are not relative. (c) Similar to (a) but for the Venus flytrap mode at 3.79 cm^{-1}. (d) Similar to (b) but for the Venus flytrap mode at 3.79 cm^{-1}.

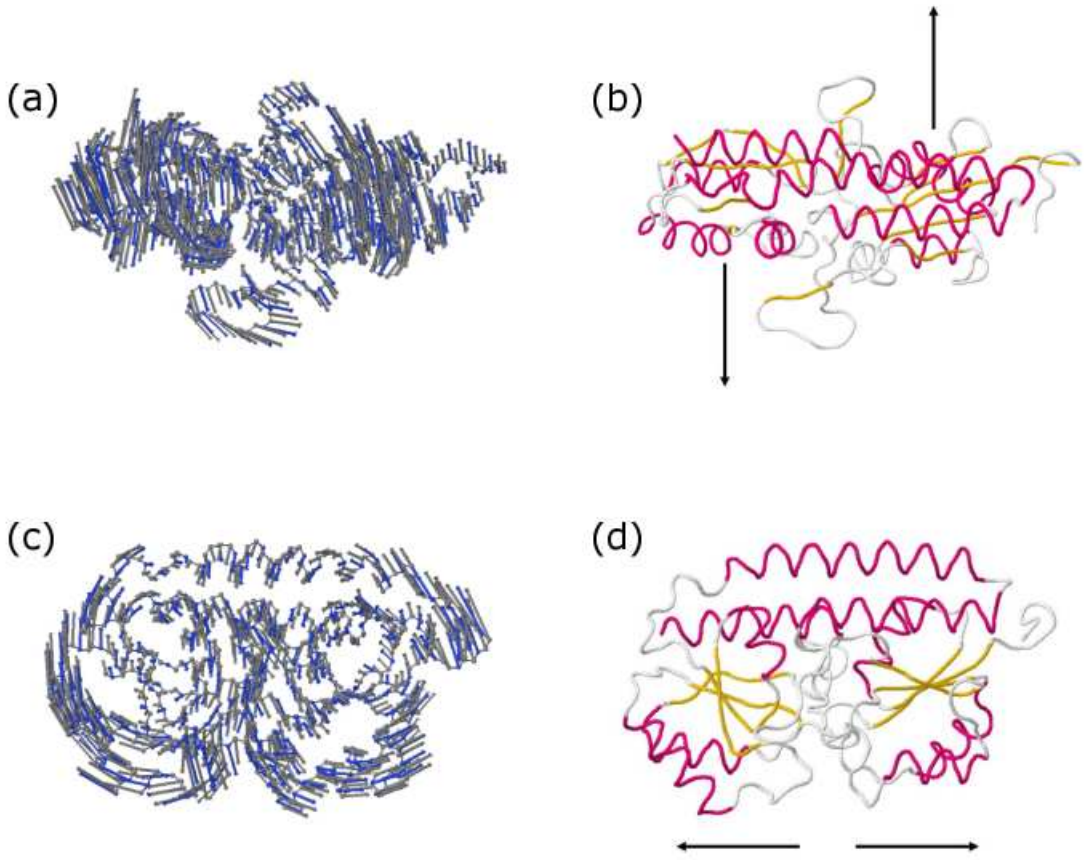

FIG. 41. Two low frequency modes of the periplasmic binding protein PsaA found with the phonon functional method. All views are from the top of the protein. (a) Backbone displacements of the low frequency shearing mode at 4.35 cm^{-1}. Large (small) arrows represent a large (small) relative displacement of the backbone atom. (b) Illustration of the lobe displacements for the 4.35 cm^{-1} shearing mode. The arrows only indicate the direction that each lobe moves and are not relative. (c) Similar to (a) but for the Venus flytrap mode at 5.13 cm^{-1}. (d) Similar to (b) but for the Venus flytrap mode at 5.13 cm^{-1}.

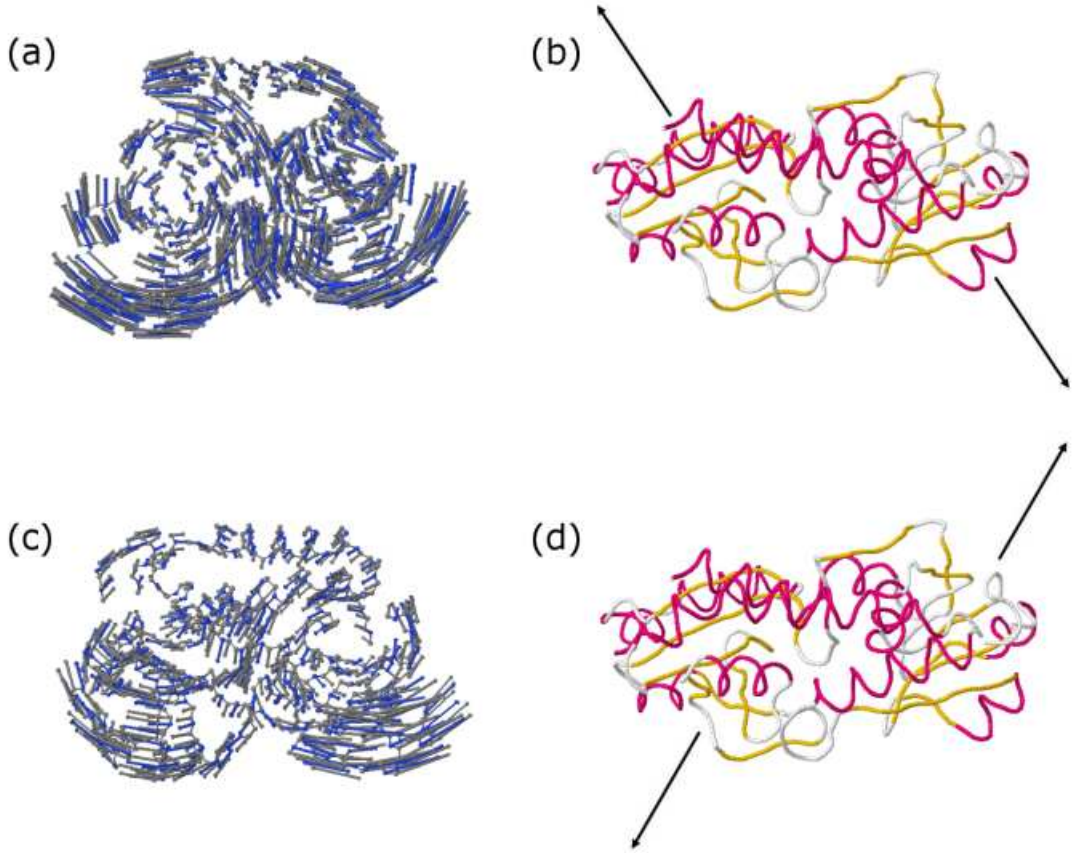

FIG. 42. Two low frequency "cross-shearing" modes of the periplasmic binding protein FhuD found with the phonon functional method. (a) Backbone displacements of the low frequency mode at 3.58 cm^{-1} as viewed from the front of the protein. Large (small) arrows represent a large (small) relative displacement of the backbone atom. (b) Illustration of the lobe displacements for the 3.58 cm^{-1} mode as viewed from the top of the protein. The arrows only indicate the direction that the lobe moves and are not relative. (c) Similar to (a) but for the mode at 3.98 cm^{-1}. (d) Similar to (b) but for the mode at 3.98 cm^{-1}.

these motions will ultimately determine the placement of fluorescent chemicals on the lobes for biosensing applications. With further NMA studies of the PBP bound with their substrates, the feasibility of using other techniques, such as Raman spectroscopy, to detect bound and unbound PBP can also be examined.

III. MOLYBDATE ABC TRANSPORTER

In the previous section, the low frequency vibrational modes of four periplasmic binding proteins (PBP) were studied using the phonon functional method. The PBP are a single part of a much larger complex which includes the adenosine triphosphate binding cassette (ABC) transporter. This molecular complex is involved in the transport of substrates (*e.g.* nutrients) across the cellular membrane. There are two main types of ABC transporters, importers and exporters. The PBP discussed in Section II are specific to gram-negative bacteria ABC importers. The PBP binds to nutrients present in the periplasm and delivers them to an appropriate ABC transporter complex, which embedded in the inner cellular membrane, then transports the nutrient into the inner cytoplasm by hydrolyzing adenosine triphosphate (ATP).

The ABC transporter consists of two transmembrane domains (TMD) and two nucleotide binding domains (NBD). The TMD is composed of 10 or more transmembrane helices which form a translocation pathway (pore) in the inner cellular membrane that allows substrates to pass through. Most ABC importers have a gating region that effectively blocks access to the translocation pathway until the substrate is ready to be imported into the cytoplasm. The NBD is present in the cytoplasm and is responsible for the binding and hydrolysis of ATP that provides the "power stroke" necessary for the transport of the substrate. A diagram of the *E. coli* vitamin B12 transporter with the three domains is shown in Figure 43. The lines in the drawing indicate the approximate edges of the lipid

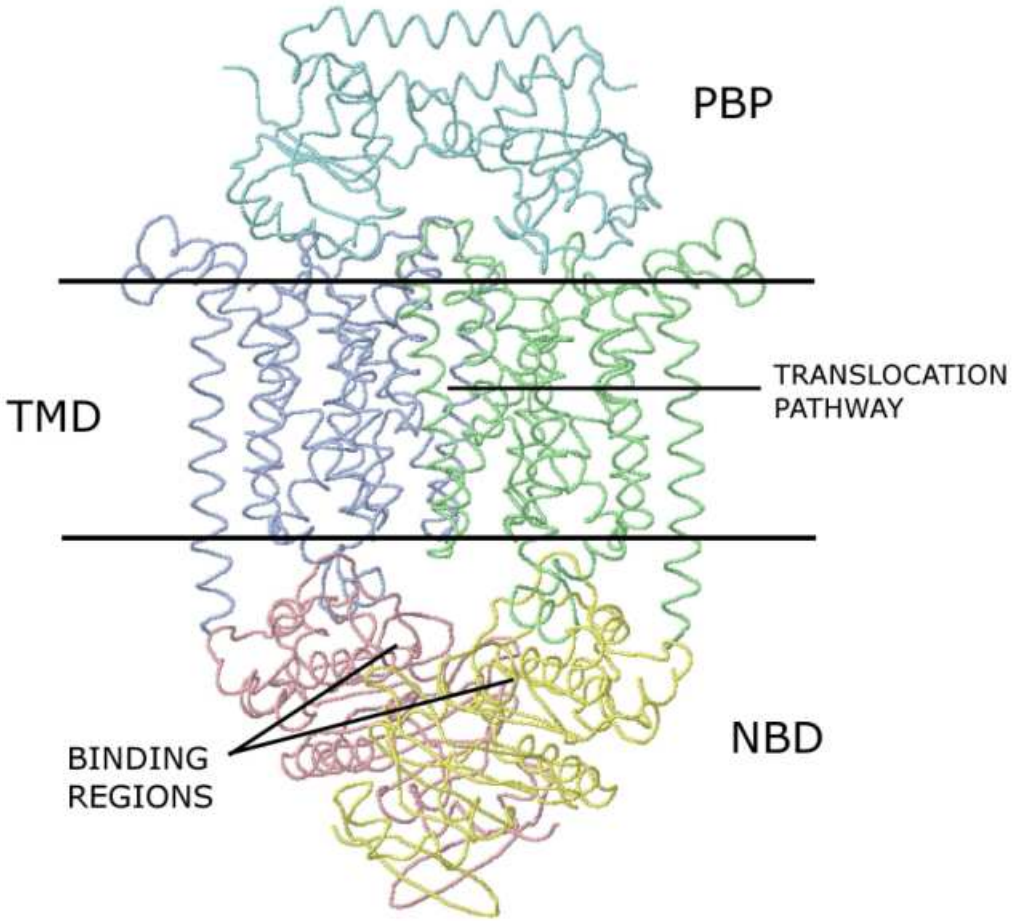

FIG. 43. Diagram of the *E. coli* vitamin B12 ABC transporter. The approximate location of the lipid bilayer slab is indicated by the two solid lines. The TMD consists of 10 or more alpha helices that penetrate the lipid bilayer to form a translocation pathway. The access to the translocation pathway is typically blocked on either the periplasm of cytoplasm side of the lipid bilayer by a gating region. Binding and/or hydrolysis of ATP by the NBD initiates the opening of the gating region allowing the PBP to release its substrate cargo.

bilayer slab. The two proteins that make up the TMD and NBD are colored differently for clarity. Exactly how the ATP powers the transport of substrates remains an area of research and controversy. Some have suggested [97, 98] that the hydrolysis of ATP provides the principal energy to import/export substrates while others [99, 100] have suggested that ATP binding alone facilitates the transport process. In summary, the ABC transporter allows for the selective transport of substrates through a translocation pathway formed in the inner cellular membrane by the two TMD by either binding and/or hydrolysis of ATP.

A wide variety of ABC transporters have been identified in nearly all organisms and understanding their mechanics can help in drug design. For example, a class of ABC exporters have been shown to have a role in the multi-drug resistance of cancer cells [101, 102]. In chemotherapy treatment of cancer, drugs are used to produce toxic conditions in cancer cells. One way that cancer cells can adapt is by over expressing ABC exporters that are capable of removing a variety of chemicals that are toxic to the cell [102]. Understanding how ABC exporters function chemically and mechanically can help identify methods that may make chemotherapy treatments more effective.

Another example of the clinical relevance of ABC transporters is cystic fibrosis. In cystic fibrosis, mutations in the cystic fibrosis transmembrane conductance regulator (CFTR) gene [103] results in an unstable transmembrane protein that typically degrades before reaching the cellular membrane [24]. The transmembrane protein made by the CFTR gene regulates the flow of chloride ions into and out of the apical membrane in epithelial cells, effecting fluid and electrolyte secretions in the intestine, pancreas, and sweat glands. The CFTR protein represents an example of an ion channel that is regulated by ATP hydrolysis [23], and is classified as an ABC transporter.

Many important questions about ABC transporters center around the transport process. What does the translocation pathway look like? What conformational changes are required to import (or export) substrates across the cell membrane? How do the various domains interact with each other during the transport process? The experimental front is pursuing some of these questions by crystallizing various ABC transporters at different stages of the transport process. This process has led to some clues about the conformational changes involved in the transport process which have been described by Locher *et al.* for the *E. coli* ABC vitamin B12 importer [88, 89]. However, the experimental evidence as yet to elucidate the specific coupling interactions between the three domains or detailed descriptions of the conformational changes that occur during transport.

Theoretical modeling of the ABC transport process has been somewhat limited and have involved, at most, the NBD and TMD [104, 105]. A lack of theoretical studies is likely due to the fact that most of the atomic structures of ABC transporters have only just recently been determined. Based on experimental evidence, the ABC transport process is believed to involve large conformational changes of the NBD and TMD domains. In addition, these domains are believed to "communicate" with each other through conformational changes that result from binding. For example, Davidson *et al.* have shown that the binding of the PBP to the TMD increases ATP-ase activity [98], suggesting a signaling mechanism between PBP, TMD and NBD domains.

In the past, large conformational changes of molecules and molecular structures have been successfully determined by normal mode analysis (NMA) and tend to compare well with experimental studies [2]. The phonon functional method presents an opportunity to model the low frequency mechanical modes of a *complete* ABC transporter complex consisting of TMD, NBD, and PBP domains with atomic detail. This is an advantage for

the study of the transport process in ABC transporters since the individual motions of the atoms involved in the gating region are likely to be critical in determining how the gating region opens.

The ABC transporter chosen for a NMA with the phonon functional method is the molybdate ABC importer from the thermophilic bacteria *A. fulgidus*. The structure of the ABC complex was determined by X-ray crystallography [91] in March of 2007 and is believed to represent a nucleotide free state before translocation of the substrate (in this case molybdate) has occurred. A diagram of the molybdate ABC transporter is shown in Figure 44. The full structure consisting of all three domains is illustrated in Figure 44 (a). The two proteins that make up each NBD and TMD dimer are colored differently for clarity. The lines indicate the approximate location of the lipid bilayer. The C-terminal "hinge" of the NBD are also labeled. Figure 44 (b) shows the TMD looking down from the periplasm side of the transporter. The two Phe 200 residues (one from each of the transmembrane proteins) are drawn in van der Waals representation. The two phenyl rings are within their van der Waals distance and act as gate, shielding the periplasmic side of the membrane from access to the translocation pathway. Figure 44 (c) illustrates the ATP binding pocket in detail. Half of the ATP binding pocket is formed from the Walker loop (colored red) and the other half is formed from the LSGGQ motif (colored blue). Each half of the two binding pockets come from one of the proteins that makes up the NBD dimer.

Coordinates for the molybdate ABC transformer were obtained from the protein data bank (PDB code 2ONK). The X-ray structure contained two TMD, two NBD, and one PBP with bound tungstate. Tungstate was used instead of molybdate in the crystallization [91] and was removed to simplify the analysis. This should not appreciably affect the normal modes or the frequencies. The final ABC transporter complex without

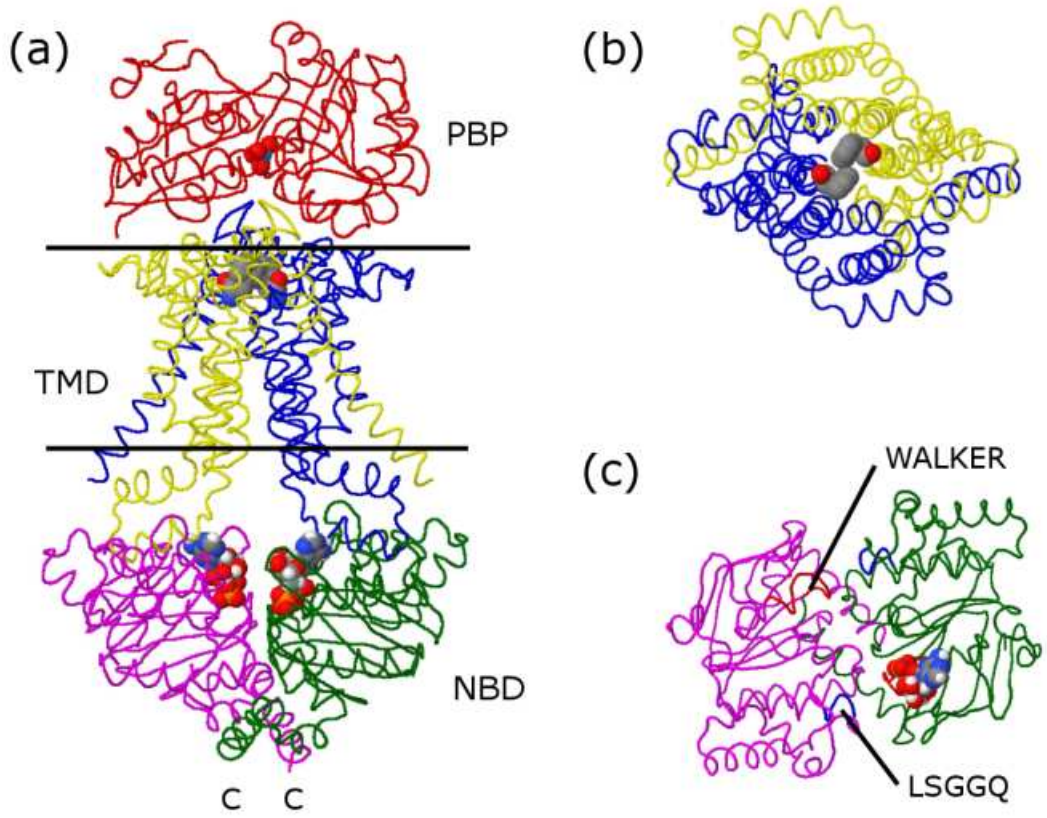

FIG. 44. Structure of the *A. fulgidus* molybdate ABC transporter. (a) The full ABC transporter complex consisting of PBP, TMD, and NBD. Each protein is colored differently for clarity. The approximate location of the lipid bilayer is indicated by the two solid lines. The residues involved in the gating region and ATP molecules are drawn in van der Waals representation. The C labels on the NBD indicate the C-terminal ends of the two proteins. (b) View of the TMD looking down from periplasmic side of the membrane. The two phenyl rings, Phe 200, involved in the gating region are drawn in van der Waals representation. (c) Detailed structure of a single ATP binding pocket. The binding pocket is formed from the Walker loop (colored red) of one the NBD proteins and the LSGGQ motif (colored blue) of the other NBD protein.

TABLE X. The ten lowest frequency modes and their corresponding participation number W for the *A. fulgidus* molybdate ABC transporter. Full participation is 20667. The frequencies are given in cm^{-1}.

ω	W	ω	W
0.73	15008	2.07	14286
0.94	14371	2.29	13749
1.15	15724	2.39	14062
1.77	14391	2.62	11676
1.86	9954	3.07	12314

the tungstate consisted of the two TMD and two NBD along with the PBP for a total of 20667 atoms. The complex was then energetically minimized using the AMBER 94 force field [9]. Interactions of the transporter complex with water were taken into account using the generalized Born implicit solvent model [13, 14, 37]. Since the generalized Born model uses a dielectric screening methodology, a 10 Å cutoff was used for both van der Waals and coulomb interactions. The minimization procedure was stopped once the root mean square (RMS) force was less than 10^{-4} eV/Å. Since the RMS force was not exactly zero to machine precision, negative eigenvalues of the dynamical matrix can occur. However, none were found from the resulting NMA with the optimized coordinates. The final RMS deviation of the optimized structure from the original X-ray structure was 1.75 Å.

Using the optimized coordinates, the lowest 100 phonon states of the ABC transporter were found by minimizing the phonon energy functional [Eq. (4.21)] using the conjugate gradient scheme described in Chapter 4 Section V. Table X lists the ten lowest frequency modes and corresponding participation numbers for the ABC transporter. A mode with full participation, such as a translation, will have a participation value of 20667.

The first three lowest modes describe a rotation (about different axes) of the NBD with respect to both the TMD and the PBP. This indicates a strong coupling of the three

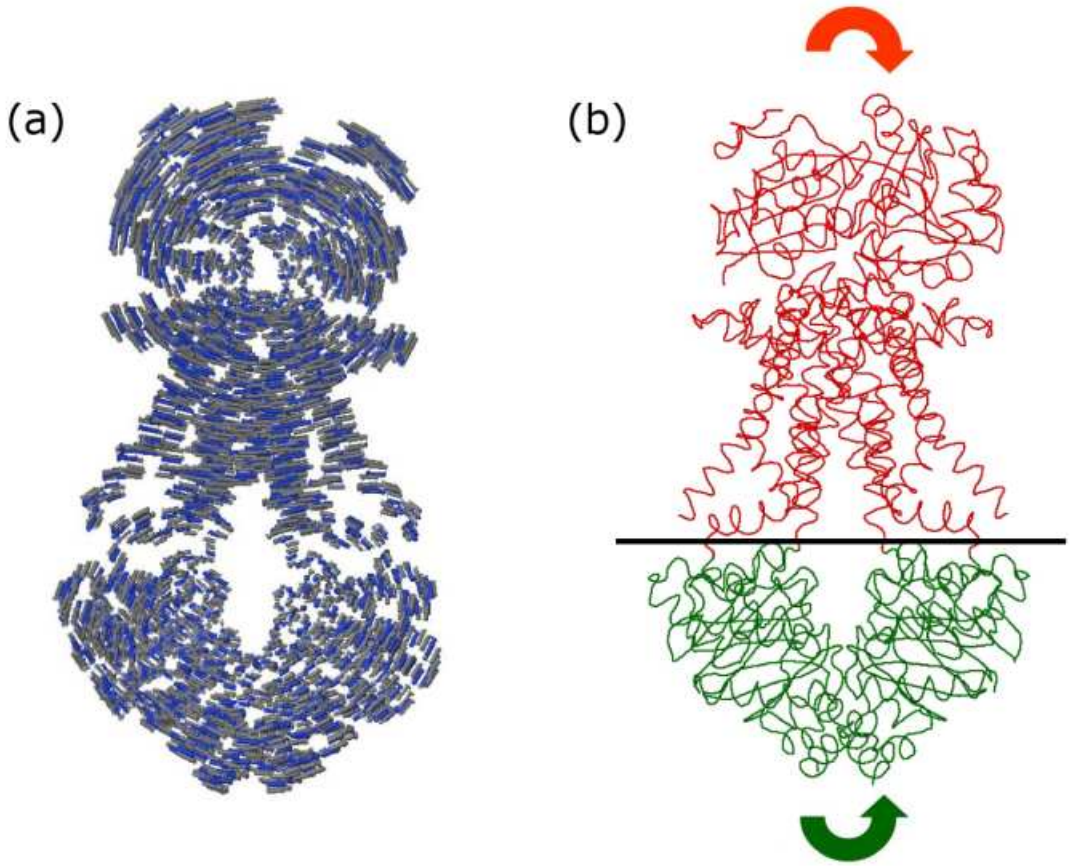

FIG. 45. Low frequency NBD rotational mode of the *A. fulgidus* molybdate ABC transporter. The frequency of the mode is 1.15 cm^{-1}. (a) Backbone displacements of the low frequency mode. Large (small) arrows represent a large (small) relative displacement of the backbone atom. (b) Illustrations of the displacements of the NBD, TMD, and PBP domains. Atoms above the line are rotating clockwise while those below the line are rotating counterclockwise.

domains. Figure 45 illustrates one of these rotational modes, the third lowest, at 1.15 cm^{-1}. Figure 45 (a) shows the relative displacements of the protein backbone atoms while (b) illustrates the basic motion with arrows.

Chen *et al.* [97] have shown in a recent experiment that the dynamic motion of the NBD involves a tweezers like motion with the NBD pivoting about the C-terminal ends of the peptides. This motion is believed to be related to the transport process since it closes the LSGGQ motif onto the Walker loop which begins the catalytic hydrolysis of ATP. Theoretically, the NBD couples this motion to the TMD to open the translocation pathway. Thus, the low frequency modes from the NMA which have the NBD moving in this fashion should hopefully describe the conformational changes of the ABC transporter that are involved in the translocation processes.

Out of the 100 low frequency phonon states found, the phonon functional method found two low frequency modes of the ABC transporter (at 1.77 cm^{-1} and 2.62 cm^{-1}) that have the NBD expanding apart in the tweezers like motion. Examination of the two modes revealed highly concerted motions of all three domains. Figure 46 shows a diagram of the displacement pattern for the 1.77 cm^{-1} mode. The NBD couples its motion to the TMD via the two alpha helix "handle bars" (colored red in the TMD region in Figure 46). As a result, the PBP is forced directly into the TMD. However, the displacements that resulted from this mode failed to move the two phenyl rings apart, leaving the pore closed.

The last tweezers like mode at 2.62 cm^{-1} can be described as a rotation of the TMD/PBP interface about the vertical axis. This motion couples to the PBP to produce a rotation of the left lobe (shown in purple) about an axis slightly out of plane. Similarly the right lobe of the PBP (colored red) rotates about the same axis but in the opposite direction. This motion is similar, but not identical, to the shearing modes which were

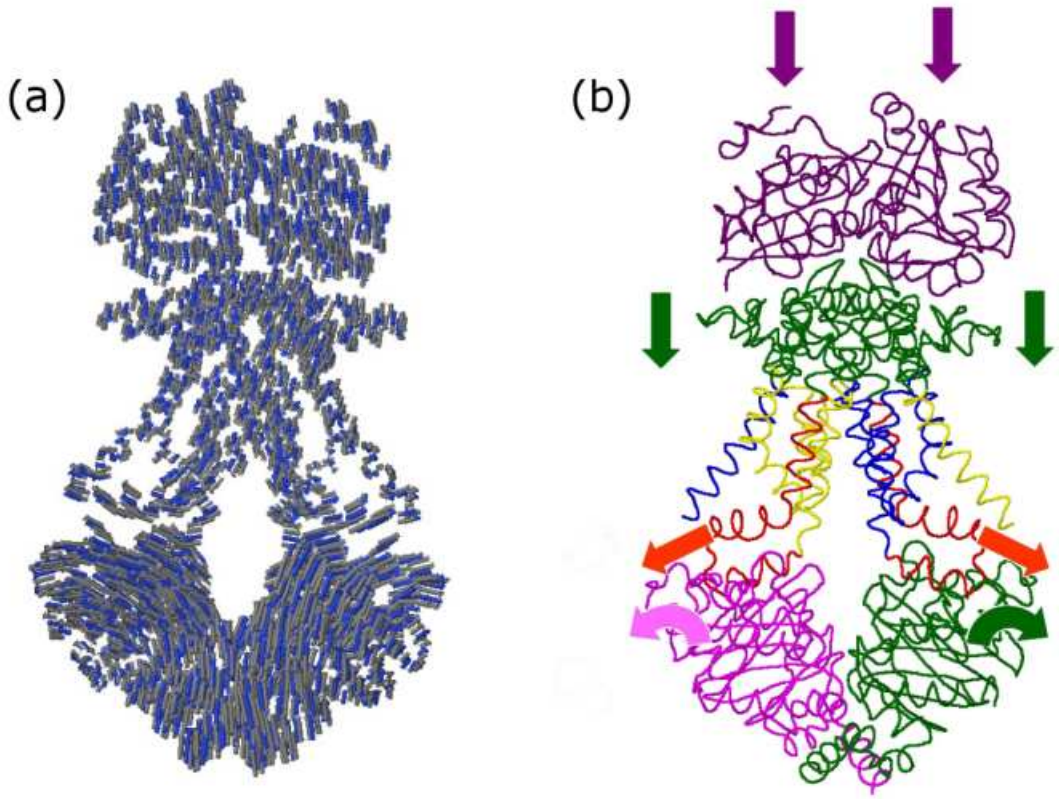

FIG. 46. The first low frequency mode of the *A. fulgidus* molybdate ABC transporter that exhibits a tweezers like motion in the NBD. The frequency of the mode is 1.77 cm^{-1}. (a) Backbone displacements of the low frequency mode. Large (small) arrows represent a large (small) relative displacement of the backbone atom. (b) Illustrations of the displacements of the NBD, TMD, and PBP domains. The PBP is colored purple while the TMD/PBP interface is colored green. The "handle bar" region of the TMD is colored red. Arrows indicate the general motion of each domain and are not relative.

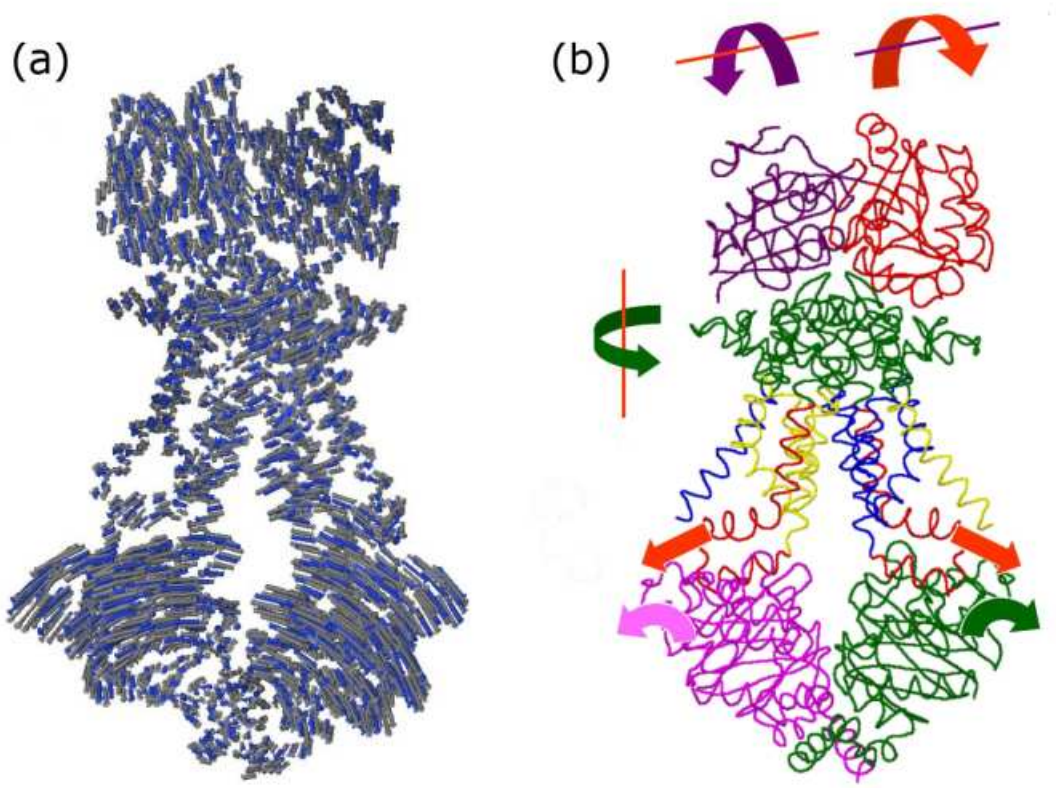

FIG. 47. The second low frequency mode of the *A. fulgidus* molybdate ABC transporter that exhibits a tweezers like motion in the NBD. The frequency of the mode is 2.62 cm^{-1}. (a) Backbone displacements of the low frequency mode. Large (small) arrows represent a large (small) relative displacement of the backbone atom. (b) Illustrations of the displacements of the NBD, TMD, and PBP domains. The two lobes of the PBP are colored red and purple and the TMD/PBP interface is colored green. The "handle bar" region of the TMD is colored red. The arrows indicate the general motion of each colored region and are not relative. Based on the relative displacements from (a) the C-terminal region of the NBD is predicted to be rigid.

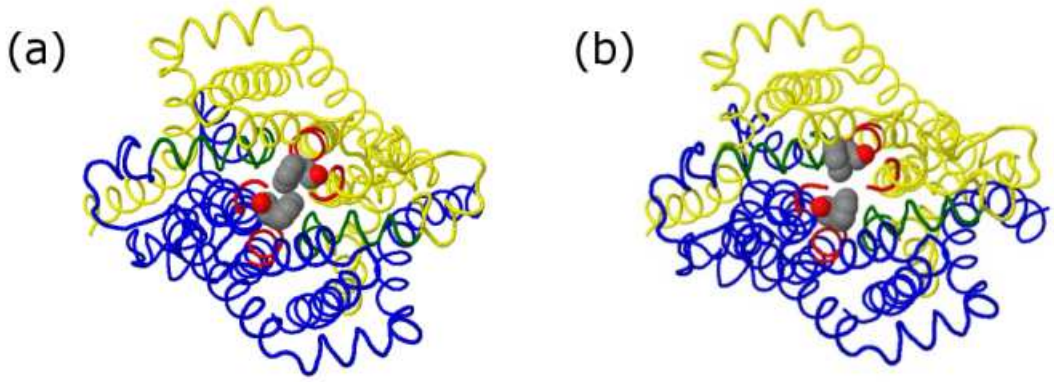

FIG. 48. Opening of the gating region of the *A. fulgidus* molybdate ABC transporter via displacements of the 2.62 cm^{-1} low frequency mode. The two TMD proteins are colored blue and yellow. The gating region is colored red. The two Phe 200 residues in the gating region are drawn in van der Waals representation. (a) The ABC transporter in its equilibrium position with gating region closed. (b) The ABC transporter after atoms in the structure are displaced along the 2.62 cm^{-1} mode. The displacement amplitude was chosen to illustrate the opening clearly.

described in Section II for the TroA and PsaA PBP. An illustration of the shearing motion can be found in Figure 40 (c) and (d). Figure 47 diagrams the 2.62 cm^{-1} mode in detail.

Examination of the 2.62 cm^{-1} found a clear opening of the gating region that results from a displacement of the atoms in the ABC structure along the 2.62 cm^{-1} mode pattern. Figure 48 illustrates the opening of the gating region as viewed looking down onto the top of the TMD. Only the TMD proteins are drawn in the figure for clarity. Figure 48 (a) shows the TMD in its equilibrium position. Figure 48 (b) was constructed by moving the atoms in the ABC structure along the displacement vector corresponding to the 2.62 cm^{-1} mode. The amplitude used to construct Figure 48 (b) was chosen so as to clearly illustrate the opening of the gating region.

Based on the two (1.77 cm^{-1} and 2.62 cm^{-1}) tweezers like modes found with the phonon functional method, a transport process can be hypothesized. The tweezers like motion of the 2.62 cm^{-1} shows that the two Phe 200 residues are pushed apart as the

NBD opens. This suggests that ATP hydrolysis provides the energy input and its energy is directed to the tweezers like motion through the dissociation of ADP. Smith *et al.* [106] have suggested just this type of reaction process. They suggest that after ATP hydrolysis, the phosphate group may remain bound to the LSGGQ half of the ATP binding pocket while the ADP molecule is bound the other half, the Walker loop. After hydrolysis, the electrostatic repulsion of the negatively charged phosphate and ADP molecules would then force the NBD apart in the tweezers like motion. Interestingly, this reaction hypothesis may explain why the ATP binding pocket is formed from two NBD with the Walker loop coming from one NBD while the LSGGQ motif coming from the other NBD. This formation of the binding pocket allows the NBD to function as a hinge that is driven apart by electrostatic repulsion of the hydrolysis products.

Although the low frequency 1.77 cm^{-1} tweezers like motion was unable to open the gating region, it may still be important for the transport process. Experimental data from Davidson *et al.* [98] suggested that the binding of PBP to the TMD is important for the NBD to begin the hydrolysis cycle. In this light, the 1.77 cm^{-1} tweezers like motion may serve a purpose in the transport cycle after all. Binding of the PBP to the TMD is likely to push and pull on the TMD. These motions are similar to the 1.77 cm^{-1} tweezers like motion. Thus, the binding of the PBP to the TMD may transmit a signal to the NBD via the 1.77 cm^{-1} mode. Stimulation of this mode will cause the NBD to rock back and forth, eventually closing the NBD. Once the NBD is closed, the hydrolysis of ATP takes place and forces the NBD apart again, this time stimulating the 2.66 cm^{-1} mode. A detailed cartoon of the transport process is illustrated in Figure 49.

In conclusion, the results of the NMA of the complete molybdate ABC transporter of *A. fulgidus* with the phonon functional method has successfully revealed two low frequency

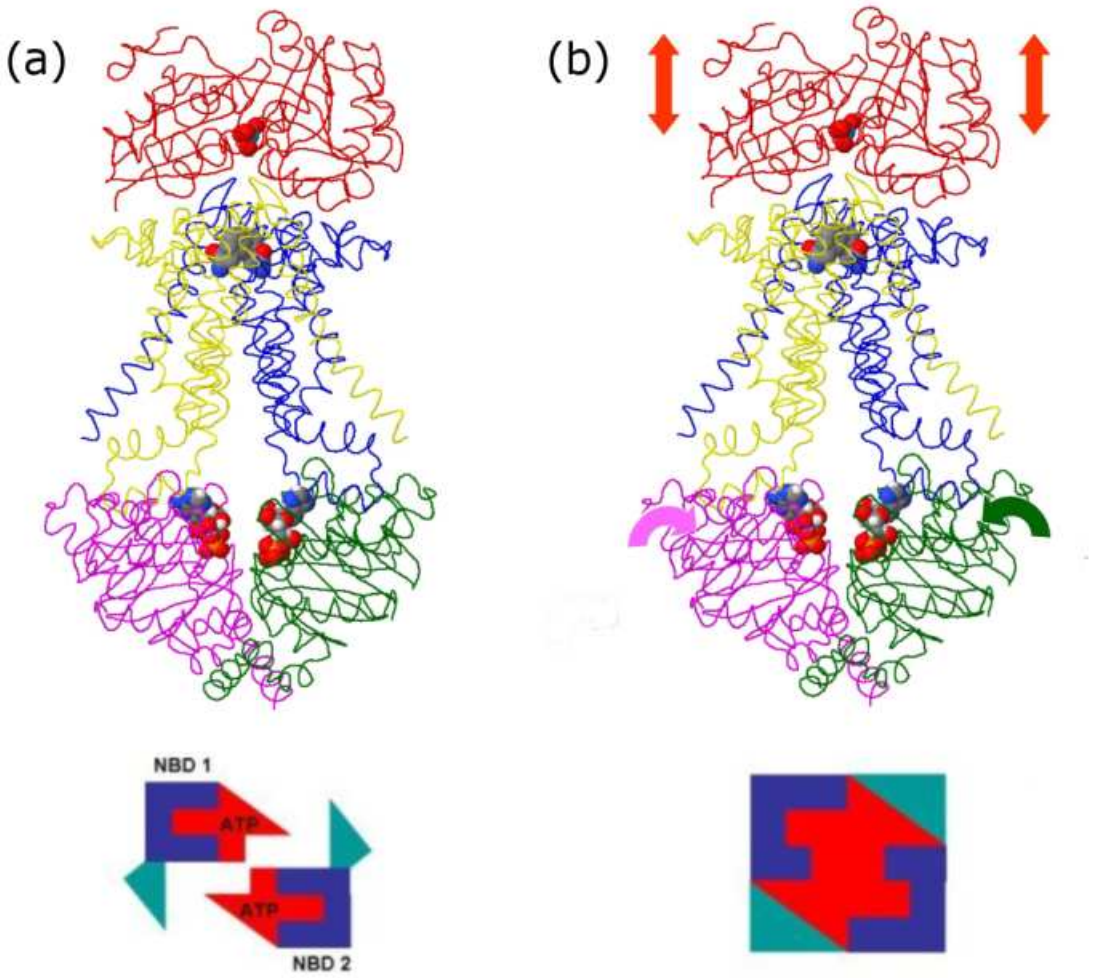

FIG. 49. Hypothetical model of the *A. fulgidus* molybdate ABC transporter reaction cycle. The model is based on a pair of low frequency modes found with the phonon functional method. The molybdate, ATP, ADP, and phosphate molecules along with the two Phe 200 residues involved in the gating region are shown in van der Waals representation. A cartoon describing the ATP hydrolysis cycle is also shown. (a) The PBP binding to the TMD while two ATP molecules bind to the two NBD proteins. (b) The PBP pushes and pulls vertically on the TMD during docking. This stimulates the 1.77 cm^{-1} mode and encourages closing of the NBD. (c) One or both of the ATP molecules are hydrolyzed releasing energy. The phosphate and ADP molecules repel forcing the NBD apart in the tweezers like motion. This motion couples to the TMD and PBP via the 2.62 cm^{-1} mode to open the gating region. (d) The molybdate molecule has passed through the translocation pathway and the TMD returns to equilibrium closing the gating region.

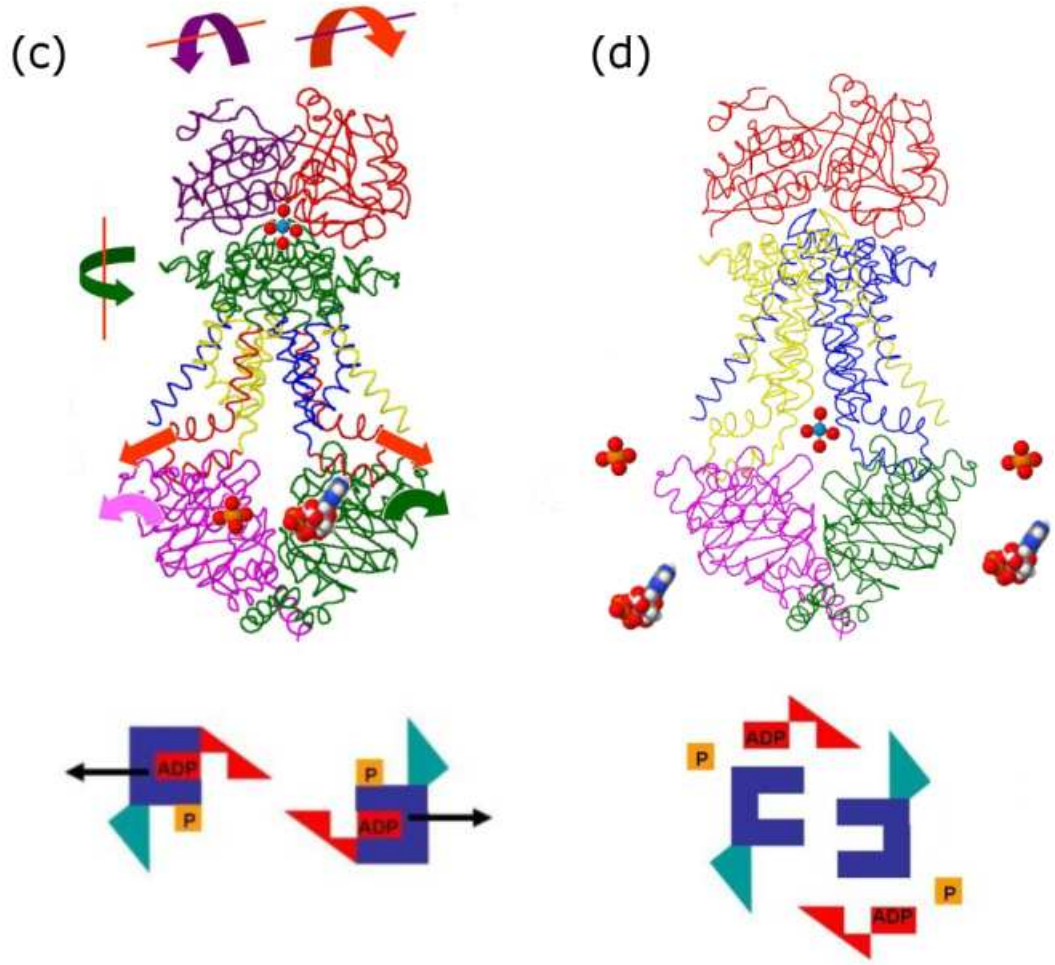

FIG. 49 (continued).

modes that may be responsible for the conformational changes of the TMD required for the transport of substrate into the cytoplasm. The resulting reaction cycle hypothesis based on the two low frequency modes, illustrated in Figure 49, fits well with other experimental evidence [97, 98]. Further normal mode analysis with other crystallized ABC transporters as well as other theoretical modeling, such as molecular dynamics, will provide more information about the ABC transport process. The clues exposed here better define the mechanisms at work in this enormously important protein complex.

CHAPTER 8

MISCELLANEOUS APPLICATIONS

I. INTRODUCTION

In this chapter, two theoretical studies are examined. In Section II, a classical molecular dynamics simulation of the M13 bacteriophage capsid is studied. The purpose of the simulation is to theoretically model and compare to a recent experiment performed by K.-T. Tsen *et al.* [25] where impulsive stimulated Raman scattering (ISRS) [69] with near infrared and visible light was used to inactivate M13 phages. The motivations and implications of using ISRS as a means to inactivate viruses and other pathogens is discussed followed by a presentation of the molecular dynamics simulation results.

Section III looks at generalizing the activation relaxation technique (ART) [28, 29] to a fully atomistic energy model capable of incorporating explicit solvent. The ART method was briefly discussed in Chapter 2 Section VI as a method for locating the many stable local minima of a molecule or molecular structure. In past ART studies, simplified structures such as the peptide bead structure of the OPEP energy model [107] were used to study the protein folding problem [48, 108], or the aggregation of Aβ segments [47] believed by some to be a key factor in Alzheimer's disease [109]. In addition to a simplified peptide structure, the OPEP energy model uses an implicit solvent model for the incorporation of solvent effects.

One unanswered question in the protein folding problem is how denaturants seem to force a peptide from existing in a single native state in water, to existing in an ensemble of many disordered states [108]. This property of proteins was originally discovered by Anfinsen's Nobel prize winning work were ribonuclease was reversibly denatured/renatured in a test tube [110]. A similar unanswered question also exists for Aβ proteins. What physiological conditions contribute to Aβ aggregation that cause the plaques seen in brain

biopsies of Alzheimer's patients? The ART method presents a possible theoretical tool to answer these questions. This is because the ART method is capable of locating other minima in the energy landscape of a protein, outside of its native state [48], or predicting the possible assembly pathways of aggregates [47]. However, the use of explicit solvent models are crucial to properly study the effects that different solvents or chemicals may have on the energy landscape of a protein or molecule.

Section III begins by first examining how the ART method can be extended to a fully atomistic molecular structure. A test of the ART method using an atomistic molecular structure with the AMBER empirical energy model is performed on the small peptide alanine dipetide. Alanine dipeptide is a very well studied molecule [111, 112] and exists in several stable structures in water solution; all with different energies. The test is performed first for only a fully atomistic structure, *i.e.* the energy model used has either no water (vacuum simulation) or an implicit solvent (generalized Born model [13]). Next, the ART algorithm is extended to the case of explicit water. This extension of ART from the original version of Mousseau *et al.* [28, 29] is called the Wet-ART method. The Wet-ART method is then tested on the alanine dipeptide molecule with explicit water solvent surrounding it. Finally, the potential problems of using atomistic molecular structures and/or explicit solvent in the ART method are discussed.

II. IMPULSIVE STIMULATED RAMAN SCATTERING SIMULATION

Recently it has been suggested that viruses could be damaged or even destroyed through an ultrasound or hyper sound excitation of their vibrational modes [8]; much like a wine glass shatters when subjected to intense high frequency sound. Since the resonant frequencies of a virus are dependent on its shape and composition, an ultrasound or hyper

sound excitation of specific frequency would, theoretically, only affect the targeted virus, leaving surrounding structures such as tissue undamaged.

The traditional treatment of infectious diseases such as viruses and bacteria has relied on the use of chemicals (drugs/vaccines) to interfere with the biological processes of the pathogen. For example, the treatment of the Human Immunodeficiency Virus (HIV) involves the use of chemicals that target and bind to one of the virus' nine proteins that are made in an infected cell. As these chemicals bind to the various proteins, they prevent them from performing their enzymatic activity, halting its reproduction cycle. The problem with drug treatments is two fold. First, drug treatments often produce dangerous side effects in the patient. Second, these chemicals create evolutionary pressure that results in mutations to the proteins such that the drugs can no longer bind to them. For example, in the treatment of HIV a patient typically is prescribed a combination of drugs (drug cocktail) that block many HIV enzymes necessary for replication such as reverse transcriptase, protease, and integrase. When the virus mutates and the drugs are no longer effective, patients must switch to a different drug regimen that may be less effective and/or produce unwanted side effects.

Using mechanical means to treat infectious disease has many positive aspects when compared to traditional drug treatments, making it a tantalizing idea. Since the vibrational modes of viral capsids are virus specific, the method is theoretically selective and can be used to target only virus particles while leaving important cellular structures and cellular biochemical processes undamaged. But more importantly, mutations of the virus are unlikely to appreciably effect the vibrational frequencies of the capsid. Thus, unlike drug therapies that will eventually become ineffective as the virus mutates, mechanical destruction of the virus could persist.

Several experiments on the subject were very recently performed by K.-T. Tsen and colleagues [25, 26, 27] using visible and near-infrared light from a pulsed laser source (Impulsive stimulated Raman scattering [69]) as a method of resonantly exciting the vibrational modes of pathogens. The results of the experiments were encouraging showing that various pathogens (such as the M13 bacteriophage) could in fact be destroyed using the low power pulsed laser. However, it still remains to be seen if the inactivation of the pathogens are a direct result from resonant excitation of their vibrational modes or if there are other physical phenomena that are involved. Still, the possibility of virus destruction using a mechanical means as opposed to standard drug therapies warrants further investigation in light of recent experimental evidence.

Performing a theoretical simulation of ISRS induced vibrations may help to elucidate the sensitive areas of the capsid that are prone to disruption and provide important insights into capsid assembly and disassembly. The simulation performed in this section seeks to model the laser experiment performed by K.-T. Tsen *et al.* by using classical molecular dynamics (MD). The theoretical simulation represents a *first attempt* at examining whether or not ISRS can break apart a viral capsid and if so, under what conditions.

In ISRS, the light scatters inelastically as it interacts with the polarizable bonds in the molecule. In Chapter 5 Section VI, a specific formula for the ISRS force on a single atom was derived from an empirical bond polarizability model [19, 21]. Since the frequency of the light is much higher than any of the vibrational frequencies of the M13 bacteriophage ($\omega << \omega_L$), Equation (5.85) for the ISRS force on a single bond can be time averaged over one period of the light (ω_L) to give

$$F_{i\alpha}^{L}(t) = \left[f_d \hat{d}_\alpha + f_E \hat{E}_\alpha \right] \frac{|E_0|^2}{2} e^{-t^2/\tau_L^2}. \tag{8.1}$$

Equation (8.1) provides an additional time dependent force that can be incorporated into

an MD simulation in addition to the five main MD forces (*e.g.* bond stretching) to describe the coupling of light to the M13 bacteriophage capsid.

The formula for the ISRS force on a bond depends on the electric field strength E_0, the pulse width of the light τ_L, and the two variables f_d and f_E. The variables f_d and f_E are dependent on the orientations of the electric field and bonds as well as the polarizability parameters for the bond. They both can be calculated using Equation (5.86). Although each bond will have unique polarizability parameters, each bond will be assigned the same set of polarizability parameters chosen to reflect the "average" type of bond in the capsid, *i.e.* single bonded carbon-carbon bonds. The parameters used were obtained from Snoke and Cardona [20] and can be found on page 91.

The M13 phage consists of a protein capsid composed of many alpha helix building blocks, each 50 amino acids in length (see Figure 31). The capsid forms a tube with an approximate length of 800 nm. At the center of the tube lies the circular ss-DNA genome of the virus. Although the experiment involved complete M13 phages (capsid plus DNA), the MD simulation is performed on only the capsid in order to reduce the total number of atoms in the MD simulation. In addition, periodic boundary conditions are also used to treat the M13 phage as an infinite tube allowing for further reductions. The lattice vector along the $\hat{z}$ axis (tube axis) was set to 161.5 Å. The two remaining lattice vectors (along the $\hat{x}$ and $\hat{y}$ axes) were set to 200 Å to avoid interactions of one infinite tube with its nearest neighbors.

One final approximation used in the MD simulations is that an implicit solvent model for the interactions of the capsid with water is used instead of explicit water. Although the presence of water is likely to play an integral part in the experiment, especially in regards to the dampening of vibrational modes, an implicit solvent will be used for simplicity.

Explicit water typically requires temperature and pressure coupling algorithms to maintain thermodynamic equilibrium of the system. The presence of an external force (from the light scattering) will drive the system out of equilibrium as energy is transferred from the capsid to the surrounding water. Care must be taken to properly account for the dynamics of the system in a non-equilibrated state. Later studies may be designed to incorporate explicit water into the simulation.

One periodic segment of the M13 capsid was minimized using the generalized Born implicit solvent model [13, 14, 37] and periodic boundary conditions. Using the minimized structure, a series of constant energy constant volume MD simulations were performed using various values for the intensity and pulse width of the light. The MD simulations were around 20 ps in length each, depending on the pulse width used. The microcanonical ensemble is used in order to make estimates of how much energy is delivered to the virus capsid from the light. In addition, one 20 ps constant temperature constant volume MD simulation of the M13 capsid was also performed *without* the ISRS force [Eq. (8.1)] to make sure the capsid is stable over a simulation time of 20 ps.

In the various MD simulations, the intensity was varied from $I = 0.7$ PW/cm^2 (Peta Watts per centimeter squared) to $I = 2.0$ PW/cm^2 and the pulse width was varied from $\tau_L = 10$ fs to $\tau_L = 10$ ps. It is quite obvious that the intensity of light used is enormous. These high intensities were used because lower intensities were unable to break apart the capsid by the end of the simulation. The implications of this will be discussed later. The pulse width is varied to stimulate either high frequency or low frequency phonons of the virus capsid. In Chapter 5 Section VI, a pulse width of $\tau_L \approx T/4$ was shown to stimulate vibrational modes having frequencies near $\omega = 2\pi/T$ the strongest. Ranging τ_L from 10 fs to 10 ps (specifically $\tau_L = 10$ fs, 100 fs, 1 ps, and 10 ps) will allow the effects of stimulating

TABLE XI. The total energy delivered to an M13 capsid from a classical impulsive stimulated Raman scattering simulation. The table represents a collection of energy values for different pulse widths (τ_L) and intensities of the light (I). An asterisk next to the value in the table indicates that the capsid was damaged by the end of the simulation. The intensities are given in PW/cm^2, pulse widths in ps, and the energies in keV. Note the unusual behavior that longer pulse widths deliver less energy to the virus for fixed intensity.

	$I = 0.7$	$I = 0.8$	$I = 0.9$	$I = 1.0$	$I = 1.5$	$I = 2.0$
$\tau_L = 0.01$	2.698	3.517	4.447	5.489	12.470*	22.152*
$\tau_L = 0.10$	0.656	0.793	0.918	1.045	1.733	2.368*
$\tau_L = 1.00$	0.488	0.537	0.587	0.617	0.859*	1.068*
$\tau_L = 10.0$	0.344	0.406	0.429*	0.465*	0.579*	0.656*

both high and low frequency modes of the capsid to be examined.

The starting time of an MD simulation is usually set arbitrarily to $t = 0$. Here, the initial time is set to $t = -5$ ps ($t = -20$ ps for $\tau_L = 10$ ps) so that a single light pulse will interact completely with the M13 capsid during the MD simulation. A time step of 1 fs was used to integrate the equations of motion when $\tau_L = 1, 10$ ps. For the other two cases of $\tau_L = 10, 100$ fs, a 0.1 fs time step was used to insure proper integration over the light pulse.

Table XI shows a compilation of the total energy delivered to the virus for various pulse widths and intensities of light. To calculate the total energy delivered, a simple difference between the final and initial energies (potential plus kinetic) of the capsid was calculated from the MD simulation data. Initially the virus was at rest and had only potential energy. One naively expects the energy delivered to the virus to increase as the pulse width of the laser increases. Scaling estimates for the total energy delivered [Eq. (5.94)] show an inverse relationship. Data points with an asterisk in Table XI indicate that the capsid was damaged for the corresponding pulse width and intensity parameters. Damage meant that the capsid showed an open hole or pore in its surface by the end of the simulation.

To illustrate what destruction of the M13 capsid entailed, Figure 50 shows snapshots of the M13 capsid trajectory over one of the MD simulations. For the MD simulation shown, the pulse width was set to $\tau_L = 1$ ps and the intensity amplitude of the light was $I = 1.5$ PW/cm^2. Similarly, snapshots of the control simulation where no ISRS force was present is shown in Figure 51. The control experiment (Figure 51) exhibited no damage by the end of the simulation. Thus, from a comparison of the ISRS simulation with the control, it is clear that the capsid was broken up as a result of the additional ISRS force.

In Chapter 5 Section VI, a formula [Eq. (5.94)] was derived for the approximate total energy that would be delivered to a viral capsid as a result of inelastic light scattering. This formula was derived from a simple driven harmonic oscillator interpretation of the scattering process. The total energy delivered (TED) was found to be proportional to the intensity of light squared and inversely proportional to the pulse width of the light,

$$TED \propto \frac{I^2}{\tau_L}. \tag{8.2}$$

Logarithmic plots of the data in Table XI are shown in Figure 52. The plots show that, in general, the TED does indeed decrease with increasing pulse width and increase as the intensity of light is increased. The logarithmic plots find that the TED predictions [Eq. (5.94)] compare well to the MD data for short pulses. For longer pulse widths, the MD data does not quite follow the I^2/τ_L dependence predicted. One likely reason for the discrepancy is that the longer pulse widths allow the bonds in the molecule sufficient time to change orientation during the pulse. This will produce a time dependence on the f_d and f_E terms in Equation (8.1), which were assumed constant for the TED derivation in Chapter 5, creating a more complicated dependence on the pulse width and intensity.

Interestingly, the MD results show that the capsid breaks apart for mostly high intensities except for the long 10 ps pulse width. For this pulse width, the MD results find

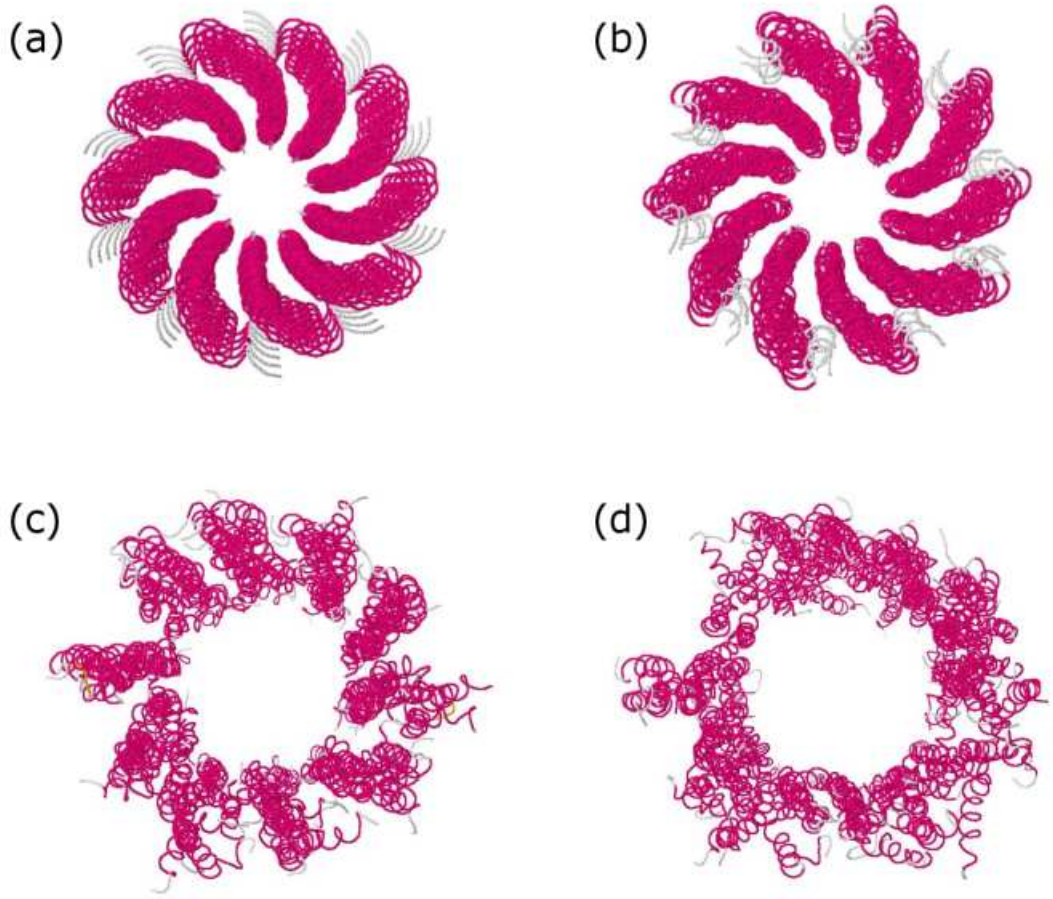

FIG. 50. Four snapshots of the M13 bacteriophage capsid taken from a 20 ps molecular dynamics simulation with no temperature or pressure bath. Impulsive forces from inelastic light scattering are present during the simulation. The pulse width of the light was $\tau_L = 1$ ps and the intensity amplitude of light was $I = 1.5$ PW/cm^2. The maximum amplitude of the intensity occurs at $t = 0$ ps ($I(t) \propto e^{-t^2/\tau_L^2}$). (a) Snapshot at time $t = -5$ ps. (b) Snapshot at time $t = 0$ ps. (c) Snapshot at time $t = 5$ ps. (d) Snapshot at time $t = 15$ ps.

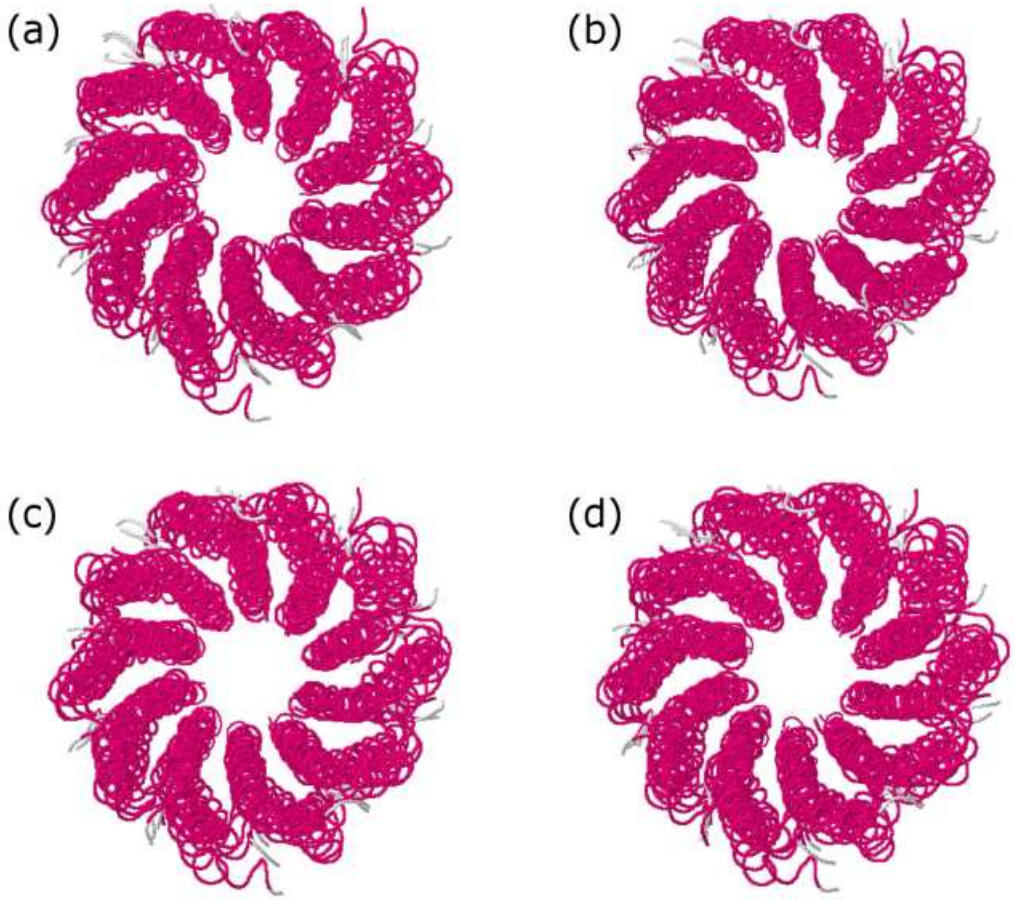

FIG. 51. Four snapshots of the M13 bacteriophage capsid taken from a 20 ps molecular dynamics simulation at constant temperature and constant volume. No impulsive forces from inelastic light scattering are present during the simulation. (a) Snapshot at time $t = 5$ ps. (b) Snapshot at time $t = 10$ ps. (c) Snapshot at time $t = 15$ ps (d) Snapshot at time $t = 20$ ps.

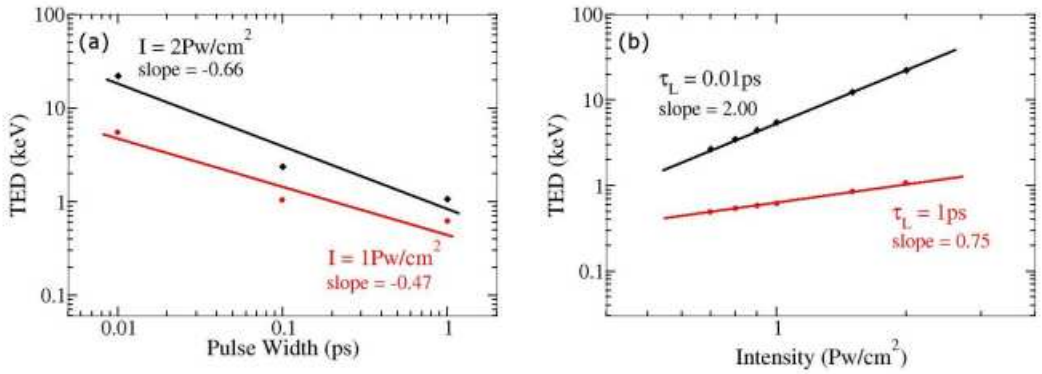

FIG. 52. Various log-log plots of the total energy delivered to the M13 capsid verses pulse width or light intensity. The total energy delivered to the capsid was calculated from molecular dynamics simulations with an external force from light present. (a) Log-log plot of the total energy delivered vs. pulse width. Data for light intensities of $I = 1$ and $I = 2$ PW/cm^2 is shown. (b) Log-log plot of the total energy delivered vs. peak light intensity. Data for pulse widths of $\tau_L = 0.01$ ps and $\tau_L = 1.0$ ps are shown.

that the capsid breaks apart at lower intensities. The driven harmonic oscillator provides a very simple interpretation of this. In Chapter 5 Section VI, the maximum amplitude of the single vibrational mode i *after* stimulation with the driving force (neglecting dampening) was found to be

$$A_i \propto \frac{I\tau_L}{\omega} e^{-\omega^2\tau_L^2/4}. \tag{8.3}$$

A plot of the maximum amplitude for various intensities and pulse widths of light is shown in Figure 53. The plot illustrates the idea of an "amplitude threshold". In order to break apart the viral capsid, it is likely that a few low frequency modes must be excited over a potential barrier. This requires that the modes responsible for the viron destruction must have a certain amplitude in order to overcome the barrier. Figure 53 (a) shows a general plot of the maximum amplitude of a vibrational mode driven with the ISRS force. Figure 53 (b) illustrates the hypothetical amplitude threshold. Light having pulse width and intensity values that are within the white area will create a mode with large enough amplitude to

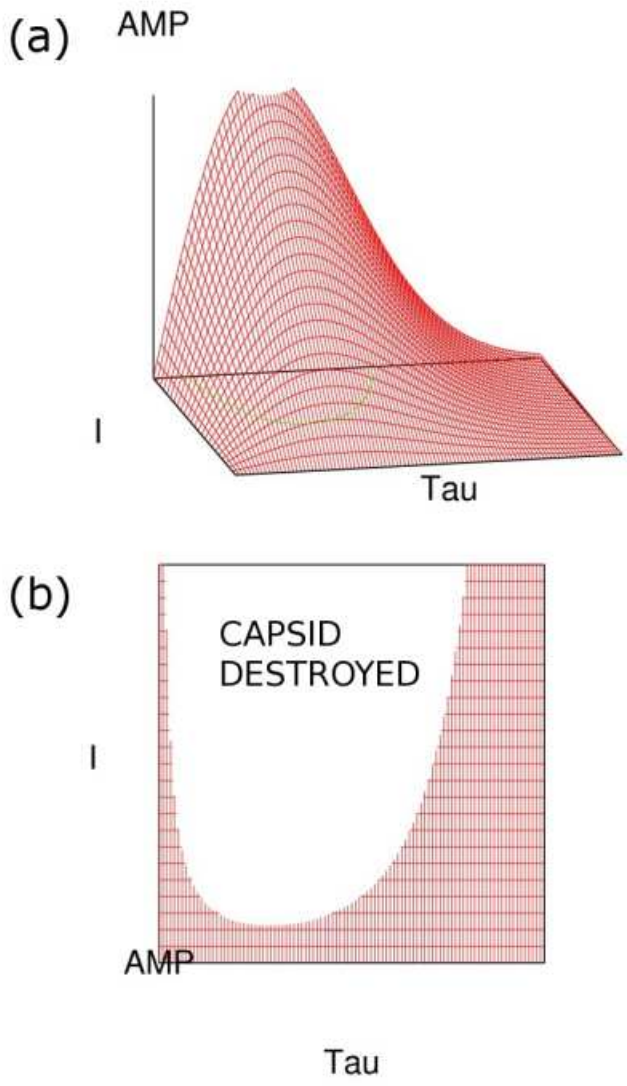

FIG. 53. Theoretical maximum amplitude of an M13 vibrational mode as the result of impulsive light scattering. The theoretical predictions are based on a simple driven harmonic oscillator model [Eq. (8.3)]. (a) Plot of the maximum amplitude for arbitrary intensity and pulse width. (b) Illustration of the "amplitude threshold". Virons scattered with light having intensity and pulse width parameters in the white area will be destroyed.

overcome the potential energy barrier that holds the capsid together. This basic explanation seems to explain the general trend of the data in Table XI.

The data from the MD simulations fits quite well to the driven harmonic oscillator model discussed in Chapter 5 Section VI. However, it is important to note that the light intensities used in the theoretical modeling are extraordinarily high. In the experiment, intensities of no more than 100 GW/cm^2 were sufficient to inactivate M13 phages in solution. One may argue that, due to the simplicity of the bond polarizability model, the ISRS force on a bond is underestimated. However if this were the main reason for the discrepancy then the bond polarizability model would be underestimating the force by roughly a factor of 10^4. Since the bond polarizability parameters $\alpha_\perp$ *etc.* are on the order of an atomic volume, it is difficult to rationalize this explanation.

Another possibility is that the short pulse width of approximately 100 fs used in the experiment is depositing energy into the numerous high frequency modes which then "cascades" down into lower frequency modes via anharmonicity. Once this energy accumulates into the low frequency modes, they will then have sufficient amplitude to overcome the potential barrier that holds the capsid together. This is a plausible explanation since the TED calculation predicts that large amounts of energy can be deposited into the capsid at low intensities by using a shorter pulse width. Thus, it is unlikely that relatively short MD simulations of 20 ps would be able to observe the cascading phenomenon. Nevertheless, the large intensities required in the MD simulations raises doubts about a direct ISRS mechanism inactivating the viral capsid through resonant excitation of its mechanical modes. What fits is that there is a fairly large energy deposition for small pulse widths which must cascade down to a few low frequency modes.

III. FULLY ATOMISTIC ART WITH EXPLICIT SOLVENT

In the ART method, the conformational space of a molecule is searched by following a three step procedure. Starting in a local minimum, the molecule is first excited along a random direction. Here the term random direction means any displacement of the individual atoms in the molecule that disrupts its structure and results in the molecule leaving its current local minimum. The random direction is referred to as the "activation" direction. As the atoms in the molecule are displaced along this direction, the molecular structure is relaxed by allowing the atoms to move along directions that are perpendicular to the activation direction. The purpose of the relaxation is to keep forces on the molecule reasonable and aligned along the activation direction. Periodically the lowest eigenvalue and eigenvector of the Hessian (matrix of second derivatives of the total potential energy) are calculated. The Hessian matrix gives information on the curvature of the potential energy function. When a negative eigenvalue is located it signals the possible location of a saddle point in the energy landscape. Step two now begins by updating the activation direction so that the atoms are moved along the eigenvector of the Hessian corresponding to the negative eigenvalue. The atoms are moved along the new activation direction and relaxed perpendicular to it (as in step 1) until the total force vanishes. Once the total force vanishes, it signals that the molecule has converged to a metastable saddle point. Finally step three commences by minimizing the molecule to a *new* local minimum. A diagram of the three steps of the ART method is shown in Figure 4 (a), (b), and (c) respectively.

This procedure has been successfully used to study the various conformations of glassy materials [28, 29], small peptide sequences [48] and a beta hairpin turn [49]. In the case of the small peptide sequences, the ART method was successful at predicting folded structures that were independent of the starting conformation. It is also important to note

that in addition to a folded structure, the ART method was also able to locate other stable conformations for each of the small peptides.

Being able to locate other stable structures of peptides or peptide aggregates may be important in the study of diseases like Alzheimer's, Creutzfeldt-Jakob Disease (CJD) or Bovine Spongiform Encephalopathy (Mad Cow). For example, some researches have suggested [109] that the key pathology in Alzheimer's disease is the increased ability of Aβ proteins to aggregate into insoluble fibers that form the senile plaques seen in the brains of Alzheimer's patients. At the present time it is unknown under what physiological conditions these senile plaques are formed or if they are even a cause of neuron death, or instead are merely a symptom of the disease. Recent evidence with mice has demonstrated that neuron death is present in locations with and *without* abundant Aβ plaques [113]. Such evidence blurs the cause of the disease requiring further investigation on both theoretical and experimental fronts.

Mousseau and colleagues have already begun to look into these questions by performing an ART simulation of a small portion of the Aβ protein that is believed to be crucial for the formation of the insoluble fiber [47]. In this study, the energy landscape of a set of six peptide chains, each containing a seven amino acid segment of the Aβ protein, were examined using ART. The energy model used was a coarse grained energy model, the optimized potential for efficient peptide-structure prediction (OPEP) [107]. One of the main simplifications of the OPEP model is that it clumps side chain atoms into a single mass or "bead" with electrostatic and van der Waals properties. In addition, the OPEP model uses an implicit solvent model for treatment of any solvent interactions. Their results provided useful information about the possible assembly methods of the insoluble fiber. However, in order to fully explore the conditions that may effect the stability of the insoluble fiber,

an ART method capable of using a fully atomistic structure of the peptide with explicit solvent is necessary.

Some questions arise when considering such an extension. How easily can the ART method be adapted to fully atomistic structure of the molecule? What changes in the algorithm are necessary to incorporate explicit solvent? In order to answer these questions, a fully atomistic ART method with and without explicit solvent can be tested by finding the local minima of a small peptide, alanine dipeptide (ADP). The basic structure of ADP can be described as the amino acid alanine with its N-terminal end attached to CO-CH_3 and its C-terminal end to NH-CH_3. The local minima of ADP are well studied [111, 112] and can be easily compared with.

The most important (and problematic) part of a fully atomistic ART method is in the selection of the activation direction. This will have a direct result on the efficiency in exploring the energy landscape. For example, if the activation directions are selected from the full Cartesian space of three degrees of freedom per atom, the majority of new local minimum are likely to involve the trivial adjustments of single atoms or small groups of atoms. As a result, the ART method will tend to find these local minima much more often (as they are much more numerous) than the ones that result from a large structural change.

In general, the choice of activation directions will be problem specific. For peptide chains such as ADP, a natural choice for the activation directions is the space of Ramachandran angles. In the Ramachandran space, each amino acid in the peptide chain has two degrees of freedom corresponding to the Ramachandran angles of ϕ and ψ. A diagram of the two Ramachandran angles for ADP is shown in Figure 54 (a) and a rotation of the ψ Ramachandran angle is depicted in Figure 54 (b). Since the three dimensional structure of a protein chain can be described in part by its Ramachandran angles, searching

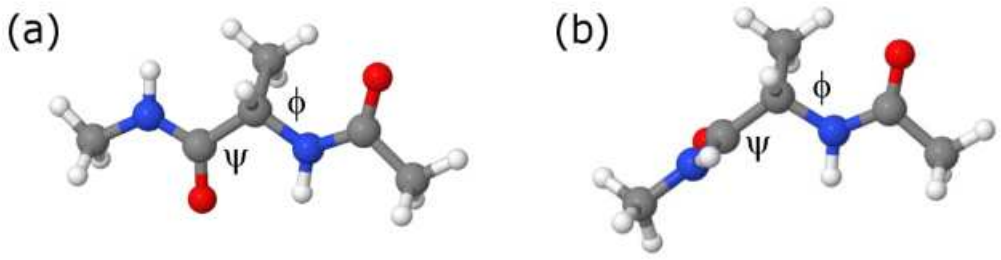

FIG. 54. Diagram of alanine dipeptide and its two Ramachandran angles ϕ and ψ. The molecule is shown in two arbitrary configurations. (a) The alanine dipeptide molecule shown in the configuration $\phi = \psi = 180°$. (b) The alanine dipeptide molecule shown in the configuration $\phi = 180°$, $\psi = 90°$.

the Ramachandran space should be much more efficient than using the standard Cartesian space.

For this choice of activation directions, the energy landscape of ADP must be described as a function of only the two Ramachandran angles, $E(\phi, \psi)$. One possible way to obtain this energy function is to evaluate the AMBER empirical energy function V [Eq. (2.1)] at the atomic coordinates of an ADP molecule that has Ramachandran angles of ϕ and ψ,

$$E(\phi, \psi) = V|_{\phi,\psi} \,. \tag{8.4}$$

It is important to note that Equation (8.4) is not a single valued function. There are many configurations of ADP that have the same Ramachandran angles yet different energies. For example, a simple adjustment of only the side chain atoms of ADP (CH_3) will most certainly result in a different value for $E(\phi, \psi)$. A very simple fix is to only allow movement of the side chain atoms after a new local minimum of $E(\phi, \psi)$ is located by the ART procedure. Thus, during all ART steps, the relative positions of each atom can only be adjusted by rotations about the Ramachandran angles. This will produce a single valued energy function $E(\phi, \psi)$.

This procedure should result in ART finding a structure of the ADP molecule that is close to a local minima in the true energy landscape V. After step three of ART, a quick all atom minimization of V will yield the true local minima.

During the ART procedure, each atom in the molecule only moves if the angles ϕ or ψ are adjusted. Thus, the position of each atom can be given in terms of a rotation matrix $\overleftrightarrow{R}(\phi, \psi)$ as

$$\vec{r}_i = \overleftrightarrow{R}(\phi, \psi)\vec{R}_i, \tag{8.5}$$

where $\vec{R}_i$ are the positions of the atoms when ϕ and ψ are both equal to zero and is a constant. Since a derivation of the matrix $\overleftrightarrow{R}(\phi, \psi)$ is somewhat involved but easy, it is not described here.

Using Equation (8.5) to describe each atom's position, the gradient of the energy landscape necessary for the ART procedure is given by the chain rule:

$$\begin{aligned} \frac{\partial E}{\partial \phi} &= \sum_{i\alpha} \frac{\partial V}{\partial r_{i\alpha}} \frac{\partial r_{i\alpha}}{\partial \phi}, \\ \frac{\partial E}{\partial \psi} &= \sum_{i\alpha} \frac{\partial V}{\partial r_{i\alpha}} \frac{\partial r_{i\alpha}}{\partial \psi}. \end{aligned} \tag{8.6}$$

The term $\partial V/\partial r_{i\alpha}$ is the derivative of the potential energy of the molecule with respect to atom i and direction $\alpha = x, y, z$. These derivatives are simply the force on each atom and are very easily calculated. The calculation of derivative $\partial r_{i\alpha}/\partial \phi$ is also easily calculated using Equation (8.5). A similar calculation can be done to find the second derivatives which are required for the formation of the Hessian matrix in the ART procedure.

Now with the activation directions and energy model discussed, the ART algorithm described above can be used to find the local minima of the fully atomistic ADP molecule. The potential energy (V) required for all of the calculations is calculated using the AMBER 94 force field model [9]. First, a vacuum calculation is performed where there are no inter-

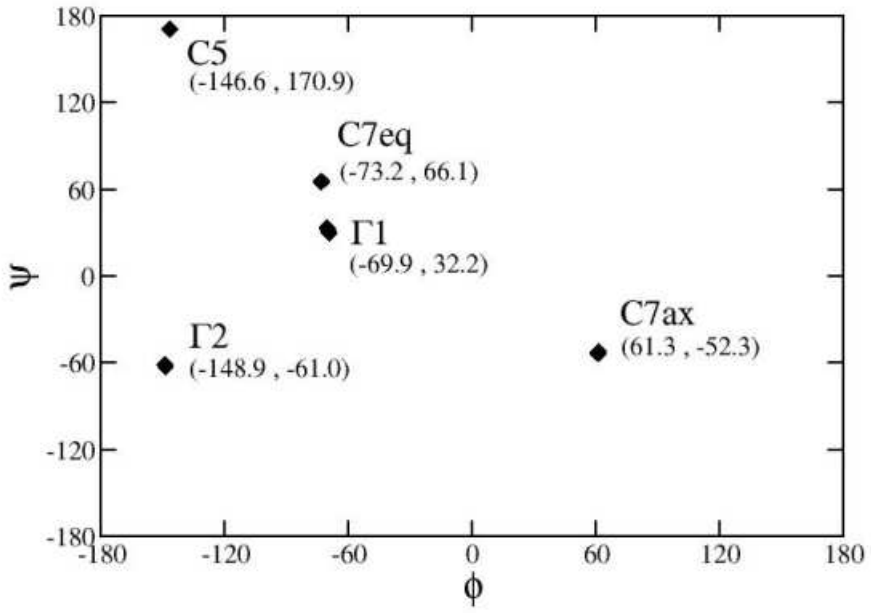

FIG. 55. Ramachandran plot of the various local minima of alanine dipeptide in vacuum which were found by using the activation relaxation technique with an atomistic structure. A total of five minima were found.

actions of ADP with either implicit or explicit solvent. All other electrostatic interactions, *i.e.* those between each atom in ADP, were accounted for. A total of 1000 ART steps were performed on an initially minimized ADP molecule. One ART step corresponds to the three ART procedural steps listed above plus the last minimization of V required to locate a true local minimum. Therefore, each ART step should result in one of the local minima of ADP being found. The minimization procedures in the ART algorithm were stopped once the root mean square (RMS) force was less than 10^{-3} eV/Å. A total of five unique conformations of ADP were found in the vacuum calculation. Figure 55 shows a Ramachandran plot of the five conforms along with their respective Ramachandran angles. Three of the conforms found in other studies [111] ($C7_{eq}$, $C7_{ax}$, and C5) are labeled in the plot. The

TABLE XII. The five conforms and energies of alanine dipeptide in vacuum. The vacuum calculation means that no interactions of alanine dipeptide with either implicit or explicit solvent are accounted for. All other electrostatic interactions are accounted for. The Ramachandran angles ϕ and ψ are given in degrees and energies are listed in electron volts. The lowest energy state is arbitrarily chosen to have an energy of $0eV$.

Conform	ϕ	ψ	Energy
$C7_{eq}$	-73.2	66.1	0.0000
$\Gamma 1$	-69.9	32.2	0.0098
$C7_{ax}$	61.3	-52.3	0.0643
C5	-146.6	170.9	0.0651
$\Gamma 2$	-148.9	-61.0	0.2668

remaining two that could not be compared with other studies are labeled arbitrarily as $\Gamma 1$ and $\Gamma 2$. Table XII summarizes the data.

The same process can be repeated for the case of an implicit solvent. The implicit solvent is modeled using the generalized Born model [13, 14, 37]. A cutoff for the electrostatic interactions is typically used in the generalized Born model. However, due to the small size of ADP, the cutoff was set to an arbitrarily large number so that all interactions were accounted for. A total of 1000 ART steps were performed on an initially minimized structure of ADP. The minimization procedures in the ART algorithm were again stopped once the RMS force was less than 10^{-3} eV/Å. The ART simulation with implicit solvent found a total of nine local minima. Oddly, the C7 conforms are not found with the generalized Born model. This of course is due to the energy model used and not the ART method itself. The generalized Born energy model predicts an additional four conforms (labeled Γ_i) which are not found in other studies [111]. Table XIII summarizes the results. A Ramachandran plot of the conforms is given in Figure 56.

In order to extend the ART method to allow for explicit water, a slight change in the three main steps of the ART algorithm is necessary. The reason for the adjustment is that

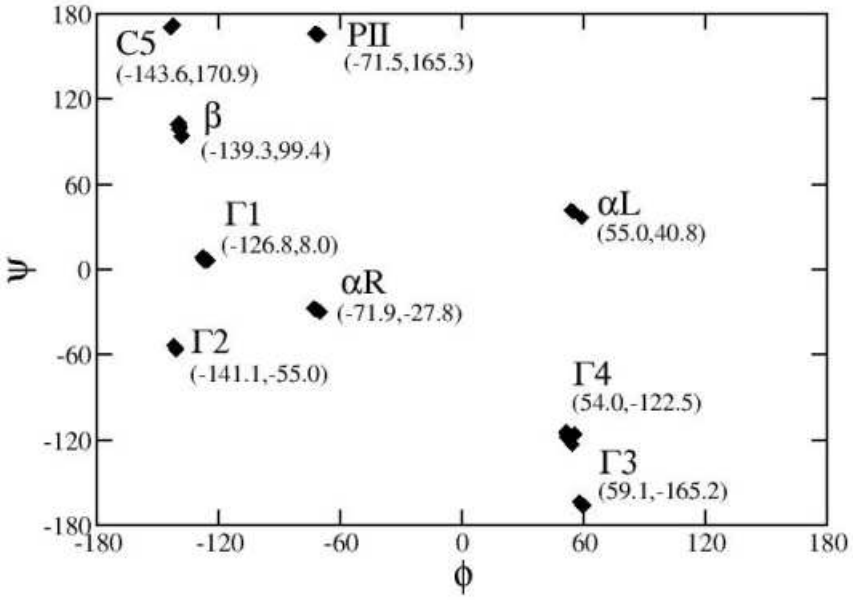

FIG. 56. Ramachandran plot of the various local minima of alanine dipeptide in implicit solvent found using the activation relaxation technique with an atomistic structure. A total of nine minima were found.

as the molecule is moved during the ART procedure, the water must naturally adjust to the molecules new structure to avoid problems such as overlaps of the water with the molecule. To allow the water to adjust naturally, classical molecular dynamics is performed on the water molecules while the ART procedure is performed on the molecule. Since molecular dynamics is being performed on the water, it can be held at a specific pressure and/or temperature. This type of procedure is similar to so called "hybrid" QM/MM methods that employ quantum mechanics on a small segment of the system that is of interest while the rest undergoes classical molecular mechanics [114]. This new algorithm is called Wet-ART.

TABLE XIII. The nine conforms and energies of alanine dipeptide in implicit solvent. The interactions of alanine dipeptide with the solvent (water) was calculated using the generalized Born model. All possible electrostatic interactions were accounted for in the calculation. The Ramachandran angles ϕ and ψ are given in degrees and energies are listed in electron volts. The lowest energy state is arbitrarily chosen to have an energy of $0eV$.

Conform	ϕ	ψ	Energy
αR	-71.9	-27.8	0.0000
PII	-71.5	165.3	0.0219
C5	-143.6	170.9	0.0342
$\Gamma 1$	-126.8	8.0	0.0565
$\Gamma 2$	-141.1	-55.0	0.0778
β	-139.3	99.4	0.1108
αL	55.0	40.8	0.1895
$\Gamma 3$	59.1	-165.2	0.2090
$\Gamma 4$	54.0	-122.5	0.2401

Obviously as the water moves, the local minima of the molecule will shift as well. The idea behind Wet-ART is that these local minima will tend to be located in the vicinity of the various conformations that the molecule can have while in explicit water. Thus, over many samplings of local minima using the three ART steps described above, the Wet-ART method should show a clustering of local minima around the various conformations of the molecule. This clustering is not much different from a true molecular dynamics simulation where the molecule will sample some space around a conformation. The advantage here is that molecular dynamics can require upwards of several *seconds* (or longer) of simulation time to find all conformations of some complex molecules, since barriers between conformations can be higher than k_bT. Since Wet-ART actively searches for new conformations, it should be able to locate them much faster.

To test the Wet-ART method, the procedure is applied to a single ADP molecule surrounded by water molecules. The three ART steps are performed on ADP while molecular dynamics is performed on the surrounding water. The results are then compared with

a 2 ns molecular dynamics simulation of ADP. In both the Wet-ART and regular molecular dynamics calculations, a single ADP molecule was placed in a periodic box with a total of 297 water molecules. The box dimensions were first adjusted using the Nosé-Klein temperature-pressure coupling algorithm [43] to a final average temperature of 300 K and pressure of 1 atmosphere. The final lattice vectors for the periodic box were roughly 20 Å in each direction which placed periodic ADP units no closer than 10 Å away from each other. The final coordinates of the water and ADP molecule represent an equilibrated system and were used as starting coordinates in both the Wet-ART and molecular dynamics simulations.

For the Wet-ART simulation, a total of 6000 ART steps were performed on the ADP molecule while the water was maintained at a temperature of 300 K using a Nosé-Hoover thermostat [40]. The volume of the periodic box was held fixed during the simulation. Equation (8.4) was used as the energy landscape for ADP. Once a local minima of $E(\phi, \psi)$ was found, the water was temporarily frozen, and all atoms of the ADP molecule minimized using V. Coulomb interactions were calculated using the particle mesh Ewald method [12] with an 8 Å cutoff for the direct sum. The minimization procedures on ADP necessary for the ART method were stopped once the RMS force on ADP was less than 5×10^{-3} eV/Å. The local minima found by Wet-ART are plotted on a Ramachandran map in Figure 57. The Wet-ART results show some clumping in two regions (displayed as boxes in Figure 57) of the Ramachandran plot. One region corresponds to the PII conform. In general though, the Wet-ART method seems to have failed to predict definitive conforms. A very simple explanation for the failure is that 6000 ART steps was not sufficient to result in the "clumping" of local minima that was expected.

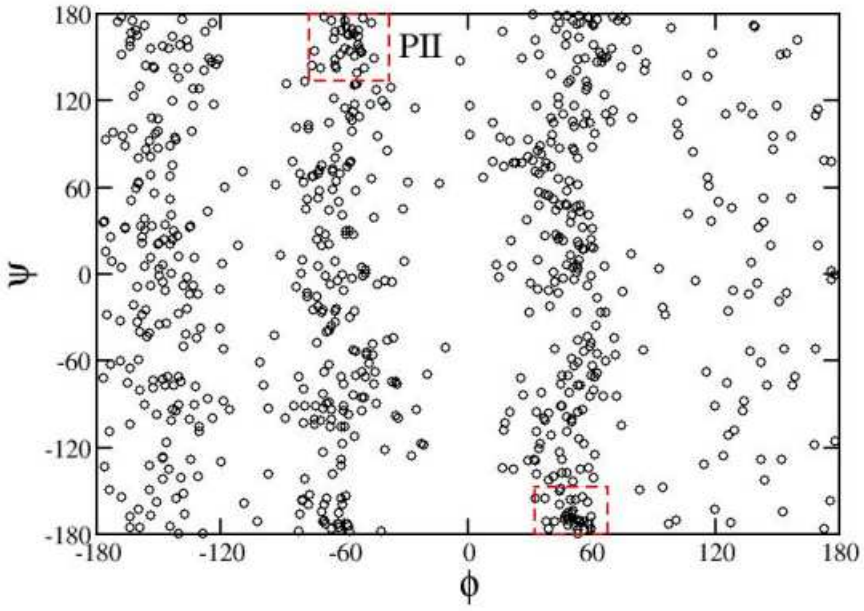

FIG. 57. Ramachandran plot of the various local minima of alanine dipeptide in explicit solvent found using the wet-activation relaxation technique. Many minima are found due to the dynamic nature of the solvent. A clustering of minima is found in the boxed regions.

For the molecular dynamics simulation, the equilibrated structure was maintained at constant volume and constant temperature of 300 K using the Nosé-Hoover thermostat. Coulomb interactions were calculated using the particle mesh Ewald method with an 8 Å cutoff for the direct sum. A total of 2 ns of molecular dynamics was performed using a 1 fs time step. Coordinates of the ADP molecule were output every 1 ps and used to calculate the current Ramachandran angles, ϕ and ψ, of the ADP molecule. A plot of the Ramachandran angles is shown in Figure 58. It is interesting to note that in the molecular dynamics simulation, 2 ns only allows the molecule to essentially sample the PII and αR conforms.

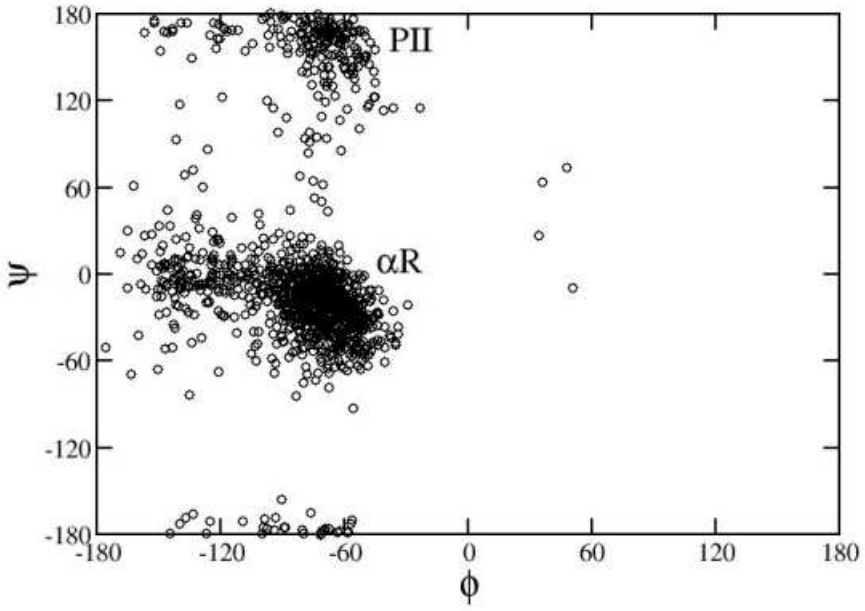

FIG. 58. A two nanosecond molecular dynamics simulation of alanine dipeptide in explicit water. The water was maintained at a constant temperature of 300 K and constant volume. The Ramachandran plot shows that the ADP molecule essentially only visits the PII and αR conforms after two nanoseconds. A broad energy well is visible around the αR conform.

Although the initial results with the small Alanine Dipeptide molecule are somewhat encouraging, using the fully atomistic ART method with implicit solvent or the Wet-ART method on larger peptide chains has been unsuccessful so far. The main reason for the failures has to do with the choice of activation vector (rotations of the Ramachandran angles). When a peptide chain has many amino acids a small rotation about a Ramachandran angle at one end of the chain will produce a large displacement at the other end of the chain. This causes either (i) the chain to overlap with itself or in the case of Wet-ART (ii) the chain to overlap with water molecules. In the Wet-ART procedure, the water molecules that overlap with the peptide chain tend to be unable to reequilibrate themselves with classical molecular dynamics and the Wet-ART algorithm fails. With better choices for activation

directions or the possible creation of “safety checks” in the algorithm, these problems may be alleviated in the future.

CHAPTER 9

CONCLUSIONS

The bulk of the work in this dissertation is centered around a new technique that allows for the *low* frequencies and corresponding displacement patterns of very large molecules or molecular complexes to be obtained with full atomistic detail. The technique, the phonon functional method, is iterative and based on order N strategies used in electronic structure theory to calculate band-structure energies by minimizing an energy functional. A key advantage of the phonon functional method is that the dynamical matrix need not be explicitly stored in computer memory. Instead the method only requires the iterative *operation* of the dynamical matrix on a vector, which can be typically calculated in Order (N) steps. This allows for the lowest vibrational modes of very large molecular systems, such as viruses, to be calculated with full atomistic detail. In addition, the phonon functional method was shown to be quite robust, lacking many of the problems of other iterative techniques [63].

Chapter 2 began the theoretical half of the dissertation with a brief overview of the empirical energy model and the software package developed for all the calculations in this work. Chapter 3 continued the theoretical portion by reviewing some basic group theory concepts which were used for the study of the highly symmetric icosahedral viruses in Chapter 6. In addition, Chapter 3 also presented a computational algorithm capable of calculating the irreducible representation matrices and character table of a group from only a set of rotation matrices that represented the group. The algorithm is somewhat similar to earlier work by Bloker and Dixon [58, 59], but has the advantage of being able to construct both the irreducible representation matrices and character table from a simple diagonalization of a Hermitian matrix. This technique has the potential to highly automate the application of group theory to complex and diverse problems.

The theoretical portion culminated with the development of the phonon functional method in Chapter 4 were the electronic band-structure problem was shown to be mathematically equivalent to the problem of finding the *lowest* frequencies and vibrational mode patterns of a large dynamical matrix. This allowed for the creation of a "phonon energy functional" with the same properties of the electronic energy functional. The phonon functional method was then tested on the ubiquitin protein. Minimization of the phonon energy functional provided the lowest frequency phonon states for the ubiquitin protein. The phonon states calculated with the energy functional compared extraordinarily well with those calculated from a standard diagonalization of the dynamical matrix with errors in the frequencies on the order of 0.01 cm^{-1}.

Chapter 6 began the application portion of the dissertation. In this chapter, the phonon functional method was used to calculate the lowest frequencies and mode patterns of three large virus capsids to atomic detail: the icosahedral satellite tobacco necrosis virus, the icosahedral cowpea chlorotic mottle virus, and the tubular M13 bacteriophage. Although the vibrational properties of viruses have been studied in the past, method developed here has allowed full atomistic detail and semi-quantitative calculations of the Raman scattering cross sections as well. These scattering profiles are useful in identifying vibrational modes that couple strongly to light and thus have the best potential to be resonantly "pumped" with inelastic Raman scattering. In each of the three cases, the Raman scattering cross sections were computed using the atomistic displacement patterns and an empirical bond polarizability model. The Raman cross sections for all of the viruses showed that a variety of the vibrational modes contributed to the overall Raman intensity.

An examination of the lowest frequency modes of the icosahedral viruses found that they were remarkably similar in flavor. Both of the icosahedral viruses studied exhibited

the three low frequency "breathing", "rotational" and "puckering" modes which have symmetry of the irreducible A representation. Low frequency modes with symmetry from other irreducible representations were also found to be similar between the two icosahedral capsids. Further examination of the vibrational mode patterns of the two viruses however illuminated subtle differences between the two. For example, the breathing, rotational, and puckering modes of the satellite tobacco necrosis virus showed a gliding of the β sheets that make up one of the 60 individual proteins of the viral capsid. These types of motions are of course specific to the satellite tobacco necrosis virus due to the unique structure of its protein. Similar motions were not found in the cowpea virus. This leads to the conclusion that the icosahedral geometry determines only the very basic type of motion *i.e.* breathing, puckering *etc.* The internal motions of the protein that result in, for example, the breathing motion of the capsid are dependent on the unique structure of the protein.

A study of the swelling process of the cowpea chlorotic mottle virus capsid was also performed using the phonon functional method. By removing the calcium ions from the optimized capsid structure, several unstable modes were found. Interestingly, unstable modes of the calcium deficient cowpea virus were found in all irreducible representations. Examination of two unstable modes (involving approximately 2000 atoms each) found a preferential expansion of the capsid at the interface between two of the three proteins.

The vibrational modes of the M13 bacteriophage were studied next using both a continuum elastic model and the phonon functional method. This allowed for a direct comparison of a continuum model with an atomistic one. The continuum model was derived in Chapter 5 along with a partner amorphous isotropic bond polarizability model to predict relative Raman intensity profiles. The results found that the continuum model can provide very good predictions of both the general displacement patterns and frequencies for the

first lowest five or six modes. After this, the continuum theory misses many modes that are predicted by the atomistic calculation. Interestingly, the atomistic model found small splittings for a variety of the M13 capsid modes that had multiple degeneracies, such as the string like modes. This was due to the detailed atomistic structure of the capsid which was treated as an isotropic material in the continuum model.

Comparison of the M13 Raman profiles predicted using displacement patterns from continuum theory and the atomistic calculation revealed some discrepancies. The atomistic calculation predicted a single large peak at 5.5 cm^{-1} whose intensity was from mostly radial-torsional modes. The continuum calculation on the other hand predicted a large contribution from an axial mode at roughly 10.4 cm^{-1} and negligible or no Raman intensities in the 0 to 5.5 cm^{-1} frequency range. The lack of Raman intensity in the continuum calculation between 0 to 5.5 cm^{-1} is a result of the model missing modes in this range when compared to the atomistic calculation. Both compared reasonably well to the experimental results which found a single Raman peak at around 8.5 cm^{-1} [84, 85].

An application of the phonon functional method to other large molecules or molecular complexes was demonstrated in Chapter 7. In this chapter, the phonon functional method was used to perform a low frequency normal mode analysis of four periplasmic binding proteins and a complete adenosine triphosphate binding cassette. The normal modes of the periplasmic binding proteins compared well with those predicted by other coarse graining methods such as the elastic network model. There were slight differences though. The most noticeable were found in the two main motions of the two periplasmic binding proteins BtuF and FhuD.

Next, a normal mode analysis was performed on the *A. fulgidus* molybdate ABC transporter. The calculations were performed on the complete atomistic structure which

consisted of the periplasmic binding protein, transmembrane, and nucleotide binding domains. The calculation represents the first known atomistic normal mode analysis of a large molecular complex. Two low frequency modes that could directly contribute to the transport process were found. One low frequency mode was argued (based on experimental evidence) to be involved in signaling the nucleotide binding domain to close. The other low frequency mode was shown to directly influence the opening of the gating region, allowing the molybdate molecule to be transported through the inner cellular membrane.

In Chapter 8, a simulation of the inelastic scattering of light from an M13 bacteriophage capsid was performed using classical molecular dynamics. The results of scattering process were found to follow many of the predictions made using a simple driven harmonic oscillator model in Chapter 5. While it was shown that the capsid can break apart as a result of inelastic light scattering, the intensities required were much higher than those used in experimental studies [25, 26]. One possibility is that the simulation times are much too short to observe the capsid breaking apart at low light intensities. The overall conclusion however was that the light intensities used in the experiments are much too small to directly break the capsid apart without a cascade mechanism of energy redistribution from high frequency to low frequency modes.

Finally, the last section of Chapter 8 examined the activation relaxation technique from the perspective of a fully atomistic structure with explicit solvent. It was concluded that the algorithm used in the traditional activation relaxation technique is not easily generalized to simulations with explicit solvent. This limits the applicability of the technique to simplified models with implicit solvents.

The main work presented in this dissertation, the phonon functional method, has been shown to provide a way to perform a low frequency normal mode analysis of large

systems completely atomistically. The method removes the N^2 dependence on memory that is typically required for a direct diagonalization of the dynamical matrix by only searching for the low frequency states. The phonon functional method significantly increases the number of atoms that can be treated with an atomistic normal mode analysis and may help to provide greater detail in conformational motion and vibrational studies of other large biomolecular systems.

REFERENCES

[1] P.L. Freddolino, A.S. Arkhipov, S.B. Larson, A. McPherson, and K. Schulten, Structure **14**, 437 (2006).

[2] F. Tama and Y.-H. Sanejouand, Protien Engineering **14**, 1 (2001).

[3] O. Marques and Y.-H. Sanejouand, Proteins **23**, 557 (1995).

[4] M.M. Tirion, Phys. Rev. Lett. **77**, 1905 (1996).

[5] F. Tama and C.L. Brooks III, Annu. Rev. Biophys. Biomol. Struct. **35**, 115 (2006).

[6] F. Tama, F.X. Gadea, O. Marques, and Y.-H. Sanejouand, Protiens: Struct. Funct. Genet. **41**, 1 (2000).

[7] F. Tama and C.L. Brooks III, J. Mol. Bio. **345**, 299 (2005).

[8] M. Babincova, P. Sorivong, and P. Babinec, Med. Hypotheses **55**, 450 (2000).

[9] W.D. Cornell, P. Cieplak, C.I. Bayly, I.R. Gould, K.M. Merz, Jr., D.M. Ferguson, D.C. Spellmeyer, T. Fox, J.W. Caldwell, and P.A. Kollman, J. Am. Chem. Soc. **117**, 5179 (1995).

[10] B.R. Brooks, R.E. Bruccoleri, B.D. Olafson, D.J. States, S. Swaminathan, and M. Karplus, J. Comp. Chem. **4**, 187 (1983).

[11] S.J. Weiner, P.A. Kollman, D.A. Case, U.C. Singh, C. Ghio, G. Alagona, S. Profeta, and P. Weiner, J. Am. Chem. Soc. **106**, 765 (1984).

[12] T. Darden, D. York, and L. Pedersen, J. Chem. Phys. **98**, 10089 (1993).

[13] D. Bashford and D.A. Case, Annu. Rev. Phys. Chem. **51**, 129 (2000).

[14] V. Tsui and D.A. Case, Biopolymers **56**, 275 (2000).

[15] M.S. Daw, Phys. Rev. B **47**, 10895 (1993).

[16] F. Mauri, G. Galli, and R. Car, Phys. Rev. B **47**, 9973 (1993).

[17] P. Ordejon, D.A. Drabold, R.M. Martin, M.P. Grumbach, Phys. Rev. B **51**, 1456 (1995).

[18] X.P. Li, R.W. Nunes, and D. Vanderbilt, Phys. Rev. B **47**, 10891 (1993).

[19] S. Go, H. Bilz, and M. Cardona, Phys. Rev. Lett. **34**, 580 (1975).

[20] D.W. Snoke and M. Cardona, Solid. Stat. Comm. **87**, 121 (1993).

[21] S. Guha, J. Menendez, J.B. Page, and G.B. Adams, Phys. Rev. B. **53**, 13106 (1996).

[22] A. Sakaguchi, S. Ferri, and K. Sode, Biochem. and Biophys. Research Comm. **336**, 1074 (2005).

[23] D.N. Sheppard and M.J. Welsh, Physiol. Rev. **79**, S23 (1999).

[24] H.A. Lewis, *et al.*, J. Biol. Chem. **280**, 1346 (2005).

[25] K.-T. Tsen, S.-W.D. Tsen, C.-L. Chang, C.-F. Hung, T.-C. Wu, and J.G. Kiang, Vir. Journ. **4**:50 (2007).

[26] K.-T. Tsen, S.-W.D. Tsen, O.F. Sankey, and J.G. Kiang, J. Phys.: Condens. Matter **19**, 472201-1/7 (2007).

[27] K.-T. Tsen, S.-W.D. Tsen, C.-L. Chang, C.-F. Hung, T.-C. Wu, and J.G. Kiang, J. Phys.: Condens. Matter **19**, 322102-1/9 (2007).

[28] R. Malek and N. Mousseau, Phys. Rev. E **62**, 7723 (2000).

[29] N. Mousseau and G.T. Barkema, Phys. Rev. E **57**, 2419 (1998).

[30] U. Essemann, L. Perera, M.L. Berkowitz, T. Darden, H. Lee, and L. Pedersen, J. Chem. Phys. **103**, 8577 (1995).

[31] P. Ewald, Annals. Phys. **64**, 253 (1921).

[32] I.J. Schoenberg, *Cardinal Spline Interpolation* (Society for Industrial and Applied Mathmatics, Philidelphia, 1973).

[33] M. Born, Z. Phys. **1**, 45 (1920).

[34] W.C. Still, A. Tempczyk, R.C. Hawley, and T. Hendrickson, J. Am. Chem. Soc. **112**, 6127 (1990).

[35] J.D. Jackson, *Classical Electrodynamics* (John Wiley and Sons, Inc., New York, 1998), p. 166.

[36] L. Onsager, J. Am. Chem. Soc. **58**, 1486 (1936).

[37] G.D. Hawkins, C.J. Cramer, and D.G. Truhlar, J. Phys. Chem. **100**, 19824 (1996).

[38] M.P. Allen and D.J. Tildesley, *Computer Simulation of Liquids* (Oxford University Press, Oxford, 1990).

[39] H.C. Anderson, J. Chem. Phys. **72**, 2384 (1980).

[40] W.G. Hoover, Phys. Rev. A **31**, 1695 (1985).

[41] S. Nosé, Mol. Phys. **52**, 255 (1984).

[42] S. Nosé, J. Chem. Phys. **81**, 511 (1984).

[43] S. Nosé and M.L. Klein, Mol. Phys. **50**, 1055 (1983).

[44] H.J.C Berendsen, J.P.M. Postma, W.F. van Gunsteren, A. DiNola, and J.R. Haak, J. Chem. Phys. **81**, 3684 (1984).

[45] M. Parrinello and A. Rahman, Phys. Rev. Lett. **45**, 1196 (1980).

[46] H. Goldstein, *Classical Mechanics* (Addison-Wesley Publishing, London, 1980).

[47] G. Wei, N. Mousseau, and P. Derreumaux, Biophys. J. **87**, 3648 (2004).

[48] G. Wei, N. Mousseau, and P. Derreumaux, J. Chem. Phys. **117**, 11379 (2002).

[49] G. Wei, P. Derreumaux, and N. Mousseau, J. Chem. Phys. **119**, 6403 (2003).

[50] G. Hummer and A. Szabo, J. Chem. Phys. **105**, 2004 (1996).

[51] R.H. Wood, E.M. Yezdimer. S. Sakane, J.A. Barriocanal, and D.J. Doren, J. Chem. Phys. **110**, 1329 (1999).

[52] E.C. Dykeman and O.F. Sankey, Phys. Rev. Lett. **100**, 028101 (2008).

[53] H.W.T. van Vlijment and M. Karplus, J. Chem. Phys. **115**, 691 (2001).

[54] H.W.T. van Vlijment and M. Karplus, J. Mol. Biol. **350**, 528 (2005).

[55] J.F. Cornwell, *Group Theory in Physics* (Academic Press, New York, 1984).

[56] S.L. Altmann and P. Herzig, *Point-Group Theory Tables* (Oxford Science Publications, Oxford, 1994)

[57] D.E. Weeks and W.G. Harter, J. Chem. Phys. **90**, 4744 (1989).

[58] E. Blokker, Int. J. of Quantum Chem. **6**, 925 (1972).

[59] J.D. Dixon, Mathematics of Comp. **24**, 707 (1970).

[60] F. Tama and C.L. Brooks III, J. Mol. Bio. **318**, 733 (2002).

[61] E. Anderson, *et al.*, *LAPACK Users Guide* (Society for Industrial and Applied Mathematics, Philidelphia, 1999).

[62] C. Lanczos, *Applied Analysis* (Dover Publications, New York, 1988).

[63] O.F. Sankey, D.A. Drabold, and A. Gibson, Phys. Rev. B **50**, 1376 (1994).

[64] W.H. Press, B.P. Flannery, S.A. Teukolsky, and W.T. Vetterling, *Numerical Recipes: The art of scientific computing* (Cambridge University Press, Cambridge, 1989).

[65] K.F. Graff, *Wave Motion in Elastic Solids* (Ohio State University Press, New York, 1991).

[66] A.A. Balandin and V.A. Fonoberov, J. Biomed. Nanotech. **1**, 90 (2005).

[67] L.D. Landau and E.M. Lifshitz, *Theory of Elasticity* (Pergammon, New York, 2001).

[68] M. Abramowitz and I.A. Stegun, *Handbook of Mathematical Functions with Formulas, Graphs, and Mathematical Tables* (Dover Publications, New York, 1964).

[69] Y.X. Yan, E.B. Gambel, Jr., and K.A. Nelson, J. Chem. Phys. **83**, 5391 (1985).

[70] E.A. Hewat, E. Neumann, and D. Blaas, Mol. Cell **10**, 317 (2002).

[71] D.M. Belnap, *et al.*, J. Virology **74**, 1342 (2000).

[72] E.C. Dykeman, O.F. Sankey, and K.-T. Tsen, Phys. Rev. E **76**, 011906 (2007).

[73] D.H. Bringloe, A.P. Gultyaev, M. Pelpel, C.W.A. Pleij, and R.H.A. Coutts, J. Gen. Vir. **79**, 1539 (1998).

[74] T.A. Jones and L. Liljas, J. Mol.Biol. **177**, 735 (1984).

[75] C.S. Babu, T. Dudev, R. Casareno, J.A. Cowen, and C. Lim, J. Am. Chem. Soc. **125**, 9318 (2003).

[76] Q. Cui, G.H. Li, J.P. Ma, M. Karplus, J. Mol. Biol. **340**, 345 (2004).

[77] L.O. Liepold, J. Revis, M. Allen, L. Oltrogge, M. Young, and T. Douglas, Phys. Biol. **2**, S166 (2005).

[78] R. Konecny, J. Trylska, F. Tama, D. Zhang, N.A. Baker, C.L. Brooks III, and J.A. McCammon, Biopolymers **82**, 106 (2005).

[79] R.F. Allison, M. Janda, and P. Ahlquist, J. Virology **172**, 321 (1989).

[80] J.E. Speir, J.A. Johnson, S. Munshi, G. Wang, S. Timothy, J.E. Baker, Structure **3**, 63 (1995).

[81] D.A. Marvin, Curr. Opin. Struct. Biol. **8**, 150 (1998).

[82] D.A. Marvin, L.C. Welsh, M.F. Symmons, W.R.P. Scott, and S.K. Strauss, J. Mol. Bio. **355**, 294 (2006).

[83] M. Tachibana, K. Kojima, R. Ikuyama, Y. Kobayashi, and M. Ataka, Chem. Phys. Lett. **332**, 259 (2000).

[84] K.-T. Tsen, E.C. Dykeman, O.F. Sankey, N.-T. Lin, S.-W.D. Tsen, and J.G. Kiang, Vir. Journ. **3**:79 (2006).

[85] K.-T. Tsen, E.C. Dykeman, O.F. Sankey, S.-W.D. Tsen, N.-T. Lin, and J.G. Kiang, Nanotechnology **17**, 5474 (2006).

[86] H. Valadie, J.J. Lacapcre, Y.-H. Sanejouand, and C. Etchebest, J. Mol. Bio. **332**, 657 (2003).

[87] S.I. Sukharev, P. Blount, B. Martinac, and C. Kung, Annu. Rev. Physiol. **59**, 633 (1997).

[88] R.N. Hvorup, B.A. Goetz, M. Niederer, K. Hollenstein, E. Perozo, and K.P. Locher, Science **317**, 1387 (2007).

[89] K.P. Locher, A.T. Lee, and D.C. Rees, Science **296**, 1091 (2002).

[90] R.J.P. Dawson and K.P. Locher, Nature **443**, 180 (2006).

[91] K. Hollenstein, D.C. Frei, and K.P. Locher, Nature **446**, 213 (2007).

[92] C. Kandt, Z. Xu, and D.P. Tieleman, Biochem. **45** 13284 (2006).

[93] B. Mao, M.R. Pear, J.A. McCammon, and F.A. Quiocho, J. Biol. Chem. **257**, 1131 (1982).

[94] Y.H. Lee, M.R. Dorwart, K.R. Hazlett, R.K. Deka, M.V. Norgard, J.D. Radolf, and C.A. Hasemann, J. Bacteriol. **184**, 2300 (2002).

[95] M.C. Lawrence, P.A. Pilling, V.C. Epa, A.M. Berry, A.D. Ogunniyi, and J.C. Paton, Structure **6**, 1553 (1998).

[96] T.E. Clarke, S.-Y. Ku, D.R. Dougan, H.J. Vogel, and L.W. Tari, Nat. Struc. Biol. **7**, 287 (2000).

[97] J. Chen, G. Lu, J. Lin, A.L. Davidson, and F.A. Quiocho, Mol. Cell **12**, 651 (2003).

[98] A.L. Davidson, H.W. Shuman, and H. Nikaido, Proc. Natl. Acad. Sci. **89**, 2360 (1992).

[99] C.F. Higgins and K.J. Linton, Nat. Struc. Mol. Bio. **11**, 918 (2004).

[100] A.A. Aleksandrov, X.-B. Chang, L. Aleksandrov, and J. Riordan, J. Physiol. **528**, 259 (2000).

[101] C.-J. Chen, J.E. Chin, K. Ueda, D.P. Clark, I. Pastan, M.M. Gottesman, and I.B. Roninson, *Cell*, **47**, 381-389 (1986).

[102] K. Ueda, C. Cardarelli, M.M. Gottesman, and I. Pastan, Proc. Natl. Acad. Sci. **84**, 3004 (1987).

[103] L.C. Tsui, Trends Genet. **8**, 392 (1992).

[104] J.-L. Liao and D.N. Beratan, Biophys. J. **87**, 1369 (2004).

[105] E.O. Oloo, C. Kandt, M.L. O'Mara, and D.P. Tieleman, Biochem. Cell Biol. **84**, 900 (2006).

[106] P.C. Smith, *et al.*, Mol. Cell **10**, 139 (2002).

[107] A. Liwo, M.R. Pincus, R.J. Wawak, S. Rackovsky, and H.A. Scheraga, Protein Sci. **2**, 1715 (1993).

[108] G.D. Rose, P.J. Fleming, J.R. Banavar, and A. Maritan, Proc. Nat. Acad. Sci. **103**, 16623 (2006).

[109] A. Mudher and S. Lovestone, Trends Neurosci. **25**, 22 (2002).

[110] C.B. Anfinsen, Science **181**, 223 (1973).

[111] H. Freedman and T.N. Truong, J. Chem. Phys. **121**, 12447 (2004).

[112] P.J. Rossky and M. Karplus, J. Am. Chem. Soc. **101**, 1913 (1979).

[113] C. Schmitz, *et al.*, Am. J. Pathology **161**, 1495 (2004).

[114] M.S. Formaneck, G. Li, X. Zhang, and Q. Cui, J. Theor. Comput. Chem. **1**, 53 (2002).

[115] V.A. Dubrovsky and V.S. Morochnik, Izv. Acad. Sci. USSR, Phys. Solid Earth **17**, 494 (1981).

[116] D.B. Murray and L. Saviot, J. Phys.: Conf. Series **92**, 012036 (2007).

[117] G. Lamm and A. Szabo, J. Chem. Phys. **85**, 7334 (1986).

[118] T. Rössler and J.B. Page, Phys. Rev. B **62**, 11460 (2000).

APPENDIX A

FUTURE STUDIES

I. IMPROVEMENTS IN NORMAL MODE ANALYSIS

As seen in this dissertation, atomistic normal mode calculations of large biomolecules with the phonon functional method presents an advance from normal mode calculations which utilize coarse graining techniques. However, their is still room for much improvement in the normal mode analysis technique itself. Here, some of the main deficiencies of the normal mode analysis technique that can be improved upon in future work are highlighted.

A. Effects of Water

The main deficiency of the normal mode calculations presented in this dissertation is due to the fact that water was only included implicitly. Further, only the electrostatic effects were considered while the damping and hydrodynamic effects were ignored. Most biological molecules are surrounded by water which will have an effect on the vibrational properties of the molecule. At the present time, the hydrodynamic and damping effects of water on the vibrational modes of virus capsids have only been examined with continuum type theories. Balandin and Fonoberov [66] have studied the damping effects of the cylindrical M13 bacteriophage in water (were the water is treated as an elastic medium) using the complex-frequency approach of Dubrovsky and Morochnik for an elastic sphere embedded in an elastic medium [115]. Their results found frequency shifts on the order of a few (≈ 2 cm^{-1}) wave numbers. Murray and Saviot also applied the Dubrovsky approach but to spherical shaped capsids [116]. Their results also found similar frequency shifts in the mechanical modes.

One possible way to include at least the damping effects of the water in the atomistic normal mode analysis is to use the Langevin dynamics technique discussed by Lamm and Szabo [117]. The Langevin scheme appears to be well suited for the study of the low frequency mechanical modes of viral capsids and may be able to be adapted for use in the

phonon functional method. If successful, the method would provide reasonable estimates of frequency shifts due to water damping.

The hydrodynamic effects of water however way prove more difficult to incorporate in an atomistic model. With further improvements however, the normal mode analysis technique may be able to provide a much more realistic picture of the low frequency vibrations of large biomolecules through the incorporation of the hydrodynamic and damping effects of the surrounding solvent.

B. Effects of Anharmonicity

A second problem with the normal mode analysis technique is due to the use of the harmonic approximation. In Chapter 4 Section II, it was shown that the harmonic approximation resulted from a truncation of the Taylor expanded potential energy of a molecule. Thus the approximation only holds for *small* oscillations about equilibrium and lacks the anharmonic higher order terms which can describe effects such as the coupling between individual modes. One of the main problems with this is that at thermal equilibrium, the amplitudes of the low frequency modes of a viral capsid are most likely higher than what can be treated accurately with a harmonic approximation. The maximum thermal amplitude of a low frequency vibration at equilibrium, A_m, can be approximated from $k_bT = m_e\omega^2 A_m^2/2$ where m_e is the effective mass of the molecule. For the molybdate ABC transporter (see Chapter 7 Section III) the main low frequency mode was found at roughly 2 cm^{-1}. Setting the effective mass equal to the approximate mass of the full transporter, $m_e \approx 10^{-22}$ kg, one finds a maximum thermal amplitude of roughly $A_m = 0.2$ Å at 300 K.

The anharmonicity of the potential energy of the ABC transporter can be examined by moving along an eigenvector of the dynamical matrix. Figure 59 shows the potential energy $U(Q\eta)$, where η is the displacement vector of the 2.62 cm^{-1} normal mode of the ABC

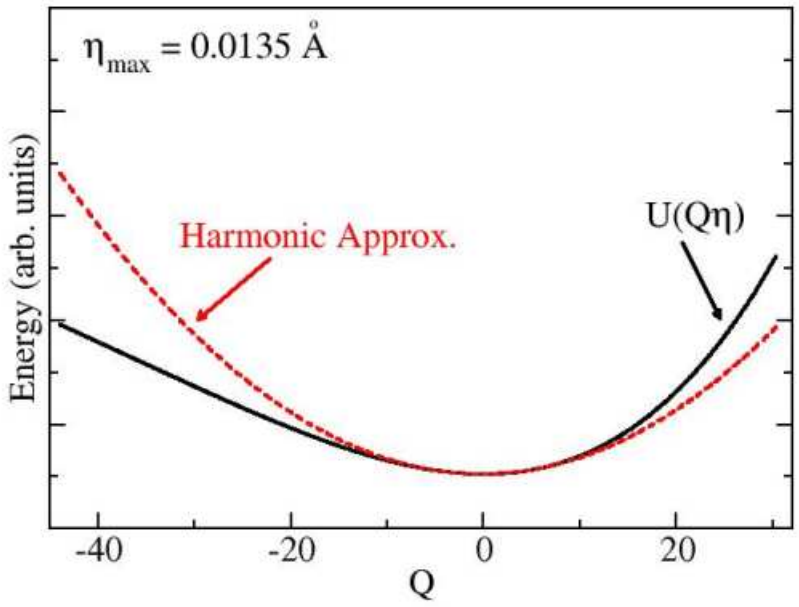

FIG. 59. Deviation of the potential energy U of the molybdate ABC transporter from the harmonic approximation as the molecule is moved (by an amount Q) along the displacement pattern corresponding to the eigenvector of the dynamical matrix with eigenvalue of 2.62 cm^{-1}. The displacement η is distributed over all atoms and the maximum component of any atom is 0.0135 Å. The solid black line is the true potential while the dashed red line corresponds to the harmonic approximation. The potential begins to deviate from the harmonic approximation when the maximum displacement of any atom is around 0.1 Å.

transporter calculated from the dynamical matrix, as a function of displacement Q along the mode. One can see that the potential begins deviating from the harmonic approximation (shown as the dashed red line) quite early, when the maximum displacement of any atom is around 0.1 Å.

Anharmonicity is also likely to play an important role in the impulsive stimulated Raman scattering (ISRS) of virus capsids, especially if ISRS is indeed exciting large amplitude vibrations of the capsids (see Chapter 8 Section II). Rössler and Page showed that in an anharmonic crystal, intrinsic localized modes (local solitons) can be excited by applying

a series of femtosecond pulses [118]. Thus, it may be possible to produce a localized mode in a virus capsid through a series of low intensity pulses that results in localized capsid damage and deactivation. Localized intrinsic modes presents another plausible explanation, in addition to the cascade theory, for the experimental observation of virus inactivation with ISRS. However an understanding of the anharmonic properties of a virus capsid is necessary in order to test such a hypothesis.

From the above arguments it is quite clear that although the phonon functional method has allowed for the study of low frequency mechanical vibrations of large biomolecular systems to atomic detail, improvements can still be pursued.

II. SAGUARO PROGRAM

At the present time, the *Saguaro* program is operational and has no known errors. However, it is expected that the program will undergo further development, most likely for the purposes of adding additional features. This section outlines how to run *Saguaro* and its basic coding structure since an extensive user manual on the program does not exist at the present time. An abbreviated manual can be downloaded from the *Saguaro* website (http://physics.asu.edu/atofs/Saguaro).

A. Running Saguaro

To run *Saguaro*, at least four files must be created by the user. Three of the files, the parameter file, the coordinate file, and the molecule file, describe the system to be simulated while the fourth file, the options file, contains information on what type of *Saguaro* simulation will be run. The options file is a free form format file where options such as constant temperature can be used by changing the value of an "option flag", with multiple option flags separated by a comma (*i.e.* iflag1=0, iflag2=0). Each flag has a default value that is set in the subroutine getoptions. Once the program starts, these values are updated

by reading the options file using a name list format. Any option flags not present in the file will cause there default value to be used. A list of all the options present in the *Saguaro* program can be found in the OPTIONS file located in the main program directory and on the *Saguaro* website. An example of an options file can be found in the tutorial folder in the main directory.

The remaining three files contain information about the system to be simulated. The parameter file contains information on the spring constants, partial charges, atomic masses, and van der Waals parameters for the atoms in the system. The coordinate file contains the atom types and atomic coordinates for every atom in the system. If the system is periodic, lattice vectors are listed at the end of the file after the coordinates. The molecule file contains information on the number of molecules in the system and if that molecule is solvent or solute. Solvent molecules are labeled with an "S" while solute molecules are labeled with an "A". If counter ions are present, these are distinguished with a "C" in the molecule file. The format of each of these three files can be found in the README file located in the main *Saguaro* directory or in the abbreviated manual located on the *Saguaro* website. Examples of these three files can also be found in the tutorial folder. The easiest way to create these three files is to use the pepalyze (peptide analyze) program located in the tools folder in the main directory. The program will create parameter, coordinate, and molecule files of a protein from its protein data bank (PDB) file.

Once the coordinate, parameter, and molecule files have been created by the user and the options for the *Saguaro* run set in the options file, the program can be executed by typing

```
Saguaro.x -i options -c coordinates -p parameters -m molecule
```

on the command line where options, coordinates, parameters, and molecule are the names

of the four files created by the user. These names are passed into the program on the command line with the flags -i, -c *etc.* Default file names exist for all of these files so if one of them is not specified, for example the parameter file, the program will attempt to open a file with the default name (sys.parm in the case of the parameter file).

At the end of the run, *Saguaro* will create various output files. Names for the output files that are different from the default names can be specified using similar flags on the command line (see the main code saguaro.f90 for the specific flags). Two files that will always be created are the output file, which contains information on the options that were set for the simulation and any errors, and the restart file which contains the current coordinates of the system (eigenvectors for the case of a vibrational analysis run). The restart file can be used (for example) to continue a molecular dynamics run by using the restart file as the initial coordinate file.

For more information on running *Saguaro*, the user should consult one of the four tutorials located in the tutorial directory of the *Saguaro* package.

B. Coding Structure

The *Saguaro* code, written in FORTRAN 90, consists of a main program wrapper saguaro.f90 which reads in the option, parameter, molecule, and coordinate files by calling subroutines getoptions and getparams. The system is then setup for its appropriate run. For example, arrays necessary for the particle mesh Ewald routine would be allocated and formed by calling pmesetup, if the user specifies this option. Next one of the four subroutines mdynamics, feperturb, art, or vibes is called to perform the appropriate simulation specified by the user in the options file. Once the simulation is complete, the main program wrapper closes any open files then ends. There are many subroutines (approximately 40-50) in *Saguaro* and to go through the details of each would be time consuming. Instead, only

details about the code that can be found in the main directories (ENERGY, INOUT, SETUP, *etc.*) will be given.

The directory CONSTRAINTS contains code required to implement constraints on velocities and/or atomic positions during constant temperature, constant pressure molecular dynamics runs. These subroutines are only called by mdynamics.

The ENERGY directory contains all of the subroutines that are used to calculate the total energy of the system and the forces on each atom. The subroutine energy does the complete force and energy calculation by calling individual potential energy subroutines such as bond which calculates the energy and forces on atoms due to bonds.

The directory FEP (free energy perturbation) contains special energy subroutines very similar to the ones in the ENERGY directory. The difference is that the energy subroutines in FEP also calculate the derivative $dE/d\lambda$ that is required for thermodynamic integration.

The HESSIAN directory contains all of the subroutines that are used to calculate the dynamical matrix operating on a vector. The subroutines dynamicalu and gdynamicalu calculate the dynamical and group dynamical matrices operating on a vector (respectively) by calling individual subroutines such as bonddu which calculate the contribution to the dynamical (or group dynamical) matrix times a vector from only the bond potential energy terms.

The directory INOUT is were the subroutines such as getoptions and getparams are located. These subroutines read and write information to files.

The MAPPING directory contains the neighbormap and symmetrymap subroutines which calculate the neighbor maps for systems with periodicity (neighbormap) or systems with symmetry of a group (symmetrymap).

The MISC directory is were various miscellaneous subroutines such as bspline (which calculates and returns the bspline function of an argument) or gramschmidt (which makes a set of vectors orthogonal) can be found. These subroutines are usually called by many other subroutines.

The directory SETUP has all of the subroutines that setup various things such as the particle mesh Ewald arrays (pmesetup) or group theory basis vectors (setupgt). These are usually called in the main saguaro program wrapper.

Finally, the directory SIMS contains the main code for the four simulations that *Saguaro* can perform. Molecular dynamics is performed by the subroutine mdynamics, free energy perturbation by feperturb, activation relaxation technique by art, and atomistic vibrational analysis with the phonon functional method by vibes.